

Cover Page



Universiteit Leiden



The handle <http://hdl.handle.net/1887/28962> holds various files of this Leiden University dissertation

**Author:** Sande, Jesse van de

**Title:** Dawn of the red and dead stellar kinematics of massive quiescent galaxies out to  $z = 2$

**Issue Date:** 2014-10-01

# Dawn of the Red and Dead

Stellar Kinematics of Massive Quiescent Galaxies out to  $z = 2$



# Dawn of the Red and Dead

Stellar Kinematics of Massive Quiescent Galaxies out to  $z = 2$

## Proefschrift

ter verkrijging van  
de graad van Doctor aan de Universiteit Leiden,  
op gezag van Rector Magnificus prof. mr. C.J.J.M. Stolker,  
volgens besluit van het College voor Promoties  
te verdedigen op woensdag 1 oktober 2014  
klokke 15:00 uur

door

**Jesse van de Sande**  
geboren te Meppel  
in 1986

## Promotiecommissie

**Promotores:** Prof. dr. M. Franx  
Prof. dr. M. Kriek (University of California at Berkeley, USA)

**Overige leden:** Prof. dr. H. J. A. Röttgering  
Prof. dr. J. Schaye  
Prof. dr. S. C. Trager (Rijksuniversiteit Groningen)  
Prof. dr. P. G. van Dokkum (Yale University, USA)  
dr. R. J. Bouwens  
dr. J. Brinchman

*"The Universe is big, it's vast, and complicated, and ridiculous,  
and sometimes — very rarely — impossible things just happen  
and we call them miracles ... and, that's the theory."*

-- The Doctor

Dit proefschrift werd ondersteund door de Nederlandse  
Organisatie voor Wetenschappelijk Onderzoek (NWO)  
en het Leids Kerkhoven Bosscha fonds.

Omslagontwerp: Pepijn van der Linden, Toek Design.

ISBN: 978-94-6259-326-8

© 2014 Jesse van de Sande

# Contents

<b>1</b>	<b>Introduction</b>	<b>1</b>
1.1	From galactic to extragalactic astronomy . . . . .	1
1.2	Early universe & structure formation . . . . .	2
1.3	Local universe . . . . .	3
1.4	High-redshift observations . . . . .	4
1.5	Massive galaxies in the early universe . . . . .	6
1.6	Current issues . . . . .	8
1.7	Thesis summary . . . . .	10
<b>2</b>	<b>The stellar velocity dispersion of a compact massive galaxy at <math>z = 1.80</math></b>	<b>15</b>
2.1	Introduction . . . . .	16
2.2	Observations and reduction . . . . .	16
2.3	Stellar population and structural properties . . . . .	17
2.3.1	Stellar population properties . . . . .	17
2.3.2	Size measurement . . . . .	19
2.3.3	Velocity dispersion . . . . .	19
2.4	Evolution . . . . .	20
2.5	Conclusions . . . . .	23
<b>3</b>	<b>Stellar kinematics of <math>z \sim 2</math> galaxies</b>	<b>27</b>
3.1	Introduction . . . . .	28
3.2	Data . . . . .	29
3.2.1	Target selection . . . . .	29
3.2.2	Imaging . . . . .	32
3.2.3	Spectroscopic observations . . . . .	33
3.2.4	Spectroscopic reduction . . . . .	33
3.3	Structural properties and stellar populations . . . . .	38
3.3.1	Stellar population properties . . . . .	38
3.3.2	Velocity dispersions . . . . .	40
3.3.3	Surface brightness profiles . . . . .	41
3.3.4	Dynamical masses . . . . .	42
3.4	Compilation of kinematic studies . . . . .	42
3.4.1	Low-redshift sample . . . . .	42
3.4.2	Intermediate- and high-redshift sample . . . . .	42
3.5	Are stellar masses reliable? . . . . .	43
3.6	Structural evolution of quiescent galaxies . . . . .	45



3.6.1	Bias towards compact galaxies . . . . .	45
3.6.2	Evolution in size . . . . .	47
3.6.3	Evolution in velocity dispersion . . . . .	48
3.6.4	Evolution in mass density . . . . .	49
3.7	Discussion . . . . .	51
3.8	Summary and conclusion . . . . .	53
3.A	Robustness of the velocity dispersion measurements . . . . .	54
3.A.1	Dependence of the velocity dispersion on the wavelength range . . . . .	56
3.A.2	Dependence of the velocity dispersion on the template choice . . . . .	56
3.A.3	Dependence of the velocity dispersion on the order of the additive polynomial . . . . .	58
3.A.4	Systematic errors on the velocity dispersion at low signal-to-noise . . . . .	59
3.A.5	Dependence of the velocity dispersion on the SPS models and template construction . . . . .	61
3.B	Aperture corrections for velocity dispersion measurements . . . . .	62
<b>4</b>	<b>The fundamental plane of massive quiescent galaxies out to <math>z \sim 2</math></b>	<b>69</b>
4.1	Introduction . . . . .	70
4.2	Data . . . . .	70
4.3	The fundamental plane . . . . .	72
4.4	Correcting for sample bias . . . . .	74
4.5	Evolution of the $M/L$ . . . . .	76
4.6	Discussion . . . . .	77
4.7	Conclusion . . . . .	78
<b>5</b>	<b>The relation between <math>M/L</math> ratio and color for massive quiescent galaxies</b>	<b>81</b>
5.1	Introduction . . . . .	82
5.2	Data . . . . .	84
5.2.1	Low and high-redshift sample . . . . .	84
5.2.2	Derived galaxy properties . . . . .	85
5.3	Empirical relation between the $M/L$ and color . . . . .	86
5.3.1	Color and the $M/L$ evolution . . . . .	86
5.3.2	Empirical relation between the $M/L$ and the color . . . . .	88
5.4	Comparisons with stellar population synthesis models . . . . .	90
5.4.1	FSPS models . . . . .	92
5.4.2	BC03 models . . . . .	92
5.4.3	Ma11 models . . . . .	94
5.4.4	Summary . . . . .	94
5.5	Constraints on the IMF . . . . .	95
5.5.1	IMF comparison . . . . .	95
5.5.2	Broken IMF . . . . .	97
5.6	Discussion and comparison to previous studies . . . . .	99
5.6.1	SED derived $M/L$ . . . . .	99
5.6.2	Intrinsic scatter . . . . .	100
5.6.3	Comparison to literature . . . . .	101

---

5.6.4	Constraints on the IMF . . . . .	102
5.6.5	Dark matter . . . . .	102
5.6.6	Metallicity & complex star formation histories . . . . .	102
5.6.7	Systematic sample variations . . . . .	103
5.7	Conclusions . . . . .	103
	<b>Nederlandse samenvatting</b>	<b>107</b>
	<b>Curriculum Vitae</b>	<b>117</b>
	<b>Nawoord</b>	<b>119</b>



# 1

## Introduction

### 1.1 From galactic to extragalactic astronomy

On a dark clear night, one can observe a dim white strip of light crossing over the night sky from horizon to horizon: the Milky Way. Galileo Galilei, in the 17th century, was the first who pointed his telescope at this white cloud of light and discovered that it consisted of a huge number of stars. Inspired by the heliocentric model of our solar system from Nicolaus Copernicus, Immanuel Kant demonstrated in the mid-18th century, that this cloud in many ways resembled our solar system, but on a larger scale. In a similar way that the Planets are gravitationally bound to the Sun, he argued that the stars in the Milky Way could be gravitationally bound to each other, forming a disk-like structure. Thus the idea of a galaxy was born, although it was not fully understood. Kant furthermore proposed that our Galaxy, the Milky Way, might not be the only such cluster of stars, but that the faint elliptical nebulae in the sky could be individual *island universes*.

Towards the end of the eighteenth century Charles Messier (1781) compiled a catalog of the brightest 109 nebulae in the northern sky, of which the Andromeda Nebulae, or Messier 31, is the most famous example. William Herschel (1786) extended this catalog to nearly 5000 nebulae, but also made the distinction between unresolved nebulae and planetary nebulae. He was convinced that the unresolved nebulae were Kant's *island universes*, whereas the planetary nebulae resembled a single star with glowing gaseous material surrounding it. In later studies with more advanced telescopes the Earl of Rosse (William Parsons; 1845) revealed that even the unresolved nebulae consisted of two classes: elliptical and spiral. While there was no general consensus on the nature of these nebulae, there were two main rivaling ideas. Firstly, these nebulae could be part of our Milky Way as advocated by Harlow Shapley. Secondly, they could be extragalactic *island universes* similar to our Milky Way, a theory supported by Heber Curtis.

Spectroscopy on spiral nebulae provided valuable insight in favor of nebulae being extragalactic stellar systems. First, absorption features in the spectra resembled those of normal stars. Moreover, the overall spectral shape was consistent with the shape expected from a large population of stars (e.g., Slipher 1918). Secondly, the spectral lines of the nebulae were Doppler shifted, with inferred velocities many times larger than the stars in our Milky Way. Edwin Hubble 1922 finally settled the debate. By measuring the periods of the variable Cepheids stars in the outskirts of the Andromeda Nebula, he was able to estimate a distance of 300 kiloparsecs, which placed M31 far outside of our Milky Way. With this fundamental measurement, it was finally established that the spiral and elliptical nebulae were actually galaxies and that our Milky Way was not the only galaxy in the universe. Now, nearly a hundred years later, our knowledge of galaxies and galaxy formation has vastly expanded.

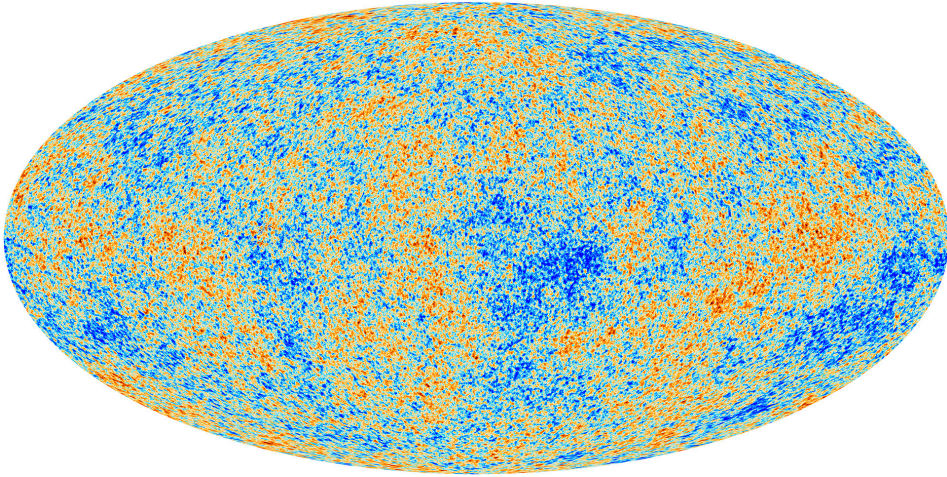


**Figure 1.1:** The anisotropies of the cosmic microwave background (CMB) radiation as observed by the Planck satellite. The CMB is a snapshot of the oldest light in our universe, from when it was only 380 000 years old. The color scale shows tiny temperature fluctuations on the order of  $10^{-5}$  Kelvin, while the early-universe was still homogeneous and isotropic. These small fluctuations will grow into galaxies and clusters of galaxies. *Image: ESA & Planck Collaboration.*

## 1.2 Early universe & structure formation

The cosmic cosmic microwave background radiation (CMB; Gamow 1948; Hu & White 1996; Bennett et al. 2013) is the oldest light in the universe. According to the current theory, the CMB is leftover radiation from the Big Bang, which was emitted only 380,000 years after the beginning of the universe. After the Big Bang, 13.8 billion years ago, the universe started expanding and consequently cooling down, which enabled protons and electrons to form neutral atoms. From that moment on the universe became transparent as atoms could no longer absorb the thermal radiation. The first light that escaped is now still visible as a blackbody spectrum at a temperature of  $2.72548 \pm 0.00057$  Kelvin, which is what is observed in the CMB radiation.

Due to the rapid early expansion, or cosmic inflation, the early universe was homogeneous and isotropic. On large scales the observed CMB is therefore very smooth; on small scales temperature fluctuations on the level of  $10^{-5}$  exist (Figure 1.1). As our universe expanded and cooled over time, these small density perturbations grew through gravitational instabilities into the first galaxies. The smaller building blocks that form first then hierarchically merge into larger galaxies and clusters of galaxies. This is the foundation for the hierarchical structure formation model.

As the early universe was still extremely hot, normal baryonic matter was unable to cool and collapse. Cold dark matter enabled galaxy formation at this time, and is now considered to be the standard model or Lambda Cold Dark Matter ( $\Lambda$ CDM) model of structure formation. In this theory only  $\sim 4\%$  of the energy density in the universe is made up of baryonic matter.

Gas, stars, dust are all made from baryonic matter. The remaining 96% of the universe's energy density consists of dark energy ( $\sim 75\%$ ), and dark matter ( $\sim 21\%$ ). While the nature of dark energy and dark matter remains unknown, clues for its existence are plentiful (e.g., Riess et al. 1998; Perlmutter et al. 1999; Clowe et al. 2006; Bradač et al. 2006; Bennett et al. 2013).

Within the gravitational collapsed perturbations, or dark matter haloes, the baryonic gas cools, and forms the first stars, giving rise to a visible galaxy. While the collapse of CDM is easily predicted from the theory of gravitation, the complex physics associated with star formation, stellar and nuclear feedback, and various other physical processes, is still not fully understood. Thus our theory on the formation of baryonic structure in the universe is still far from complete.

### 1.3 Local universe

While the extragalactic nature of many nebulae was only discovered in the 20th century, the large diversity in morphology was already identified long before (e.g., Herschel 1786; Earl of Rosse, 1845). Hubble (1936) was the first to construct a classification scheme, one that is still in use today. In Hubble's classification scheme, galaxies are classified by morphology into two separate classes: elliptical and spiral galaxies. Ellipticals vary in shape from round to elongated, with a smooth distribution of red-dominated light. Spirals consist of a red-central concentration, or bulge, with a surrounding disk with blue spiral structure. Roughly half of all spiral galaxies exhibit a prominent bar feature in their center which can extend out to the spiral arms. Based on his morphological classification, Hubble suggested that galaxies evolved from ellipticals into spirals. Hence, elliptical galaxies are commonly referred to as early-types, whereas spiral galaxies are known as late-type galaxies.

Galaxy morphology also correlates with other galaxy properties such as age, mass, and dynamics. In the local universe, ellipticals are predominantly massive, and consist of an old stellar population with very little ongoing star formation. Elliptical galaxies are supported by random motion of stars and this random motion is predominantly radial. These galaxies are commonly found in high-density environments such as groups and galaxy clusters. Spiral galaxies have lower masses and still show strong ongoing star formation, in particular in their disks. The motion of the stars in spiral galaxies are dominated by rotation. These galaxies are mostly observed in low-density environments.

Early-type galaxies furthermore obey a tight relationship between the half-light radius, the stellar velocity dispersion, and the average surface brightness. This structural scaling relation is known as the fundamental plane (FP; Faber & Jackson 1976; Djorgovski & Davis 1987; Dressler et al. 1987), and any of these three parameters can be estimated from the other two. Although spiral galaxies show a great diversity in many properties, they still obey a scaling relation between the intrinsic luminosity (proportional to the stellar mass) and rotational velocity. This relation is known as the Tully-Fisher relation (Tully & Fisher, 1977).

Given the fact that early-types are typically more massive, and contain old stellar populations, it is currently thought that galaxies evolve from disks to ellipticals, opposite as to Hubble proposed. Furthermore, it suggests that the process that is responsible for the morphological transition might also be responsible for quenching the star formation in galaxies. However, until the 21st century, extragalactic studies were based on relatively small numbers

of galaxies, which makes it harder to find the underlying mechanisms for the transition from spiral to elliptical.

The revolution came with observations from the Sloan Digital Sky Survey (SDSS; York et al. 2000), which provided the community with a large, well-understood statistical sample of galaxies. To date, this survey has provided optical photometry in five filterbands in combination with high-resolution spectra for over 800,000 galaxies in the northern-hemisphere. The photometry allowed for the determination of a galaxy's most basic properties: total luminosity, half-light or effective radius, and color gradient. The spectra yielded accurate redshifts, stellar spectral features, and stellar velocity dispersions. Combined, these measurements provided the framework for the most fundamental relations in galaxies such as the mass-size relation (Shen et al., 2003), the fundamental plane for elliptical galaxies (Bernardi et al., 2003), and also showed the environmental dependence of the relationships between stellar mass, structure, color, and star formation (Kauffmann et al. 2003, Blanton et al. 2005). One of the most important results from the SDSS is the clear bimodality of galaxies in the color-mass space (Figure 1.2). In this diagram early-type and late-type galaxies form two distinct classes. Early-type galaxies are found to have very red colors due to their old stellar populations, and lie on a tight relation in mass and  $u - r$  color known as the red sequence. Late-type galaxies have a larger range in  $u - r$  color, but are on average very blue due to the ongoing star formation. They have lower masses and reside in what is known as the blue cloud (Kauffmann et al. 2003, Blanton et al. 2005). Similarly to color, the bimodality is also present in other correlations with mass, such as the amplitude of the 4000 Å break (a stellar spectral feature from older stars that formed ionized metals), concentration of the light profile (Sérsic index), and specific star-formation rate.

The origin of this bimodality is perhaps the most fundamental question in extragalactic astronomy. One way to address this problem is by studying massive red-sequence galaxies, which are, according to the hierarchical merging theory, the final products of galaxy evolution. Detailed studies of massive elliptical galaxies in the local universe have proven to be invaluable, and tight scaling relations such as the fundamental plane, the red sequence, and their uniform old stellar populations provide a benchmark for galaxy evolution studies. Yet, observations of the present-day universe only provides an archaeological record of an early-type galaxy's past. In order to fully understand the formation and assembly of early-type galaxies, it is essential to observe galaxies at different stages in their evolution.

## 1.4 High-redshift observations

Due to the finite speed of light, an observation of a distant object offers us a view in the past. By observing galaxies at different distances, i.e., at different redshifts, we can study galaxies at earlier times, and thus witness the different epochs of galaxy evolution. Common techniques that are used at low redshift for determining morphology, effective radii, stellar masses and stellar population properties become, however, progressively harder at high redshift. Galaxies get fainter as their distance increases and require longer exposure times with large telescopes such as the Very Large Telescope (VLT) or Keck in order to obtain a similar signal-to-noise (S/N) as compared to low redshift. In particular, spectroscopy becomes increasingly difficult as the observed light is dispersed over a broad-wavelength range. Furthermore, at high red-

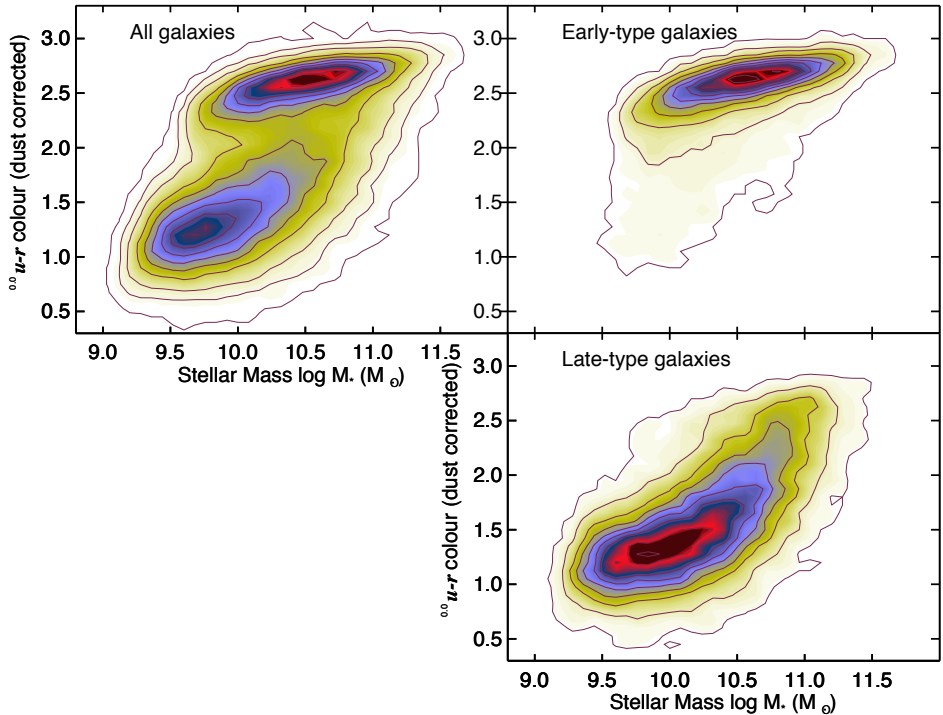


Figure 1.2: Bimodality in the local galaxy population, as shown in this rest-frame  $u - r$  color vs. stellar mass diagram from Schawinski et al. (2014). The left panel shows all galaxies, whereas the right panel separates early-type (top) and late-type (bottom) galaxies. On average red-sequence galaxies are more massive than blue-cloud galaxies.

shift the rest-frame optical light is redshifted to the near-infrared (NIR) wavelengths where spectroscopy is more challenging as compared to optical wavelengths.

Yet, spectroscopy is required for determining accurate redshifts, which are essential for converting raw measurements into physical quantities such as size, total luminosity, and total stellar mass. For late-type galaxies with active star formation, a redshift is relatively easily obtained from bright emission lines, but for early-types with quiescent stellar populations, redshifts are measured from stellar absorption features in the faint stellar continuum.

A faster and cheaper technique for determining redshifts, using only photometry, is more commonly used, but this also comes with larger uncertainties. This technique is based on fitting a galaxy's observed photometric spectral energy distribution with templates from stellar population synthesis (SPS) models. Current SPS models provide an ensemble of templates for a large range in stellar population properties such as age and metallicity. A good template-fit to the observed data will provide a photometric redshift, stellar mass, and other important stellar population parameters. For obtaining statistical galaxy samples, large areas in the sky are observed in a multi-wavelength observing campaign using a set of carefully chosen filterbands, which range from the ultraviolet (UV) to the infrared (IR). This yields accurate photometry



and SEDs for thousands of galaxies at various redshifts.

While the overall shape of the SED can yield relatively accurate photometric redshift, some features in the SED provide even better results. For example, star-forming galaxies exhibit a sharp break around  $912\text{\AA}$  due to the Lyman-limit in the neutral hydrogen gas in the interstellar and intergalactic medium. At  $z > 3$ , this feature can be detected with optical broad-band filters and is called the Lyman-break technique (Steidel et al. 1996a; 1996b). Early-type galaxies, with older stellar populations, have a spectral feature known as the Balmer/D4000-break, which is observable in the rest-frame optical. However at  $z = 2$ , the rest-frame optical light is redshifted into the NIR, where observations are technically more challenging as compared to optical wavelengths. Still, for both star-forming and quiescent galaxies, this SED fitting technique has proven to be extremely useful for obtaining photometric redshifts with an accuracy of 5% (Brammer et al., 2008).

Another difficult complication of studying galaxies out to  $z = 1.5$  is that the angular size of an object decreases when observed at larger distances. This means that small galaxies at high redshift can no longer be resolved, which impedes morphological studies. Fortunately, due to the expansion and the shape of the universe, the minimum angular scale is reached around  $z = 1.5$ , after which galaxies grow in angular size again. While the diffraction limit of large telescopes is much smaller than the angular size of galaxies at high redshift, turbulence in the Earth's atmosphere degrades our images such that galaxies become unresolved from ground-based observatories. On good nights the full width at half maximum (FWHM) of the observed point spread function (PSF), or seeing, can be as good as 0.4-0.6 arcseconds ( $''$ ), but is more typically around  $0''.8$ - $1''.0$ , while sizes of small massive galaxies are around  $0''.1$ - $0''.2$ . The Hubble Space Telescope (HST) has much better resolution, as it operates in space, outside of the Earth's atmosphere. In particular the Advanced Camera for Surveys (ACS) in the optical and Wide Field Camera 3 (WFC3) in the NIR are capable of reaching a FWHM of  $0''.05$ , and  $0''.12$  respectively. Still, even with these state-of-the-art facilities such as HST, morphological measurements of galaxies at high redshift remain challenging.

## 1.5 Massive galaxies in the early universe

The first observations of galaxies at high redshift pictured a universe which was very different from the current universe. Using the Lyman-break technique, HST surveys mostly detected galaxies with very high star formation rates at  $z > 2$  (e.g., Papovich et al. 2005). Furthermore, from HST-NICMOS imaging, these Lyman-break galaxies were found to be compact and often have irregular morphologies (e.g. Dickinson 2000). Ordinary spirals and ellipticals seemed to be largely absent at these redshifts. Yet, cosmological simulations suggested that the progenitors of elliptical galaxies formed at  $z \sim 6$ , after which they became very massive within a short amount of time ( $M_* > 10^{11} M_\odot$ ) (Kereš et al. 2005; Khochfar & Silk 2006; De Lucia et al. 2006; Naab et al. 2007; Naab et al. 2009; Joung et al. 2009; Dekel et al. 2009; Kereš et al. 2009; Oser et al. 2010; Feldmann et al. 2010; Oser et al. 2012.)

However, due to observational challenges and selection effects early studies of the high-redshift universe were biased towards bright star-forming late-type galaxies, as quiescent early-type galaxies are faint in the rest-frame UV and thus not detected in optical surveys. Instead, early-type galaxies emit most of their flux in the rest-frame optical which corresponds

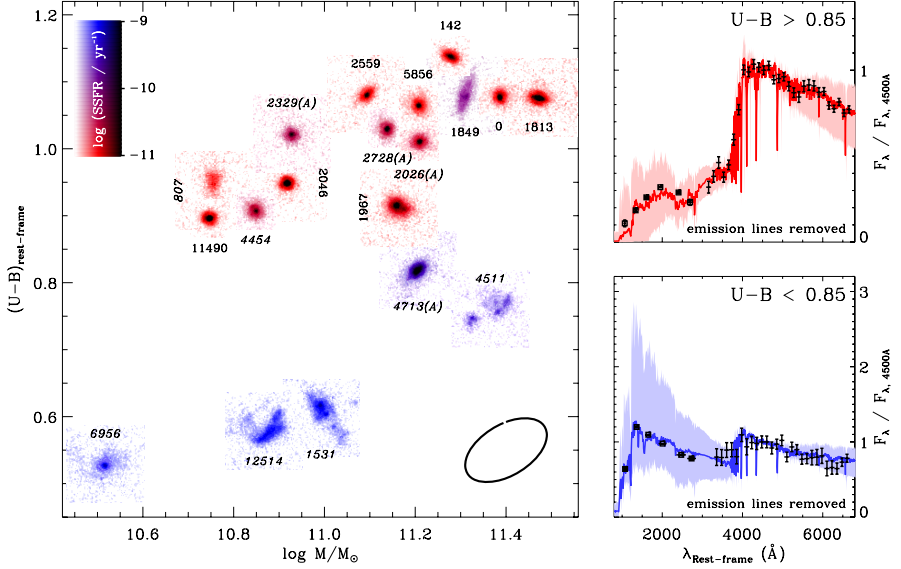


**Figure 1.3:** The Hubble sequence at  $z \sim 2$  from Kriek et al. (2009b). Left: rest-frame  $U - B$  color vs. stellar mass for massive galaxies with rest-frame optical spectroscopy. Different symbols are postage stamp images from HST-NICMOS-2, and the color coding represents the specific star-formation rate. A clear bimodality is visible, i.e., there is evidence of the red-sequence and blue-cloud as seen in Figure 1.2. Right: Stacked SEDs from GNIRS spectra and SPS models for red (top panel) and blue (bottom panel) galaxies, which shows that the two populations are truly distinct.

to the observed NIR for galaxies at  $z = 2$ .

With the advent of deep NIR surveys, which were designed to observe the rest-frame optical light of galaxies at high redshift (e.g., Labbé et al. 2003), distant red galaxies were indeed detected at  $z = 2$  (e.g., Franx et al. 2003; van Dokkum & Stanford 2003, Labbé et al. 2005). NIR surveys typically selected galaxies in the NIR  $K$ -band, which means that they are no longer biased towards star-forming galaxies. Furthermore, as the rest-frame optical selection is a good proxy to mass selection, NIR surveys have become standard for obtaining a mass-complete sample of galaxies out to  $z \sim 3$  (e.g., Wuyts et al. 2008; Williams et al. 2009; Whitaker et al. 2011; Muzzin et al. 2013a). With the wealth of information from broad to medium-band photometry and NIR spectroscopy, it has become clear that quiescent galaxies make up about half the galaxy population at high stellar masses (Daddi et al., 2005; Kriek et al., 2006; Muzzin et al., 2013b). Furthermore, the Hubble sequence might already exist at  $z \sim 2$  (Figure 1.3, Kriek et al. 2008, 2009b; Szomoru et al. 2011). With increasingly deeper NIR surveys, massive quiescent galaxies have now been detected out to  $z \sim 4$  (Straatman et al., 2014).

Even more surprising, these massive quiescent galaxies in the early-universe have been found to be extremely compact as compared to their present-day counterparts (Daddi et al., 2005; van der Wel et al., 2005; di Serego Alighieri et al., 2005; Trujillo et al., 2006; Longhetti

et al., 2007; Toft et al., 2007; Buitrago et al., 2008; van Dokkum et al., 2008; van der Wel et al., 2008; Cimatti et al., 2008; Franx et al., 2008; Damjanov et al., 2009; Cenarro & Trujillo, 2009; Bezanson et al., 2009; van Dokkum et al., 2010; Whitaker et al., 2012). At a fixed mass, massive quiescent galaxies at  $z \sim 2$  have smaller effective radii by a factor 4-5 as compared to  $z \sim 0$  galaxies. Almost none of these massive compact galaxies are observed in the local-universe (Trujillo et al., 2009; Taylor et al., 2010), which implies that massive galaxies must have undergone severe structural evolution. Thus, it is unlikely that early-type galaxies formed in an initial monolithic collapse, after which they passively evolved. If that were the case, their present-day counterparts would be too small and too red (van Dokkum et al., 2008; Kriek et al., 2008; Bezanson et al., 2009; Ferré-Mateu et al., 2012). Instead, these  $z \sim 2$  galaxies are likely the cores of present-day ellipticals that have grown in an inside-out fashion, mainly by adding stellar mass to the outer parts over time (Hopkins et al., 2009b; van Dokkum et al., 2010; Szomoru et al., 2012; Saracco et al., 2012).

The dominant physical mechanism for this structural evolution is still a subject of ongoing debate. In the hierarchical structure formation theory, merging is considered a natural process and is expected to play an important role in the structural and morphological evolution of massive galaxies (e.g. Kauffmann et al., 1996; Kauffmann, 1996; De Lucia et al., 2006; Khochfar & Silk, 2006; De Lucia & Blaizot, 2007; Guo & White, 2008; Kormendy et al., 2009; Hopkins et al., 2010). Observations of early-type galaxies out to high redshifts indeed show evidence of mergers taking place (van Dokkum, 2005; Tran et al., 2005; Bell et al., 2006a,b; Lotz et al., 2008; Jogee et al., 2009; Newman et al., 2012; Man et al., 2012). However, size growth due to major mergers seems to be unlikely, as there are not enough major mergers that can account for the large size evolution, and the predicted increase in size is insufficient in bringing  $z \sim 2$  galaxies closer to the  $z \sim 0$  mass-size relation (e.g., Naab et al. 2007; Nipoti et al. 2009; Bundy et al. 2009; de Ravel et al. 2009; Bluck et al. 2009). Minor mergers, however, are expected to occur more frequently in the lifetime of a massive galaxy, and could offer a solution to this problem. With only a few assumptions from the Virial theorem, Cole et al. (2000), Naab et al. (2009), and Bezanson et al. (2009) show that minor mergers are very efficient in increasing the size of a galaxy, without a significant increase in mass. Simulations of merging galaxies also predict that minor-mergers are likely the dominant process for increasing galaxy sizes (Hopkins et al. 2009; Oser et al. 2012; Hilz et al. 2013; Bédorf & Portegies Zwart 2013). From observations, several studies suggest that minor mergers could be responsible for the size growth at  $0 < z < 1$ , while at higher redshift there might not be enough minor mergers to explain the observed growth (Oogi & Habe, 2012; Nipoti et al., 2012; Cimatti et al., 2012; Newman et al., 2012).

## 1.6 Current issues

As with any new major discovery, there has been a debate about the reality of this structural evolution. Errors in the size and mass estimates are possible explanations for the compactness of massive high-redshift galaxies. Initial concerns that the size is being underestimated due to an envelope of low-surface brightness light, have been addressed with deep HST-WFC3 imaging. Szomoru et al. (2010; 2012) measure the surface brightness profiles for a sample of quiescent galaxies at  $1.5 < z < 2.5$ , using a method that properly measures low surface

brightness flux at large radii. They find that quiescent galaxies have effective radii that are a factor  $\sim 4$  smaller than those of low-redshift quiescent galaxies of similar mass, and have no excess flux at large radii. Subsequent work by van der Wel et al. (2014; and references therein) confirms these results. Other methods, such as stacking, also show that sizes increase over time. (e.g., van der Wel et al. 2008; Cassata et al. 2010; van Dokkum et al. 2008, 2010). The light could also be more concentrated due to the presence of active galactic nuclei (AGNs) in these galaxies. However, spectra of subsamples of these galaxies show that the light is dominated by evolved stellar populations, not AGNs (Kriek et al. 2006, 2009; Onodera et al. 2012)

Color gradients in galaxies can also lead to large discrepancies when comparing sizes at different redshifts. A small amount of recent star formation in the center of a galaxy can create a bias toward small sizes, as the light from the young hot blue stars out-shines the older population. This issue becomes less of a problem when looking at the redmost possible wavelengths, but this becomes increasingly harder at  $z > 2$  where the rest-frame optical is redshifted to the NIR wavelengths. Szomoru et al. (2013) accurately measure the surface brightness in several filterbands and find that the overwhelming majority of galaxies has negative radial color gradients, such that the cores of galaxies are redder than the outskirts. Furthermore, they show that stellar half-mass radii from the mass profiles are on average  $\sim 25\%$  smaller than rest-frame  $g$ -band half-light radii. Thus, these results show that the small sizes at high redshift are not due to systematic uncertainties.

The question of whether stellar masses are accurate out to  $z \sim 2$  remains, however, a serious concern. An overestimate in stellar mass would bring the galaxies closer to the  $z \sim 0$  mass-size relation. To date, basically all (stellar) masses have been derived by fitting SEDs. This method suffers from many systematic uncertainties in SPS models, metallicity, star formation history (SFH), and the stellar initial mass function (IMF) (e.g., Maraston et al. 2006; Muzzin et al. 2009; Conroy et al. 2009).

SPS models are now widely used for fitting the SEDs of galaxies, and can be used effectively to derive many physical properties, such as redshift, stellar mass, star formation rate, dust content, and metallicity. Generally, these models construct simple stellar populations (SSPs) from basic inputs: stellar evolution theory in the form of stellar-isochrones, stellar spectral libraries, and an IMF. Combined with a dust-law and star-formation history, SPS models create composite stellar populations (CSPs), that can be used for fitting galaxy SEDs.

As there are many different model approaches and assumptions involved, it has been largely confirmed that stellar mass are sensitive to the choice of SPS model (e.g., Wuyts et al. 2007; Cimatti et al. 2008; Muzzin et al. 2009; Longhetti & Saracco 2009; Conroy et al. 2009). In particular the different treatment of the thermally pulsating asymptotic giant branch (TP-AGB) stars between the Bruzual & Charlot (2003) and the Maraston (2005) models received a lot of attention. As the TP-AGB phase is most prominent for stellar populations around 1 Gyr, the stellar masses of galaxies at high redshift will be more affected than stellar masses at low-redshift. However, as shown by Conroy & Gunn (2010), Kriek et al. (2010), and Zibetti et al. (2013), the contribution from TP-AGB to the total light is much lower than expected from the Maraston (2005) models. Another important uncertainty comes from the SFH of a galaxy, since a large population of older stars can be hidden behind a much brighter young population. Different assumption on metallicity can further affect the stellar mass estimates. From a detailed study on a sample of massive galaxies at  $z \sim 2$ , Muzzin et al. (2009) find that with a maximally old stellar population superposed with a young component, the stel-

lar masses can be 0.08–0.22 dex larger as compared to exponentially declining SFHs, while different metallicities lower the stellar mass estimates by 0.10–0.16 dex.

A more fundamental uncertainty in stellar mass estimates arises from the choice of the IMF. The IMF describes the distribution of initial masses for a population of stars (e.g., Salpeter 1955; Kroupa 2002; Chabrier 2003; Kroupa et al. 2013). As stellar evolution is strongly correlated with the initial mass of a star, the IMF is an important diagnostic tool when studying large quantities of stars simultaneously. For example, with increasing initial mass, a star's mass-to-light ratio ( $M/L$ ) and lifetime strongly decreases. Therefore, the integrated light of a galaxy will be dominated by the most massive stars that are still alive. Consequently, we only directly measure the mass and star-formation rate of the most massive stars still alive. The shape of IMF allows us to account for the faint low-mass stars. The IMF is therefore crucial for an accurate estimate of the total stellar mass (e.g., Courteau et al. 2013) and total star formation rate (e.g., Madau & Dickinson 2014).

The most straightforward technique to measure the IMF is counting individual stars in our Galaxy (e.g., Salpeter 1955; Kroupa 2001; Chabrier 2003). Measurements of the IMF in other galaxies are based on the integrated light of the entire stellar population. From high-S/N spectroscopic studies of nearby massive galaxies, several studies constrained the low-mass end of the IMF, either from gravity-sensitive stellar absorption features (van Dokkum et al. 2010; Spiniello et al. 2012; Smith et al. 2012; van Dokkum & Conroy 2012; Ferreras et al. 2013), or from independent mass measurements such as detailed stellar dynamics (Dutton et al. 2012; Cappellari et al. 2012, 2013), and gravitational lensing (Grillo et al. 2009; Auger et al. 2010; Treu et al. 2010; Thomas et al. 2011; Spiniello et al. 2011). In the disk of the Milky Way, the IMF is well described by a power-law  $dN/dM \propto M^{-\alpha}$ , with a slope of  $\alpha = 2.35$  for  $m > 1M_{\odot}$  (Salpeter, 1955), while below this mass, the form of the IMF is lognormal (Chabrier, 2003). The IMF may slightly vary among early-type galaxies, compared to the Milky Way. The data favor that the slope of the IMF steepens with increasing velocity, such that the cores of the most massive elliptical galaxies have a "bottom-heavy" (Salpeter or steeper) IMF (e.g., van Dokkum & Conroy 2012; Cappellari et al. 2013; Ferreras et al. 2013), but some results remain uncertain (e.g., Smith 2014).

In conclusion, uncertainties in the stellar mass estimates due to different SPS models, SFHs and metallicity can be as large as 0.6 dex (factor  $\sim 4$ ) for bright red galaxies at  $z \sim 2$  (Conroy et al., 2009) while the IMF gives rise to another 0.2 dex of uncertainty. Direct stellar kinematic mass measurements, which are not affected by these uncertainties, are needed to confirm whether the stellar masses of quiescent galaxies are accurate out to  $z \sim 2$ .

## 1.7 Thesis summary

In this Thesis we assess the stellar mass estimates at high redshift, by comparing them to dynamical mass measurements, that are derived from the effective radii and stellar velocity dispersions. We furthermore explore key relations such as the Fundamental Plane, and investigate correlations between the mass-to-light ratio and color. This thesis work is built upon high-quality spectra with full UV-NIR wavelength coverage of five massive quiescent ( $> 10^{11} M_{\odot}$ ) galaxies at  $z \sim 2$ , obtained with X-Shooter on the VLT. We combine these spectra with HST and ground-based multi-band photometry. Our sample is furthermore complemented with

different stellar kinematic studies from the literature at  $z \sim 2$  to  $z \sim 0$ .

In **Chapter 2** we perform a pilot study by deriving the dynamical mass of a massive quiescent galaxy at  $z = 1.8$ . From the spectrum we determine a velocity dispersion of  $294 \pm 51 \text{ km s}^{-1}$ , and combine it with a size derived from HST-WFC3 image in order to derive a dynamical mass. We find that the dynamical and photometric stellar mass are in good agreement. Furthermore, the velocity dispersion at a fixed dynamical mass is a factor of  $\sim 1.8$  higher at  $z = 1.8$  compared to  $z = 0$ . This results suggests that stellar masses at high redshift are robust, and thus supports the claim that massive, quiescent galaxies with high stellar mass densities exist at  $z \sim 2$ .

Using our full sample, in **Chapter 3** we study the structural evolution of massive quiescent galaxies from  $z \sim 2$  to the present-day. We measure high stellar velocity dispersions ( $290\text{--}450 \text{ km s}^{-1}$ ) from the spectra, and small sizes, from the HST-WFC3  $H_{160}$  and UKIDSS-UDS K-band images. The derived dynamical masses for these galaxies show that they are very massive ( $11.2 < \log M_{\text{dyn}}/M_{\odot} < 11.8$ ). At all redshifts, stellar and dynamical masses are tightly correlated and dynamical mass, which includes baryonic and dark matter, is always higher than stellar mass. Thus, we infer that the stellar masses are broadly correct, and that the apparent size evolution of massive galaxies in photometric studies cannot be explained by errors in the photometric masses. We confirm that at fixed mass, the effective radius increases, and the velocity dispersion decreases with time. The mass density within one effective radius decreases by more than an order of magnitude, while within 1 kpc it decreases only mildly. This finding suggests that massive quiescent galaxies at  $z \sim 2$  grow in an inside-out manner, consistent with the expectations from minor mergers.

We explore the existence of a Fundamental Plane of massive quiescent galaxies at high redshift in **Chapter 4**, with the aim of measuring the evolution of the  $M/L$  from  $z \sim 2$  to the present-day. We find a strong evolution of the zero point from  $z \sim 2$  to  $z \sim 0$ :  $\Delta \log_{10} M/L_g \propto (-0.49 \pm 0.03) z$ . However, at  $z > 1$  we find that the spectroscopic sample is bluer in rest-frame  $g - z$  colors, as compared to a larger mass complete sample of quiescent galaxies. We use the color offsets to estimate a  $M/L$  correction. We find that the implied FP zero point evolution after correction is significantly smaller:  $\Delta \log_{10} M/L_g \propto (-0.39 \pm 0.02) z$ . This is consistent with an apparent formation redshift of  $z_{\text{form}} = 6.62^{+3.19}_{-1.44}$  for the underlying population, ignoring the effects of progenitor bias.

In **Chapter 5** we explore the dynamical mass-to-light ( $M/L$ ) ratio and rest-frame colors of massive quiescent galaxies out to  $z \sim 2$ . Our galaxy sample spans a large range in  $M/L$  ratios: 1.8 dex in rest-frame  $\log M/L_u$ , 1.6 dex in  $\log M/L_g$ , and 1.2 dex in  $\log M/L_K$ . We find that there is a strong correlation between the  $M/L$  ratio for different bands and rest-frame colors, that is well approximated by a linear relation. We find that it is possible to estimate the  $M/L$  of an early-type galaxy with an accuracy of  $\sim 0.26$  dex from a single rest-frame optical color. Next, we compare the measured  $M/L$  vs. rest-frame color with different SPS models. With a Salpeter IMF, none of the SPS models are able to simultaneously match the optical and infrared colors and  $M/L$ . We test whether a different slope of the IMF provides a better match to the data. However, our results show that variations between different SPS models (with the same IMF) are comparable to the IMF variations. More complete and higher resolution empirical stellar libraries, improved stellar evolution models, and larger spectroscopic samples at high redshift, are needed to provide more accurate constraints on the IMF.

## References

- Auger, M. W., Treu, T., Gavazzi, R., et al. 2010, *ApJ*, 721, L163
- Bédorf, J., & Portegies Zwart, S. 2013, *MNRAS*, 431, 767
- Bell, E. F., Naab, T., McIntosh, D. H., et al. 2006a, *ApJ*, 640, 241
- Bell, E. F., Phleps, S., Somerville, R. S., et al. 2006b, *ApJ*, 652, 270
- Bennett, C. L., Larson, D., Weiland, J. L., et al. 2013, *ApJS*, 208, 20
- Bernardi, M., Sheth, R. K., Annis, J., et al. 2003, *AJ*, 125, 1866
- Bezanson, R., van Dokkum, P. G., Tal, T., Marchesini, D., Kriek, M., Franx, M., & Coppi, P. 2009, *ApJ*, 697, 1290
- Blanton, M. R., Eisenstein, D., Hogg, D. W., Schlegel, D. J., & Brinkmann, J. 2005, *ApJ*, 629, 143
- Bluck, A. F. L., Conselice, C. J., Bouwens, R. J., et al. 2009, *MNRAS*, 394, L51
- Brammer, G. B., van Dokkum, P. G., & Coppi, P. 2008, *ApJ*, 686, 1503
- Bruzual, G., & Charlot, S. 2003, *MNRAS*, 344, 1000
- Buitrago, F., Trujillo, I., Conselice, C. J., et al. 2008, *ApJ*, 687, L61
- Bradač, M., Clowe, D., Gonzalez, A. H., et al. 2006, *ApJ*, 652, 937
- Bundy, K., Fukugita, M., Ellis, R. S., et al. 2009, *ApJ*, 697, 1369
- Cappellari, M., Scott, N., Alatalo, K., et al. 2013, *MNRAS*, 432, 1709
- Cappellari, M., McDermid, R. M., Alatalo, K., et al. 2012, *Nature*, 484, 485
- Cassata, P., Giavalisco, M., Guo, Y., et al. 2010, *ApJ*, 714, L79
- Cenarro, A. J., & Trujillo, I. 2009, *ApJ*, 696, L43
- Chabrier, G. 2003, *PASP*, 115, 763
- Cimatti, A., Cassata, P., Pozzetti, L., et al. 2008, *A&A*, 482, 21
- Cimatti, A., Nipoti, C., & Cassata, P. 2012, *MNRAS*, 422, L62
- Cole, S., Lacey, C. G., Baugh, C. M., & Frenk, C. S. 2000, *MNRAS*, 319, 168
- Clowe, D., Bradač, M., Gonzalez, A. H., et al. 2006, *ApJ*, 648, L109
- Conroy, C., & Gunn, J. E. 2010, *ApJ*, 712, 833
- Conroy, C., Gunn, J. E., & White, M. 2009, *ApJ*, 699, 486
- Courteau, S., Cappellari, M., de Jong, R. S., et al. 2013, arXiv:1309.3276
- Daddi, E., Renzini, A., Pirzkal, N., et al. 2005, *ApJ*, 626, 680
- Damjanov, I., McCarthy, P. J., Abraham, R. G., et al. 2009, *ApJ*, 695, 101
- De Lucia, G., & Blaizot, J. 2007, *MNRAS*, 375, 2
- De Lucia, G., Springel, V., White, S. D. M., Croton, D., & Kauffmann, G. 2006, *MNRAS*, 366, 499
- Dekel, A., Sari, R., & Ceverino, D. 2009, *ApJ*, 703, 785
- de Ravel, L., Le Fèvre, O., Tresse, L., et al. 2009, *A&A*, 498, 379
- di Serego Alighieri, S., Vernet, J., Cimatti, A., et al. 2005, *A&A*, 442, 125
- Djorgovski, S., & Davis, M. 1987, *ApJ*, 313, 59
- Dressler, A., Faber, S. M., Burstein, D., et al. 1987, *ApJ*, 313, L37
- Dutton, A. A., Mendel, J. T., & Simard, L. 2012, *MNRAS*, 422, L33
- Faber, S. M., & Jackson, R. E. 1976, *ApJ*, 204, 668
- Ferreras, I., La Barbera, F., de la Rosa, I. G., et al. 2013, *MNRAS*, 429, L15
- Feldmann, R., Carollo, C. M., Mayer, L., et al. 2010, *ApJ*, 709, 218
- Ferré-Mateu, A., Vazdekis, A., Trujillo, I., et al. 2012, *MNRAS*, 423, 632
- Franx, M., van Dokkum, P. G., Schreiber, N. M. F., et al. 2008, *ApJ*, 688, 770
- Franx, M., Labbé, I., Rudnick, G., et al. 2003, *ApJ*, 587, L79
- Grillo, C., Gobat, R., Lombardi, M., & Rosati, P. 2009, *A&A*, 501, 461
- Guo, Q., & White, S. D. M. 2008, *MNRAS*, 384, 2
- Herschel, W. 1786, *Royal Society of London Philosophical Transactions Series I*, 76, 457
- Hilz, M., Naab, T., & Ostriker, J. P. 2013, *MNRAS*, 429, 2924
- Hopkins, P. F., Hernquist, L., Cox, T. J., Keres, D., & Wuyts, S. 2009a, *ApJ*, 691, 1424
- Hopkins, P. F., Bundy, K., Murray, N., et al. 2009b, *MNRAS*, 398, 898
- Hopkins, P. F., Bundy, K., Croton, D., et al. 2010, *ApJ*, 715, 202
- Hu, W., & White, M. 1996, *ApJ*, 471, 30
- Hubble, E. 1936, *Science*, 84, 509
- Jogee, S., Miller, S. H., Penner, K., et al. 2009, *ApJ*, 697, 1971
- Joung, M. R., Cen, R., & Bryan, G. L. 2009, *ApJ*, 692, L1
- Kauffmann, G., Heckman, T. M., White, S. D. M., et al. 2003, *MNRAS*, 341, 33

- Kauffmann, G. 1996, *MNRAS*, 281, 487
- Kauffmann, G., Charlot, S., & White, S. D. M. 1996, *MNRAS*, 283, L117
- Kereš, D., Katz, N., Fardal, M., Davé, R., & Weinberg, D. H. 2009, *MNRAS*, 395, 160
- Kereš, D., Katz, N., Weinberg, D. H., & Davé, R. 2005, *MNRAS*, 363, 2
- Khochfar, S., & Silk, J. 2006, *ApJ*, 648, L21
- Kormendy, J., Fisher, D. B., Cornell, M. E., & Bender, R. 2009, *ApJS*, 182, 216
- Kriek, M., Labbé, I., Conroy, C., et al. 2010, *ApJ*, 722, L64
- Kriek, M., van Dokkum, P. G., Franx, M., Illingworth, G. D., & Magee, D. K. 2009, *ApJ*, 705, L71
- Kriek, M., van Dokkum, P. G., Labbé, I., et al. 2009b, *ApJ*, 700, 221
- Kriek, M., van der Wel, A., van Dokkum, P. G., Franx, M., & Illingworth, G. D. 2008, *ApJ*, 682, 896
- Kriek, M., van Dokkum, P. G., Franx, M., et al. 2006, *ApJ*, 649, L71
- Kroupa, P., Weidner, C., Pflamm-Altenburg, J., et al. 2013, *Planets, Stars and Stellar Systems. Volume 5: Galactic Structure and Stellar Populations*, 115
- Kroupa, P. 2002, *Science*, 295, 82
- Kroupa, P. 2001, *MNRAS*, 322, 231
- Labbé, I., Franx, M., Rudnick, G., et al. 2003, *AJ*, 125, 1107
- Labbé, I., Huang, J., Franx, M., et al. 2005, *ApJ*, 624, L81
- Longhetti, M., & Saracco, P. 2009, *MNRAS*, 394, 774
- Longhetti, M., Saracco, P., Severgnini, P., et al. 2007, *MNRAS*, 374, 614
- Lotz, J. M., Davis, M., Faber, S. M., et al. 2008, *ApJ*, 672, 177
- Madau, P., & Dickinson, M. 2014, arXiv:1403.0007
- Man, A. W. S., Toft, S., Zirm, A. W., Wuyts, S., & van der Wel, A. 2012, *ApJ*, 744, 85
- Maraston, C., Daddi, E., Renzini, A., et al. 2006, *ApJ*, 652, 85
- Maraston, C. 2005, *MNRAS*, 362, 799
- Messier, C. 1781, *Connaissance des Temps for 1784*, p. 227–267, 227
- Muzzin, A., Marchesini, D., Stefanon, M., et al. 2013b, *ApJ*, 777, 18
- Muzzin, A., Marchesini, D., Stefanon, M., et al. 2013a, *ApJS*, 206, 8
- Muzzin, A., Marchesini, D., van Dokkum, P. G., et al. 2009, *ApJ*, 701, 1839
- Naab, T., Johansson, P. H., & Ostriker, J. P. 2009, *ApJ*, 699, L178
- Naab, T., Johansson, P. H., Ostriker, J. P., & Efstathiou, G. 2007, *ApJ*, 658, 710
- Nipoti, C., Treu, T., Leauthaud, A., et al. 2012, *MNRAS*, 422, 1714
- Nipoti, C., Treu, T., Auger, M. W., & Bolton, A. S. 2009, *ApJ*, 706, L86
- Newman, A. B., Ellis, R. S., Bundy, K., & Treu, T. 2012, *ApJ*, 746, 162
- Onodera, M., Renzini, A., Carollo, M., et al. 2012, *ApJ*, 755, 26
- Oogi, T. & Habe, A. 2012, *MNRAS*, 42
- Oser, L., Naab, T., Ostriker, J. P., & Johansson, P. H. 2012, *ApJ*, 744, 63
- Oser, L., Ostriker, J. P., Naab, T., Johansson, P. H., & Burkert, A. 2010, *ApJ*, 725, 2312
- Papovich, C., Dickinson, M., Giavalisco, M., Conselice, C. J., & Ferguson, H. C. 2005, *ApJ*, 631, 101
- Perlmutter, S., Aldering, G., Goldhaber, G., et al. 1999, *ApJ*, 517, 565
- Riess, A. G., Filippenko, A. V., Challis, P., et al. 1998, *AJ*, 116, 1009
- Salpeter, E. E. 1955, *ApJ*, 121, 161
- Saracco, P., Gargiulo, A., & Longhetti, M. 2012, *MNRAS*, 422, 3107
- Schawinski, K., Urry, C. M., Simmons, B. D., et al. 2014, *MNRAS*, 440, 889
- Shen, S., Mo, H. J., White, S. D. M., et al. 2003, *MNRAS*, 343, 978
- Slipher, V. M. 1918, *Publications of the American Astronomical Society*, 3, 98
- Smith, R. J. 2014, arXiv:1403.6114
- Smith, R. J., Lucey, J. R., & Carter, D. 2012, *MNRAS*, 426, 2994
- Spiniello, C., Trager, S. C., Koopmans, L. V. E., & Chen, Y. P. 2012, *ApJ*, 753, L32
- Spiniello, C., Koopmans, L. V. E., Trager, S. C., Czoske, O., & Treu, T. 2011, *MNRAS*, 417, 3000
- Steidel, C. C., Giavalisco, M., Dickinson, M., & Adelberger, K. L. 1996a, *AJ*, 112, 352
- Steidel, C. C., Giavalisco, M., Pettini, M., Dickinson, M., & Adelberger, K. L. 1996b, *ApJ*, 462, L17
- Straatman, C. M. S., Labbé, I., Spitler, L. R., et al. 2014, *ApJ*, 783, L14
- Szomoru, D., Franx, M., van Dokkum, P. G., et al. 2013, *ApJ*, 763, 73
- Szomoru, D., Franx, M., & van Dokkum, P. G. 2012, *ApJ*, 749, 121
- Szomoru, D., Franx, M., Bouwens, R. J., et al. 2011, *ApJ*, 735, L22
- Szomoru, D., Franx, M., van Dokkum, P. G., et al. 2010, *ApJ*, 714, L244



- Taylor, E. N., Franx, M., Glazebrook, K., et al. 2010, *ApJ*, 720, 723  
Thomas, J., Saglia, R. P., Bender, R., et al. 2011, *MNRAS*, 415, 545  
Toft, S., van Dokkum, P., Franx, M., et al. 2007, *ApJ*, 671, 285  
Tran, K.-V. H., van Dokkum, P., Franx, M., et al. 2005, *ApJ*, 627, L25  
Treu, T., Auger, M. W., Koopmans, L. V. E., et al. 2010, *ApJ*, 709, 1195  
Trujillo, I., Cenarro, A. J., de Lorenzo-Cáceres, A., et al. 2009, *ApJ*, 692, L118  
Trujillo, I., Förster Schreiber, N. M., Rudnick, G., et al. 2006, *ApJ*, 650, 18  
Tully, R. B., & Fisher, J. R. 1977, *A&A*, 54, 661  
van der Wel, A., Franx, M., van Dokkum, P. G., et al. 2014, *ApJ*, 788, 28  
van der Wel, A., Holden, B. P., Zirm, A. W., et al. 2008, *ApJ*, 688, 48  
van der Wel, A., Franx, M., van Dokkum, P. G., et al. 2005, *ApJ*, 631, 145  
van Dokkum, P. G., & Conroy, C. 2012, *ApJ*, 760, 70  
van Dokkum, P. G., et al. 2010, *ApJ*, 709, 1018  
van Dokkum, P. G., et al. 2008, *ApJ*, 677, L5  
van Dokkum, P. G. 2005, *AJ*, 130, 2647  
van Dokkum, P. G., Förster Schreiber, N. M., Franx, M., et al. 2003, *ApJ*, 587, L83  
Whitaker, K. E., Labbé, I., van Dokkum, P. G., et al. 2011, *ApJ*, 735, 86  
Whitaker, K. E., Kriek, M., van Dokkum, P. G., et al. 2012, *ApJ*, 745, 179  
Williams, R. J., Quadri, R. F., Franx, M., van Dokkum, P., & Labbé, I. 2009, *ApJ*, 691, 1879  
Wuyts, S., Labbé, I., Schreiber, N. M. F., et al. 2008, *ApJ*, 682, 985  
Wuyts, S., Labbé, I., Franx, M., et al. 2007, *ApJ*, 655, 51  
York, D. G., Adelman, J., Anderson, J. E., Jr., et al. 2000, *AJ*, 120, 1579  
Zibetti, S., Gallazzi, A., Charlot, S., Pierini, D., & Pasquali, A. 2013, *MNRAS*, 428, 1479

## 2 | The stellar velocity dispersion of a compact massive galaxy at $z = 1.80$ using X-Shooter: confirmation of the evolution in the mass-size and mass-dispersion relations

### Abstract

Recent photometric studies have shown that early-type galaxies at fixed stellar mass were smaller and denser at earlier times. In this chapter we assess that finding by deriving the dynamical mass of such a compact quiescent galaxy at  $z=1.8$ . We have obtained a high-quality spectrum with full UV-NIR wavelength coverage of galaxy NMBS-C7447 using X-Shooter on the Very Large Telescope. We determined a velocity dispersion of  $294 \pm 51 \text{ km s}^{-1}$ . Given this velocity dispersion and the effective radius of  $1.64 \pm 0.15 \text{ kpc}$  (as determined from *Hubble Space Telescope* Wide Field Camera 3 F160W observations) we derive a dynamical mass of  $1.7 \pm 0.5 \times 10^{11} M_{\odot}$ . Comparison of the full spectrum with stellar population synthesis models indicates that NMBS-C774 has a relatively young stellar population (0.40 Gyr) with little or no star formation and a stellar mass of  $M_{\star} \sim 1.5 \times 10^{11} M_{\odot}$ . The dynamical and photometric stellar mass are in good agreement. Thus, our study supports the conclusion that the mass densities of quiescent galaxies were indeed higher at earlier times, and this earlier result is not caused by systematic measurement errors. By combining available spectroscopic measurements at different redshifts, we find that the velocity dispersion at fixed dynamical mass was a factor of  $\sim 1.8$  higher at  $z=1.8$  compared to  $z=0$ . Finally, we show that the apparent discrepancies between the few available velocity dispersion measurements at  $z > 1.5$  are consistent with the intrinsic scatter of the mass-size relation.

Jesse van de Sande, Mariska Kriek, Marijn Franx, Pieter G. van Dokkum,  
Rachel Bezanson, Katherine E. Whitaker, Gabriel Brammer, Ivo Labbé,  
Paul J. Groot, and Lex Kaper  
*The Astrophysical Journal Letters*, 736, L9:L16, (2011)

## 2.1 Introduction

In hierarchical structure formation models, the most massive early-type galaxies are assembled last (e.g., Springel et al., 2005). This simple picture seems difficult to reconcile with recent studies showing that the first massive, quiescent galaxies were already in place when the universe was only  $\sim 3$  Gyr old (e.g., Labbé et al. 2005; Kriek et al. 2006; Williams et al. 2009). The recent discovery that these high-redshift galaxies still grow significantly in size (e.g., Daddi et al. 2005; Trujillo et al. 2006; van Dokkum et al. 2008), and mass (van Dokkum et al., 2010) solves this apparent conflict. The observed compact high-redshift galaxies may simply be the cores of local massive early-type galaxies, which grow inside-out by accreting (smaller) galaxies (e.g., Naab et al. 2009; Bezanson et al. 2009; van der Wel et al. 2009), and thus assemble a significant part of their mass at later times (see also Oser et al. 2010).

However, the results may be interpreted incorrectly due to systematic uncertainties. First, sizes may have been underestimated, as low-surface brightness components might have been missed (Mancini et al., 2010). Nonetheless, recent work using stacking techniques (e.g., van der Wel et al. 2008; Cassata et al. 2010; van Dokkum et al. 2010), and ultra-deep *Hubble Space Telescope* Wide Field Camera 3 (*HST*-WFC3) data (e.g., Szomoru et al., 2010), demonstrated that radial profiles can now be measured with high accuracy extending to large radii. Second, the stellar mass estimates suffer from uncertainties in stellar population synthesis (SPS) models, the paucity of spectroscopic redshifts, and furthermore rely on assumptions regarding the initial mass function (IMF) and metallicity (e.g., Conroy et al., 2009). Direct kinematic mass measurements, which are not affected by these uncertainties, are needed to confirm the high stellar masses and densities of these galaxies.

Kinematic measurements have only recently become possible for high-redshift galaxies (e.g., Cenarro & Trujillo, 2009). Using optical spectroscopy, Newman et al. (2010) have explored the epoch up to  $z \sim 1.5$ . With near-infrared (NIR) spectroscopy these studies have been pushed to even higher redshift. Using a  $\sim 29$  hr spectrum of an ultra-compact galaxy at  $z = 2.2$  obtained with Gemini Near-IR Spectrograph (Kriek et al., 2009), van Dokkum et al. (2009b) found a high, though uncertain velocity dispersion of  $\sigma = 510_{-95}^{+165}$  km s $^{-1}$ . Onodera et al. (2010) used the MOIRCS on the Subaru telescope to observe the rest-frame optical spectrum of a less-compact, passive, ultra-massive galaxy at  $z = 1.82$ , but the low spectral resolution only allowed the determination of an upper limit to the velocity dispersion of  $\sigma < 326$  km s $^{-1}$ . With the lack of high-quality dynamical data at  $z > 1.5$  there still is no general consensus on the matter of compact quiescent galaxies.

Here we present the first high signal-to-noise ratio (S/N), high-resolution, UV-NIR spectrum of a  $z = 1.80$  galaxy observed with X-Shooter (D'Odorico et al., 2006) on the Very Large Telescope (VLT). Throughout the chapter we assume a  $\Lambda$ CDM cosmology with  $\Omega_m = 0.3$ ,  $\Omega_\Lambda = 0.7$ , and  $H_0 = 70$  km s $^{-1}$  Mpc $^{-1}$ . All broadband data are given in the AB-based photometric system.

## 2.2 Observations and reduction

The target is selected from the NEWFIRM Medium-Band Survey (NMBS; van Dokkum et al. 2009; Whitaker et al. 2011). This target, NMBS-C7447 ( $\alpha = 10^{\text{h}}00^{\text{m}}06.955^{\text{s}}$ ,  $\delta =$

02<sup>d</sup>17<sup>m</sup>33.603<sup>s</sup>), was selected as it is among the brightest ( $K_{\text{tot}} = 19.64$ ), quiescent galaxies in the COSMOS field. As the galaxy was selected for its apparent magnitude, it is probably younger than the typical quiescent galaxy at its redshift (Whitaker et al., 2010). A radio counterpart was detected, with  $L = 9.789 \times 10^{24} \text{ W m}^{-2} \text{ Hz}^{-1}$  (Schinnerer et al., 2010).

The galaxy was observed for 2 hr with X-Shooter on the VLT/UT2 on 2010 January 21st, with clear sky conditions and an average seeing of 0''.8 X-Shooter consists of three arms: UVB, VIS, and NIR, resulting in a simultaneous wavelength coverage from 3000 Å to 24800 Å. The NIR part of the spectrum is the most interesting, as it covers many of the strong rest-frame optical stellar absorption features. A 0''.9 slit was used ( $R = 5600$  at 1.5 μm). The 2 hr of observing time were split in 8 exposures of 15 minutes each with an ABA'B' on-source dither pattern. A telluric standard of type B9V was observed for calibration purposes.

We use a similar procedure to reduce cross-dispersed NIR spectra as in Kriek et al. (2008); details will be given in Chapter 3. The resulting two-dimensional spectrum was visually inspected for emission lines, but none were found. A one-dimensional spectrum was extracted by adding all lines (along wavelength direction), with flux greater than 0.1 times the flux in the central row, using optimal weighting. Our results do not change if we take a different flux limit for extraction. This high-resolution spectrum has a S/N 10.4 Å<sup>-1</sup> in rest frame in  $H$ . A low-resolution spectrum was constructed by binning the two-dimensional spectrum in wavelength direction. Using a bi-weight mean, 20 good pixels, i.e., not affected by skylines or strong atmospheric absorption, were combined. The one-dimensional spectrum was extracted from this binned two-dimensional spectrum in a similar fashion as the high-resolution spectrum (see Figure 2.1).

For the UVB and VIS arm, the two-dimensional spectra were reduced using the ESO pipeline (1.2.2, Goldoni et al. 2006). Correction for the atmospheric absorption and one-dimensional extraction were performed in a similar way as the NIR arm as described above.

## 2.3 Stellar population and structural properties

### 2.3.1 Stellar population properties

We estimate the redshift, age, dust content, star formation timescale, metallicity, stellar mass, star formation rate (SFR), and their confidence intervals by fitting the low-resolution spectrum in combination with the broadband photometry with SPS models. We use the fitting code FAST (Kriek et al., 2009b) in combination with the stellar templates by Bruzual & Charlot (2003) (hereafter BC03; see Kriek et al. 2010). An exponentially declining star formation history with timescale  $\tau$  is assumed, together with a Chabrier (2003) IMF, and the Calzetti et al. (2000) reddening law. We scale the mass by the ratio between the total F160W flux in the best-fit GALFIT model (see Section 2.3.2), and the total  $H$  band flux in the NMBS catalog. The galaxy spectrum is best-fit with a stellar mass of  $M_{\star} = 1.5 \times 10^{11} M_{\odot}$ ,  $\tau = 0.03$  Gyr, an age of 0.40 Gyr, SFR of  $0.002 M_{\odot} \text{ yr}^{-1}$ ,  $A_V = 0.20$ , solar metallicity, and a redshift of 1.800 (see Figure 2.1). In order to account for systematic uncertainties (e.g., Conroy et al., 2009), we will assume an error of  $\sim 0.2$  dex in  $M_{\star}$ . The galaxy is not detected at 24 μm, leading to a  $3 \sigma$  ( $\sim 20 \mu\text{Jy}$ ) upper limit to the dust-enshrouded SFR of  $< 15 M_{\odot} \text{ yr}^{-1}$ .



### 2.3.2 Size measurement

We obtained *HST*-WFC3 F160W imaging of NMBS-C7447 in 2010 October (*HST*-GO-12167.1, see Figure 2.2) to measure its size by fitting a Sérsic radial surface brightness profile (Sérsic, 1968), using the two-dimensional fitting program GALFIT (version 3.0.2; Peng et al. 2010). The blue object to the north was masked in the fit, as it is unclear whether it is part of the galaxy. All parameters, including the sky, were left free for GALFIT to determine, and three nearby field stars were used for the point-spread-function (PSF) convolution.

In WFC3 F160W we find a mean circularized effective radius of  $1.64 \pm 0.15$  kpc, a mean Sérsic  $n$ -parameter of  $5.3 \pm 0.4$ , and an axis ratio  $b/a = 0.71 \pm 0.01$ . The uncertainties reflect both sky noise and PSF uncertainties, which were simulated using different field stars. We find the same effective radius if we use the residual-corrected method as described by Szomoru et al. (2010). We also analyzed an ACS  $I$ -band image from the COSMOS survey (Scoville et al. 2007; Koekemoer et al. 2007). The target has an effective radius of  $r_e = 1.95 \pm 0.20$  kpc with  $n = 5.6 \pm 0.4$ , using the same PSF stars as for WFC3. An arclike feature is present in the residual image, to the southeast of the object (within  $1''.5$ , and  $\sim 3$  mag fainter than the main target). This may indicate that the galaxy is undergoing a tidal interaction (see also van Dokkum & Brammer 2010). In what follows, we will use the mean effective radius obtained with WFC3 F160W( $H$ ), as this band coincides with rest-frame optical for our  $z \sim 1.8$  galaxy.

### 2.3.3 Velocity dispersion

We use our high-resolution spectrum, and the Penalized Pixel-Fitting method (pPXF) developed by Cappellari & Emsellem (2004) to measure an accurate stellar velocity dispersion for NMBS-C7447. Four different templates were used: the best-fit BC03 SPS model ( $\sigma = 85$   $\text{kms}^{-1}$ ), Munari synthetic stellar library (Munari et al. 2005,  $\sigma = 6.4$   $\text{kms}^{-1}$ ), Indo US Library (Valdes et al. 2004,  $\sigma = 38.2$   $\text{kms}^{-1}$ ), and the Miles library (Sánchez-Blázquez et al. 2006,  $\sigma = 71.9$   $\text{kms}^{-1}$ ). Except for the best-fit SPS model, pPXF was used to construct an optimal

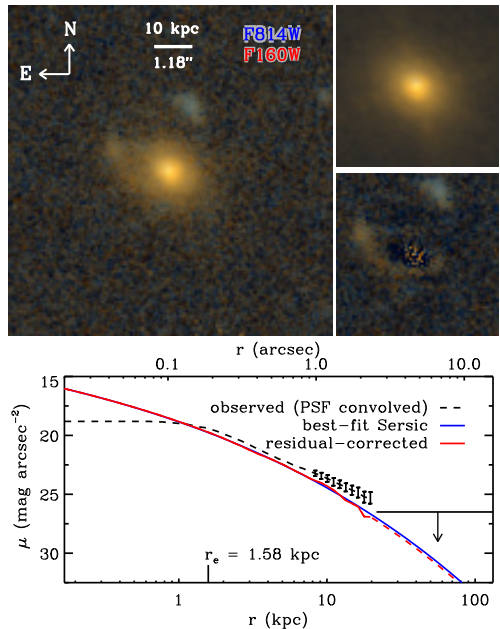


Figure 2.2: Left panel: *HST* color image of NMBS-C7296, consisting of ACS-F775W (blue) and WFC3-F160W (red). Top right panel: best-fit Sérsic model convolved with the PSF from GALFIT. The best-fit effective radius is  $r_e = 1.64 \pm 0.15$  kpc and  $n = 5.3 \pm 0.4$ . Bottom right panel: remaining residual after subtracting the model from the observed image divided by the noise. Bottom panel: observed radial profile of NMBS-C7447, in comparison with the best-fit Sérsic profile and the residual-corrected profile, as described by Szomoru et al. (2010).

template in combination with a 30th-order Legendre Polynomial. The fit was restricted to  $4020 \text{ \AA} < \lambda < 6400 \text{ \AA}$ , in order to exclude the Balmer break region and the noisier  $K$ -band. Figure 2.1 (bottom panels) shows the high-resolution spectrum with the best-fit velocity dispersion model from pPXF in red using the best-fit SPS model.

After correcting for instrumental resolution ( $\sigma=23 \text{ km s}^{-1}$ ) and the spectral resolution of the templates, we find a best-fitting velocity dispersion of  $\sigma_{\text{obs}}=284\pm 51 \text{ km s}^{-1}$ . The error was determined in the following way. We subtracted the best-fit template from the spectrum. This residual was randomly rearranged in wavelength space and added to best-fit template. We determined the velocity dispersion of 1000 simulated spectra. Our quoted error is the standard deviation of the resulting distribution of  $\sigma$ . When we include the Balmer break region in the fit, the formal error decreases, but the derived dispersion becomes very dependent on the chosen stellar template. Fitting the full-wavelength range gives a consistent result of  $\sigma_* = 328\pm 35 \text{ km}$ , but we prefer to use the method above as it is the most robust.

The stellar velocity dispersion is corrected to match the average dispersion as would be observed within an aperture radius of  $r_e$ . Our approach is similar to Cappellari et al. (2006), but taken into account the effects of a non-circular aperture, seeing, and optimized extraction. The aperture correction is only 3.5%, resulting in a velocity dispersion of  $\sigma_e=294\pm 51 \text{ km s}^{-1}$  (see Chapter 3).

The dynamical mass is derived using

$$M_{\text{dyn}} = \frac{\beta(n) \sigma_*^2 r_e}{G} \quad (2.1)$$

where  $\beta(n)$  is an analytic expression as a function of the Sérsic index, as described by Cappellari et al. (2006). Using  $n = 5.27$ , we find  $\beta = 5.16$ , and a dynamical mass for NMBS-C7447 of  $1.7\pm 0.5 \times 10^{11} M_{\odot}$ .

## 2.4 Evolution

In this section we compare our results to low- and high-redshift measurements, and discuss the implications for the evolution of quiescent galaxies. Figure 2.3 shows our results, together with other kinematical studies at  $z > 1$ , and galaxies from the Sloan Digital Sky Survey (SDSS) at  $0.05 < z < 0.07$  (York et al., 2000). The SDSS structural parameters are from Franx et al. (2008), though we only select non-starforming galaxies (i.e., specific SFR  $< 0.3/t_H$ , see Williams et al. 2009). For all galaxies, velocity dispersions were corrected as described in Section 2.3.3, and stellar masses were converted to a Chabrier (2003) IMF. All dynamical masses were derived using Equation 2.1.

Many high-redshift studies rely on photometric stellar masses, which suffer from large uncertainties (e.g., Conroy et al., 2009). Here, we test these stellar masses by comparing them to our dynamical measurements (Figure 2.3(a)). The dynamical and stellar mass for NMBS-C7447 are in agreement, and consistent with the relation for low-redshift galaxies. Given this good agreement, we should be able to predict the velocity dispersion from the size and stellar mass measurements.

We assume a constant ratio of  $M_{\text{dyn}}/M_* = 1.68$ , which is the average ratio for the SDSS sample, to account for dark matter and systematic uncertainties in the stellar mass estimate.

We show the results in Figure 2.3(b). The predicted velocity dispersions of NMBS-C7447, and the other  $z > 1.5$  galaxies are consistent with the observed velocity dispersions. This illustrates the robustness of our size and mass measurements.

In Figure 2.3(c) we show the velocity dispersion vs. the effective radius. Similar to what has been found for other high-redshift studies, NMBS-C7447 has a clear offset from the low-redshift galaxy population. Its velocity dispersion is higher compared to  $z \sim 0.06$  galaxies with similar radii. The mass size relation is shown in Figure 2.3(d) and (e). The effective radius of our galaxy is smaller compared to local galaxies at similar masses, confirming other studies at high redshift. From Figure 2.3(f), where we show the dynamical mass vs. the observed velocity dispersion, we find that NMBS-C7447 has a higher velocity dispersion than similar-mass SDSS galaxies, in agreement with other studies of high-redshift compact galaxies.

We parameterize the mass-size relation by (Shen et al. 2003, van der Wel et al. 2008):

$$r_e = r_c \left( \frac{M_{\text{dyn}}}{10^{11} M_{\odot}} \right)^b. \quad (2.2)$$

Using a least-squares fit to the low-redshift galaxy sample, we find  $r_c = 3.32\text{kpc}$ , and  $b = 0.50$ . When comparing NMBS-C7447 to local galaxies at fixed dynamical mass, we find that the effective radius is a factor  $\sim 2.5$  smaller. We use a similar approach for the velocity dispersion as a function of dynamical mass (Figure 2.3(f)):

$$\sigma_{\star} = \sigma_c \left( \frac{M_{\text{dyn}}}{10^{11} M_{\odot}} \right)^b, \quad (2.3)$$

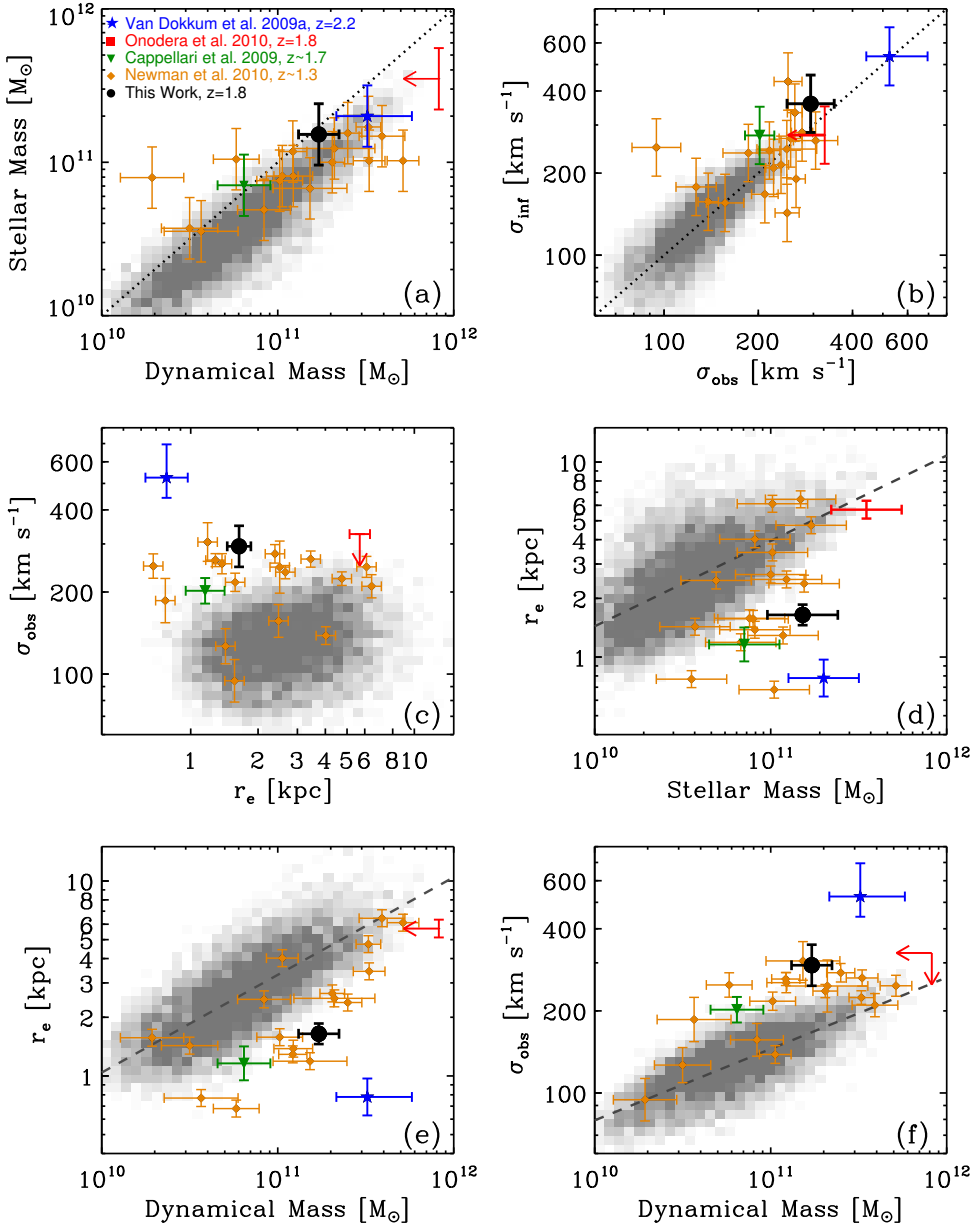
with  $\sigma_c = 145\text{kms}^{-1}$ , and  $b = 0.26$ . NMBS-C7447 has a higher velocity dispersion by a factor  $\sim 1.8$  compared to the low-redshift relation.

Figure 2.4 shows the evolution of the sizes and velocity dispersions of the galaxies, normalized to a standard dynamical mass using Equations 2.2 and 2.3. We add the sample by van der Wel et al. (2008) for a more complete redshift coverage, with stellar masses derived from the FIRES (Förster Schreiber et al., 2006) and FIREWORKS catalog (Wuyts et al., 2008). We use a simple power law fit  $r_e \propto (1+z)^{\alpha}$  for galaxies with  $M_{\text{dyn}} > 3 \times 10^{10} M_{\odot}$  and find  $\alpha = -0.98 \pm 0.09$ . This is in agreement with van der Wel et al. (2008), but slightly higher than Newman et al. (2010). Our results imply a growth in size at fixed mass by a factor of  $\sim 2.5$  from  $z \sim 1.8$  to the present day. When assuming a similar power law for the velocity dispersion ( $\sigma_{\star} \propto (1+z)^{0.51 \pm 0.07}$ ), we find a decrease in velocity dispersion by a factor of  $\sim 1.5$  from  $z \sim 1.8$  to the present day at fixed mass.

Figures 2.4a and b show that the scatter in the relation in the normalized size and velocity dispersion is large at fixed redshift. At  $z > 1.5$ , three galaxies have been observed with a range in normalized dispersions of a factor of  $\sim 2.5$ . This may lead to the conclusion that the measurements have large unidentified errors and cannot be trusted yet. On the other hand, intrinsic scatter in the galaxy properties may cause this rather large observed scatter. We can test this directly by using the deviations of the galaxies in the mass-size relation.

If the scatter is due to variations in the intrinsic properties, we expect that the deviations of the galaxies in the mass-size relation correlate with the deviations of the galaxies in the mass-dispersion relation. If the scatter is observational, there is no expected correlation. In Figure 2.4(c), we compare the deviation from the  $M_{\star} - r_e$  relation to the deviations in the





**Figure 2.3:** Comparison of NMBS-C7447 (black filled circle) with other high-redshift studies (see legend in panel (a)) and quiescent low-redshift galaxies in the SDSS (grey scale). (a) Dynamical vs. stellar mass. The dynamical and stellar masses are consistent, but differ by a constant factor, which can be due to dark matter and systematic effects on the stellar mass estimates. (b) Measured vs. inferred velocity dispersions (as inferred from the stellar mass and size). The observed dispersion agrees well with inferred dispersion, which implies that the stellar mass and size measurements are robust. (c)  $\sigma_{\text{obs}}$  vs.  $r_e$ . NMBS-C7447 is offset from the low-redshift galaxies plane. (d and e)  $r_e$  vs. stellar and dynamical mass. The dashed gray lines are the best-fit low-redshift relations (Equation 2.2). NMBS-C7447 is a factor of  $\sim 2.5$  smaller than low-redshift galaxies at fixed mass. (f)  $\sigma_{\text{obs}}$  vs. dynamical mass. The velocity dispersion of NMBS-C7447 is a factor  $\sim 1.8$  higher than similar-mass low-redshift galaxies.

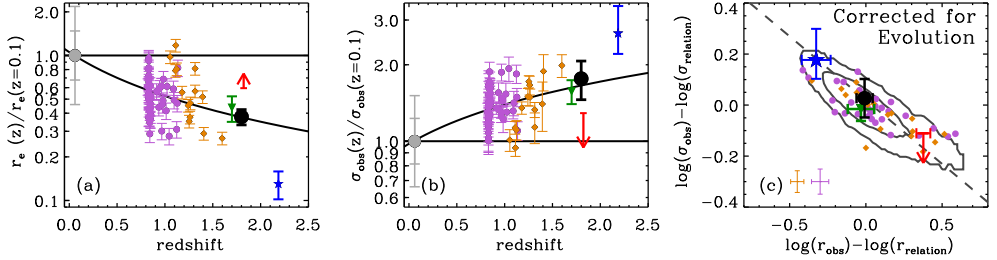


**Figure 2.4:** Evolution in effective radius and velocity dispersion at fixed dynamical mass, thus corrected for the  $M_{\text{dyn}} - r_e$  and  $M_{\text{dyn}} - \sigma_{\text{obs}}$  relations from Figure 2.3(c) and 2.3f. We only select galaxies with  $M_{\text{dyn}} > 3 \times 10^{10} M_{\odot}$ . Symbols are as described in Figure 2.3, with the addition of data from van der Wel et al. 2008 (purple circles). The gray filled circle at  $z \sim 0.06$  shows the median from the SDSS, with the error indicating the  $1\sigma$  and  $2\sigma$  scatter. The solid lines show a simple best fit to the data of  $(1+z)^{-0.98 \pm 0.09}$  for the evolution in effective radius, and  $(1+z)^{0.51 \pm 0.07}$  for the velocity dispersion. (c) Scatter in the  $M_{\star} - r_e$  relation vs. the scatter in the  $M_{\text{dyn}} - \sigma_{\text{obs}}$  relations, together with the  $1\sigma$  and  $2\sigma$  contours of the SDSS galaxies, all corrected for evolution. The discrepancy between the different measurements is expected based on the intrinsic scatter in the low-redshift relations.

$M_{\text{dyn}} - \sigma_{\text{obs}}$  relation. The deviation of the  $M_{\star} - r_e$  and  $M_{\text{dyn}} - \sigma_{\text{obs}}$  relations were derived using the evolution of these relations at fixed mass as shown in Figures 2.4(a) and (b).

We can predict, using the virial theorem, how the points would lie if the scatter is intrinsic, i.e., due to variations in the galaxy structure. This line is shown in Figure 2.4(c), and we see that the galaxies lie very close to this line. In addition, we show the area which is covered by the SDSS galaxies in the same diagram ( $1\sigma$  and  $2\sigma$  contours). Almost all data points lie within these contours. Hence we conclude that the scatter is mostly *intrinsic*, and not observational. A direct measure of the average offset of the sizes and dispersions can be obtained by increasing the number of observed galaxies to about 30, which would reduce the error by a factor of  $\sim 3$ . Alternatively, the average mass-size relation can be used to determine the average offset at  $z = 1.5 - 2$ . Thus we conclude that the difference between our results and those by van Dokkum et al. (2009b) and Onodera et al. (2010) are due to intrinsic scatter in galaxy properties.

## 2.5 Conclusions

In this chapter we have presented the first high-S/N, high-resolution, spectrum of a compact massive quiescent galaxy at  $z = 1.80$  observed with X-Shooter. Using this spectrum we have determined the stellar mass and velocity dispersion:  $M_{\star} \sim 1.5 \times 10^{11} M_{\odot}$ ,  $\sigma_{\text{obs}} = 294 \pm 51 \text{ km s}^{-1}$ . From *HST*-WFC3 imaging we find that  $r_e = 1.64 \pm 0.15 \text{ kpc}$ . The stellar mass and dynamical mass agree well ( $M_{\text{dyn}} = 1.7 \pm 0.5 \times 10^{11} M_{\odot}$ ), and are consistent with the local SDSS relation. Our results suggest that stellar masses at high redshift are robust, and thus supports the claim that massive, quiescent galaxies with high stellar mass densities at  $z \sim 2$  exist.

When comparing this galaxy to low-redshift early-type galaxies, we find that it is structurally different. At fixed dynamical mass, NMBS-C7447 is smaller by a factor  $\sim 2.5$ , and has a higher velocity dispersion by a factor of  $\sim 1.8$ .

Despite the high accuracy of our derived stellar parameters, our study is still limited to a

single high-redshift galaxy, and it brings the total number of stellar kinematic measurements for individual galaxies at  $z > 1.5$  to three. We have shown that the differences between the three measurements can be explained by the scatter in the mass-size relation. A larger sample of compact massive quiescent galaxies at high redshift is needed to accurately measure the structural evolution of these galaxies with cosmic time.

## Acknowledgements

We thank Johan Fynbo and Joanna Holt on the reduction of the UVB and VIS X-Shooter data, and the NMBS team for their contribution. This research was supported by grants from the Netherlands Foundation for Research (NWO), the Leids Kerkhoven-Bosscha Fonds. Support for program HST-GO-12167.1 was provided by NASA through a grant from the Space Telescope Science Institute.

## References

- Bezanson, R., van Dokkum, P. G., Tal, T., Marchesini, D., Kriek, M., Franx, M., & Coppi, P. 2009, *ApJ*, 697, 1290
- Bruzual, G., & Charlot, S. 2003, *MNRAS*, 344, 1000
- Calzetti, D., Armus, L., Bohlin, R. C., Kinney, A. L., Koornneef, J., & Storchi-Bergmann, T. 2000, *ApJ*, 533, 682
- Cappellari, M., & Emsellem, E. 2004, *PASP*, 116, 138
- Cappellari, M., et al. 2006, *MNRAS*, 366, 1126
- Cappellari, M., et al. 2009, *ApJ*, 704, L34
- Cassata, P., et al. 2010, *ApJ*, 714, L79
- Cenarro, A. J., & Trujillo, I. 2009, *ApJ*, 696, L43
- Chabrier, G. 2003, *PASP*, 115, 763
- Conroy, C., Gunn, J. E., & White, M. 2009, *ApJ*, 699, 486
- Daddi, E., et al. 2005, *ApJ*, 626, 680
- D'Odorico, S., et al. 2006, *Proc. SPIE*, 6269,
- Förster Schreiber, N. M., et al. 2006, *AJ*, 131, 1891
- Franx, M., van Dokkum, P. G., Schreiber, N. M. F., Wuyts, S., Labbé, I., & Toft, S. 2008, *ApJ*, 688, 770
- Goldoni, P., et al. 2006, *Proc. SPIE*, 6269,
- Koekemoer, A. M., et al. 2007, *ApJS*, 172, 196
- Kriek, M., et al. 2006, *ApJ*, 649, L71
- Kriek, M., et al. 2008, *ApJ*, 677, 219
- Kriek, M., van Dokkum, P. G., Labbé, I., Franx, M., Illingworth, G. D., Marchesini, D., & Quadri, R. F. 2009a, *ApJ*, 700, 221
- Kriek, M., van Dokkum, P. G., Franx, M., Illingworth, G. D., & Magee, D. K. 2009b, *ApJ*, 705, L71
- Kriek, M., et al. 2010, *ApJ*, 722, L64
- Labbé, I., et al. 2005, *ApJ*, 624, L81
- Mancini, C., et al. 2010, *MNRAS*, 401, 933
- Munari, U., Sordo, R., Castelli, F., & Zwitter, T. 2005, *A&A*, 442, 1127
- Naab, T., Johansson, P. H., & Ostriker, J. P. 2009, *ApJ*, 699, L178
- Newman, A. B., Ellis, R. S., Treu, T., & Bundy, K. 2010, *ApJ*, 717, L103
- Onodera, M., et al. 2010, *ApJ*, 715, L6
- Oser, L., Ostriker, J. P., Naab, T., Johansson, P. H., & Burkert, A. 2010, *ApJ*, 725, 23
- Peng, C. Y., Ho, L. C., Impey, C. D., & Rix, H.-W. 2010, *AJ*, 139, 2097
- Sánchez-Blázquez, P., et al. 2006, *MNRAS*, 371, 703
- Schinnerer, E., et al. 2010, *ApJS*, 188, 384
- Scoville, N., et al. 2007, *ApJS*, 172, 1
- Sérsic, J. L. 1968, *Cordoba, Argentina: Observatorio Astronomico*, 1968,
- Shen, S., Mo, H. J., White, S. D. M., Blanton, M. R., Kauffmann, G., Voges, W., Brinkmann, J., & Csabai, I. 2003, *MNRAS*, 343, 978
- Springel, V., et al. 2005, *Nature*, 435, 629
- Szomoru, D., et al. 2010, *ApJ*, 714, L244
- Trujillo, I., et al. 2006, *MNRAS*, 373, L36
- Valdes, F., Gupta, R., Rose, J. A., Singh, H. P., & Bell, D. J. 2004, *ApJS*, 152, 251
- van Dokkum, P. G., et al. 2008, *ApJ*, 677, L5
- van Dokkum, P. G., et al. 2009a, *PASP*, 121, 2
- van Dokkum, P. G., Kriek, M., & Franx, M. 2009b, *Nature*, 460, 717
- van Dokkum, P. G., et al. 2010, *ApJ*, 709, 1018
- van Dokkum, P. G., & Brammer, G. 2010, *ApJ*, 718, L73
- van der Wel, A., Holden, B. P., Zirm, A. W., Franx, M., Rettura, A., Illingworth, G. D., & Ford, H. C. 2008, *ApJ*, 688, 48
- van der Wel, A., Bell, E. F., van den Bosch, F. C., Gallazzi, A., & Rix, H.-W. 2009, *ApJ*, 698, 1232
- Whitaker, K. E., et al. 2010, *ApJ*, 719, 1715
- Whitaker, K. E., et al. 2011, in press, *arXiv:1105.4609*
- Williams, R. J., Quadri, R. F., Franx, M., van Dokkum, P., & Labbé, I. 2009, *ApJ*, 691, 1879
- Wuyts, S., Labbé, I., Schreiber, N. M. F., Franx, M., Rudnick, G., Brammer, G. B., & van Dokkum, P. G. 2008, *ApJ*, 682, 985
- York, D. G., et al. 2000, *AJ*, 120, 1579



# 3 | Stellar kinematics of $z \sim 2$ galaxies and the inside-out growth of quiescent galaxies

## Abstract

Using stellar kinematics measurements, we investigate the growth of massive, quiescent galaxies from  $z \sim 2$  to today. We present X-Shooter spectra from the UV to NIR and dynamical mass measurements of five quiescent massive ( $> 10^{11} M_{\odot}$ ) galaxies at  $z \sim 2$ . This triples the sample of  $z > 1.5$  galaxies with well constrained ( $\delta\sigma < 100 \text{ km s}^{-1}$ ) velocity dispersion measurements. From spectral population synthesis modeling we find that these galaxies have stellar ages that range from 0.5-2 Gyr, with no signs of ongoing star formation. We measure velocity dispersions (290-450  $\text{km s}^{-1}$ ) from stellar absorption lines and find that they are 1.6-2.1 times higher than those of galaxies in the Sloan Digital Sky Survey at the same mass. Sizes are measured using GALFIT from *Hubble Space Telescope* Wide Field Camera 3  $H_{160}$  and UDS  $K$ -band images. The dynamical masses correspond well to the spectral energy distribution based stellar masses, with dynamical masses that are  $\sim 15\%$  higher. We find that  $M_*/M_{\text{dyn}}$  may decrease slightly with time, which could reflect the increase of the dark matter fraction within an increasing effective radius. We combine different stellar kinematic studies from the literature, and examine the structural evolution from  $z \sim 2$  to  $z \sim 0$ : we confirm that at fixed dynamical mass, the effective radius increases by a factor of  $\sim 2.8$ , and the velocity dispersion decreases by a factor of  $\sim 1.7$ . The mass density within one effective radius decreases by a factor of  $\sim 20$ , while within a fixed physical radius (1 kpc) it decreases only mildly (factor of  $\sim 2$ ). When we allow for an evolving mass limit by selecting a population of galaxies at fixed number density, a stronger size growth with time is found (factor of  $\sim 4$ ), velocity dispersion decreases by a factor of  $\sim 1.4$ , and interestingly, the mass density within 1 kpc is consistent with no evolution. This finding suggests that massive quiescent galaxies at  $z \sim 2$  grow inside-out, consistent with the expectations from minor mergers.

Jesse van de Sande, Mariska Kriek, Marijn Franx, Pieter G. van Dokkum,  
Rachel Bezanson, Rychard J. Bouwens, Ryan F. Quadri,  
Hans-Walter Rix, and Rosalind E. Skelton  
*The Astrophysical Journal*, 771, 85:110, (2013)

### 3.1 Introduction

Recent studies have shown that a considerable fraction of massive galaxies at  $1.5 < z < 2.5$  have quiescent stellar populations (e.g., Labbé et al. 2005; Kriek et al. 2006; Williams et al. 2009). Among the most massive galaxies ( $M_* > 10^{11} M_\odot$ ) approximately 40% are no longer forming stars (e.g., Whitaker et al. 2011; Brammer et al. 2011). Surprisingly, these massive quiescent galaxies have been found to be extremely compact (e.g., Daddi et al. 2005; Trujillo et al. 2006; van Dokkum et al. 2008; Franx et al. 2008; van der Wel et al. 2008; and numerous others), compared to their likely present-day counterparts.

Searches for ultra-dense low-redshift counterparts by Trujillo et al. (2009) and Taylor et al. (2010a) found only a handful of compact sources at  $z \sim 0$ , which have relatively young stellar populations (Trujillo et al. 2009; Ferré-Mateu et al. 2012). The dearth of massive, old compact objects at low redshift implies that massive galaxies must have undergone severe structural evolution in size.

Errors in the size estimates have been invoked as a possible explanation for the compactness of massive high-redshift galaxies. Initial concerns that the size may have been underestimated, due to an envelope of low surface brightness light, have been addressed with deep *Hubble Space Telescope* Wide Field Camera 3 (*HST*-WFC3) imaging (Szomoru et al. 2010; 2012), and by stacking results (e.g., van der Wel et al. 2008; Cassata et al. 2010; van Dokkum et al. 2008, 2010). The light could also be more concentrated due to the presence of active galactic nuclei (AGNs) in these galaxies. However, spectra of subsamples of these galaxies have shown that the light is dominated by evolved stellar populations, not AGNs (Kriek et al. 2006, 2009; van de Sande et al. 2011; Onodera et al. 2012).

The question of whether stellar masses are accurate out to  $z \sim 2$  remains, however, a serious concern: an overestimate in stellar mass would bring the galaxies closer to the  $z \sim 0$  mass-size relation. To date, basically all (stellar) masses have been derived by fitting the spectral energy distributions (SEDs). This method suffers from many systematic uncertainties in stellar population synthesis (SPS) models (e.g., Conroy et al. 2009; Muzzin et al. 2009) and is essentially untested at  $z > 1.5$ .

Direct stellar kinematic mass measurements, which do not suffer from these uncertainties, can be derived by measuring the galaxy's velocity dispersion and the shape and extent of its luminosity profile, i.e., the Sérsic  $n$  parameter and effective radius. In particular, for low-redshift galaxies in the Sloan Digital Sky Survey (SDSS), Taylor et al. (2010b) showed that stellar mass is a very good predictor of dynamical mass, but only when non-homology of luminosity profile is properly accounted for using a Sérsic-dependent virial factor (e.g., Cappellari et al. 2006). Although dynamical measurements of massive galaxies are common at low redshift, spectroscopic studies become much more difficult at higher redshift as the bulk of the light, and stellar absorption features used to measure kinematics, shift redward into the near-infrared (NIR; e.g., Kriek et al. 2009; van Dokkum et al. 2009).

New technology such as the new red arm of the LRIS spectrograph at Keck (working beyond 1) makes it possible to measure velocity dispersions up to  $z \sim 1.5$  (Newman et al. 2010, Bezanson et al. 2013). Deep NIR spectroscopy is, however, required to push stellar kinematic studies to even higher redshift. From a  $\sim 29$  hr spectrum of an ultra-compact galaxy at  $z = 2.2$  obtained with Gemini Near-IR Spectrograph (Kriek et al., 2009), van Dokkum et al. (2009) found a high, though uncertain, velocity dispersion of  $\sigma = 510_{-95}^{+165} \text{ km s}^{-1}$ .

Onodera et al. (2012) used the MOIRCS on the Subaru telescope to observe the rest-frame optical spectrum of a less-compact, passive, ultra-massive galaxy at  $z = 1.82$ , but the low spectral resolution and signal-to-noise ratio (S/N) severely limited the accuracy of their velocity dispersion:  $\sigma = 270 \pm 105 \text{ km s}^{-1}$ . X-Shooter (D’Odorico et al. 2006; Vernet et al. 2011), the new Ultraviolet (UV) to NIR spectrograph at the Very Large Telescope (VLT), can provide the required S/N and resolution. The capabilities of X-Shooter for this kind of measurements were demonstrated in van de Sande et al. (2011), who found  $294 \pm 51 \text{ km s}^{-1}$  for a massive quiescent galaxy at  $z = 1.8$ . Toft et al. (2012) also use X-Shooter and present a dynamical measurement of a galaxy at redshift  $z = 2.04$  with similar results. Taken all together, these results indicate that the dynamical and stellar masses are consistent with  $z \sim 0$ . With the small number of measurements beyond  $z > 1.5$ , however, the sample is still too small to draw any firm conclusions on whether the stellar masses are truly reliable.

Here we present a sample of five massive quiescent galaxies with high S/N, medium-resolution, UV-NIR spectra at  $1.4 < z < 2.1$  observed with X-Shooter on the VLT. The main goal of this chapter will be to test if the stellar mass measurements at high redshift are reliable.

The chapter is organized as follows. In Section 3.2 we, present our sample of high-redshift galaxies, the photometric and spectroscopic data, and describe our data reduction. In Section 3.3 we determine structural properties and stellar populations, and derive stellar and dynamical masses. We complement our results with stellar kinematic results from other studies at low and high redshift in Section 3.4. In Section 3.5, we compare our dynamical to the stellar masses. In Section 3.6 we study the structural evolution of high-redshift quiescent massive galaxies. In Section 3.7, we compare our results with previous measurements and hydrodynamical simulations. Finally, in Section 3.8, we summarize our results and conclusions. Throughout the chapter we assume a  $\Lambda$ CDM cosmology with  $\Omega_m=0.3$ ,  $\Omega_\Lambda = 0.7$ , and  $H_0 = 70 \text{ km s}^{-1} \text{ Mpc}^{-1}$ . All broadband data are given in the AB-based photometric system.

## 3.2 Data

### 3.2.1 Target selection

The galaxies in this chapter are drawn from the NMBS-I (Whitaker et al., 2010) and the UKIDSS-UDS (Williams et al., 2009). They were selected to be bright in the  $H$ -band, and to have  $z > 1.4$ , in order to obtain sufficient S/N. The SED from the broadband and medium-band photometry was required to indicate that they have quiescent stellar populations, and the rest-frame optical imaging could not show signs of large disturbance due to e.g., mergers. We note that NMBS-COS7447 was presented in van de Sande et al. (2011), and UDS-19627 was presented in Toft et al. (2012). All data for both galaxies have been re-analyzed according to the following procedure for consistency. Our selection had no priors on mass or size, but could be biased in either one of these parameters. Full information on the photometric properties of the targets is listed in Table 3.1.

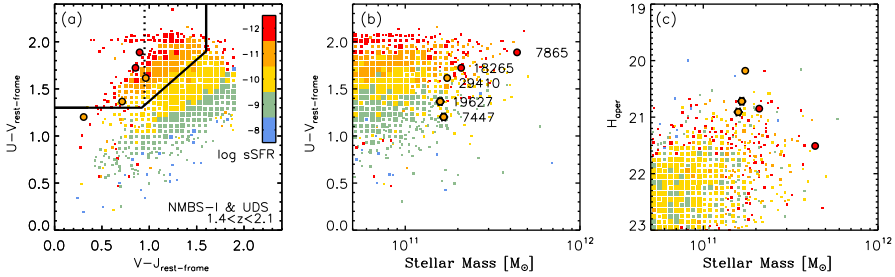
To investigate possible biases, we compare our targets to a sample of galaxies with mass  $> 10^{10.5} M_\odot$  at  $1.4 < z < 2.1$  from the NMBS-I and the UDS. Rest-frame  $U - V$  and  $V - J$  colors are commonly used to distinguish between star-forming and quiescent galaxies at this



Table 3.1: Photometric properties

Catalog	ID	$J_{\text{aper}}$	$H_{\text{aper}}$	$K_{\text{aper}}$	$K_{\text{tot}}$	$(U - V)_{\text{rf}}$	$(V - J)_{\text{rf}}$	$24 \mu\text{m}$ [ $\mu\text{Jy}$ ]	$\text{SFR}_{24\mu\text{m}}$ $M_{\odot} \text{ yr}^{-1}$
NMBS-COS	7447	21.09	20.72	20.63	19.64	1.20	0.31	18	13
NMBS-COS	18265	22.67	20.85	20.61	19.62	1.72	0.85	18	15
NMBS-COS	7865	22.75	21.51	21.07	20.02	1.89	0.90	18	19
UDS	19627	21.40	20.91	20.65	20.19	1.37	0.71	30	29
UDS	29410	20.59	20.18	19.81	19.36	1.62	0.96	$232 \pm 15$	$241 \pm 16$

Aperture and total magnitudes for our targets. Aperture magnitudes have been measured in fixed 1.5 arcsec diameter aperture for targets in NMBS-I, while the targets in UDS have 1.75 arcsec diameter apertures. Rest-frame colors have been derived from the spectra in Johnson  $U$ ,  $V$ , and  $2MASSJ$  filters. For the  $24 \mu\text{m}$  fluxes we provide  $3\text{-}\sigma$  upper-limits of  $18 \mu\text{Jy}$  for the galaxies in NMBS-COSMOS (Whitaker et al., 2012), and  $30 \mu\text{Jy}$  for UDS-19627 (Toft et al., 2012), as these galaxies are not detected with MIPS. UDS-29410 has a strong MIPS detection, which is likely due to an obscured AGN.



**Figure 3.1:** Comparison of our spectroscopic sample to the full population at similar redshift. Symbol size of the squares represent the density of galaxies from the NMBS-I and UDS at  $1.4 < z < 2.1$  with mass  $> 10^{10.5} M_{\odot}$ . (a) Rest-frame  $U-V$  and  $V-J$  colors. Color coding is based upon the sSFR derived from SED fitting, red colors indicate low sSFR (quiescent), and blue colors indicate high sSFR (star-forming). Galaxies in the top left region, as marked by the black line, all have low sSFR rates. This region is therefore often used to select quiescent galaxies at high redshift (Williams et al., 2009). All but one of our galaxies fall within this region, but their sSFR indicate that they are all have quiescent stellar populations. The vertical dotted line discriminates between young post-starburst like (left) vs. old quiescent (right) as indicated by Whitaker et al. (2012). The strong Balmer absorption lines spectroscopically confirm the young ages of this sample. (b) Rest-frame  $U-V$  vs. stellar mass. At fixed mass, we find that most of our galaxies have similar colors to the entire population, except for NMBS-COS7447 and UDS-19627 on the blue side. (c)  $H$ -band aperture magnitude vs. stellar mass. It is clear that our sample was selected on magnitude, and at fixed mass they are among the brightest galaxies, consistent with their post-starburst nature.

redshift (e.g., Williams et al. 2009). Figure 3.1(a) shows the UVJ-diagram for all galaxies at redshifts between  $1.4 < z < 2.1$  with mass  $> 10^{10.5} M_{\odot}$ , together with the sample presented here. The sizes of the squares indicate the density of galaxies. For our targets, the rest-frame colors have been measured from the spectra, while for the full sample rest-frame colors are based on the broadband and medium-band data. As demonstrated by Williams et al. (2009), non-star-forming galaxies can be identified using a color selection indicated by the black lines. Within this selection region, our targets fall in the area occupied by young, quiescent galaxies (Whitaker et al., 2012).

Table 3.2: Targets and observations

Catalog	ID	R.A.	Dec.	Exp. Time [min]	Slit Size NIR [arcsec]	S/N $J$ [ $\text{\AA}^{-1}$ ]	S/N $H$ [ $\text{\AA}^{-1}$ ]	S/N $4020 < \lambda < 7000$ [ $\text{\AA}^{-1}$ ]	Telluric Standard Star <i>Hipparcos ID</i>
NMBS-COS	7447	10:00:6.96	2:17:33.77	120	0'9	4.98	8.48	6.31	050307, 000349
NMBS-COS	18265	10:00:40.83	2:28:52.15	90	0'9	3.37	6.99	4.18	050684, 000349
NMBS-COS	7865	10:00:17.73	2:17:52.75	434	0'9	1.64	5.86	4.12	049704, 057126, 046054, 040217, 059987
UDS	19627	2:18:17.06	-5:21:38.83	300	0'6, 0'9	3.80	7.94	5.90	012377, 114656, 008352, 000328, 015389
UDS	29410	2:17:51.22	-5:16:21.84	120	0'9	3.75	7.09	4.35	012377

R.A. and Dec. are given in the J2000 coordinate system. Exposure times are given for the NIR arm, the UVB and VIS arms had slightly shorter exposure times due to the longer read out. Except for UDS19627, all targets were observed with a 0'9 slit in the NIR. S/N ratios have been determined from comparing the residual of the velocity dispersion fit to the flux, and are given for the  $J$  – and  $H$  –band as well as for the region in which we determine the velocity dispersion. Last column gives the Tellurics Standard Stars from the Hipparcos catalog that were observed before and after each target.

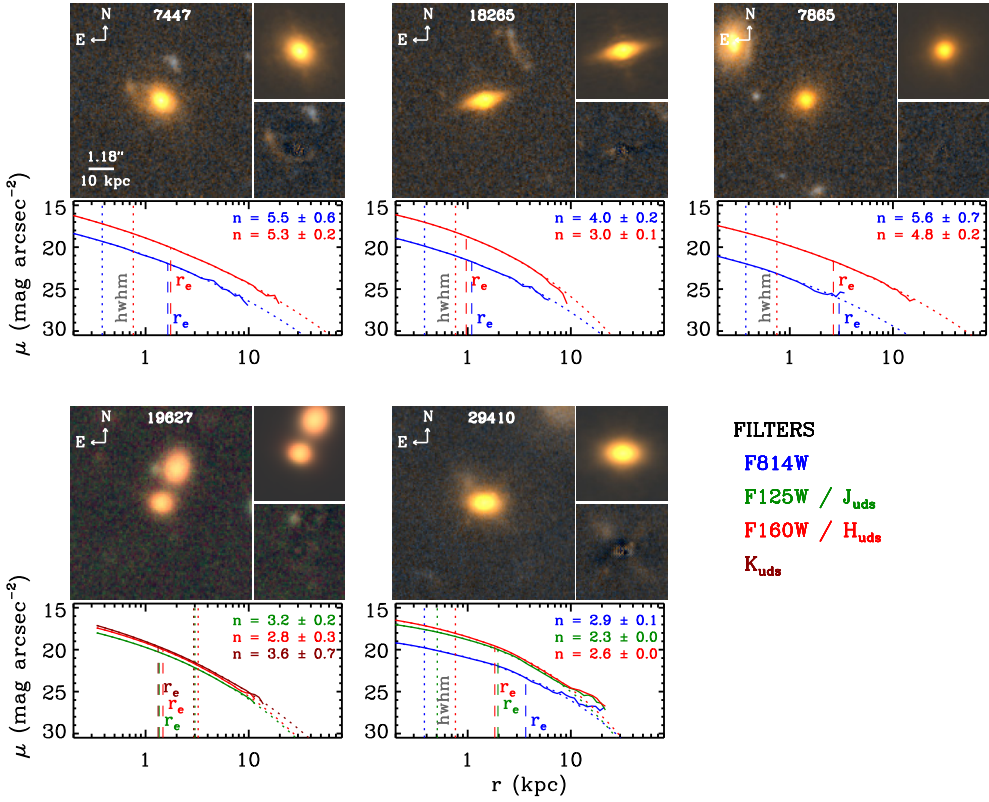


Figure 3.2: Color images of our five spectroscopic targets. Except for UDS-19627, all galaxies have available *HST*-WFC3 Imaging. For each target we show the composite color image on the left side, the best Sérsic model from GALFIT and the residual after we subtract the best-fitting model from the original image on the right side. The lower panel shows the intrinsic surface brightness profile with all available bands. Different colors show the different filters, as indicated on the bottom right. Vertical dashed lines show the effective radii for each profile, while the dotted lines shows the FWHM/2 of the PSF. We find color gradients, such that the redder bands have smaller effective radii, for all galaxies but NMBS-COS7447. For that case, the sizes are similar within the errors, but this could be caused by the extra flux of the red arc-like feature in the southeast.

The median specific star formation rates (sSFR), as indicated by the different colors, are in good agreement with the full high-redshift sample at the same place in the UVJ diagram. For their mass, however, NMBS-COS7447 and UDS-19627 have slightly bluer colors as compared to the full sample (Figure 3.1(b)). At fixed mass, the targets are among the brightest galaxies, except for NMBS-I-7865 (3.1(c)). This may not come as a surprise as they are among the youngest quiescent galaxies, and thus have relatively low  $M/L$ .

### 3.2.2 Imaging

Four different imaging data sets are used to measure the surface brightness profiles of our galaxies, as summarized below. (1) All our targets in the NMBS-I COSMOS field were ob-

served with *HST*-WFC3  $H_{160}$  as part of the program *HST*-GO-12167 (PI: Franx). Each target was observed for one orbit (2611 sec), using a four point dither pattern, with half pixel offsets. Reduction of the data was done in a similar way as to the reduction described in Bouwens et al. (2010), but without sigma-clipping in order to avoid masking the centers of stars. The drizzled images have a pixel scale of  $0''.06$ , with a full width at half-maximum (FWHM) of the point-spread function (PSF) of  $\sim 0''.16$ . (2) Our NMBS-I targets are complemented with *HST*-ACS  $I_{814}$  imaging from COSMOS (v2.0, Koekemoer et al. 2007; Massey et al. 2010), which has a  $0''.03$  pixel scale and PSF-FWHM of  $\sim 0''.11$ . (3) For UDS-29410 we make use of the *HST*-ACS F814W, *HST*-WFC3  $J_{125}$  and  $H_{160}$  from UDS-CANDELS (Grogin et al. 2011; Koekemoer et al. 2011). These data have the same properties as the data described in (1) and (2). (4) For UDS-19627 we use ground based data from UKIDSS-UDS, (Lawrence et al. 2007; Warren et al. 2007) Data Release 8 in the  $J$ ,  $H$ , and  $K$ -band, as no *HST* data is available. Imaging in all three bands were drizzled to a pixel scale  $0''.134$ , and the FWHM of the PSF is  $0''.7$  in the  $K$ -band.

### 3.2.3 Spectroscopic observations

Observations were performed with X-Shooter on the VLT UT2 (D'Odorico et al. 2006; Ver-net et al. 2011). X-Shooter is a second generation instrument on the VLT that consists of three arms: UVB, VIS, and NIR. The wavelength coverage ranges from  $3000 \text{ \AA}$  to  $24800 \text{ \AA}$  in one single exposure. The galaxies were observed in both visitor and service mode, and the observations were carried out between 2010 January and 2011 March (Programs: Fynbo 084.A-0303(D), Van de Sande 084.A-1082(A), Franx 085.A-0962(A), Toft 086.B-0955(A)). Full information on the targets and observations is listed in Table 3.2. All observations had clear sky conditions and an average seeing of  $0''.8$ . A  $0''.9$  slit was used in the NIR, except for the 1st hour of UDS-19627 where a  $0''.6$  slit was used. For the  $0''.9$  slit, this resulted in a spectral resolution of 5100 at  $1.4 \mu\text{m}$ . Observing blocks were split into exposures of 10-15 minutes each with an  $ABA'B'$  on-source dither pattern. For most targets, a telluric standard of type B8V-B9V was observed before and after our primary target, in order to create a telluric absorption spectrum at the same airmass as the observation of our target.

### 3.2.4 Spectroscopic reduction

Data from the three arms of X-Shooter must be analyzed separately and then combined to cover the full range from the UV to NIR. In the NIR we identified bad pixels in the following way. The data were corrected for dark current, flatfielded, and sky subtracted using the average of the preceding and subsequent frames. The ESO pipeline (ver. 1.3.7; Goldoni et al. 2006) was used to derive a wavelength solution for all orders. The orders were then straightened using integer pixel shifts to retain the pixels affected by cosmic-rays and bad pixels. Additional sky subtraction was done on the rectified orders, by subtracting the median in the spatial direction. Cosmic rays and bad pixels were identified by LA-Cosmic (van Dokkum & Franx, 2001), and a bad pixel mask was created.

Further  $3\sigma$  clipping was done on the different exposures, corrected for dithers, to identify any remaining outliers. The bad pixel masks of different orders were combined into a single

Table 3.3: Stellar population synthesis properties

Catalog	ID	$z_{phot}$	$z_{spec}$	$\log \tau$ (yr)	$\log Age$ (yr)	$Z$	$A_V$ (mag)	$\log M_*$ ( $M_\odot$ )	$\log SFR$ ( $M_\odot \text{yr}^{-1}$ )	$\log sSFR$ ( $\text{yr}^{-1}$ )
NMBS-COS	7447	$1.71 \pm 0.03$	1.800	7.80	8.74	0.020	0.00	11.27	-0.08	-11.35
NMBS-COS	18265	$1.60 \pm 0.03$	1.583	7.00	8.96	0.020	0.45	11.42	-99.00	-99.00
NMBS-COS	7865	$2.02 \pm 0.05$	2.091	7.20	9.41	0.008	0.05	11.68	-99.00	-99.00
UDS	19627	$1.94 \pm 0.06$	2.036	7.90	8.74	0.050	0.20	11.24	0.56	-10.68
UDS	29410	$1.44 \pm 0.02$	1.456	7.90	8.82	0.050	0.35	11.29	-99.00	-11.28

Derived stellar population synthesis properties from FAST. We use stellar templates from Bruzual & Charlot 2003, with an exponentially declining star formation history with timescale  $\tau$ , together with a Chabrier (2003) IMF, and the Calzetti et al. (2000) reddening law. No errors are provided, as the 68% confidence all fall within one grid point. The real errors are dominated by systematic uncertainties.

file and then transformed back to the raw frame for each exposure. Masks will follow the same rectification and wavelength calibration steps as the science frames.

Next the flatfielded and sky subtracted observations were rectified and wavelength calibrated, only this time we used interpolation when rectifying the different orders. Again, additional sky subtraction was done. Per order, all exposures were combined, with exclusion of bad pixels and those contaminated with cosmic rays present in the mask file.

The telluric spectra were reduced in the same way as the science frames. We constructed a response spectrum from the telluric stars in combination with a stellar model for a B8V/B9V star from a blackbody curve and models from Munari et al. (2005). Residuals from Balmer absorption features in the spectrum of the tellurics were removed by interpolation. All the orders of the science observations were corrected for instrumental response and atmospheric absorption by dividing by the response spectrum.

The different orders were then combined, and in regions of overlap weighted using the S/N of the galaxy spectrum. A noise spectrum was created by measuring the noise in the spatial direction below and above the galaxy. If the regions exceeded an acceptable noise limit, from contamination by OH lines or due to low atmospheric transmission, this spatial region was discarded for further use. The two-dimensional (2D) spectra were visually inspected for emission lines, but none were found. A one-dimensional (1D) spectrum was extracted by adding all lines (along the wavelength direction), with flux greater than 0.1 times the flux in the central row, using optimal weighting.

Absolute flux calibration was performed by scaling the spectrum to the available photometric data. The scaling was derived for each individual filter that fully covered the spectrum. For our targets in NMBS-I we used the following filters:  $J$ ,  $J2$ ,  $J3$ ,  $H$ ,  $H1$ ,  $H2$ , and,  $Ks$ , while for the targets in the UDS we only used  $J$  and  $H$ . We then used an error-weighted average obtained from the broadband magnitudes, and scaled the whole spectrum using this single value. After scaling, no color residuals were found, and no further flux corrections were applied to the spectrum.

A low resolution spectrum was constructed by binning the 2D spectrum in wavelength direction. Using a bi-weight mean, 20 good pixels, i.e., not affected by skylines or strong atmospheric absorption, were combined. The 1D spectrum was extracted from this binned

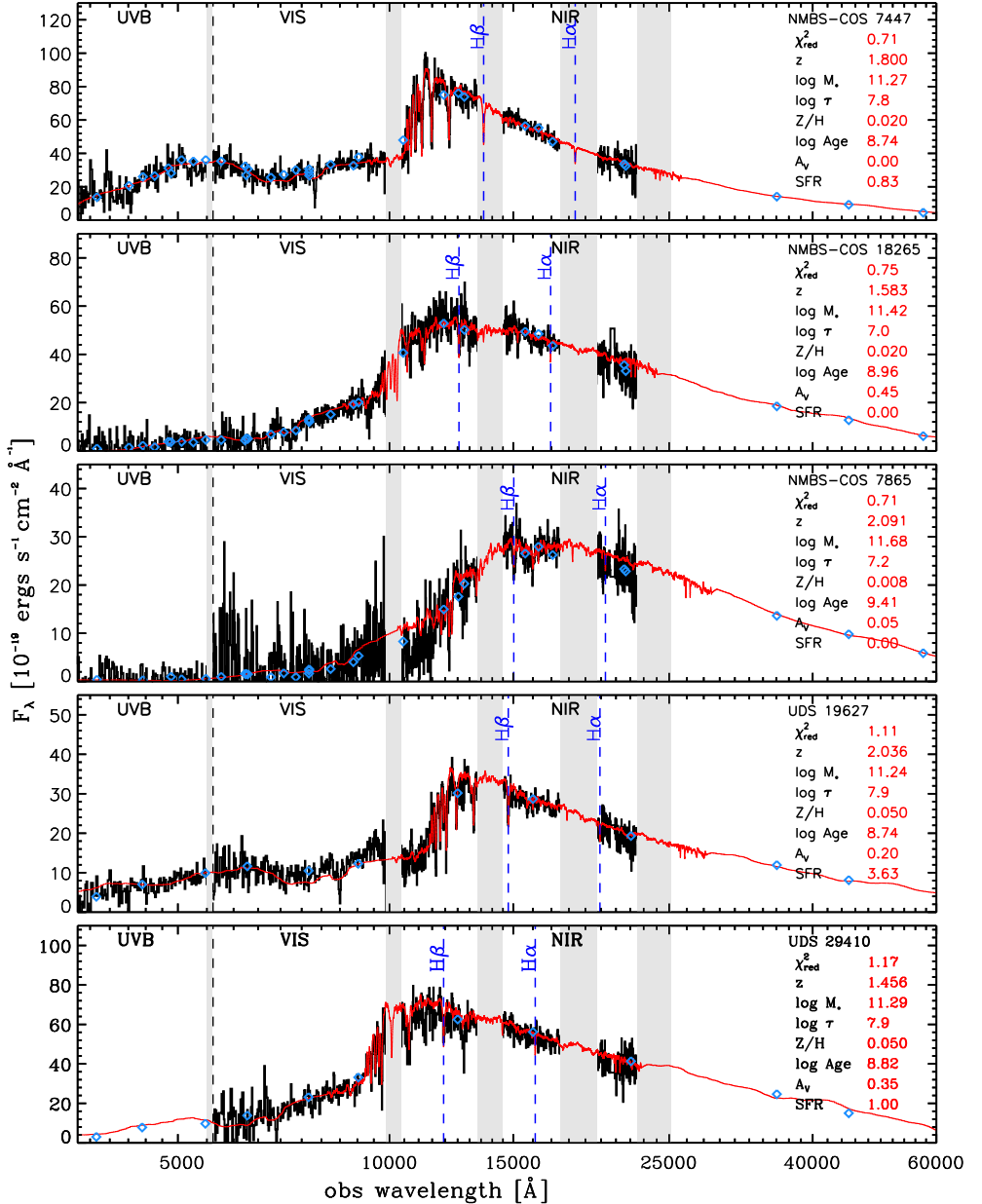


Figure 3.3: UV to NIR X-Shooter spectra in combination with medium- and broad-band data (blue diamonds). The binned spectra ( $\sim 10 \text{ \AA}$ ) are in black, together with the best-fitting BC03  $\tau$ -model as shown in red. Gray areas indicate regions with strong atmospheric absorption. The UVB spectrum is missing for UDS-29410, due to an instrument problem during the observations. The good agreement between the BC03 models and the spectroscopic data over this large wavelength range is astonishing. Both NMBS-COS7865 and UDS-19627 show a small deviation from the best-fitting model around 1, which is caused by the absence of good telluric calibrators. From stellar population synthesis modeling, we find a variety of ages that range from 0.5-2 Gyr. We find no emission lines, and other signs of star formation, and with little to no dust (see Section 3.3.1).

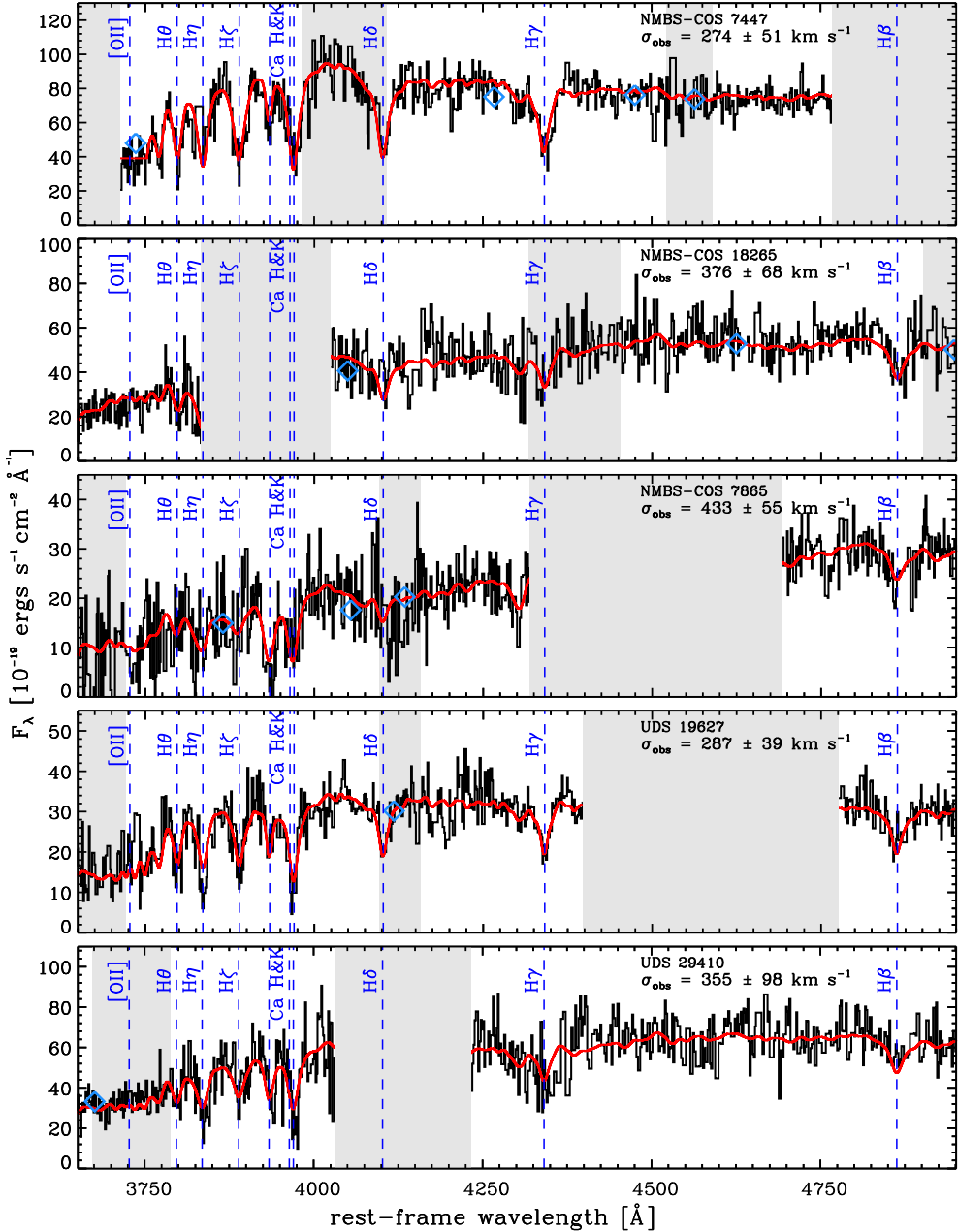


Figure 3.4: Rest-frame optical part of the spectrum focused on the Balmer break. As in Figure 3.3, the X-Shooter spectrum is shown in black, but this time in higher resolution ( $\sim 4 \text{ \AA}$  observed, or  $\sim 100 \text{ km s}^{-1}$  rest-frame). The most prominent absorption and emission features are indicated by the blue dashed lines. The clear detection of absorption lines enables us to measure stellar velocity dispersions. We use pPXF to fit the best-fitting BC03  $\tau$  model to the spectrum and find velocity dispersions that range from 275–435  $\text{km s}^{-1}$ . The convolved best-fit BC03 template is shown in red.

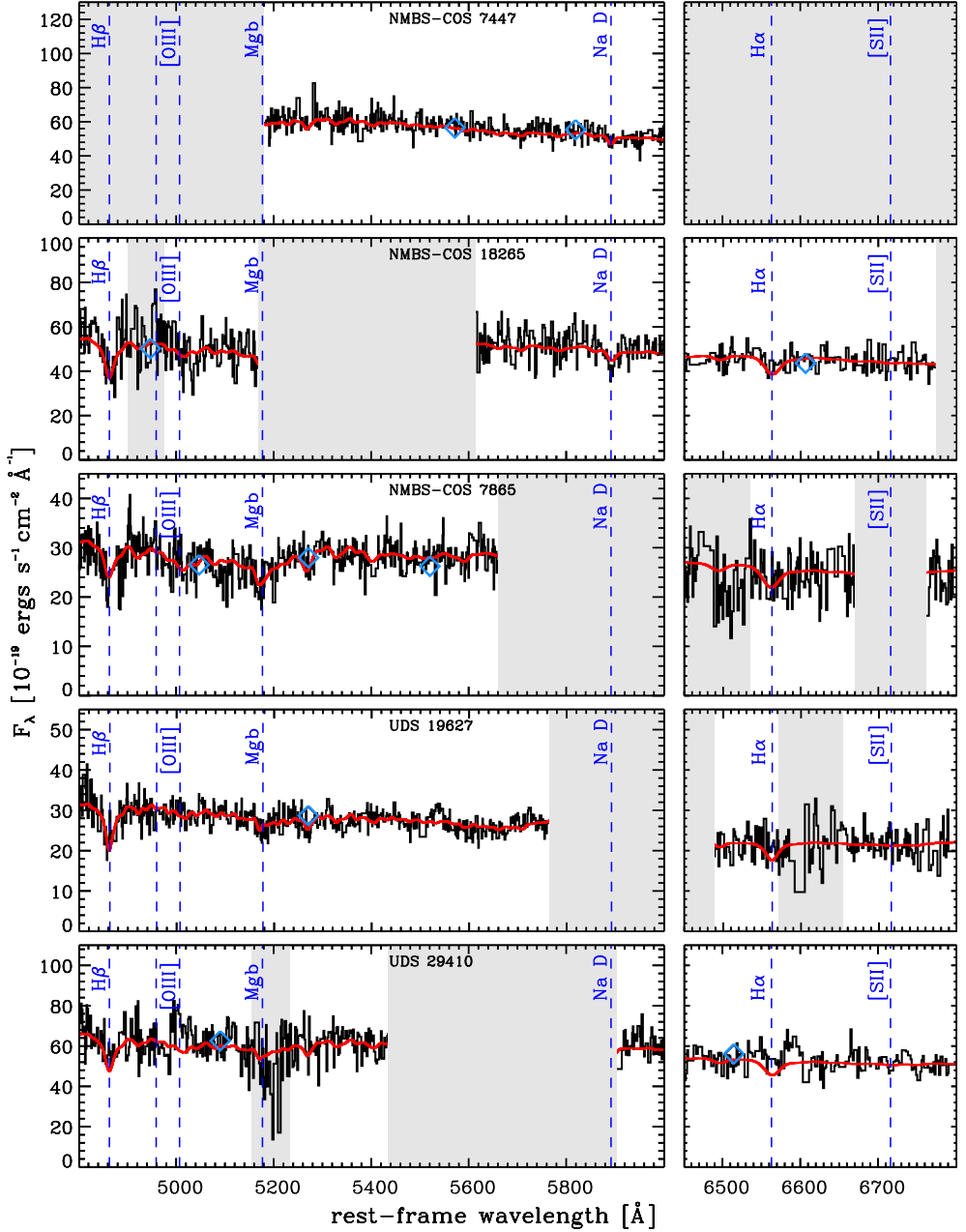


Figure 3.5: Rest-frame optical part of the spectrum focused on  $Mgb$ ,  $NaD$ , and  $H\alpha$ . As in Figure 3.4, the X-Shooter spectrum is shown in black, with high resolution of  $\sim 4 \text{ \AA}$  observed, or  $\sim 100 \text{ km s}^{-1}$  rest-frame. The most prominent absorption and emission features are indicated by the blue dashed lines. The convolved best-fit BC03 template is shown in red.



2D spectrum in a similar fashion as the high resolution spectrum (see Figure 3.3 – 3.5).

For the UVB and VIS arms we used the ESO reduction pipeline (ver 1.3.7, Goldoni et al. 2006) to correct for the bias, flatfield, and dark current, and to derive the wavelength solution. The science frames were also rectified using the pipeline, but thereafter, treated in exactly the same way as the rectified 2D spectra of the NIR arm, as described above.

### 3.3 Structural properties and stellar populations

#### 3.3.1 Stellar population properties

We estimate the stellar population properties by fitting the low-resolution ( $\sim 10 \text{ \AA}$  in the observed frame) spectrum in the visual and NIR in combination with the broadband and medium-band photometry with SPS models. We exclude the UVB part of the spectrum due to the lower S/N and the extensive high S/N broadband photometry in this wavelength region. Stellar templates from Bruzual & Charlot (2003, BC03) are used, with an exponentially declining star formation history (SFH) with timescale  $\tau$ , together with a Chabrier (2003) initial mass function (IMF), and the Calzetti et al. (2000) reddening law.

Using the FAST code (Kriek et al., 2009), we fit a full grid in age, dust content, star formation timescale, and metallicity. We adopt a grid for  $\tau$  between 10 Myr and 1 Gyr in steps of 0.1 dex. The age range can vary between 0.1 Gyr and 10 Gyr, but the maximum age is constrained to the age of the universe at that particular redshift. We note, however, that this constraint has no impact on our results as the galaxies are young. Step size in age is set as high as the BC03 templates allow, typically 0.01 dex. Metallicity can vary between  $Z = 0.004$  (subsolar),  $Z = 0.08$ ,  $Z = 0.02$ (solar), and  $Z = 0.05$  (supersolar). Furthermore, we allow dust attenuation to range from 0 to 2 mag with step size of 0.05. The redshift used here is from the best-fitting velocity dispersion (see Section 3.3.2). Results are summarized in Table 3.3.

Due to our discrete grid and the high quality data, and also because metallicity and age are limited by the BC03 models, our 68% confidence levels are all within one grid point. Our formal errors are therefore mostly zero, and not shown in Table 3.3. This does not reflect the true uncertainties, which are dominated by the choice of SPS models, IMF, SFH, and extinction law (see, e.g., Conroy et al. 2009; Muzzin et al. 2009).

The low sSFR confirms the quiescent nature of the galaxies in our sample, and they match well with the sSFR of the general population in the same region of the UVJ diagram (Figure 3.1(a)). We find a range of metallicities, with the oldest galaxy having the lowest metallicity. However, due to the strong degeneracy between age and metallicity, we do not believe this result to be significant. Overall, the dust content in our galaxies is low.

We find very similar results for NMBS-C7447 as compared to van de Sande et al. (2011), and the small differences can be explained by the newer reduction. For UDS-19627 we find a slightly lower mass as compared to Toft et al. (2012), which is likely due to the lower dust fraction that we find, i.e.,  $A_v = 0.2$  vs.  $A_v = 0.77$  from Toft et al. (2012).

Table 3.4: Compilation of masses and structural parameters for high-redshift galaxies

Reference <sup>a</sup>	ID	$z_{spec}$	$r_e$	$n_{serstic}$	$b/a$	$\sigma_e$	$\sigma_e/\sigma_{app}$	$\beta(n)$	$\log M_{dm}$	$\log M_{*,corr}$	Filter
0	7447	1.800	$1.75 \pm 0.21$	$5.27 \pm 0.23$	$0.71 \pm 0.02$	$287_{-55}^{+52}$	1.048	5.16	$11.24_{-0.13}^{+0.13}$	11.22	$H_{F160W}$
0	18265	1.583	$0.97 \pm 0.12$	$2.97 \pm 0.06$	$0.26 \pm 0.02$	$400_{-78}^{+66}$	1.065	6.61	$11.38_{-0.11}^{+0.13}$	11.32	$H_{F160W}$
0	7865	2.091	$2.65 \pm 0.33$	$4.82 \pm 0.15$	$0.83 \pm 0.02$	$446_{-54}^{+59}$	1.031	5.42	$11.82_{-0.09}^{+0.09}$	11.64	$H_{F160W}$
0	19627	2.036	$1.32 \pm 0.17$	$3.61 \pm 0.73$	$0.48 \pm 0.06$	$304_{-39}^{+43}$	1.059	6.18	$11.24_{-0.09}^{+0.10}$	11.20	$K$
0	29410	1.456	$1.83 \pm 0.23$	$2.59 \pm 0.03$	$0.54 \pm 0.02$	$371_{-90}^{+114}$	1.045	6.88	$11.61_{-0.15}^{+0.19}$	11.24	$H_{F160W}$
.....	.....	.....	.....	.....	.....	.....	.....	.....	.....	.....	.....

This Table will be published in its entirety in the electronic edition of ApJ, and can also be downloaded from <http://www.strw.leidenuni.nl/~sande/data/>. A portion is shown here for guidance regarding its form and content. Spectroscopic redshifts  $z_{spec}$  are obtained from the velocity dispersion fit as described in Section 3.3.2. Structural parameters  $r_e$ ,  $n_{serstic}$ , and  $b/a$  are derived using GALFIT on available imaging, as described in Section 3.3.3.  $\sigma_e$  is the velocity dispersion within a circular aperture of size  $r_e$  from Section 3.3.2, and  $\sigma_e/\sigma_{app}$  is the aperture correction we apply to the observed velocity dispersion as described in Appendix 3.B. From Equation 3.2 we calculated  $\beta(n)$ , and dynamical masses are derived using Equation 3.1. Stellar masses as given here are corrected to account for the difference between the catalog magnitude and our measured magnitude. The filter in which the structural parameters are measured is given in the last column.

(a) References: 0) this work 1) Bezanson et al. (2013); 2) van Dokkum et al. (2009); 3) Onodera et al. (2012); 4) Cappellari et al. (2009); 5) Newman et al. (2010); 6) van der Wel et al. (2008) and Blakeslee et al. (2006); 7) Toft et al. (2012).

The galaxies in our sample are not detected at  $24 \mu\text{m}$ , leading to a  $3\text{-}\sigma$  upper-limit of  $18 \mu\text{Jy}$  for the galaxies in NMBS-COSMOS, and  $30 \mu\text{Jy}$  for UDS-19627 (see Whitaker et al. 2012; Toft et al. 2012). UDS-29410 has a strong detection at  $24 \mu\text{m}$  of  $232 \pm 15 \mu\text{Jy}$ . From these upper limits we calculate the dust-enshrouded SFRs that are listed in Table 3.2. We find a high SFR for UDS-29410, but we find no other signs for this high SFR. That is, we find no emission lines and the best fitting SPS model indicates a low SFR. Therefore, we think that the strong  $24 \mu\text{m}$  detection is likely due to an obscured AGN.

### 3.3.2 Velocity dispersions

The clear detection of absorption lines in our spectra, together with the medium resolution of X-Shooter, enable the measurement of accurate stellar velocity dispersions. We use the unbinned spectra in combination with the Penalized Pixel-Fitting (pPXF) method by Cappellari & Emsellem (2004) and our best-fitting BC03 models as templates. Spectra were resampled onto a logarithmic wavelength scale without using interpolation, but with masking of the bad pixels. The effect of template mismatch was reduced by simultaneously fitting the template with a  $\sim 17$ -order Legendre Polynomial. Our results depend only slightly on the choice of the order of the polynomial (Appendix 3.A). Together with the measured velocity dispersion, the fit also gives us the line-of-sight velocity, and thus  $z_{\text{spec}}$ .

We also look at dependence of the velocity dispersion on the template choice. In particular for the younger galaxies in our sample that show a clear signature of A-type stars, we find a dependence of the measured velocity dispersion as a function of template age. A more stable fit is obtained when restricting the wavelength range to  $4020 \text{ \AA} < \lambda < 7000 \text{ \AA}$ , which excludes the Balmer break region (see also Appendix 3.A).

The errors on the velocity dispersion were determined in the following way. We subtracted the best-fit model from the spectrum. Residuals are shuffled in wavelength space and added to the best-fit template. We then determined the velocity dispersion of 500 of these simulated spectra. Our quoted error is the standard deviation of the resulting distribution of the measured velocity dispersions. When we include the Balmer break region in the fit, the formal random error decreases, but the derived dispersion becomes more dependent on the chosen stellar template. In total we have three high-quality measurements, and two with medium quality. We note that if we exclude the two galaxies with medium-quality measurements from our sample, our main conclusions would not change.

The velocity dispersion found here for NMBS-C7447 agrees well with the results from van de Sande et al. (2011). For UDS-19627 we find a slightly lower value as compared to Toft et al. (2012). However, they use a different method for constructing the template for the velocity dispersion fit. When we fit the spectrum of UDS-19627 in the same way as was described in Toft et al. (2012), we find a similar answer as theirs.

All dispersions are corrected for the instrumental resolution ( $\sigma = 23 \text{ km s}^{-1}$ ) and the spectral resolution of the templates ( $\sigma = 85 \text{ km s}^{-1}$ ). Furthermore, we apply an aperture correction to our measurements as if they were observed within a circular aperture radius of  $r_e$ . In addition to the traditional correction for the radial dependence of velocity dispersion (e.g., Cappellari et al. 2006), we account for the effects of the non-circular aperture, seeing and optimal extraction of the 1-D spectrum. The aperture corrections are small with a median of 4.8% (See Appendix 3.B). The final dispersions and corresponding uncertainties are given in Table 3.4.

### 3.3.3 Surface brightness profiles

Radial profiles are measured for all galaxies on all available imaging as described in Section 3.2.2. Galaxies are fitted by 2D Sérsic radial surface brightness profiles (Sérsic, 1968), using GALFIT (ver. 3.0.2; Peng et al. 2010). Relatively large cutouts of  $25'' \times 25''$  were provided to GALFIT to ensure an accurate measurement of the background, which was a free parameter in the fit. All neighboring sources were masked using a segmentation map obtained with SExtractor (Bertin & Arnouts, 1996). In the case of UDS-19627, the close neighbor was fitted simultaneously. Bright unsaturated field stars were used for the PSF convolution. All parameters, including the sky, were left free for GALFIT to determine.

Even though galaxies at low redshift are well-fitted by single Sérsic profiles (e.g., Kormendy et al. 2009), this does not necessarily have to be true for galaxies at  $z \sim 2$ . Therefore, we correct for missing flux using the method described in Szomoru et al. (2010). We find very small deviation in residual-corrected effective radii, with a median absolute deviation of 3.4%. Color images and measured profiles are shown in Figure 3.2.

We repeated the measurements using a variety of PSF stars ( $N \sim 25$ ). We find an absolute median deviation in the half-light radius of  $\sim 3\%$  for *HST*-WFC3,  $\sim 3.5\%$  for *HST*-ACS, and  $\sim 10\%$  for the ground-based UDS-UKIDSS data, due to variations in the PSF. The largest source of uncertainty in the measured profiles is, however, caused by the error in the sky background estimate. Even though these galaxies are among the brightest at this redshift, using the wrong sky value can result in large errors for both  $r_e$  and  $n$ . We determine the error in the sky background estimate by measuring the variations of the residual flux in the profile between 5 and 15 arcsec. For sizes derived from *HST*-ACS, the absolute median deviation in the effective radius due to the uncertainty in background is  $\sim 13\%$ , and for *HST*-WFC3  $\sim 12\%$ . Due to the deeper ground-based UDS-UKIDSS data, the uncertainty for UDS-19627 due to the sky is  $\sim 8\%$ . All of our results are summarized in Table 3.4.

We note that we find a smaller size and larger  $n$  for UDS-19627 as compared to Toft et al. (2012), which cannot be explained within the quoted errors. We have compared our results with the size measurements from Williams et al. (2009) and R. J. Williams (2012, private communication), who also use UDS-UKIDSS data for measuring structural parameters. They too find a smaller size in the  $K$  band of  $r_e = 1.63$  kpc, with a similar axis ratio of  $q = 0.53$ , while keeping the Sérsic index fixed to  $n = 4$ . Furthermore, we compare the size of UDS-29410 obtained from the ground-based UDS-UKIDSS data, to the size from *HST*-WFC3 to test how reliable the ground-based data are for measuring structural parameters. From the ground-based UDS  $H$  band we find  $r_e = 1.97 \pm 0.11$  kpc, and  $n = 2.47 \pm 0.22$  for UDS-29410 which is consistent with the measurements using the *HST*-WFC3 data within our  $1\sigma$  errors. From these two independent results, we are confident that our size measurement for UDS-19627 is correct. In what follows, we will use the mean effective radius and Sérsic  $n$  from the band which is closest to rest-frame optical  $r'$ . The effective radii reported here are circularized,  $r_e = \sqrt{ab}$ .

### 3.3.4 Dynamical masses

Combining the size and velocity dispersion measurements we are now able to estimate dynamical masses using the following expression:

$$M_{\text{dyn}} = \frac{\beta(n) \sigma_e^2 r_e}{G}. \quad (3.1)$$

Here  $\beta(n)$  is an analytic expression as a function of the Sérsic index, as described by Cappellari et al. (2006):

$$\beta(n) = 8.87 - 0.831n + 0.0241n^2. \quad (3.2)$$

This is computed from theoretical predictions for  $\beta$  from spherical isotropic models described by the Sérsic profile, for different values of  $n$ , and integrated to one  $r_e$  (cf. Bertin et al. 2002). The use of a Sérsic-dependent virial constant  $\beta(n)$  gives a better correspondence between  $M_{\text{dyn}}$  and  $M_*$  for galaxies in the SDSS (Taylor et al., 2010b). This does require however, that the total stellar masses are also derived using the luminosity of the derived Sérsic profile. Thus we correct our total stellar mass, as derived from the total magnitude as given in the catalogs (measured with SExtractor), to the total magnitude from the Sérsic fit. We note that the values for  $\beta$  that we find are all close to 5, a value often used in the literature (e.g., Cappellari et al. 2006). Our dynamical masses and corrected stellar masses are given in Table 3.4.

## 3.4 Compilation of kinematic studies

In order to study the structural evolution of quiescent galaxies, we combine the results from different kinematic studies at various redshifts. Where possible, we apply similar corrections as described above.

### 3.4.1 Low-redshift sample

At low redshift we select galaxies from the SDSS DR7. Stellar masses are based on MPA<sup>1</sup> fits to the photometry following the method of Kauffmann et al. (2003), and Salim et al. (2007). Star formation rates (SFRs) are based on Brinchmann et al. (2004). Structural parameters are from the NYU Value-Added Galaxy Catalog (NYU-VAGC, Blanton et al. 2005). For all galaxies, velocity dispersions were aperture corrected as described in Section 3.3.2, and stellar masses are calculated with a Chabrier (2003) IMF. We furthermore correct the stellar masses using the total magnitude from the best Sérsic fit. All dynamical masses were derived using Equation 3.1. For making an accurate comparison between low- and high-redshift galaxies, we only select non-star-forming galaxies, i.e.,  $s\text{SFR} < 0.3/t_H$  (see Williams et al. 2009), where  $t_H$  is the age of the universe at the given redshift.

### 3.4.2 Intermediate- and high-redshift sample

Our high redshift sample consists of a collection of both optical and NIR spectroscopic studies of individual galaxies. van der Wel et al. (2008) present a sample of quiescent galaxies at  $z \sim 1$ ,

<sup>1</sup><http://www.mpa-garching.mpg.de/SDSS/DR7/>

which itself is a compilation of three studies in the following fields: Chandra Deep Field South (CDF-S; van der Wel et al. 2004; 2005), the Hubble Deep Field North (HDF-N; Treu et al. 2005a; 2005b), and cluster galaxies in MS 1054-0321 at  $z = 0.831$  (Wuyts et al., 2004). We derive stellar masses for this sample by running the stellar population code FAST on available catalogs, i.e., FIREWORKS (Wuyts et al., 2008) for the CDF-S, R. Skelton et al. (in preparation) for the HDF-N, and FIRES (Förster Schreiber et al., 2006) for MS 1054-0321. For CDF-S and HDF-N the stellar masses are corrected using the total magnitude from the best  $n = 4$  fit to be consistent with the structural parameters from van der Wel et al. (2008). For MS 1054-0321, we use structural parameters and stellar mass corrections based on the results by Blakeslee et al. (2006), who fit Sérsic profiles with  $n$  as a free parameter. We note that Martinez-Manso et al. (2011) also study a sample of four  $z \sim 1$  galaxies, but find dynamical masses that are significantly lower than their stellar masses, in contrast to the result by van der Wel et al. (2008).

Other high-redshift results included here are from Newman et al. (2010) and Bezanson et al. (2013), who use the upgraded red-arm of LRIS on Keck to obtain UV rest-frame spectra of galaxies at  $z \sim 1.3$  and  $z \sim 1.5$  respectively. Velocity dispersions for two galaxies at  $z = 1.41$  are presented by Cappellari et al. (2009), and have been observed with VLT-FORS2 (see also Cenarro & Trujillo 2009). Using NIR spectrographs, Onodera et al. (2012, Subaru-MOIRCS) and van Dokkum et al. (2009, GNIRS) obtained velocity dispersions for two galaxies at  $z = 1.82$  and  $z = 2.186$ . Similar to the current study, Toft et al. (2012) study UDS-19627 using VLT X-Shooter. Dynamical masses were derived using to Equation 3.1. Note that for the studies of Cappellari et al. (2009), Onodera et al. (2012), van Dokkum et al. (2009), and Toft et al. (2012) no stellar mass corrections were applied due to the absence of the necessary information. All structural and kinematic properties of our high-redshift sample are listed in Table 3.4.

### 3.5 Are stellar masses reliable?

The main goal of this chapter is to see whether the stellar masses at  $z \sim 2$  are reliable. Here we compare our stellar masses, as derived from the spectra and photometry, to our dynamical masses, which are derived from effective radii and stellar velocity dispersions (Figure 3.6). Gray squares represent the density of non-star-forming, low-redshift galaxies from the SDSS as described in Section 3.4.1. Other symbols are the high-redshift studies as described in Section 3.4.2. The one-to-one relation for  $M_{\text{dyn}}$  and  $M_*$  is indicated by the dashed line. Note that the region above the line is nonphysical with stellar masses being higher than the dynamical mass.

Most  $z > 1.5$  galaxies in this sample are very massive, in the range  $11.2 < \log M_{\text{dyn}}/M_{\odot} < 11.8$ . At all redshifts, stellar and dynamical masses are tightly correlated and dynamical mass, which includes baryonic and dark matter, is on average higher than stellar mass. Thus, we infer that the stellar masses of our galaxies are broadly correct, and that the apparent size evolution of massive galaxies in photometric studies cannot be explained by errors in the photometric masses (see also van der Wel et al. 2008).

Figure 3.7a shows the ratio of the stellar and dynamical mass as function of redshift for all galaxies with stellar mass  $> 10^{11} M_{\odot}$ . We see that the average ratio at low-redshift for massive galaxies is a factor of 0.59 with a scatter of 0.12 dex. We note that For MS 1054-0321, the ratio of the stellar to dynamical mass are slightly higher as compared to low redshift galaxies. Up to redshift  $z \sim 1.5$  we find a similar value ( $\sim 0.5$ ) with similar scatter, but at higher redshift, the ratio seems to decline. For galaxies at  $z > 1.5$  we find a median ratio of  $M_*/M_{\text{dyn}} = 0.9$ . We quantify the evolution in this ratio by fitting the relation:

$$M_*/M_{\text{dyn}} \propto (1+z)^{\alpha}. \quad (3.3)$$

We use a linear least-squares fit in log-log space using the function *MPFIT* (Markwardt, 2009), which takes the errors on each individual data point into account. We find a best-fitting value of  $\alpha = 0.17 \pm 0.11$ , which is shown as the solid black line in Figure 3.7(a). The uncertainty is derived from 1000 bootstrap simulations, where we draw data points randomly from the sample. The quoted error is the standard deviation from the resulting distribution of points. Even though the fit is statistically significant at the  $1 - \sigma$  level, due to the relatively large measurements errors as compared to low redshift, and the possible selection bias of the high-redshift samples, we are cautious to draw any strong conclusions from this result.

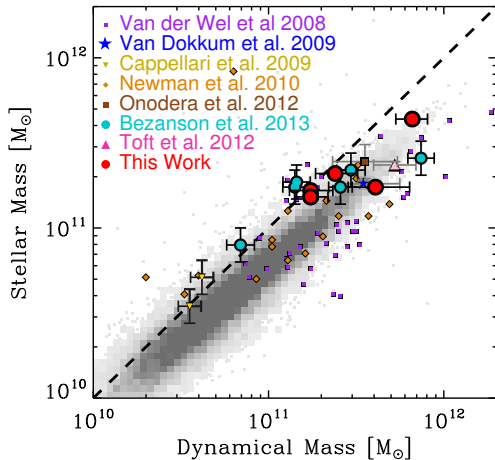
It is tempting to speculate that the evolution in  $M_*/M_{\text{dyn}}$  might have been caused by a decrease in the dark matter fraction as a function of redshift. For galaxies growing in size over time, the dark matter fraction within  $r_c$  will also increase. As the dark matter profile is less steep than the stellar mass profile, the dark matter to stellar mass fraction increases with radius, in a similar fashion as shown here (e.g., Hopkins et al. 2009). If so, this could also indicate that the IMF at high-redshift is very similar to the IMF at low-redshift.

Figure 3.7(b) shows  $M_*/M_{\text{dyn}}$  vs. the evolution of the effective radius at fixed dynamical mass (see Section 3.6.2 and Figure 3.9). Although there is significant scatter, we do find the galaxies with high  $M_*/M_{\text{dyn}}$  also tend to have smallest size at fixed dynamical mass. Galaxies that are closest to the present-day mass-size relation (dashed vertical line) show lower ratios of stellar to dynamical mass.

We test this claim by using the the following equation:

$$M_*/M_{\text{dyn}} \propto (r_c(z) / r_c(z \sim 0.1))^{\alpha}. \quad (3.4)$$

We find  $\alpha = -0.16 \pm 0.10$ , where the error is determined in a similar way as described for Equation 3.3 using the bootstrap method. Furthermore, we use the Spearman's rank test on



**Figure 3.6:** Comparison of the stellar mass vs. the dynamical mass. Gray squares are non-star-forming galaxies from the SDSS. Different symbols are from a compilation of high-redshift galaxies as described in Section 3.4.2. The dashed line is for equal dynamical and stellar mass. Low-redshift galaxies are all below the line, as is expected given the contribution of dark matter. All our high-redshift galaxies have dynamical masses that are close to the stellar mass. This suggests that the stellar mass measurements at high-redshift are robust for passive galaxies.

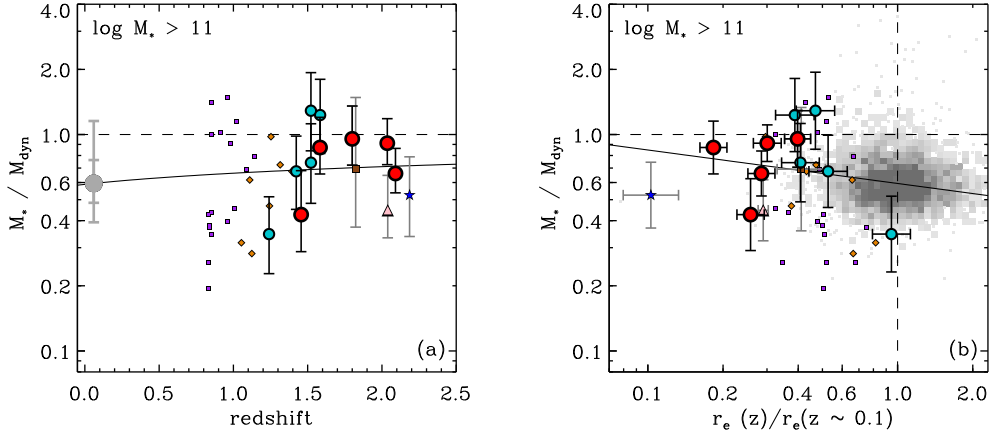


**Figure 3.7:** (a) Stellar mass divided by the dynamical mass vs. redshift. Galaxies below the line have dynamical mass greater than the stellar mass, above the line is the non-physical regime. For SDSS galaxies with stellar mass  $> 10^{11} M_{\odot}$ , we find that they have a median  $M_*/M_{\text{dyn}}$  of 0.59. Up to redshift  $z = 1.5$  we find a similar slightly lower median value ( $\sim 0.5$ ), but it rapidly increases at  $z > 1.5$  with median a of  $M_*/M_{\text{dyn}} = 0.9$ . The solid line is the best-fit  $M_*/M_{\text{dyn}} \propto (1+z)^{0.17 \pm 0.11}$ . We caution that this result might be biased due to the selection effects as explained in Section 3.3, and relatively large measurement errors. (b) Stellar mass divided by the dynamical mass vs. the evolution in the effective radius at fixed dynamical mass. Galaxies which have small effective radii at fixed dynamical mass also show higher ratios of  $M_*/M_{\text{dyn}}$ , although there is a significant scatter. The solid line is the best-fit  $M_*/M_{\text{dyn}} \propto (r_e(z)/r_e(z \sim 0.1))^{0.16 \pm 0.10}$ .

the intermediate- and high-redshift data. This confirms that there is an anti-correlation with a probability of 96%. The best-fitting Spearman's rank correlation coefficient is  $-0.28 \pm 0.08$ . Even though we find a weak anti-correlation, this agrees with the idea that the decreasing ratio of  $M_*/M_{\text{dyn}}$  with time might be correlated to the size growth of massive galaxies.

## 3.6 Structural evolution of quiescent galaxies

In this section, we will re-examine the structural evolution of massive quiescent galaxies but now using dynamical measurements.

### 3.6.1 Bias towards compact galaxies

As noted in Section 3.2.1, this sample is biased towards young quiescent galaxies. Therefore, we will first investigate whether our sample and that of Bezanson et al. (2013) are biased in size as compared to other high-redshift galaxies. We gathered structural properties of galaxies from two studies that use CANDELS data in the UDS and GOODS-South fields (Patel et al. 2012; Szomoru et al. 2012). We compare to a subsample of these galaxies that are determined to be quiescent from their rest-frame U-V and V-J colors (see e.g., Figure 3.1(a)). When comparing the effective radii vs. the stellar mass in Figure 3.8(a), we find that our galaxies (red circles) and those of Bezanson et al. (2013, cyan circles) are in general more compact as compared to the high-redshift CANDELS galaxies (small green circles).



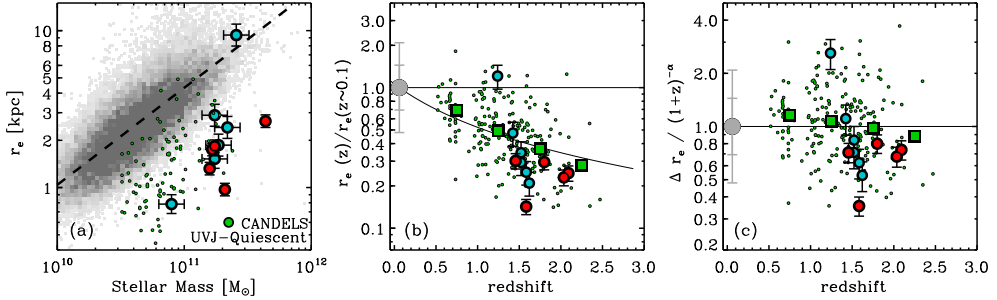


**Figure 3.8:** Structural comparison of our spectroscopic sample to the full quiescent galaxy population. (a) Effective radii vs. mass for low- and high-redshift galaxies. Gray squares are non-star-forming  $z \sim 0$  galaxies from the SDSS, with the dashed line the best-fit to Equation 3.5. High-redshift quiescent galaxies ( $1.4 < z < 2.1$ ) from CANDELS (Grogin et al. 2011; Koekemoer et al. 2011) are shown as small green circles, together with our spectroscopic sample shown as red circles, and the sample by Bezanson et al. (2013) shown as cyan circles. At fixed mass, our high-redshift galaxies have smaller effective radii, similar to what has been found by many studies. (b) Evolution in effective radius at fixed stellar mass, thus corrected for the  $M_* - r_e$  relation in panel (a). Big green squares are the median effective radii in bins of redshift for the CANDELS data. The solid line is the best-fit  $r_e \propto (1+z)^{-1.02 \pm 0.05}$ . At similar redshift, we find that our sample and that of Bezanson et al. (2013) are mostly below this fit, indicating that our samples are biased towards smaller effective radii. (c) Similar to the panel (b), but now divided by  $(1+z)^{-1.02}$  for a better comparison of our spectroscopic sample to the CANDELS data. When comparing the median of our sample to the binned median of other quiescent galaxies at similar redshift, we find smaller effective radii by a factor  $\sim 1.28$ . This might be explained by our selection which is based on aperture magnitude, which tends to be biased towards smaller galaxies.

For low-redshift galaxies we parametrize the mass-size relation by:

$$r_e = r_c \left( \frac{M_*}{10^{11} M_\odot} \right)^b \quad (3.5)$$

(Shen et al. 2003; van der Wel et al. 2008). Using a linear least-squares fit in log-log space, we find best fitting values of  $r_c = 4.32$  kpc and  $b = 0.62$ . This is slightly different from the fit by Shen et al. (2003) who find  $r_c = 4.16$  kpc and  $b = 0.56$ . The difference may be explained by different selection criteria, and their use of an older release version of SDSS. Figure 3.8(b) shows the evolution in effective radius, by comparing galaxies with similar mass at different redshifts. Using both the SDSS and the CANDELS data, we examine the amount of evolution in size by fitting the following relation:

$$r_e \propto (1+z)^\alpha, \quad (3.6)$$

We find  $\alpha = -1.02 \pm 0.05$  (linear fit in log-log space). Our spectroscopic targets and those of Bezanson et al. (2013) are mostly below this best-fit relation, being smaller by a factor of  $\sim 1.28$  as compared to median in redshift bins (big green squares). This is especially clear from Figure 3.8(c), where we correct for the evolution in size.

This bias might be explained by the method our targets are selected. As our selection is based on the magnitude within a fixed aperture of  $1''.5$ , instead of the total magnitude, we create a bias towards compact galaxies. For galaxies with similar total magnitudes, the smaller galaxies will be brighter within a photometric aperture, and thus make it into our sample.

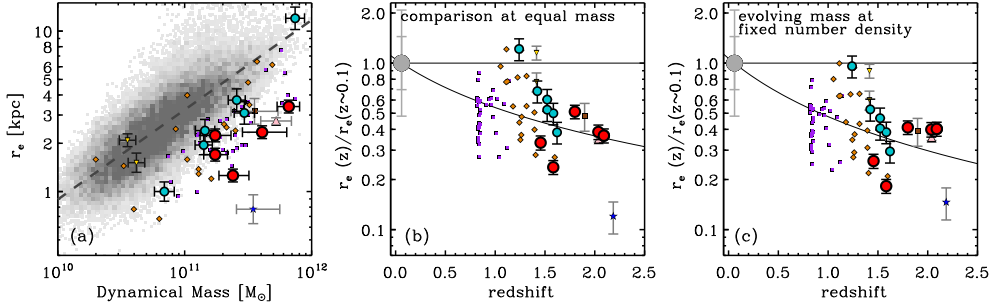


**Figure 3.9:** Redshift evolution of the effective radius of passive galaxies. (a) Size vs. dynamical mass. The dashed line is the best-fit derived using Equation 3.7 for non-star-forming SDSS galaxies. At fixed dynamical mass, we find that  $z \sim 2$  galaxies (red circles) are smaller by a factor  $\sim 3$  compared to low-redshift galaxies. (b) Evolution of the effective radius at fixed dynamical mass vs. redshift. The solid line is the best-fit  $r_e \propto (1+z)^{-0.97 \pm 0.1}$ , similar to what has been found by other stellar kinematic studies at high-redshift. Similar to Figure 3.8, our sample is below the best-fit line to the entire high-redshift sample. (c) Evolution of the effective radius using an evolving mass function at constant number density. We now compare galaxies at high-redshift, to more massive galaxies at low-redshift, assuming the mass evolves as  $\Delta \log M/M_{\odot} \sim 0.15z$ . This time, we find an even stronger evolution, with  $r_e \propto (1+z)^{-1.16 \pm 0.1}$ .

In what follows, we correct for this bias by increasing our sizes and those of Bezanson et al. (2013) by a factor of 1.28, and decreasing the velocity dispersion by a factor of  $\sqrt{1.28}$ .

### 3.6.2 Evolution in size

In Figure 3.9(a) we plot effective radius vs. dynamical mass. Symbols are the same as in Figure 3.7. For the low-redshift galaxies we parametrize the mass-size relation according to the following equation

$$r_e = r_c \left( \frac{M_{\text{dyn}}}{10^{11} M_{\odot}} \right)^b, \quad (3.7)$$

and find  $r_c = 3.23$  kpc and  $b = 0.56$  (dashed line). This is in good agreement with  $b = 0.56$  and  $r_c = 3.26$  kpc as found by van der Wel et al. (2008). At fixed dynamical mass, we see that all our galaxies have smaller effective radii as compared to low-redshift. This finding is further illustrated in Figure 3.9(b), where we compare the effective radii at fixed dynamical mass to the mass-size relation at  $z \sim 0$ . The solid line is the best-fit as described by equation 3.6, with  $\alpha = -0.97 \pm 0.1$ . This result is in agreement to with what has been found in previous kinematical studies (van der Wel et al. 2008; Newman et al. 2010). The scatter between different studies is considerable, with the work by van Dokkum et al. (2009) having the largest size difference while that by Onodera et al. (2012) having the smallest. Our sample falls in between these two extremes, i.e., we find smaller sizes as compared to Onodera et al. (2012), but larger effective radii than van Dokkum et al. (2009).

Instead of comparing galaxies sizes at fixed dynamical mass, we will now take into account that galaxies do grow in mass (e.g., Patel et al. 2012). In van Dokkum et al. (2010) they find that, for a sample selected at a constant number density, the stellar mass evolves as

$$\log M_n/M_{\odot} = 11.45 - 0.15z. \quad (3.8)$$

The number density on which this result is based,  $n = 2 \times 10^{-4} \text{Mpc}^{-3}$ , corresponds to an average mass of  $\log M_*/M_\odot \sim 11.2$  at  $z \sim 2$ , similar to our sample. Assuming that the mass evolves as  $\Delta \log M/M_\odot \sim 0.15z$ , we will compare effective radii for galaxies at different redshifts. For example, a galaxy with  $\log M_{\text{dyn}}/M_\odot = 11$  at  $z \sim 2$  will be compared with a  $z \sim 0$  galaxy with  $\log M_{\text{dyn}}/M_\odot = 11.3$ .

However, the evolution in stellar mass is determined for a complete sample of both star forming and quiescent galaxies, while in this chapter we only look at quiescent galaxies. Therefore, we assess whether the evolution in size at constant cumulative number density is different for the quiescent population as compared to the full population. This was already done for galaxies in CANDELS by Patel et al. (2012) at  $n_{\text{cum}} = 1.4 \times 10^{-4} \text{Mpc}^{-3}$ , which corresponds to a median mass of  $\log M_*/M_\odot \sim 10.9$  at  $z \sim 1.8$ . The sample studied here, however, has a median mass of  $\log M_*/M_\odot \sim 11.2$  at  $z \sim 1.8$ , which corresponds to  $n_{\text{cum}} = 2.5 \times 10^{-5} \text{Mpc}^{-3}$ . Thus, we repeat the analysis by Patel et al. (2012), but now using our CANDELS sample (Section 3.6.1) at this lower constant cumulative number density. Our results are similar to Patel et al. (2012), i.e., the quiescent population has smaller effective radii as compared to full population, but the difference in size between the quiescent and star-forming population is slightly smaller at  $z < 1.8$  as compared to Patel et al. (2012). The difference is due to the fact that at our lower constant cumulative number density, we find a higher fraction of quiescent galaxies. Therefore, the effective radii of the full population will be closer to the effective radii of the quiescent population, as compared to Patel et al. (2012). To correct for this difference in size, we increase the effective radii of all the quiescent galaxies in our combined sample by the size difference of the quiescent population as compared to the full. We correct each galaxy individually by finding the correction factor at this particular redshift. Below  $z < 1.8$ , the median correction factor is  $\sim 1.05$ , while at  $z \sim 2.1$  the correction factor is  $\sim 1.6$ .

Figure 3.9(c) shows the evolution in size at fixed number density as a function of redshift. Not surprisingly, the evolution in effective radii is more extreme, as we are now comparing  $z \sim 2$  galaxies to more massive, and therefore bigger galaxies at  $z \sim 0$ . Using Equation 3.6, we find that  $\alpha = -1.16 \pm 0.1$  provides the best fit. In conclusion, assuming that galaxies evolve in both mass and size, we find that the effective radii have to grow by a factor  $\sim 4$  from  $z \sim 2$  to the present day.

### 3.6.3 Evolution in velocity dispersion

In Figure 3.10(a) we compare the stellar velocity dispersion within one  $r_e$  vs. the dynamical mass for both low- and high-redshift samples. The dashed line is the parametrization of the  $\sigma_e - M_{\text{dyn}}$  relation for low- $z$  galaxies using the following equation:

$$\sigma_e = \sigma_c \left( \frac{M_{\text{dyn}}}{10^{11} M_\odot} \right)^b. \quad (3.9)$$

We find that  $\sigma_c = 148.9 \text{ km s}^{-1}$  and  $b = 0.24$ . Our high-redshift sample is clearly offset from low-redshift galaxies in the SDSS, i.e., at fixed mass they have higher velocity dispersions. Comparison of the velocity dispersion at fixed dynamical mass, as seen in 3.10b, shows a clear evolution in  $\sigma_e$ , such that velocity dispersion decreases over time. From this figure the

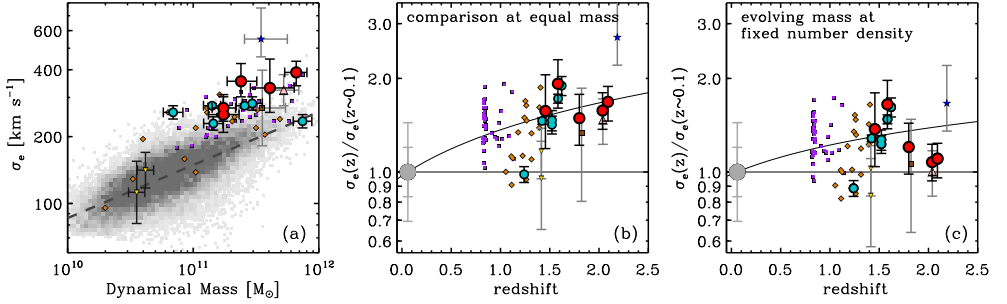


**Figure 3.10:** Redshift evolution in stellar velocity dispersion within one effective radius ( $\sigma_e$ ). (a)  $\sigma_e$  vs. dynamical mass. At fixed dynamical mass, we find that our galaxies have higher velocity dispersion as compared to low-redshift galaxies. (b) Evolution of velocity dispersions at fixed dynamical mass vs. redshift. We find the  $\sigma_e \propto (1+z)^{0.49 \pm 0.08}$ , i.e., at fixed dynamical mass the velocity dispersion decreases by a factor of  $\sim 1.7$  from  $z \sim 2$  to the present day. (c) Evolution of the velocity dispersion for an evolving mass function at constant number density. Opposite to the evolution in size, we now find a milder evolution of  $\sigma_e \propto (1+z)^{0.31 \pm 0.08}$ .

increase in accuracy for the velocity dispersion measurements of this study, as compared to other studies at similar redshift, is also clearly noticeable. Again we use the following simple relation to quantify the amount of evolution:

$$\sigma_e \propto (1+z)^\alpha, \quad (3.10)$$

and find that  $\alpha = 0.49 \pm 0.08$ . From  $z \sim 2$  to  $z \sim 0$  the stellar velocity dispersions decrease by a factor  $\sim 1.7$ . Again, we note that we apply a correction to the velocity dispersions in our sample, in order to correct for the bias towards more compact galaxies (section 3.6.1).

If we now compare low- and high-redshift galaxies using an evolving mass function as described above, we find that the velocity dispersion decreases less with cosmic time than when compared at fixed dynamical mass. Here, we also take into account that quiescent galaxies at constant cumulative number density are smaller as compared to the full sample, and therefore they have higher velocity dispersions. Similar to as described above, we therefore corrected the velocity dispersions of all galaxies in our combined sample. At  $z < 1.8$ , velocity dispersions on average decrease by a factor of  $\sim \sqrt{1.05}$ , while at  $z \sim 2.1$  they decrease by a factor of  $\sim \sqrt{1.6}$ . If we use equation 3.10, we find that  $\alpha = 0.31 \pm 0.08$ . In other words, the velocity dispersion within one  $r_e$  decreases by a factor  $\sim 1.4$  from  $z \sim 2$  to present-day.

### 3.6.4 Evolution in mass density

Next, we will focus on the central and effective mass densities using a similar approach as described in Saracco et al. (2012). In short, using the intrinsic Sérsic profile we can calculate the fraction of the luminosity that is within 1 kpc as compared to the total luminosity. For a Sérsic profile this ratio is given by (Ciotti, 1991):

$$\frac{L_{1\text{kpc}}}{L_{\text{tot}}} = \frac{\gamma(2n, x)}{\Gamma(2n)}. \quad (3.11)$$

Here,  $\Gamma(2n)$  is the complete gamma function,  $\gamma(2n, x)$  the incomplete gamma function,  $x = b_n(r_{1\text{kpc}}/r_e)^{1/n}$ , with  $b_n = 1.9992n - 0.3271$ . Using this ratio we can now calculate the

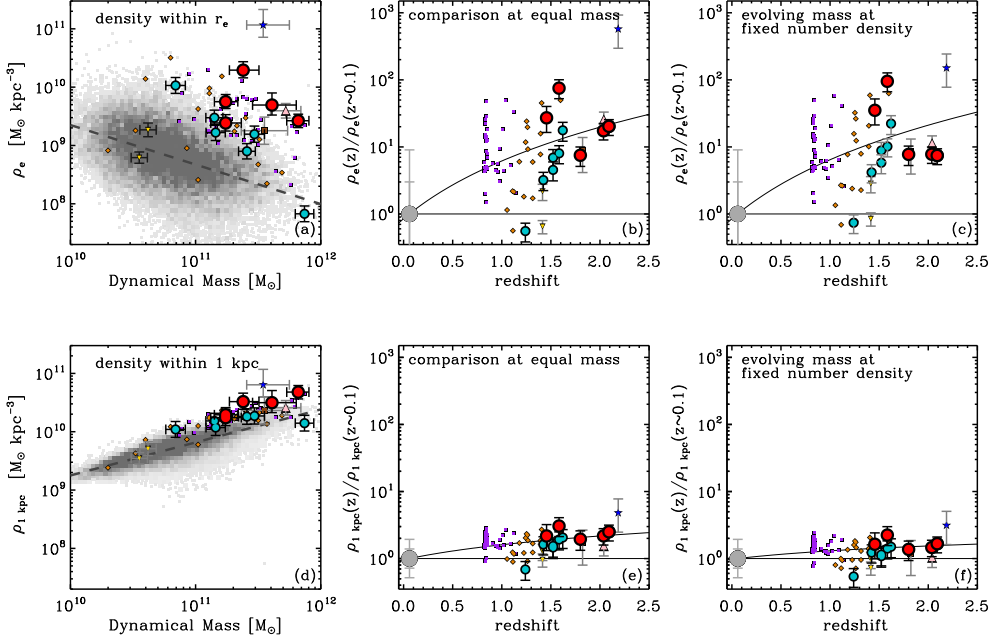


**Figure 3.11:** Redshift evolution of the central and effective densities, as calculated according to Equations 3.13 and 3.14. Top row shows the results for the effective mass density, while the bottom row shows the mass density within 1 kpc. *Left panels:* the density within  $r_e$  vs. dynamical mass (a). We find that low-redshift galaxies show a large scatter at fixed dynamical mass. Still, our high-redshift galaxies have higher densities within  $r_e$  at fixed mass. In contrast to  $\rho_e$ , the density within 1 kpc vs. dynamical mass (d) shows very little scatter, and we find only a small difference between low- and high-redshift galaxies. *Middle panels:* evolution in the density at fixed dynamical mass vs. redshift. We find a strong evolution for the effective density (b) with  $\rho_e \propto (1+z)^{2.86 \pm 0.15}$ , or a decrease by a factor of  $\sim 2$  from high-redshift to  $z \sim 0$ . For the central density, however, we only find that  $\rho_{1\text{kpc}} \propto (1+z)^{0.74 \pm 0.15}$ , or a decrease of  $\sim 2.3$ . *Right panels:* evolution of the density with an evolving mass at constant number density. Similar to the effective radii, we find a stronger evolution for the effective density, i.e.,  $\rho_e \propto (1+z)^{2.93 \pm 0.15}$ , while the central density requires very little to no evolution ( $\rho_{1\text{kpc}} \propto (1+z)^{0.42 \pm 0.15}$ ).

dynamical mass within one 1 kpc and within  $r_e$  from the total mass:

$$M_{1\text{kpc}} = \frac{L_{1\text{kpc}}}{L_{\text{tot}}} M_{\text{dyn}}. \quad (3.12)$$

Here we assume that the dynamical mass profile follows the light profile, and furthermore that the mass-to-light ratio of the galaxy is radially constant. The detection of small color gradients in our galaxies indicates, however, that this is not the case, but the effect on the derived densities is small (Saracco et al. 2012; see also Szomoru et al. 2012). Finally, the densities are calculated as follows:

$$\rho_{1\text{kpc}} = \frac{M_{1\text{kpc}}}{4/3\pi r_{1\text{kpc}}^3}, \quad (3.13)$$

and

$$\rho_e = \frac{0.5M_{\text{dyn}}}{4/3\pi r_e^3}. \quad (3.14)$$

As for  $r_e$  and  $\sigma_e$ , we now compare the density as a function of dynamical mass (see Figure 3.11). The top row shows the results for the mass density within one effective radius, while the bottom row compares the central density within 1 kpc. The first thing to notice is the large scatter for low-redshift galaxies when looking at  $\rho_e$  vs.  $M_{\text{dyn}}$ , while  $\rho_{1\text{kpc}}$  vs.  $M_{\text{dyn}}$  shows a tight relation. The density-mass relation can be parametrized by:

$$\rho = \rho_c \left( \frac{M_{\text{dyn}}}{10^{11} M_{\odot}} \right)^b. \quad (3.15)$$

For the density within  $r_e$  we find  $\rho_{c,e} = 4.7 \times 10^8 M_{\odot} \text{kpc}^{-3}$  and  $b_e = -0.68 \pm 0.15$ , and for the central density within 1 kpc  $\rho_{c,1\text{kpc}} = 6.6 \times 10^9 M_{\odot} \text{kpc}^{-3}$  and  $b_{1\text{kpc}} = 0.56$ .

When we compare the galaxies in our high-redshift sample to galaxies in the SDSS, we find that they have higher densities within  $r_e$ . Comparison at equal dynamical mass shows that the effective densities are higher by a factor of  $\sim 50$  (Figure 3.11(b)) for our sample. The same comparison, but now for the central density within 1 kpc, reveals only mild evolution, approximately a factor of  $\sim 3$  from  $z \sim 2$  to the present. When fitting

$$\rho \propto (1+z)^\alpha, \quad (3.16)$$

we find that  $\alpha_e = 2.86 \pm 0.15$ , while  $\alpha_{1\text{kpc}} = 0.74 \pm 0.15$ .

Instead of comparing galaxies at fixed mass, we again take into consideration that galaxies evolve in mass when comparing low- and high-redshift galaxies. Again, we correct for the fact that quiescent galaxies at constant cumulative number density are smaller as compared to the full sample. This time, we find that  $\rho_e$  evolves even faster as compared to the equal mass comparison  $\alpha_e = 2.93 \pm 0.15$ . The density within 1 kpc, however, requires a decrease less than a factor of  $\sim 2$ , with  $\alpha_{1\text{kpc}} = 0.42 \pm 0.15$ , from  $z \sim 2$  to the present

## 3.7 Discussion

In the previous section we have found that in order for the high-redshift galaxies in our sample to evolve into typical present-day early-type galaxies, strong structural evolution is required. Effective radii need to increase, and the velocity dispersion within  $r_e$  has to decrease. The density within the effective radius has to decrease by more than an order of magnitude. However, the central density can remain almost the same, consistent with inside-out growth.

The dominant physical mechanism for this structural evolution is still a subject of ongoing debate. Size growth dominated by major mergers seems to be unlikely as it would increase the masses too much, which would make extremely massive galaxies too common in the local universe. As the mass and size increase at approximately at the same rate in major mergers, the galaxies would also remain too compact for their mass. Minor merging could offer a solution to the problem, as it can grow a galaxy in effective radius ( $r_e$ ) steeper than  $r_e \propto M_*$  (Villumsen 1983; Naab et al. 2009; Bezanson et al. 2009; Hopkins et al. 2009b). In this scenario, the observed compact high-redshift galaxies may simply be the cores of local massive early-type

galaxies, which grow inside-out by accreting (smaller) galaxies, and thus assemble a significant part of their mass at later times (van der Wel et al. 2009; Oser et al. 2010). In this section we will examine whether dry minor merging agrees with our findings.

From a simple estimate, based on the virial theorem, Bezanson et al. (2009) predict how the effective radii changes if a massive galaxy undergoes a series of minor mergers. With only eight 1:10 mergers, the effective radii can grow by a factor of  $\sim 5$  while only having the mass increase by a factor of  $\sim 2$ . This is also described by Naab et al. (2009), who state that if an initial system undergoes a mass increase by a factor of 2 due to accretion of very small systems, then the final radius of the system is four times larger, the velocity dispersion is reduced by a factor of 2, and the density is reduced by a factor of 32. This analytic prediction is confirmed by their hydrodynamical cosmological simulation and consistent with the observational size evolution as presented here.

Using hydrodynamic simulations of galaxy mergers, Hopkins et al. (2009), also find evidence for size evolution. When they compare the effective radii of quiescent galaxies at fixed mass, they find an evolution in size of  $r_e \propto (1+z)^{-0.48}$  for galaxies with  $\log M_*/M_\odot = 11$ , which is weaker than found by this study and many others. Oser et al. (2012) find a size evolution in their hydro simulation, which is much stronger:  $r_e \propto (1+z)^{-1.44}$ , on the high side of current observational results.

Oser et al. (2012) find a similar evolution in velocity dispersion of  $\sigma \propto (1+z)^{0.44}$ , to that found in this work. In contrast, Hopkins et al. (2009), predict that high-redshift quiescent galaxies have roughly the same or at most a factor  $\sim 1.25$  larger velocity dispersions.

Evolution of the density is also discussed in both Bezanson et al. (2009) and Hopkins et al. (2009b). Based on photometric data, both studies find that while the density within one effective radius is higher at high-redshift, the central density of high-redshift galaxies is very similar to local massive ellipticals. From hydro simulations, Naab et al. (2009) show that the central density within 1kpc decreases by a factor of 1.5 from  $z = 2$  to  $z = 0$ , caused by dynamical friction from the surviving cores of the infalling systems. Similarly, Oser et al. (2012) show that the central density evolves only weakly, while the density within  $r_e$  decreases rapidly by more than an order of magnitude, in good agreement with what we find here. From a study of central galaxies in three  $\sim 10^{13} M_\odot$  galaxy groups, simulated at high resolution in cosmological hydrodynamical simulations, Feldmann et al. (2010) come to the same conclusion. They find that the effective density of these galaxies decreases by 1-2 orders of magnitude between  $z = 1.5$  and  $z = 0$ , while the density within 2 kpc stays roughly constant.

This is in contrast with the findings of Saracco et al. (2012), who find no evidence for higher mass densities within one effective radius when comparing their  $z \sim 1.5$  galaxies to low-redshift cluster galaxies. Furthermore, the large scatter that they observed in the effective density and the apparent evolution, is simply due a peculiar analytic feature in the Sérsic profile.

In Figure 3.7(a) we show that the ratio of  $M_*/M_{\text{dyn}}$  appears to have evolved from  $z \sim 2$  to  $z \sim 0$ . As compared to SDSS galaxies with  $\log M_*/M_\odot > 11$ , we find that the median  $M_*/M_{\text{dyn}}$  is higher by 50% at  $z > 1.5$ , and that  $M_*/M_{\text{dyn}} \propto (1+z)^{0.17 \pm 0.011}$ . However, this result is uncertain due to the selection effects inherent in this sample and large measurement errors in both masses. We note that this effect is predicted by simulations; as the effective radius of a galaxy grows, the dark matter fraction within  $r_e$  will also increase. Hopkins et al. (2009) predicts evolution by a factor of  $\sim 1.25$  for galaxies with  $\log M_*/M_\odot = 11$ , with the

effect increasing with stellar mass. Hilz et al. (2012) also find a strong evolution in the dark matter fraction in their hydro-simulation, and predict that quiescent galaxies at  $z \sim 2$  have lower dark matter fractions (80%). They mention that it is mainly driven by the strong size increase, which therefore probes a larger region that is dominated by dark matter.

### 3.8 Summary and conclusion

In this chapter, we present deep UV-NIR spectroscopy of five massive ( $> 10^{11} M_{\odot}$ ) galaxies at  $z \sim 2$ , using X-Shooter on the VLT. These spectra enable us to measure stellar velocity dispersions with higher accuracy than done before at this redshift: we triple the sample of  $z > 1.5$  galaxies with well constrained ( $\delta\sigma < 100 \text{ km s}^{-1}$ ) velocity dispersion measurements. We find that the stellar velocity dispersions are high (290-450  $\text{km s}^{-1}$ ) compared to equal-mass galaxies in the SDSS.

We combine these kinematic results with size measurements using GALFIT on *HST*-WFC3  $H_{160}$  and UDS  $K$ -band imaging, and use these measurements to derive dynamical masses. Stellar masses are obtained from SPS modeling on the VIS-NIR spectra in combination with the available broadband and medium-band data. The SPS-modeling shows that our galaxies have ages ranging from 0.5 to 2 Gyr, and show no signs of on-going star formation.

We find good correspondence between the dynamical and stellar masses, with the dynamical mass being higher by  $\sim 15\%$ . Our results suggest that stellar mass measurements for quiescent galaxies at high-redshift are robust.

We complement our results with stellar kinematic results from other studies at low and high redshift to study the structural evolution of massive quiescent galaxies. At fixed dynamical mass, we find that the effective radius increases by a factor of  $\sim 2.8$ , while the velocity dispersion decreases by a factor of  $\sim 1.7$  from  $z \sim 2$  to the present day. Furthermore, we study how the mass density within  $r_e$  and 1 kpc evolves with time. We find a strong decrease of the mass density within one effective radius (factor of  $\sim 21$ ), while it only decreases mildly within 1 kpc (factor of  $\sim 2.3$ ). Instead of comparing galaxies at fixed dynamical mass, we also use an evolving mass limit as defined by fixed number density. By accounting for concurrent mass growth in our comparison of high- and low-redshift galaxy populations, we find an even stronger evolution in galaxy sizes (factor of  $\sim 4$ ). We find that velocity dispersion decreases less dramatically with time, differing by only a factor of  $\sim 1.4$  between  $z \sim 2$  and  $z \sim 0$ . Finally, for the mass density within  $r_e$ , we find a stronger evolution, but interestingly, the mass density within 1 kpc is consistent with no evolution. This finding implies that massive quiescent galaxies grow inside out.

We examine if our results are compatible with the current idea of inside-out growth through dry minor mergers. Our findings are qualitatively consistent with predictions from hydrodynamical simulations which show similar evolution in size, velocity dispersion, and mass density within one effective radius.

Finally, we find that even though the stellar masses are consistent with the dynamical masses, the ratio of  $M_*/M_{\text{dyn}}$  may slightly decrease with time. This, too, is predicted by minor merging simulations, which show that the size growth due to minor merging will also change the fraction of dark matter as compared to the stellar mass within an effective radius. This is due to the fact that the dark matter profile is less steep than the stellar mass profile, and thus



the dark matter to stellar mass fraction increases with radius.

Despite the vastly improved accuracy of our derived dynamical masses and stellar population parameters, the broader inferences of our study are still limited by the small number of high-redshift galaxies with such information. We have shown that our sample is biased towards younger galaxies, compared to a stellar mass limited sample at  $z \sim 2$ , with smaller effective radii as compared to the full population of quiescent galaxies at  $z \sim 2$ . Only with a larger unbiased sample of massive quiescent galaxies at high redshift can we start to comprehend the final phase that massive galaxies go through in becoming today's ellipticals.

## Acknowledgments

We thank Daniel Szomoru for providing his residual-correct code and the galaxy sizes for GOODS-S CANDELS; Andrew Newman for providing the corrected stellar masses; Shannon Patel for the structural parameters of galaxies in UDS CANDELS; and Ivo Labbé for helpful comments regarding the SFRs from 24 flux. It is a pleasure to acknowledge the contribution to this work by the NMBS collaboration. We also thank Adam Muzzin for useful discussions.

This research was supported by grants from the Netherlands Foundation for Research (NWO), the Leids Kerkhoven-Bosscha Fonds. Support for the program *HST*-GO-12167.1 was provided by NASA through a grant from the Space Telescope Science Institute.

This work is based on observations taken by the CANDELS Multi-Cycle Treasury Program with the NASA/ESA *HST*, which is operated by the Association of Universities for Research in Astronomy, Inc., under NASA contract NAS5-26555.

This publication also makes use of the Sloan Digital Sky Survey (SDSS). Funding for the creation and distribution of the SDSS Archive has been provided by the Alfred P. Sloan Foundation, the Participating Institutions, the National Aeronautics and Space Administration, the National Science Foundation, the U.S. Department of Energy, the Japanese Monbukagakusho, and the Max Planck Society. The SDSS Web site is <http://www.sdss.org/>. The SDSS Participating Institutions are the University of Chicago, Fermilab, the Institute for Advanced Study, the Japan Participation Group, Johns Hopkins University, the Max Planck Institut fur Astronomie, the Max Planck Institut fur Astrophysik, New Mexico State University, Princeton University, the United States Naval Observatory, and the University of Washington.

### 3.A Robustness of the velocity dispersion measurements

As it has only recently become possible to measure velocity dispersions at high redshift, the stability of these measurements has barely been tested. In this appendix, we will study the effect of fitted wavelength range, template choice, degree of the additive polynomial, S/N of the spectra, and the choice of stellar populations models.

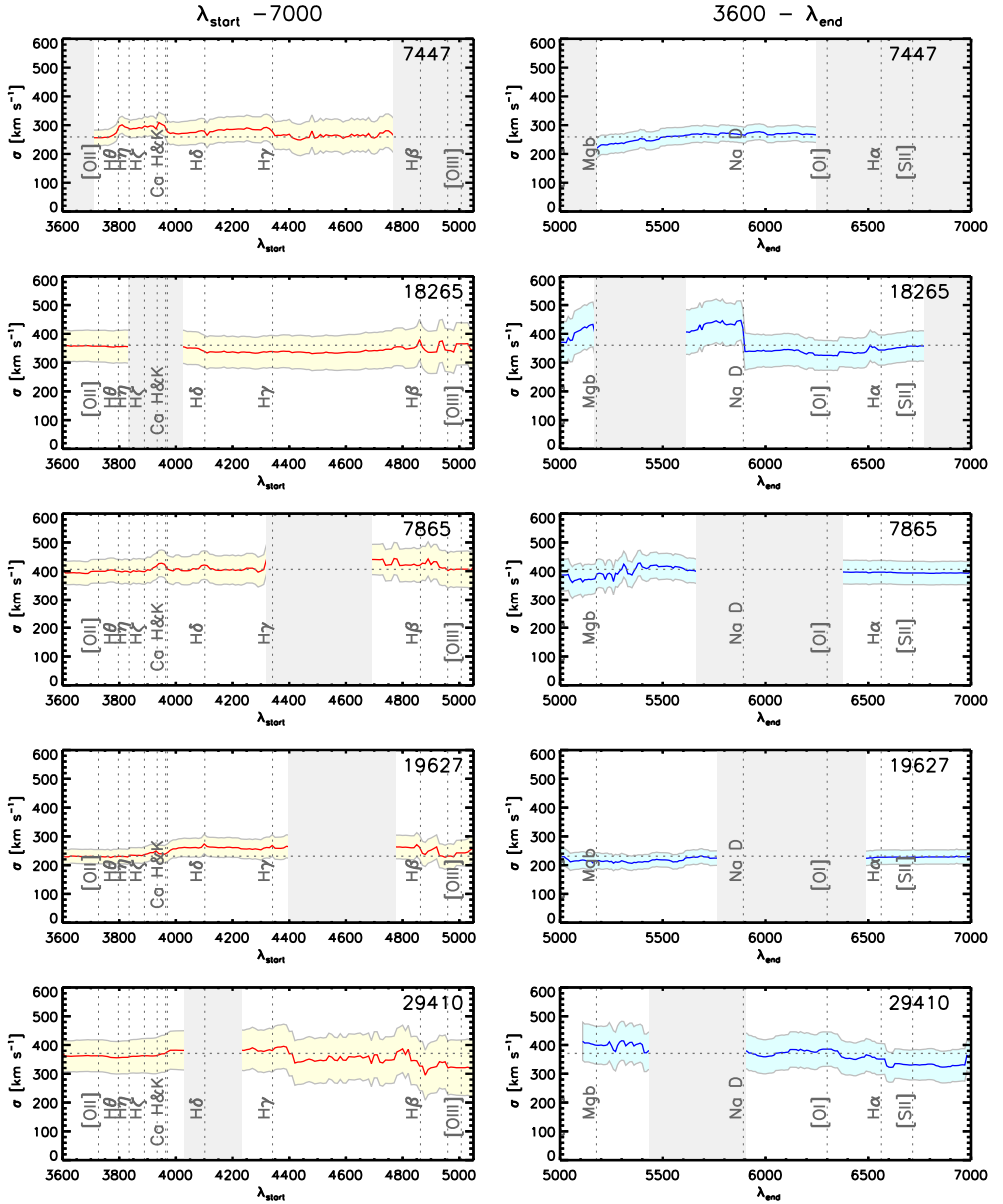


Figure 3.12: Velocity dispersion vs. wavelength range. Left panel shows the results for  $\lambda_{\text{start}} < \lambda < 7000 \text{ \AA}$ , while the right panel is for  $3600 \text{ \AA} < \lambda < \lambda_{\text{end}}$ . The horizontal shaded region indicates the  $1\text{-}\sigma$  error from pPXF, and the dashed horizontal line indicates the velocity dispersion when fitting the full range. Most prominent absorption lines are indicated, and the regions affected by strong sky-lines and atmospheric absorption are shown in gray. Overall, we find a stable solution for the velocity dispersion while changing the wavelength range. For NMBS-C7447 and UDS-19627, we do find a small increase in the region around the Balmer break. For NMBS-C18265, we find that excluding Na D has a great impact on the velocity dispersion.

### 3.A.1 Dependence of the velocity dispersion on the wavelength range

Our sample spans a redshift range of  $1.4 < z < 2.1$ , which means that different parts of the rest-frame spectra will be affected by sky-lines and atmospheric absorption for each galaxy. This can be seen from Figure 3.4, we often lose strong absorption features in our spectrum, which affects the region of the rest-frame spectrum that we can fit. Here we investigate how stable the measured velocity dispersion is as a function of the wavelength range.

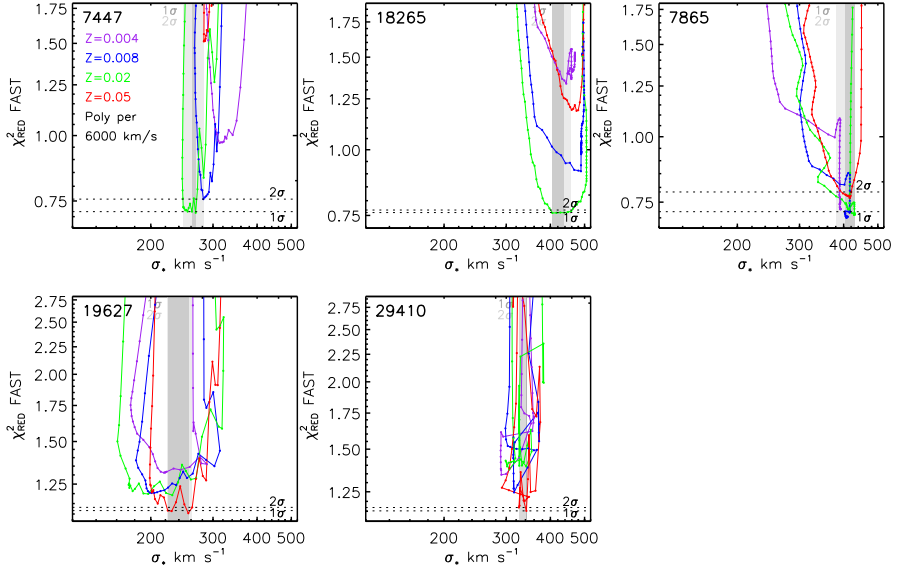
For the velocity dispersion fitting in this chapter, the lower wavelength limit is set by stellar libraries and models, as no systematic high-resolution observations exist below  $3550 \text{ \AA}$ . The higher wavelength limit is set by lower S/N in our spectra in the observed K-Band. Our approach for testing the wavelength dependence of the fit is as follows. First, we use the full-range spectrum to determine a best-fit polynomial (1 order per  $10\,000 \text{ km s}^{-1}$ ), which is used to correct for the difference between the observed and the template continuum. Next, we repeat the measurement with a zeroth-order polynomial while changing the start or end wavelength. The polynomial is not a free parameter in this fit, as this would make it impossible to separate between the effect of the polynomial and the wavelength range. Note also, that we use a single template for all fits as determined from the full Visual+NIR spectrum together with broadband and medium-band data (see Section 3.3.1).

Figure 3.12 shows the results for the different sources. The left panel shows the result where we change the starting wavelength, i.e., the wavelength range is  $\lambda_{\text{start}} < \lambda < 7000 \text{ \AA}$ , whereas the panels on the right show the effect of changing the end wavelength,  $3600 \text{ \AA} < \lambda < \lambda_{\text{end}}$ . The first thing to notice is that the measured dispersions are remarkably stable, even when most of the absorption lines have been excluded from the fit. The two galaxies with the youngest ages and strong Balmer absorption lines (NMBS-C7447 and UDS-19627) show a change in the velocity dispersion in the region of the Balmer break. NMBS-C7447 shows an increase for  $\lambda_{\text{start}} > 3800 \text{ \AA}$ , but decreases after Ca H&K have been removed from the fit. UDS-19627 shows an increase of  $50 \text{ km s}^{-1}$  when the Balmer break is excluded. When we reduce the red part of the spectrum (Figure 3.12, right panels), we also find a stable fit, except for NMBS-C18265. After excluding Na D from the fit, the velocity dispersion increases by a  $\sim 100 \text{ km s}^{-1}$ . We think this is because NMBS-C18265 has a more evolved stellar populations than say for example NMBS-C7447. With the Ca H&K lines masked out due to atmospheric absorption, Na D is one of the strongest lines in the spectrum, and its exclusion could explain the sudden change in the measured dispersion.

To summarize, for most galaxies we find only a mild dependence on the wavelength range that is used in the fit. We do find that with decreasing wavelength range, the random error increases. Finally, even in the absence of strong absorption features like Ca H&K, we find similar velocity dispersions as compared to the full range fit. Due to template mismatch, we only fit  $\lambda > 4020 \text{ \AA}$  in our final results, as is explained in the next section.

### 3.A.2 Dependence of the velocity dispersion on the template choice

Next, we study how different templates may influence the measured velocity dispersion. We use a sample of BC03  $\tau$ -models, as presented in Section 3.3.1. In particular, we are interested in the effect of template age and metallicity. In Figure 3.13 we show the reduced  $\chi^2$  from the SPS-modeling, vs. the velocity dispersions measured using this template. The different points



**Figure 3.13:** Reduced  $\chi^2$  from SPS-modeling vs. velocity dispersion for different templates. Different points indicate different template ages, while different colors show different metallicities. All fits are done on the full-wavelength range and with one-order per  $6000 \text{ km s}^{-1}$  for the additive polynomial. The narrower the horizontal distribution is, the more stable the velocity dispersion is. For most sources, we find a stable solution for the velocity dispersion by using different templates, except for UDS-19627, which shows a large range in velocity dispersions.

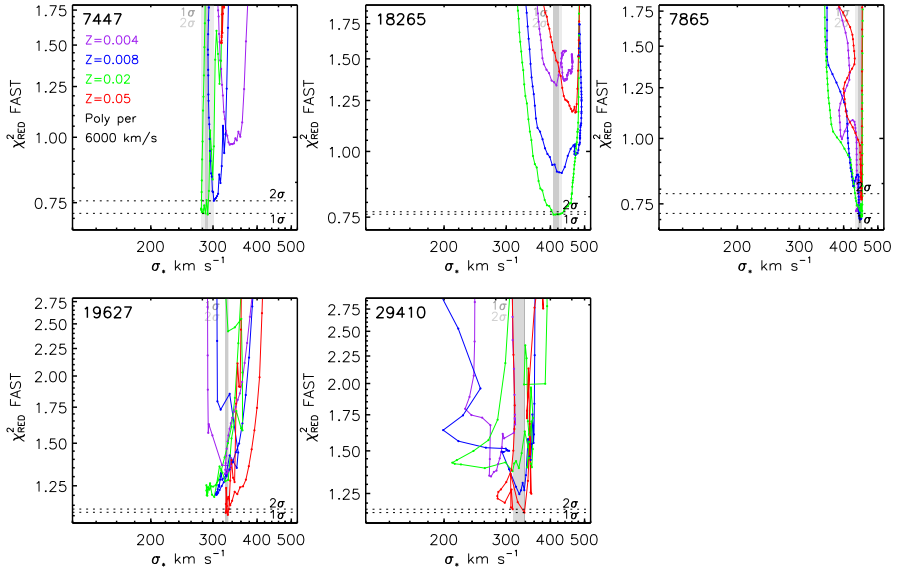


**Figure 3.14:** Reduced  $\chi^2$  vs. velocity dispersion for different templates, similar to Figure 3.13 but now excluding the Balmer break ( $\lambda > 4020 \text{ \AA}$ ). Whereas with the full wavelength range UDS 19627 showed a large variation in the velocity dispersion as a function of template, this time we do find a stable solution, as the distribution is narrower. The other sources also, show a decrease in the uncertainty due to different templates, except for UDS-29410. However, this is due to lower S/N of this spectrum and the shorter fitted wavelength range as before.

represent different ages of the templates, with the minimum  $\chi^2$  corresponding to the best-fit age as listed in Table 3.3. The different colors indicate the different metallicities. We show the  $\chi^2$  from the SPS-modeling instead of the  $\chi^2$  from the dispersion fit, as the former is derived from the full Visual and NIR spectrum plus all the broadband and medium-band photometric data. This large wavelength range yields better constraints for the stellar population, thus larger relative ranges in  $\chi^2$  as compared to the  $\chi^2$  from the dispersion fit. Also, as we add high-order additive polynomials to the templates from fitting the velocity dispersion (in this case one order per  $6\,000\text{ km s}^{-1}$ ), the effect of different template-ages is mostly washed out, and we get a small relative  $\chi^2$ .

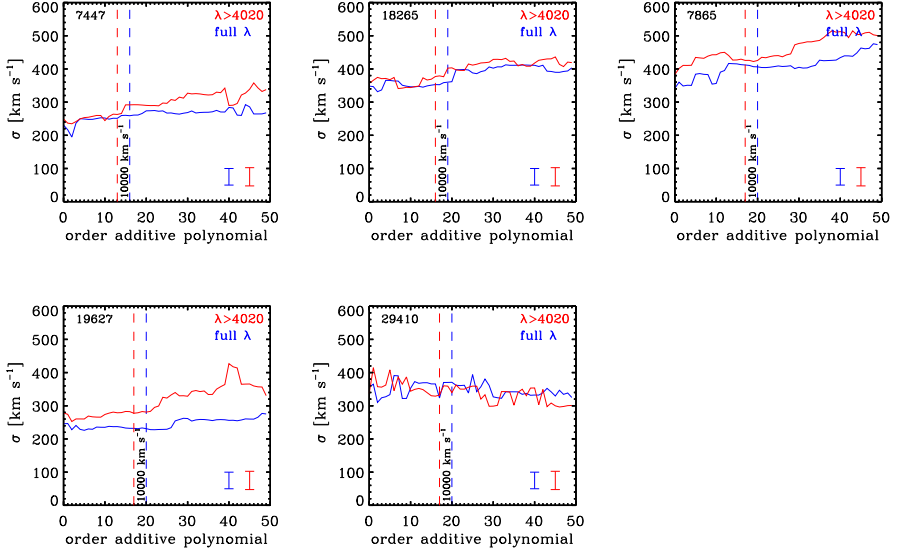
In Figure 3.13 we see that for most galaxies the velocity dispersion for templates allowed within  $2\sigma$  gives consistent results. Different metallicities do give different velocity dispersions at their minimum  $\chi^2$ , but this is a mere reflection of the age-metallicity degeneracy. Different metallicities have different best-fitting ages, which in turn give different velocity dispersion. At a  $1 - \sigma$  level, we only have a handful of best-fitting templates, for which we obtain similar velocity dispersions. UDS-19627 is the exception, which shows a large dependency of the measured velocity dispersion as a function of template age within the  $1 - \sigma$  allowed range. At the  $1 - \sigma$  level, we find a range of  $\sim 30\text{ km s}^{-1}$ , due to template uncertainty, while the random error is one of the lowest, only  $\sim 30\text{ km s}^{-1}$ . Even though templates with  $\chi^2$  of 1.20 or higher are statistically considered a bad fit, the large range in the velocity dispersion is worrying. If we could not have constrained the best-fitting template from the full range spectrum and broadband data, the measured velocity dispersion would be highly uncertain.

However, if we exclude the Balmer break from the velocity dispersion fit, the dependency on template age almost completely disappears (Figure 3.14). UDS-19627 shows the most dramatic change, where we suddenly see a tight range of best-fitting velocity dispersions. We do note that the velocity dispersion has increased, as was already shown in Figure 3.12. UDS-29410 appears to have a slightly higher template uncertainty if we only fit for  $\lambda > 4020\text{ \AA}$ , but this is driven by the lower S/N of the spectrum as we now use a shorter wavelength range.

To conclude, we find a systematic uncertainty due to templates with different ages. This is caused by the Balmer break, present in the relatively young galaxies in our sample. By only fitting for  $\lambda > 4020\text{ \AA}$ , the uncertainty due to template mismatch almost completely disappears. In that case, templates with different metallicities do give different velocity dispersions, but this is most likely caused by the underlying age-metallicity degeneracy.

### 3.A.3 Dependence of the velocity dispersion on the order of the additive polynomial

In order to correct for stellar continuum emission differences between the observed galaxy spectrum and the template, we use an additive Legendre polynomial. If we would not apply such a correction, the fitting routine could try to correct for this discrepancy by changing the velocity dispersion. Values that are typically used in the literature vary from  $5000$  to  $15000\text{ km s}^{-1}$  per order. We do not use multiplicative Legendre polynomials, because the S/N of the spectra are too low, and it would add another degree of uncertainty to the fit. Here, we test the influence of the additive polynomial to our measured velocity dispersions. Again we use the best-fit  $\tau$ -model as a template while varying the additive polynomials from 0 to 50. We fit both the full-wavelength range and the wavelength range with  $\lambda > 4020\text{ \AA}$ .



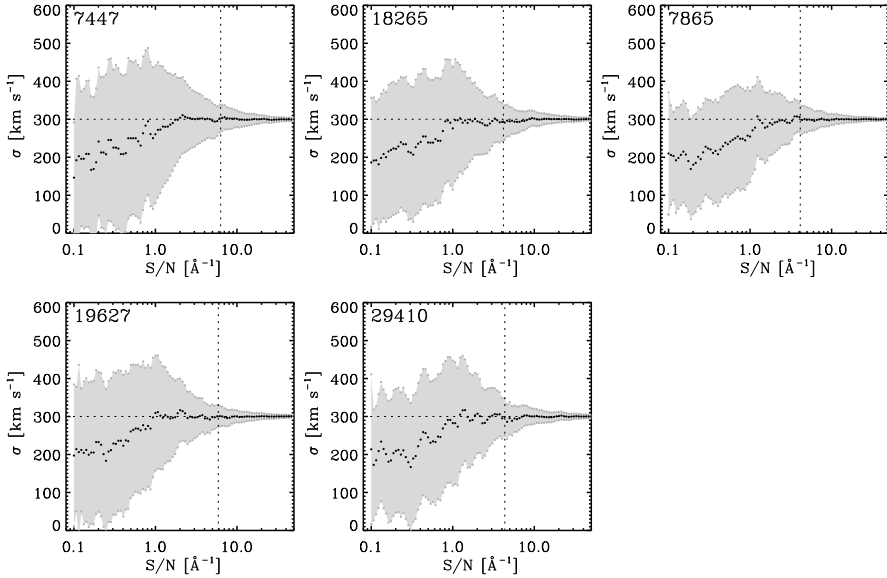
**Figure 3.15:** Velocity dispersion as measured with different order additive polynomials. The full-wavelength range fit is shown in blue, while the fit with  $\lambda > 4020 \text{ \AA}$  is shown in red. We find an increase of the velocity dispersion with increasing order. The fit is most stable when using a polynomial with order between 10 and 30. The vertical dashed lines shows the order that corresponds to  $10000 \text{ km s}^{-1}$ , the polynomial that we use for obtaining science results.

Figure 3.15 shows the results, with the blue line representing the full-wavelength fit, while the red line shows the results for  $\lambda > 4020 \text{ \AA}$ . The vertical dashed line indicates the polynomial with one order per  $10000 \text{ km s}^{-1}$ . Overall we find that by increasing the additive polynomial, the measured velocity dispersion increases. In general we find that between polynomials of 10 and 30, the smallest increase in the velocity dispersion occurs, and this appears to be the most stable region. For this reason, we use one order per  $10000 \text{ km s}^{-1}$  for our science results.

### 3.A.4 Systematic errors on the velocity dispersion at low signal-to-noise

While it is clear that a decrease in the S/N of the spectra will increase the random errors on the velocity dispersion, it could also cause systematic offsets (e.g., see Franx et al. 1989). A concern would be that low S/N would lead to an overestimate of the velocity dispersions. Therefore, in this section we test if there are systematic effects when changing the S/N for each source. The S/N we refer to in this section is derived in the region in which we also fit the velocity dispersion, i.e.,  $4020 \text{ \AA} < \lambda_{\text{rest-frame}} < 7000 \text{ \AA}$ .

For each source, we calculated the effect of S/N in a similar fashion as we derived the uncertainty on the velocity dispersion in Section 3.3.2. First, we subtracted the best-fit model from the spectrum. This residual now corresponds to the noise for this particular S/N of this source. We multiply this residual by a certain factor to obtain a new (higher or lower) S/N as compared to our reference S/N. These residuals are then randomly rearranged in wavelength space and added to the best-fit template that has been convolved to a velocity dispersion of  $300 \text{ km s}^{-1}$ . We then determined the velocity dispersion of simulated spectra with this S/N,



**Figure 3.16:** Comparison of the recovered velocity dispersion vs. the S/N of simulated spectra. The vertical dashed line shows the original S/N of the spectrum, and the horizontal dashed line shows the input velocity dispersion of  $300 \text{ km s}^{-1}$ . The black dots show the median of a 100 simulations for each S/N, while the gray area shows the median absolute deviation from these 100 simulations. We find no systematic offset from the input velocity dispersion for  $S/N > 1 \text{ \AA}^{-1}$ , while below this S/N we find that the recovered velocity dispersion is systematically lower.

and repeat this shuffling 100 times. Lastly, we repeat this procedure for a large range in S/N from  $0.1$  to  $100 \text{ \AA}^{-1}$ . We note that uncertainties due to template mismatch are not included in this analysis.

In Figure 3.16 we show the results, with the different values of the S/N on the horizontal axis. We see that increasing the S/N will also decrease the random error in the velocity dispersions. On average, we find that in order to reach a uncertainty of less than 10% on the velocity dispersion measurement, you need an S/N of  $8 \text{ \AA}^{-1}$  or higher. NMBS-COS 7865 shows the lowest random error at fixed S/N, which is older stellar population of the galaxy. No systematic offset in the velocity dispersion is found for an S/N of  $1 \text{ \AA}^{-1}$ . Below this value, however, we find that the velocity dispersion is systematically underestimated as the S/N decreases, though the offset is still smaller than the random errors. We note that Franx et al. (1989) already presented simple arguments for predicting the systematic error. They show that the systematic offset of the velocity dispersion can be derived from error in the measured velocity, and goes as  $\Delta\sigma \propto 0.5dv^2/\sigma$ . We verified from these simulations that this is indeed the case. From this analytic approximation, we furthermore conclude that the systematic uncertainties of our measured velocity dispersion are small.

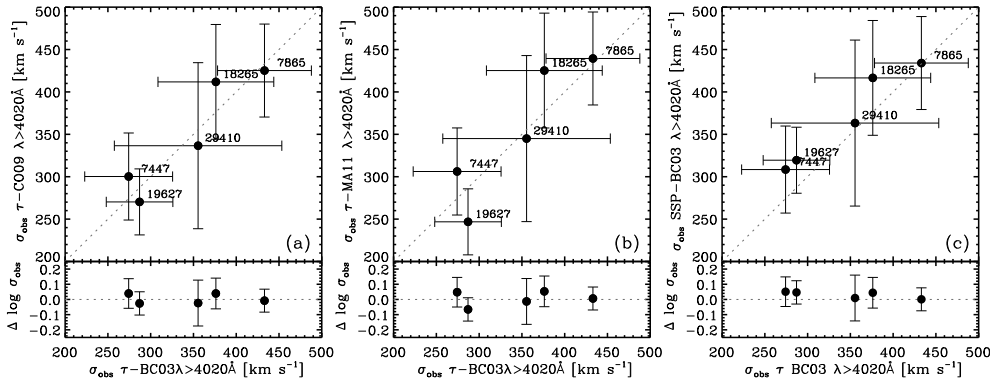


**Figure 3.17:** Comparison of the velocity dispersion when using different methods. Left panel: velocity dispersion as derived with the models of BC03 and Conroy et al. (2009). Even though the models are based on different stellar libraries with different resolution, the velocity dispersions measured with these models are consistent. Middle panel the same as the left panel but now using BC03 and Maraston & Strömbäck (2011) for comparison. In general, we find consistent results within the errors, but UDS19627 has a lower velocity dispersion when we use the Ma11 models. Right panel: velocity dispersion as derived with optimal template construction vs. the best-fitting  $\tau$ -model. The optimal template is constructed from BC03 SSP models with a full range in age and metallicity. Dispersions from the optimal template construction are slightly higher, but well within the errors.

### 3.A.5 Dependence of the velocity dispersion on the SPS models and template construction

Here, we test how our velocity dispersions would change if we make different choices for the SPS-model, and test the difference between a single  $\tau$ -model and a template constructed from different combinations of single stellar population (SSP) models. The left and middle panel of Figure 3.17 show what would happen if we would choose the Flexible-SPS models by Conroy et al. (2009, FSPS) or the models by Maraston & Strömbäck (2011, Ma11). These models are based on a different stellar library with slightly higher resolution as compared to BC03, i.e., MILES (Sánchez-Blázquez et al., 2006) vs. STELIB (Le Borgne et al., 2003). If a systematic uncertainty in the measured velocity dispersion is present, for example due to the resolution or details that go into the SPS-models, it would show up in this comparison. We determined a best-fit  $\tau$  model using the FSPS and Ma11 models in exactly the same way as was done for the BC03 models (see Section 3.3.1). When comparing the velocity dispersions derived by using the BC03 and FSPS  $\tau$ -models, we do not find any significant difference (left panel of Figure 3.17). In the middle panel we compare Ma11 and BC03. Here too, we find a good correspondence. For UDS19627 the Ma11 models give a lower velocity dispersion, though still within the  $1 - \sigma$  error. These results confirm that our measurements are stable against the choice of SPS-model and template with different resolution.

Finally, in Figure 3.17 (right panel) we compare the velocity dispersion from the best-fit  $\tau$ -model, vs. an optimal template constructed by pPXF. This optimal template is built from a full spectral library from BC03 SSP models, with full range in age and metallicity. We note that the optimal template construction only uses the wavelength regime provided in the dispersion fit ( $3600 \text{ \AA} < \lambda < 7000 \text{ \AA}$ ), and does not take into account the effects of dust. The velocity dispersions from the optimal templates are slightly higher as compared to the



single  $\tau$ -model, although it is well below the random error. Interestingly, the galaxy with the largest dust-contribution, NMBS-C18265, also shows the largest difference between the two different fitting techniques. In this chapter, we choose to use the best-fitting  $\tau$ -model as the dispersion template, as this is the best representation of the stellar population. As the stellar mass is also based on this  $\tau$ -model, we use the same stellar population when comparing the stellar to the dynamical mass.

### 3.B Aperture corrections for velocity dispersion measurements

Here, we investigate the effects of different apertures and extraction methods on the observed velocity dispersion. The standard approach is to use a power-law to scale the observed velocity dispersion, measured within a certain  $r_{\text{aper}}$ , to the velocity dispersion as if measured within  $r_{e/8}$ , using the following expression by Jorgensen et al. (1995):

$$\frac{\sigma_{\text{aper}}}{\sigma_{e/8}} = \left( \frac{r_{\text{aper}}}{r_e/8} \right)^{-0.04}. \quad (3.17)$$

Or using a more recent result from the SAURON survey (Cappellari et al., 2006):

$$\frac{\sigma_{\text{aper}}}{\sigma_e} = \left( \frac{r_{\text{aper}}}{r_e} \right)^{-0.066 \pm 0.035}. \quad (3.18)$$

In the case of Jorgensen et al. (1995), the velocity dispersions have been measured in the range of  $-1.5 < \log(r_{\text{aper}}/r_e) < -0.5$ , and for Cappellari et al. (2006) for  $-1.0 < \log(r_{\text{aper}}/r_e) < 0$ . In this work however, we are outside this range with  $\log(r_{\text{aper}}/r_e) > 0.5$ , that is  $r_e$  being much smaller than  $r_{\text{aper}}$ . Also, the galaxies in our sample have effective radii much smaller than the FWHM of the PSF, which is why the standard approach most likely will not be valid. We analyze this problem in two steps. Firstly, we use an analytic description for the kinematic profile and match this to the observed relation as found by Cappellari et al. (2006). Secondly, using our model we study the behavior of the observed velocity dispersion for different apertures (both circular and non-circular) and different FWHM for the PSF. Our reference model will be a circular aperture with size  $r_e$ , without the effects of seeing.

A good description of the kinematic profile for early galaxies is given by (see e.g., Treu et al. 1999; Bertin et al. 2002) :

$$\sigma(r) = \left( \frac{r}{r_e} \right)^d \times \sigma_{\text{cst}}, \quad (3.19)$$

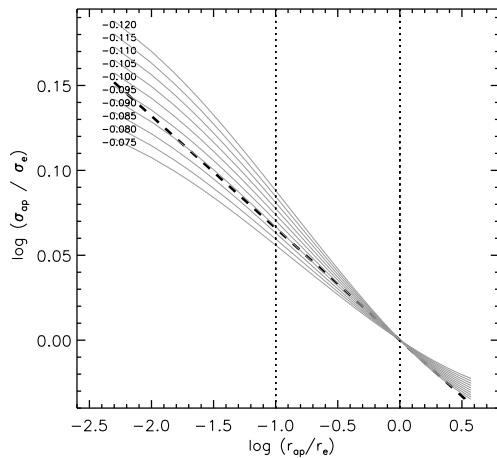


**Figure 3.18:** Comparison of the observed vs. the analytic kinematic profile. The black dashed line is the observed relation from Cappellari et al. (2006), and is valid between for  $-1.0 < \log(r_{\text{aper}}/r_e) < 0$  using  $d = -0.089$ , shown as the vertical dashed lines. For different values of  $d$  in Equation 3.19, we evaluated Equation 3.20 which is shown as the different gray lines. Between  $-1.0 < \log(r_{\text{aper}}/r_e) < 0$ , we find the best match between the observed and analytic kinematic profile when using  $d = -0.089$ .

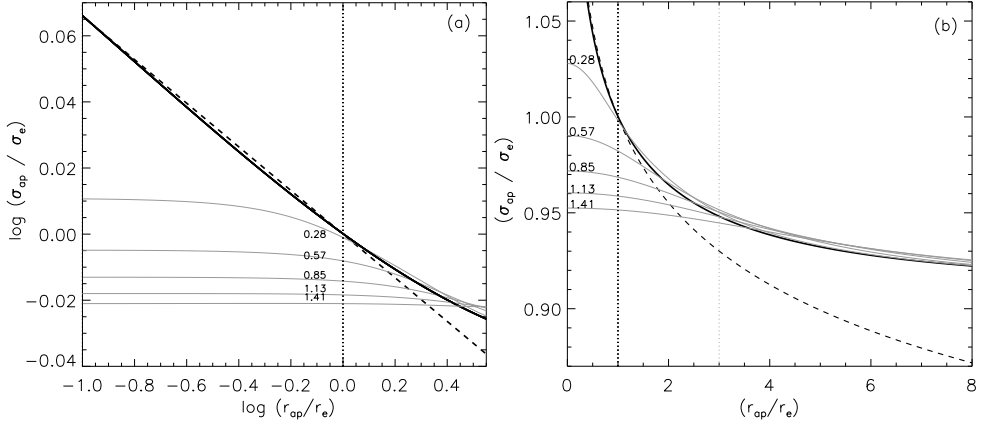


**Figure 3.19:** Comparison of the observed vs. the analytic kinematic profile, similar to Figure 3.18 but now including the effect of seeing. Panel (a) shows the kinematic in log-log space, while the panel (b) is in linear units. The black dashed line is the observed relation from Cappellari et al. (2006), while the solid black line shows our reference model (no PSF). The gray lines show different assumption for the seeing, where the numbers indicate the FWHM of the PSF in arcsec. The vertical black dotted line shows where  $r_{ap} = r_e$ , and the vertical gray dotted line shows a typical  $r_{aper}/r_e$  for our observations. With increasing FWHM, we find that the kinematic profiles becomes less steep for the inner part, as is expected from the convolution with the PSF. In the outer part of the kinematic profile, we see very little change as compared to our reference model.

with  $-0.1 < d < 0$ . The observed kinematic profile within a circular aperture will be a projection of  $\sigma(r)^2$  and the galaxies intensity profile :

$$\sigma^2(r_{aper}) = \frac{\int_0^{r_{aper}} \sigma^2(r) I_{gal}(r) 2\pi r dr}{\int_0^{r_{aper}} I_{gal}(r) 2\pi r dr}. \quad (3.20)$$

Here,  $I_{gal}(r)$  is the Sérsic Profile:

$$I(r) = I_c \exp \left\{ -b_n \left[ \left( \frac{r}{r_e} \right)^{1/n} - 1 \right] \right\} \quad (3.21)$$

To avoid numerical issues in the center, we approximate Equation 3.19 and Equation 3.21 by:

$$\sigma(r) = \left( \frac{r + r_{core}}{r_e} \right)^d \times \sigma_{cst}, \quad (3.22)$$

$$I(r) = I_c \exp \left\{ -b_n \left[ \left( \frac{r + r_{core}}{r_e} \right)^{1/n} - 1 \right] \right\} \quad (3.23)$$

where  $r_{core}$  is chosen to be  $1/30r_e$ . We can estimate the power  $d$  by evaluating Equation 3.20 for different values of  $d$  and comparing the results to Equation 1 from Cappellari et al. (2006). Figure 3.18 shows the Cappellari et al. (2006) relation (dashed black line) and our model with different values for  $d$ , normalized to  $r_e$  (gray lines). We find a best fitting value for

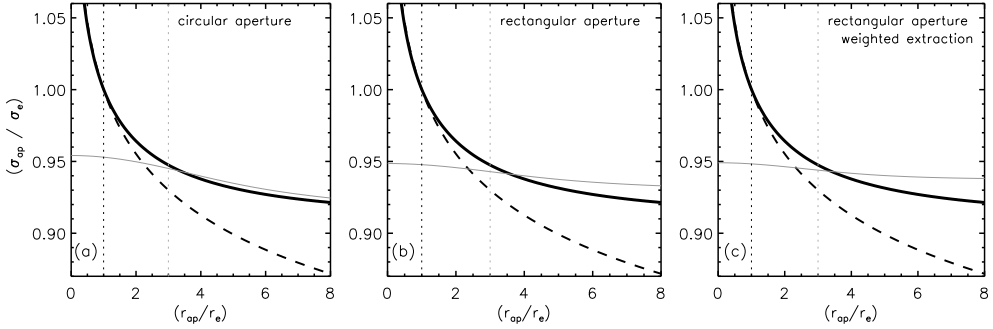


**Figure 3.20:** Observed kinematic profile in different apertures: circular, rectangular, and rectangular including a weight function according to Equation 3.25. The dashed line is the Cappellari et al. (2006) relation, the solid line is our reference model (circular aperture, no PSF), and the gray line is the modeled kinematic including the effect of the PSF. The vertical gray dashed line shows a typical  $r_{\text{aper}}/r_e$  for our observations. We note that  $r_{\text{aper}}$  is in the direction along the slit.

$d = -0.089$  in the region of  $(-1.0 < \log(r_{\text{aper}}/r_e) < 0)$ . Notice that for  $\log(r_{\text{aper}}/r_e) > 0.0$  our model deviates from the simple power law in Equation 3.19.

Now that we have found the intrinsic kinematic profile, we can explore the influence of the PSF on the observed dispersion. The PSF is modeled using a combination of two Gaussians, where  $\sigma_1 = 2\sigma_2$ , and both Gaussians having equal flux. This PSF is then convolved with the kinematic and intensity profiles:

$$\sigma^2(r_{\text{aper}}) = \frac{\int_0^{r_{\text{aper}}} \{ [\sigma^2(r) I_{\text{gal}}(r)] \otimes \text{PSF} \} 2\pi r dr}{\int_0^{r_{\text{aper}}} \{ [I_{\text{gal}}(r)] \otimes \text{PSF} \} 2\pi r dr}. \quad (3.24)$$

Again we compare the observed kinematic profile from Cappellari et al. (2006) and our analytic results from Equation 3.24, which includes the effect of the PSF, and are shown in Figure 3.19. If we compare the black line, which is our reference model, to the gray lines, which include the effect of the PSF, we see that the inner profile ( $\log(r_{\text{aper}}/r_e) < 0.5$ ) is mostly affected and the kinematic profile becomes less steep. This is also particularly clear from Figure 3.19b where we see that very little changes for  $r_{\text{aper}}/r_e > 4$  as compared to the reference model.

Instead of using a circular aperture, we now consider the case of a rectangular aperture, similar to what is used in the spectra from X-Shooter. Equation 3.24 can be modified to include a weight function  $g(y)$  which is commonly used in optimized extraction. The integral in Equation 3.25 is also replaced by a Riemann sum. In the  $x$  direction (slit width) the aperture size is always the same, i.e., 0.9 for X-Shooter spectra, but the  $y$  direction is now parallel to  $r_{\text{aper}}$ :

$$\sigma^2(x_{\text{aper}}, y_{\text{aper}}) = \frac{\sum_0^{x_{\text{aper}}} \sum_0^{y_{\text{aper}}} \{ [\sigma^2(x, y) I_{\text{gal}}(x, y)] \otimes \text{PSF} \} g(y) \Delta x \Delta y}{\sum_0^{x_{\text{aper}}} \sum_0^{y_{\text{aper}}} \{ [I_{\text{gal}}(x, y)] \otimes \text{PSF} \} g(y) \Delta x \Delta y}. \quad (3.25)$$

Figure 3.20 shows the difference between using a circular aperture, a rectangular aperture

without a weighting function, and a rectangular aperture including a weighting function. The slit width that was used is  $0''.9$ , with the FWHM of the PSF also being  $0''.9$ . The spectrum was extracted with  $r_{\text{aper}} = 0''.45$ . We see that the correction is slightly higher for the rectangular aperture as compared to the circular aperture at  $r_{\text{aper}}/r_e = 2.25$ . The behavior at  $r_{\text{aper}}/r_e > 3$  is very different for the three different cases. When using a rectangular aperture with optimized extraction, the observed profile is flatter as compared to the other models. The corrections are on average between 3% and 5%.

From Figure 3.20, it is clear that by using a simple power law for the aperture correction, we would overestimate the corrections by a large fraction. Furthermore, we have shown that it is vital to use a suitable aperture and include the effects of seeing, especially when  $r_{\text{aper}}/r_e > 2$ . The corrections applied to our final results are derived for the rectangular aperture, including a weighting function.

## References

- Bezanson, R., van Dokkum, P. G., Tal, T., Marchesini, D., Kriek, M., Franx, M., & Coppi, P. 2009, *ApJ*, 697, 1290
- Bezanson, R., van Dokkum, P., van de Sande, J., Franx, M., & Kriek, M. 2013, *ApJ*, 764, L8
- Bertin, E., & Arnouts, S. 1996, *A&AS*, 117, 393
- Bertin, G., Ciotti, L., & Del Principe, M. 2002, *A&A*, 386, 149
- Blakeslee, J. P., Holden, B. P., Franx, M., et al. 2006, *ApJ*, 644, 30
- Blanton, M. R., Schlegel, D. J., Strauss, M. A., et al. 2005, *AJ*, 129, 2562
- Bouwens, R. J., Illingworth, G. D., Oesch, P. A., et al. 2010, *ApJ*, 709, L133
- Brammer, G. B., Whitaker, K. E., van Dokkum, P. G., et al. 2011, *ApJ*, 739, 24
- Brinchmann, J., Charlot, S., White, S. D. M., et al. 2004, *MNRAS*, 351, 1151
- Bruzual, G., & Charlot, S. 2003, *MNRAS*, 344, 1000
- Calzetti, D., Armus, L., Bohlin, R. C., Kinney, A. L., Koornneef, J., & Storchi-Bergmann, T. 2000, *ApJ*, 533, 682
- Cappellari, M., & Emsellem, E. 2004, *PASP*, 116, 138
- Cappellari, M., et al. 2006, *MNRAS*, 366, 1126
- Cappellari, M., et al. 2009, *ApJ*, 704, L34
- Cassata, P., et al. 2010, *ApJ*, 714, L79
- Cenarro, A. J., & Trujillo, I. 2009, *ApJ*, 696, L43
- Chabrier, G. 2003, *PASP*, 115, 763
- Ciotti, L. 1991, *A&A*, 249, 99
- Conroy, C., Gunn, J. E., & White, M. 2009, *ApJ*, 699, 486
- Daddi, E., et al. 2005, *ApJ*, 626, 680
- D'Odorico, S., et al. 2006, *Proc. SPIE*, 6269,98
- Feldmann, R., Carollo, C. M., Mayer, L., et al. 2010, *ApJ*, 709, 218
- Ferré-Mateu, A., Vazdekis, A., Trujillo, I., et al. 2012, *MNRAS*, 423, 632
- Förster Schreiber, N. M., Franx, M., Labbé, I., et al. 2006, *AJ*, 131, 1891
- Franx, M., Illingworth, G., & Heckman, T. 1989, *ApJ*, 344, 613
- Franx, M., van Dokkum, P. G., Schreiber, N. M. F., Wuyts, S., Labbé, I., & Toft, S. 2008, *ApJ*, 688, 770
- Goldoni, P., Royer, F., François, P., Horrobin, M., Blanc, G., Vernet, J., Modigliani, A., & Larsen, J. 2006, *Proc. SPIE*, 6269,80
- Grogin, N. A., Kocevski, D. D., Faber, S. M., et al. 2011, *ApJS*, 197, 35
- Hilz, M., Naab, T., & Ostriker, J. P. 2012, *arXiv:1206.5004*
- Hopkins, P. F., Hernquist, L., Cox, T. J., Keres, D., & Wuyts, S. 2009a, *ApJ*, 691, 1424
- Hopkins, P. F., Bundy, K., Murray, N., et al. 2009b, *MNRAS*, 398, 898
- Jorgensen, I., Franx, M., & Kjaergaard, P. 1995, *MNRAS*, 276, 1341
- Kauffmann, G., Heckman, T. M., White, S. D. M., et al. 2003, *MNRAS*, 341, 33
- Koekemoer, A. M., Aussel, H., Calzetti, D., et al. 2007, *ApJS*, 172, 196
- Koekemoer, A. M., Faber, S. M., Ferguson, H. C., et al. 2011, *ApJS*, 197, 36
- Kormendy, J., Fisher, D. B., Cornell, M. E., & Bender, R. 2009, *ApJS*, 182, 216
- Kriek, M., et al. 2006, *ApJ*, 649, L71
- Kriek, M., van Dokkum, P. G., Labbé, I., Franx, M., Illingworth, G. D., Marchesini, D., & Quadri, R. F. 2009, *ApJ*, 700, 221 1
- Labbé, I., et al. 2005, *ApJ*, 624, L81
- Lawrence, A., Warren, S. J., Almaini, O., et al. 2007, *MNRAS*, 379, 1599
- Le Borgne, J.-F., Bruzual, G., Pelló, R., et al. 2003, *A&A*, 402, 433
- Maraston, C., & Strömbäck, G. 2011, *MNRAS*, 418, 2785
- Markwardt, C. B. 2009, *Astronomical Data Analysis Software and Systems XVIII*, 411, 251
- Martinez-Manso, J., Guzman, R., Barro, G., et al. 2011, *ApJ*, 738, L22
- Massey, R., Stoughton, C., Leauthaud, A., et al. 2010, *MNRAS*, 401, 371
- Munari, U., Sordo, R., Castelli, F., & Zwitter, T. 2005, *A&A*, 442, 1127
- Muzzin, A., Marchesini, D., van Dokkum, P. G., et al. 2009, *ApJ*, 701, 1839
- Naab, T., Johansson, P. H., & Ostriker, J. P. 2009, *ApJ*, 699, L178
- Newman, A. B., Ellis, R. S., Treu, T., & Bundy, K. 2010, *ApJ*, 717, L103
- Onodera, M., Renzini, A., Carollo, M., et al. 2012, *arXiv:1206.1540*
- Oser, L., Ostriker, J. P., Naab, T., Johansson, P. H., & Burkert, A. 2010, *ApJ*, 725, 23
- Oser, L., Naab, T., Ostriker, J. P., & Johansson, P. H. 2012, *ApJ*, 744, 63

- Patel, S. G., van Dokkum, P. G., Franx, M., et al. 2012, arXiv:1208.0341
- Peng, C. Y., Ho, L. C., Impey, C. D., & Rix, H.-W. 2010, *AJ*, 139, 2097
- Salim, S., Rich, R. M., Charlot, S., et al. 2007, *ApJS*, 173, 267
- Sánchez-Blázquez, P., et al. 2006, *MNRAS*, 371, 703
- Saracco, P., Gargiulo, A., & Longhetti, M. 2012, *MNRAS*, 422, 3107
- Sérsic, J. L. 1968, *Cordoba, Argentina: Observatorio Astronomico*, 1968,
- Shen, S., Mo, H. J., White, S. D. M., Blanton, M. R., Kauffmann, G., Voges, W., Brinkmann, J., & Csabai, I. 2003, *MNRAS*, 343, 978
- Skelton, R. et al. in preparation
- Szomoru, D., et al. 2010, *ApJ*, 714, L244
- Szomoru, D., Franx, M., & van Dokkum, P. G. 2012, *ApJ*, 749, 121
- Taylor, E. N., Franx, M., Glazebrook, K., et al. 2010a, *ApJ*, 720, 723
- Taylor, E. N., Franx, M., Brinchmann, J., van der Wel, A., & van Dokkum, P. G. 2010b, *ApJ*, 722, 1
- Toft, S., Gallazzi, A., Zirm, A., et al. 2012, *ApJ*, 754, 3
- Treu, T., Stiavelli, M., Casertano, S., Møller, P., & Bertin, G. 1999, *MNRAS*, 308, 1037
- Treu, T., Ellis, R. S., Liao, T. X., & van Dokkum, P. G. 2005a, *ApJ*, 622, L5
- Treu, T., Ellis, R. S., Liao, T. X., et al. 2005b, *ApJ*, 633, 174
- Trujillo, I., et al. 2006, *MNRAS*, 373, L36
- Trujillo, I., Cenarro, A. J., de Lorenzo-Cáceres, A., et al. 2009, *ApJ*, 692, L118
- van de Sande, J., Kriek, M., Franx, M., et al. 2011, *ApJ*, 736, L9
- van Dokkum, P. G. 2001, *PASP*, 113, 1420
- van Dokkum, P. G., et al. 2008, *ApJ*, 677, L5
- van Dokkum, P. G., Kriek, M., & Franx, M. 2009, *Nature*, 460, 717
- van Dokkum, P. G., et al. 2010, *ApJ*, 709, 1018
- van der Wel, A., Franx, M., van Dokkum, P. G., & Rix, H.-W. 2004, *ApJ*, 601, L5
- van der Wel, A., Franx, M., van Dokkum, P. G., et al. 2005, *ApJ*, 631, 145
- van der Wel, A., Holden, B. P., Zirm, A. W., et al. 2008, *ApJ*, 688, 48
- van der Wel, A., Bell, E. F., van den Bosch, F. C., Gallazzi, A., & Rix, H.-W. 2009, *ApJ*, 698, 1232
- Vernet, J., Dekker, H., D'Odorico, S., et al. 2011, *A&A*, 536, A105
- Villumsen, J. V. 1983, *MNRAS*, 204, 219
- Warren, S. J., Hambly, N. C., Dye, S., et al. 2007, *MNRAS*, 375, 213
- Whitaker, K. E., et al. 2010, *ApJ*, 719, 1715
- Whitaker, K. E., Labbé, I., van Dokkum, P. G., et al. 2011, *ApJ*, 735, 86
- Whitaker, K. E., Kriek, M., van Dokkum, P. G., et al. 2012, *ApJ*, 745, 179
- Williams, R. J., Quadri, R. F., Franx, M., van Dokkum, P., & Labbé, I. 2009, *ApJ*, 691, 1879
- Wuyts, S., van Dokkum, P. G., Kelson, D. D., Franx, M., & Illingworth, G. D. 2004, *ApJ*, 605, 677
- Wuyts, S., Labbé, I., Schreiber, N. M. F., et al. 2008, *ApJ*, 682, 985



## 4

# The fundamental plane of massive quiescent galaxies out to $z \sim 2$

## Abstract

The Fundamental Plane (FP) of early-type galaxies, relating the effective radius, velocity dispersion and surface brightness, has long been recognized as a unique tool for analyzing galaxy structure and evolution. With the discovery of distant quiescent galaxies and the introduction of high sensitivity near-infrared spectrographs, it is now possible to explore the FP out to  $z \sim 2$ . In this chapter we study the evolution of the FP out to  $z \sim 2$  using kinematic measurements of massive quiescent galaxies ( $M_* > 10^{11} M_\odot$ ). We find preliminary evidence for the existence of a FP out to  $z \sim 2$ . The scatter of the FP, however, increases from  $z \sim 0$  to  $z \sim 2$ , even when taking into account the larger measurement uncertainties at higher redshift. We find a strong evolution of the zero point from  $z \sim 2$  to  $z \sim 0$ :  $\Delta \log_{10} M/L_g \propto (-0.49 \pm 0.03) z$ . In order to assess whether our spectroscopic sample is representative of the early-type galaxy population at all redshifts, we compare their rest-frame  $g - z$  colors with those from a larger mass complete sample of quiescent galaxies. At  $z > 1$  we find that the spectroscopic sample is bluer. We use the color offsets to estimate a mass-to-light ratio ( $M/L$ ) correction. The implied FP zero point evolution after correction is significantly smaller:  $\Delta \log_{10} M/L_g \propto (-0.39 \pm 0.02) z$ . This is consistent with an apparent formation redshift of  $z_{\text{form}} = 6.62^{+3.19}_{-1.44}$  for the underlying population, ignoring the effects of progenitor bias. A more complete spectroscopic sample is required at  $z \sim 2$  to properly measure the  $M/L$  evolution from the FP evolution.

Jesse van de Sande, Mariska Kriek, Marijn Franx,  
Rachel Bezanson, and Pieter G. van Dokkum

*Revised version*

*Accepted for publication in the Astrophysical Journal*



## 4.1 Introduction

The Fundamental Plane (FP) of early-type galaxies is the empirical relation between the effective radius  $r_e$ , stellar velocity dispersion within one effective radius  $\sigma_e$ , and the average surface brightness within one effective radius  $I_e$  (e.g., Djorgovski & Davis 1987; Dressler et al. 1987; Jorgensen et al. 1996). Traditionally, the offset in the FP is interpreted as the mass-to-light ratio ( $M/L$ ) evolution of galaxies (e.g., Faber et al. 1987), under the assumption that early-type galaxies form a homologous family, and that all the evolution is caused by the change in luminosity. Holden et al. (2010) indeed suggests that this assumption is correct, finding that out to  $z \sim 1$  the slope of the FP does not change. By extending  $M/L$  evolutionary studies to higher redshift, it is possible to put constraints on the formation epoch of massive galaxies.

The evolution of the  $M/L$  has been studied extensively out to  $z \sim 1.3$  (e.g., van Dokkum & van der Marel 2007; Holden et al. 2010). The general consensus is that the evolution of the  $M/L$  appears to evolve as  $\Delta \ln M/L_B \propto z$ . With recent studies showing that the first massive, quiescent galaxies were already in place when the universe was only  $\sim 3$  Gyr old (e.g., Kriek et al. 2006; Williams et al. 2009), the question arises whether the FP already existed at this early epoch and how the  $M/L$  evolved.

With the advent of new NIR spectrographs, such as VLT-X-SHOOTER and Keck-MOSFIRE, it is now possible to obtain rest-frame optical spectra of quiescent galaxies out to  $z \sim 2$ . For example, in van de Sande et al. (2011; 2013) we obtained stellar kinematic measurements for five massive quiescent galaxies at  $1.4 < z < 2.1$  (see also Toft et al. 2012; Belli et al. 2014b). Combined with high-resolution imaging and multi-wavelength catalogs, these recently acquired kinematic measurements enable the extension of FP studies beyond  $z \sim 1.3$ .

In this Chapter, we explore the existence of a FP at  $z \sim 2$ , and use the FP to measure the evolution of the  $M/L$  from  $z \sim 2$  to the present-day for massive quiescent galaxies. In a parallel study, Bezanson et al. (2013b) presented the mass FP evolution. Throughout the chapter we assume a  $\Lambda$ CDM cosmology with  $\Omega_m=0.3$   $\Omega_\Lambda = 0.7$ , and  $H_0 = 70 \text{ km s}^{-1} \text{ Mpc}^{-1}$ . All broadband data are given in the AB-based photometric system.

## 4.2 Data

For the work presented in this chapter, we use a variety of datasets, which all contain accurate kinematic measurements of individual galaxies and high quality broadband photometric catalogs. For more details see Table 4.1 and Chapter 5. All velocity dispersions presented here are aperture corrected to one effective radius following the method as described in van de Sande et al. (2013).

Stellar masses are derived using the FAST code (Kriek et al., 2009). We use the Bruzual & Charlot (2003) Stellar Population Synthesis (SPS) models and assume an exponentially declining star formation history, the Calzetti et al. (2000) dust attenuation law, and the Chabrier (2003) stellar initial mass function. For galaxies in the SDSS, stellar masses are from the MPA-JHU DR7<sup>1</sup> release which are based on Brinchmann et al. (2004).

<sup>1</sup><http://www.mpa-garching.mpg.de/SDSS/DR7/>

Table 4.1: Data references sample

Survey & Field	$N_{\text{gal}}$	$z$	Spectroscopy	Telescope & Instrument	Photometric Catalog	Structural Parameters
SDSS DR7	4621	$0.05 < z < 0.07$	Abazajian et al. (2009)	SDSS	Blanton et al. (2005)	Simard et al. (2011)
NMBS-COSMOS	3	$0.7 < z < 0.9$	Bezanson et al. (2013b)	Keck-DEIMOS	Skelton et al. (2014)	Bezanson et al. (2011)
UKIDSS-UDS	10	$0.6 < z < 0.7$	Bezanson et al. (2013b)	Keck-DEIMOS	Whitaker et al. (2011)	van der Wel et al. (2012)
	3	$0.6 < z < 0.7$	Bezanson et al. (2013b)	Keck-DEIMOS	Skelton et al. (2014)	van der Wel et al. (2012)
	1	$0.6 < z < 0.7$	Bezanson et al. (2013b)	Keck-DEIMOS	Williams et al. (2009)	van der Wel et al. (2012)
MS 1054-0321	8	$z = 0.83$	Wuyts et al. (2004)	Keck-LRIS	Föster Schreiber et al. 2006	Blakeslee et al. (2006)
GOODS-S	7	$0.9 < z < 1.2$	van der Wel et al. (2005)	VLT-FORS2	Skelton et al. (2014)	van der Wel et al. (2012)
GOODS-N	1	$z = 1.315$	Newman et al. (2010)	Keck-LRIS	Skelton et al. (2014)	van der Wel et al. (2012)
EGS	8	$1.0 < z < 1.3$	Belli et al. (2014a)	Keck-LRIS	Skelton et al. (2014)	van der Wel et al. (2012)
COSMOS	6	$1.1 < z < 1.3$	Belli et al. (2014a)	Keck-LRIS	Skelton et al. (2014)	van der Wel et al. (2012)
GOODS-S	1	$z = 1.419$	Belli et al. (2014a)	Keck-LRIS	Skelton et al. (2014)	van der Wel et al. (2012)
NMBS-COSMOS	4	$1.2 < z < 1.5$	Bezanson et al. (2013a)	Keck-LRIS	Whitaker et al. (2011)	Bezanson et al. (2013a)
NMBS-AEGIS	2	$1.4 < z < 1.6$	Bezanson et al. (2013a)	Keck-LRIS	Whitaker et al. (2011)	Bezanson et al. (2013a)
NMBS-COSMOS	2	$1.6 < z < 2.1$	van de Sande et al. (2013)	VLT-XShooter	Skelton et al. (2014)	van de Sande et al. (2013)
UKIDSS-UDS	1	$1.4 < z < 2.1$	van de Sande et al. (2013)	VLT-XShooter	Whitaker et al. (2011)	van de Sande et al. (2013)
	1	$1.4 < z < 2.1$	van de Sande et al. (2013)	VLT-XShooter	Skelton et al. (2014)	van de Sande et al. (2013)
	1	$1.4 < z < 2.1$	van de Sande et al. (2013)	VLT-XShooter	Williams et al. (2009)	van de Sande et al. (2013)
COSMOS	1	$z = 1.823$	Onodera et al. (2012)	Subaru-MOIRCS	Muzzin et al. (2013a)	Onodera et al. (2012)
MUSYC 1255	1	$z = 2.286$	van Dokkum et al. (2009)	Gemini-GNIRS	Blanc et al. (2008)	van Dokkum et al. (2009)
COSMOS	2	$2.1 < z < 2.3$	Belli et al. (2014b)	Keck-MOSFIRE	Skelton et al. (2014)	Belli et al. (2014b)

The photometry and thus also the stellar mass are corrected for missing flux using the best-fit Sérsic luminosity (Taylor et al., 2010). Effective radii and other structural parameters, such as Sérsic index and axis ratio, are determined using 2D-Sérsic fits with GALFIT (Peng et al., 2010). The effective radii are circularized, i.e.,  $r_e = \sqrt{ab}$ . All rest-frame fluxes, including those for the SDSS sample, are calculated using the photometric redshift code EAZY (v46; Brammer et al. 2008).

We derive the average surface brightness within one  $r_e$  ( $I_e$ , in units of  $L_{\odot,g} \text{ pc}^{-2}$ ) by dividing the total luminosity in the rest-frame  $g$ -band by  $2\pi r_e^2$ . Absolute  $g$ -band magnitudes are calculated with  $M_{\odot,g} = 5.14$ , which we derive from the solar spectrum taken from the CALSPEC database<sup>2</sup>.

We adopt a mass limit ( $M_* > 10^{11} M_{\odot}$ ) to homogenize the final sample. We note, however, that our sample remains relatively heterogeneous and in particular the higher redshift samples are biased toward the brightest galaxies (see also Section 4.4). We furthermore use the  $U - V$  vs.  $V - J$  rest-frame color selection criteria to remove star-forming galaxies from our sample (e.g., Wuyts et al. 2007; Williams et al. 2009). Quiescent galaxies are selected to have  $U - V > (V - J) \times 0.88 + 0.59$ . This criteria is slightly different from previous work, as we do not require that  $U - V > 1.3$  or  $V - J < 1.5$ . The latter criteria removes post-starburst galaxies and very old galaxies, respectively.

### 4.3 The fundamental plane

The FP is traditionally written as:

$$\log_{10} r_e = a \log_{10} \sigma_e + b \log_{10} I_{e,g} + c_r \quad (4.1)$$

with  $r_e$  in kpc,  $\sigma_e$  in  $\text{km s}^{-1}$ , and  $I_{e,g}$  in  $L_{\odot,g} \text{ pc}^{-2}$ . In this chapter, we adopt the slope from Jorgensen et al. (1996), i.e.,  $a = 1.20$ , and  $b = -0.83$ . While detailed studies on galaxies in the SDSS have shown that the slope is steeper, i.e.,  $a = 1.404$ , and  $b = -0.76$  (Hyde & Bernardi, 2009), we nonetheless adopt the Jorgensen et al. (1996) values, for an easier comparison with previous high-redshift studies. We do not fit the slope ourselves at high redshift, as our sample is too small and biased at  $z > 1$ . However, we note that Holden et al. (2010) find the same slope of the FP at  $z \sim 1$  as Jorgensen et al. (1996).

While the projection of the FP along the effective radius is most often shown, the projection along  $\log_{10} I_e$  directly shows the evolution in the  $M/L$ , which is thought to be the main driver in the evolution of the FP zero point. The top row in Figure 4.1 shows the following projection:

$$\log_{10} I_e = a \log_{10} \sigma_e + b \log_{10} r_e + c_l, \quad (4.2)$$

with  $a = 1.45$ ,  $b = -1.20$ , and  $c_l = -0.11$ . We determine the zero point  $c_l$  using a least-square fit, using the *IDL* function *MPFIT* (Markwardt, 2009). The zero point evolves rapidly with redshift: 0.30, 0.54, 0.96 dex, at  $z \sim 0.75$ ,  $z \sim 1.25$ ,  $z \sim 2.00$ , respectively.

<sup>2</sup><http://www.stsci.edu/hst/observatory/cdbs/calspec.html>

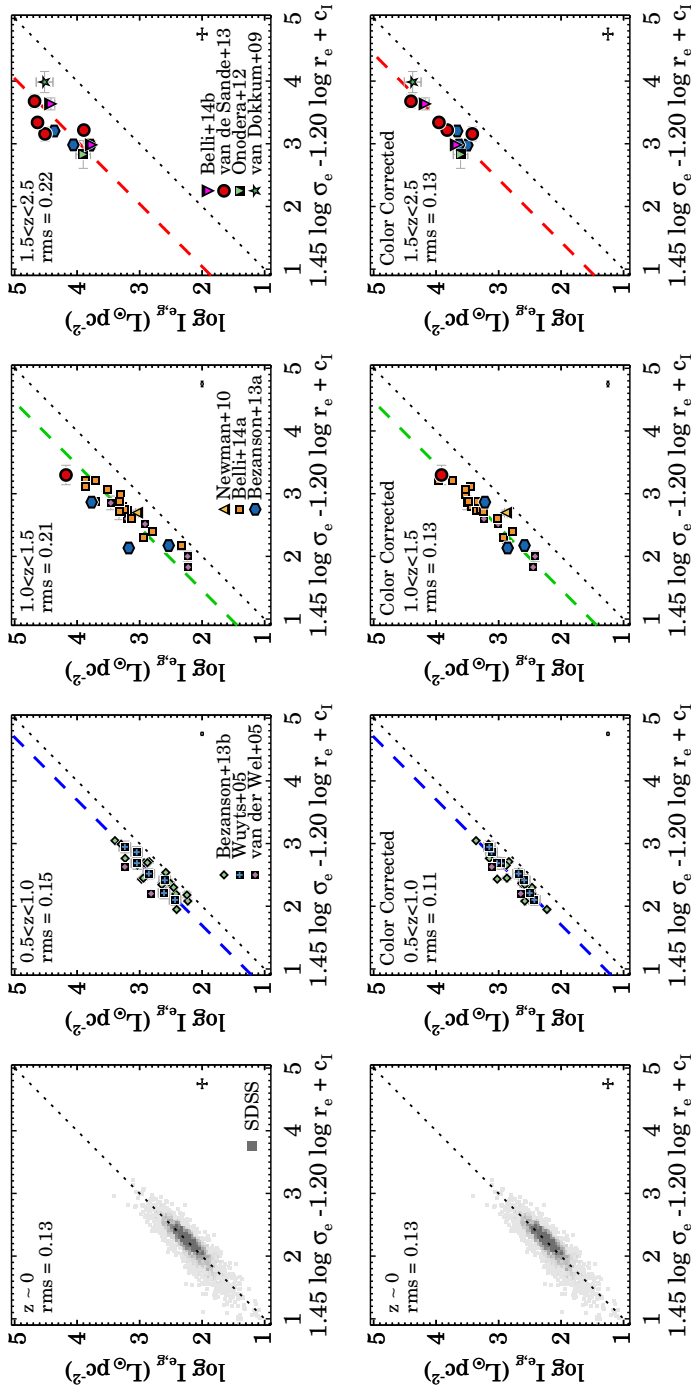


Figure 4.1: Edge on projections of the FP of massive quiescent galaxies ( $M_* > 10^{11} M_\odot$ ) from low to high redshift. Top: at  $z > 0.5$  galaxies no longer fall on the SDSS FP (dotted line), with the dashed line indicating the best-fit relation. The rms scatter increases from  $z \sim 0 - z \sim 2$ , and cannot be explained by larger measurement errors at  $z > 1$  alone. Bottom: Similar as top row, but now including a color correction applied to all galaxies in our spectroscopic sample, to fix the sample bias toward bright young galaxies (see Section 4.4). With the correction applied, we find that the scatter around the FP now reduces for the three high-redshift bins, implying that a tight FP exists out to  $z \sim 2$ .

The top row in Figure 4.1 suggests that the FP exist out to  $z \sim 2$ . However, to quantify the existence of a FP, we consider the scatter before and after the FP fit, i.e., the rms scatter in  $\log_{10} I_c$  vs. the scatter in  $(a \log_{10} \sigma_e + b \log_{10} r_e) - \log_{10} I_c$  or  $\Delta \log_{10} I_c$ .

For example, for galaxies in the SDSS for which we know the FP exists, the scatter in  $\log_{10} I_c$  is  $0.26 \pm 0.003$  dex before the fit, while after the fit, we measure  $\Delta \log_{10} I_c = 0.13 \pm 0.002$  dex. At  $z = 2$  we find a decrease as well, from  $\log_{10} I_c = 0.33 \pm 0.04$  dex, before the fit, to  $\Delta \log_{10} I_c = 0.25 \pm 0.04$  after the fit. This hints to the existence of a FP at  $z \sim 2$ , although the scatter in dex is almost twice as high compared to  $z \sim 0$ .

We use Monte-Carlo simulations to determine if the scatter could be due to measurement uncertainties alone. We find that scatter induced by observational errors is 0.14 dex at  $z \sim 2$ , resulting in an intrinsic scatter of 0.20 dex. Compared to the FP scatter at  $z \sim 0$ , the intrinsic scatter at  $z \sim 2$  is still higher. The larger scatter could have been caused by the large range in age and the bias toward post-starburst galaxies.

## 4.4 Correcting for sample bias

In order to explain the larger scatter in the FP of our high-redshift sample, we compare the rest-frame  $g - z$  colors of our spectroscopic sample to a larger photometric and more complete galaxy sample. We use galaxies from the 3D-HST survey (v4.1; Brammer et al. 2012; Skelton et al. 2014), which were selected to be massive ( $M_* > 10^{11} M_\odot$ ), non-star-forming according to their  $U - V$  vs.  $V - J$  colors (see Section 4.2), and have a reduced  $\chi^2 < 5$  for the best-fit stellar population model to their SED. Rest-frame fluxes for the reference sample were derived with EAZY, in a similar fashion as for the spectroscopic sample and are based on photometric redshifts.

In Figure 4.2(a) we show the comparison of the rest-frame  $g - z$  color as a function of redshift. The reference sample is binned in redshift, with the median of each bin shown as a big gray circle. The dashed line shows the best fit of the color as a function of redshift:  $(g - z)_{\text{fit}} = -0.16z + 1.49$ . There is very little difference between the reference and the spectroscopic sample at  $0 < z < 1$ , while at  $z > 1$  the spectroscopic sample becomes increasingly bluer compared to the median of the reference sample. At  $z > 1.4$  we furthermore see a large spread in colors, where some galaxies follow the median of galaxy the population, while other galaxies are offset by more than 0.5 mag.

All spectroscopic samples are relatively blue at higher redshift, as it is easier to obtain high signal-to-noise spectra for quiescent galaxies compared to the much fainter older quiescent galaxies. In order to estimate the effect of this bias, we use the color difference with the reference sample to calculate a  $M/L$  correction for the individual galaxies in our spectroscopic sample.

First, we measure the relative evolution of the  $M/L$  from the FP as shown in the top panels of Figure 4.1, under the assumption that  $a$ , and  $b$  do not evolve with redshift:

$$\Delta \log_{10} M/L = c_z - c_0. \quad (4.3)$$

Here  $c_0$  is the FP zeropoint at redshift zero, while  $c_z$  is determined from the residuals from the FP for each individual galaxy at redshift  $z$ :

$$c_z = (a \log_{10} \sigma_e + b \log_{10} r_e) - \log_{10} I_c \quad (4.4)$$

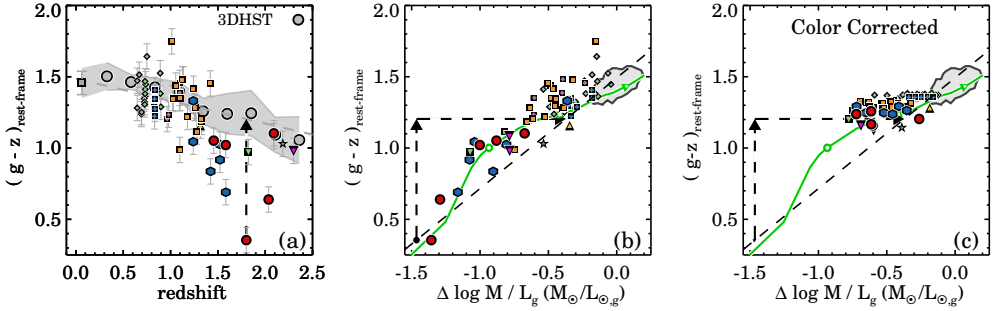


**Figure 4.2:** Redshift evolution of rest-frame  $g-z$  color and  $M/L$  correction from color offset. (a)  $(g-z)_{\text{rest-frame}}$  colors for our high-redshift spectroscopic sample compared to a larger and more complete photometric sample from the 3DHST survey with a similar mass selection as shown by the large gray circles. The gray area indicates the  $1-\sigma$  scatter. For the reference sample we measure that  $(g-z)_{\text{rest-frame}}$  evolves as  $-0.16z$  (dashed gray line). At  $z > 1$  the spectroscopic sample becomes increasingly bluer than the reference sample, indicating a rather strong selection bias. (b)  $\log_{10} M/L_g$  vs. rest-frame  $g-z$  color. Massive galaxies from the SDSS are shown by the gray contour, which encloses 68% of all galaxies. The green line shows a Ma11 model, and the dashed black line shows the linear approximation to the model ( $\log_{10} M/L \propto 1.29(g-z)_{\text{rest-frame}}$ ). We use the model approximation to correct the  $M/L$  using the color offset. The correction is demonstrated with the arrows for the galaxy with the lowest  $M/L$  and bluest color. (c) Corrected  $M/L$ s and  $g-z$  colors. The correction is small for most low-redshift galaxies ( $\sim 0.2$  dex), while the galaxies at  $z > 1.5$  have larger corrections of  $\sim 0.2 - 1.0$  dex.

Note that we have  $\Delta \log_{10} M/L = \Delta \log_{10} I_e$ .

Next, we use the relation between the rest-frame  $g-z$  color and the derived  $\Delta \log_{10} M/L$  as shown in Figure 4.2(b) to derive the  $M/L$  correction. There is a correlation between the color and  $M/L$ , where the bluest galaxies have the lowest  $M/L$ . This correlation is also predicted by SPS models, on which we base our  $M/L$  correction. In Figure 4.2(b) we show a Maraston & Strömbäck (2011, Ma11) solar metallicity model (green line), with a truncated star formation history and constant star formation for the first 0.5-Gyr. Different ages in this model are indicated on the green line by the circle (0.3-Gyr), diamond (1.0-Gyr), and triangle (10-Gyr). We approximate the Ma11 model by a simple linear fit:  $\log_{10} M/L \propto 1.29(g-z)_{\text{rf}}$  (dashed black line). We use this fit to estimate the  $M/L$  correction.

As an example, we highlight the bluest galaxy in our sample, NMBS-Cos-7447 at  $z \sim 1.8$ . In Figure 4.2(a), the black arrow indicates the color offset to the  $(g-z)_{\text{rest-frame}}$  color-redshift relation. The same galaxy has an extremely low  $M/L$  as is clear from Figure 4.2(b). Here the vertical arrow is again the color offset of this galaxy, but the horizontal arrow now points toward the  $M/L$  that the galaxy would have, if it would fall on the color-redshift relation from Figure 4.2(a). The  $M/L$  correction that we apply to this individual galaxy is therefore the length of the horizontal arrow. In other words, for each galaxy we lower the  $M/L$  by 1.29 times the color offset, where the factor 1.29 comes from the linear fit to the Ma11 model (dashed line). We note, however, that a steeper  $M/L$  vs. color relation yields larger  $M/L$  corrections, and thus impacts the  $M/L$  evolution in Section 4.5. We show the corrected colors and  $M/L$  for the entire sample in Figure 4.2(c). The rest-frame  $g-z$  color and  $M/L$  of the spectroscopic sample is now similar to that of the reference sample.

With the  $M/L$  (or  $\Delta \log_{10} I_e$ ) correction applied, we can return to the FP which is shown in the bottom row of Figure 4.1. As before, the dashed colored lines indicate the best-fit FP

with the following zero points in each redshift bin: 0.30, 0.53, and 0.62 dex, from low to high redshift. Note that the  $z \sim 2$  zero point is significantly lower than before the correction. The scatter around the FP is greatly reduced for all three redshift bins. In particular for the highest redshift bin, which had the largest spread in  $(g - z)_{\text{rf}}$  color, the scatter has decreased by almost a factor two. More quantitatively, the scatter after the FP fit is:  $\Delta \log_{10} I_c = 0.11 \pm 0.02$ ,  $0.13 \pm 0.02$ ,  $0.14 \pm 0.02$ , from low to high redshift, respectively. We note that the small scatter is most likely a lower limit, as we do not include the intrinsic color scatter in our analysis.

## 4.5 Evolution of the M/L

In Figure 4.3 we show the  $M/L$  as derived from the FP offset relative to  $z \sim 0$ , as a function of redshift for all galaxies. We indicate the different zero points from Figure 4.1 as dashed lines. The red solid line is a linear least-square fit to all data, which describes the evolution of the  $M/L$ :  $\Delta \log_{10} M/L_g \propto (-0.49 \pm 0.03) z$ . Here we have anchored the fit to the median of the  $z \sim 0$  SDSS galaxies. When excluding SDSS from the fit, the evolution is more rapid:  $\Delta \log_{10} M/L_g \propto (-0.61 \pm 0.09) z$ .

The evolution is similar to a previous result by van Dokkum & van der Marel (2007), who find that the  $M/L \propto (-0.555 \pm 0.042) z$  in the rest-frame  $B$ -band. Here, the effect of using a slightly bluer rest-frame filter makes very little difference, i.e., our measured  $M/L$  evolution in the rest-frame  $B$ -band is only slightly faster as compared to the  $g$ -band:  $\Delta \log_{10} M/L_B \propto (-0.53 \pm 0.03) z$ .

For a fair comparison with previous studies, we also restrict the fit to  $z < 1.4$ , and find a slower evolution than other studies:  $\Delta \log_{10} M/L_g \propto (-0.45 \pm 0.01) z$ . This suggests that the relatively fast evolution of the entire sample is mainly driven by galaxies at  $z > 1.4$ . This is furthermore evident from Figure 4.3(a) in which almost all  $z > 1.4$  galaxies fall below the best fit for the entire sample.

Figure 4.3(b) shows the  $M/L$  evolution with redshift, with the  $M/L$  correction included. This time, we find a milder evolution in the  $M/L$  than before:  $\Delta \log_{10} M/L_g \propto (-0.39 \pm 0.02) z$ , shown by the red line. Our corrected  $M/L$  evolution is similar to previous studies by e.g., van Dokkum & Stanford (2003) ( $-0.460 \pm 0.039$ ), and Holden et al. (2005) ( $-0.426 \pm 0.04$ ), but slower than the evolution found by van Dokkum & van der Marel (2007) ( $-0.555 \pm 0.04$ ), and Holden et al. (2010) ( $-0.60 \pm 0.04$ ). If we would have used a steeper  $M/L$  vs. color relation for the correction, (e.g.,  $\log_{10} M/L \propto 1.80(g - z)_{\text{rest-frame}}$ ) the  $M/L$  evolution would be slower:  $\Delta \log_{10} M/L_g \propto (-0.36 \pm 0.03) z$ .

We also show the single burst Ma11 model from Figure 4.2, with a formation redshift of infinity. Using the same Ma11 model, we fit the average formation redshift of the biased sample (Figure 4.3(a)), and estimate  $z_{\text{form}} = 3.29^{+0.55}_{-0.56}$ . For our corrected sample (Figure 4.3(b)) we estimate the apparent  $z_{\text{form}} = 6.62^{+3.19}_{-1.44}$ . The large difference highlights the strong selection bias in the sample. Both estimates ignore the progenitor bias, which is very strong given the fact that the number density of massive galaxies changes by a factor of  $\sim 10$  from  $z \sim 2$  to  $z \sim 0$  (Muzzin et al., 2013b). Therefore, the corrected  $z_{\text{form}}$  should be regarded as an upper limit for a mass-complete sample that is not supplemented by newly quenched galaxies at later times. We note that we would find a lower  $z_{\text{form}}$  if we were to include progenitor bias in our

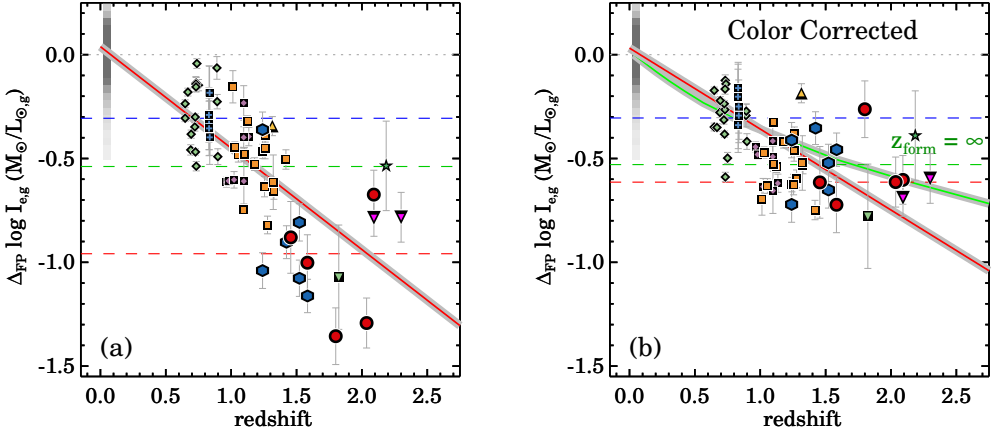


**Figure 4.3:** (a) Redshift evolution of the residuals from the FP. We show the residual from the FP,  $\Delta \log_{10} I_{e,g}$  vs. redshift as compared to  $z \sim 0$ , with the dashed colored lines corresponding to the best-fit offset for the different redshift regimes indicated in Figure 4.1. The red line shows the best fit described by  $\Delta \log_{10} M/L \propto -0.49z \pm 0.03$ , where we have anchored the fit to the median of the SDSS data. We find a similar evolution of the  $M/L$  as compared to previous work, while the high-redshift data at  $z > 1.25$  have lower  $M/L$ . (b) Similar to (a), but now including a correction based on the offset from the  $(g - z)_{\text{rest-frame}}$  relation. This time, we find a milder evolution of  $\Delta \log_{10} M/L \propto (-0.39 \pm 0.02) z$  indicated by the red line, while we show the uncorrected evolution as the dashed gray line. We also include a single burst Ma11 model, with solar metallicity, and with  $z_{\text{form}} = \infty$  (green line).

analysis, or if we would use an evolving mass limit in our sample-selection. A more detailed study of this effect would require a mass-complete spectroscopic sample.

## 4.6 Discussion

In Section 4.4 we have corrected our sample for the bias toward young quiescent galaxies. In this correction we assume that all quiescent galaxies at a particular redshift have the same color and thus the same age. This assumption is an oversimplification, and the scatter in the FP is actually partly due to age variations (e.g., Graves et al. 2009). Furthermore, the age variations of quiescent galaxies may increase with redshift, as shown by Whitaker et al. (2010). Thus, it is very likely that the scatter in the FP will be induced by larger age variations at higher redshift.

However, as we apply the same correction at all redshifts, we do show that the scatter in the FP due to variation in other properties than age (e.g., evolution in stellar mass, size, velocity dispersion, and metallicity) is approximately constant over time. Though, our  $M/L$  evolution is not necessarily the  $M/L$  evolution of progenitors and descendants of a fixed population, as the masses, sizes, and velocity dispersions of these galaxies likely evolve systematically with redshift. Using a simple model, we can estimate the effect of structural evolution on the FP and  $M/L$  evolution. Given that mass evolves as  $\Delta \log_{10} M/M_{\odot} \sim 0.15z$  (van Dokkum et al., 2010), we found that  $\Delta r_e \propto M^{1.83} \simeq M^2$ , and  $\Delta \sigma_e \propto M^{-0.49} \simeq M^{-0.5}$  in van de Sande et al. (2013). Thus, if mass grows by a factor  $f$ , the  $M/L$  evolution (from Equations



4.3&4.4) including structural evolution can be written as follows:

$$\Delta \log_{10} M/L \simeq a \log_{10}(f^{-0.5} \sigma_e) + b \log_{10}(f^2 r_e) - \log_{10}(f^{-3} I_c) \quad (4.5)$$

The bias in the  $M/L$  evolution induced by structural evolution can therefore be approximated by  $(-0.5a + 2b + 3) \log_{10} f$ . Assuming a mass growth factor of 0.3 dex, we find that the offset in the  $M/L$  due to structural evolution is small:  $\sim 0.04$  dex. We note that if velocity dispersion does not evolve, this effect is larger:  $\sim 0.2$  dex.

## 4.7 Conclusion

In this chapter, we have used stellar kinematic and structural measurements of massive quiescent galaxies ( $M_* > 10^{11} M_\odot$ ) out to  $z \sim 2$  to study the evolution of the rest-frame  $g$ -band fundamental plane. We utilize this empirical relation between the size, stellar velocity dispersion, and the surface brightness, to constrain the evolution of the  $M/L$ .

We find preliminary evidence for the existence of a FP out to  $z \sim 2$ , but with larger scatter as compared to the present-day FP for massive quiescent galaxies from the SDSS. There is a rapid evolution of the FP zero point from  $z \sim 0$  to  $z \sim 2$ :  $\Delta \log_{10} M/L_g \propto (-0.49 \pm 0.03) z$ . Furthermore, we find that the  $M/L_g$  evolution for galaxies at  $z > 1.4$  is faster than for galaxies at  $z < 1.4$ .

The larger scatter and fast evolution can be explained by the fact that our spectroscopic sample becomes increasingly bluer at high redshift compared to a mass complete sample of quiescent galaxies. We calculate the color difference between the galaxies and the mass complete sample, and estimate the systematic effect on the  $M/L$ .

With this correction applied, the evolution of the  $M/L$ , as derived from the FP, is slower:  $\Delta \log_{10} M/L_g \propto (-0.39 \pm 0.02) z$ . A simple model, ignoring progenitor bias, would imply a formation redshift of  $z_{\text{form}} = 6.62_{-1.44}^{+3.19}$  for a mass complete sample. The difference between the evolution of our observed sample and the underlying population, highlights the need for a more detailed study of a mass complete spectroscopic sample.

## Acknowledgments

We thank the NMBS and 3DHST collaborations, Rik Williams, Ryan Quadri, and Andrew Newman for providing ancillary data. This work is based on observations taken by the 3D-HST Treasury Program (GO-12177,12328) with the NASA/ESA-HST, which is operated by the Association of Universities for Research in Astronomy, Inc., under NASA contract NAS5-26555.

## References

- Abazajian, K. N., Adelman-McCarthy, J. K., Agüeros, M. A., et al. 2009, *ApJS*, 182, 543
- Belli, S., Newman, A. B., Ellis, R. S., & Konidaris, N. P. 2014b, *ApJ*, 788, L29
- Belli, S., Newman, A. B., & Ellis, R. S. 2014a, *ApJ*, 783, 117
- Bezanson, R., van Dokkum, P., van de Sande, J., Franx, M., & Kriek, M. 2013a, *ApJ*, 764, L8
- Bezanson, R., van Dokkum, P. G., van de Sande, J., et al. 2013b, *ApJ*, 779, L21
- Bezanson, R., van Dokkum, P. G., Franx, M., et al. 2011, *ApJ*, 737, L31
- Blakeslee, J. P., Holden, B. P., Franx, M., et al. 2006, *ApJ*, 644, 30
- Blanc, G. A., Lira, P., Barrientos, L. F., et al. 2008, *ApJ*, 681, 1099
- Blanton, M. R., Schlegel, D. J., Strauss, M. A., et al. 2005, *AJ*, 129, 2562
- Brammer, G. B., van Dokkum, P. G., & Coppi, P. 2008, *ApJ*, 686, 1503
- Brammer, G. B., van Dokkum, P. G., Franx, M., et al. 2012, *ApJS*, 200, 13
- Brinchmann, J., Charlot, S., White, S. D. M., et al. 2004, *MNRAS*, 351, 1151
- Bruzual, G., & Charlot, S. 2003, *MNRAS*, 344, 1000
- Calzetti, D., Armus, L., Bohlin, R. C., et al. 2000, *ApJ*, 533, 682
- Chabrier, G. 2003, *PASP*, 115, 763
- Djorgovski, S., & Davis, M. 1987, *ApJ*, 313, 59
- Dressler, A., Faber, S. M., Burstein, D., et al. 1987, *ApJ*, 313, L37
- Faber, S. M., Dressler, A., Davies, R. L., Burstein, D., & Lynden-Bell, D. 1987, *Nearly Normal Galaxies. From the Planck Time to the Present*, 175
- Förster Schreiber, N. M., Franx, M., Labbé, I., et al. 2006, *AJ*, 131, 1891
- Graves, G. J., Faber, S. M., & Schiavon, R. P. 2009, *ApJ*, 698, 1590
- Holden, B. P., van der Wel, A., Franx, M., et al. 2005, *ApJ*, 620, L83
- Holden, B. P., van der Wel, A., Kelson, D. D., Franx, M., & Illingworth, G. D. 2010, *ApJ*, 724, 714
- Hyde, J. B., & Bernardi, M. 2009, *MNRAS*, 396, 1171
- Jorgensen, I., Franx, M., & Kjaergaard, P. 1996, *MNRAS*, 280, 167
- Kriek, M., van Dokkum, P. G., Labbé, I., et al. 2009, *ApJ*, 700, 221
- Kriek, M., van Dokkum, P. G., Franx, M., et al. 2006, *ApJ*, 649, L71
- Maraston, C., & Strömbäck, G. 2011, *MNRAS*, 418, 2785
- Markwardt, C. B. 2009, *Astronomical Data Analysis Software and Systems XVIII*, 411, 251
- Muzzin, A., Marchesini, D., Stefanon, M., et al. 2013a, *ApJS*, 206, 8
- Muzzin, A., Marchesini, D., Stefanon, M., et al. 2013b, *ApJ*, 777, 18
- Newman, A. B., Ellis, R. S., Treu, T., & Bundy, K. 2010, *ApJ*, 717, L103
- Onodera, M., Renzini, A., Carollo, M., et al. 2012, *ApJ*, 755, 26
- Peng, C. Y., Ho, L. C., Impey, C. D., & Rix, H.-W. 2010, *AJ*, 139, 2097
- Simard, L., Mendel, J. T., Patton, D. R., Ellison, S. L., & McConnell, A. W. 2011, *ApJS*, 196, 11
- Skelton, R. E., Whitaker, K. E., Momcheva, I. G., et al. 2014, *arXiv:1403.3689*
- Taylor, E. N., Franx, M., Brinchmann, J., van der Wel, A., & van Dokkum, P. G. 2010, *ApJ*, 722, 1
- Toft, S., Gallazzi, A., Zirm, A., et al. 2012, *ApJ*, 754, 3
- van de Sande, J., Kriek, M., Franx, M., et al. 2013, *ApJ*, 771, 85
- van de Sande, J., Kriek, M., Franx, M., et al. 2011, *ApJ*, 736, L9
- van der Wel, A., Bell, E. F., Häussler, B., et al. 2012, *ApJS*, 203, 24
- van der Wel, A., Franx, M., van Dokkum, P. G., et al. 2005, *ApJ*, 631, 145
- van Dokkum, P. G., Whitaker, K. E., Brammer, G., et al. 2010, *ApJ*, 709, 1018
- van Dokkum, P. G., Kriek, M., & Franx, M. 2009, *Nature*, 460, 717
- van Dokkum, P. G., & van der Marel, R. P. 2007, *ApJ*, 655, 30
- van Dokkum, P. G., & Stanford, S. A. 2003, *ApJ*, 585, 78
- Whitaker, K. E., Labbé, I., van Dokkum, P. G., et al. 2011, *ApJ*, 735, 86
- Whitaker, K. E., van Dokkum, P. G., Brammer, G., et al. 2010, *ApJ*, 719, 1715
- Williams, R. J., Quadri, R. F., Franx, M., van Dokkum, P., & Labbé, I. 2009, *ApJ*, 691, 1879
- Wuyts, S., van Dokkum, P. G., Kelson, D. D., Franx, M., & Illingworth, G. D. 2004, *ApJ*, 605, 677
- Wuyts, S., Labbé, I., Franx, M., et al. 2007, *ApJ*, 655, 51



## 5

# The relation between dynamical mass-to-light ratio and color for massive quiescent galaxies out to $z \sim 2$ and comparison with stellar population synthesis models

## Abstract

In this chapter, we explore the relation between the dynamical mass-to-light ratio ( $M/L$ ) and rest-frame color of massive quiescent galaxies out to  $z \sim 2$ . We use a galaxy sample with measured stellar velocity dispersions in combination with *Hubble Space Telescope* and ground-based multi-band photometry. Our galaxy sample spans a large range in  $M/L$ : 1.8 dex in rest-frame  $\log M_{\text{dyn}}/L_u$ , 1.6 dex in  $\log M_{\text{dyn}}/L_g$ , and 1.3 dex in  $\log M_{\text{dyn}}/L_K$ . There is a strong correlation between the  $M/L$  for different wavebands and rest-frame color that is well approximated by a linear relation. The root-mean-square scatter in the  $\log M_{\text{dyn}}/L$  residuals is  $\sim 0.26$  dex. Thus, it is possible to estimate the  $M/L$  of an early-type galaxy with an accuracy of  $\sim 0.26$  dex from a single rest-frame optical color. Next, we compare the measured  $M/L$  vs. rest-frame color with different stellar population synthesis (SPS) models. With a Salpeter stellar initial mass function (IMF), none of the SPS models are able to simultaneously match the  $M_{\text{dyn}}/L_g$  vs.  $(g - z)_{\text{rest-frame}}$  color and the  $M_{\text{dyn}}/L_K$  vs.  $(g - K)_{\text{rest-frame}}$  color. We test whether a different slope of the IMF provides a better match to the data. By changing the slope we are still unable to simultaneously match the low  $M/L$  of the bluest galaxies in combination with the other data. We find that an IMF with a slope between  $\alpha = 2.35$  and  $\alpha = 1.35$  provides the best match. We also explore a broken IMF with a Salpeter slope at  $< 1M_{\odot}$  and  $> 4M_{\odot}$  and a slope  $\alpha$  in the intermediate region. Based on the rms scatter we find that the data favor a slope of  $\alpha = 1.35$  over  $\alpha = 2.35$ . Nonetheless, our results show that variations between different SPS models (with the same IMF) are comparable to the IMF variations. An important source of uncertainty is that galaxies evolve in complex ways. We assume in our analysis that the variation in  $M/L$  and color is driven by differences in age, and that other contributions, such as differences in metallicities and dark matter contributions, are small.

Jesse van de Sande, Mariska Kriek, Marijn Franx,  
 Rachel Bezanson, and Pieter G. van Dokkum  
*Revised version*  
 To be resubmitted to the *Astrophysical Journal*

## 5.1 Introduction

For a good understanding of galaxy evolution, accurate stellar mass estimates are very important (for a recent review see Courteau et al. 2013). Nearly all galaxy properties, among which structure, star formation activity, and the chemical enrichment history are strongly correlated with the stellar mass (e.g., Kauffmann et al. 2003; Tremonti et al. 2004; Gallazzi et al. 2005). Furthermore, the evolution of the stellar mass function (e.g., Bundy et al. 2006; Marchesini et al. 2009; Muzzin et al. 2013b; Ilbert et al. 2013) provides strong constraints on galaxy formation models (see e.g., De Lucia & Blaizot 2007).

In contrast to the luminosity, the stellar mass of a galaxy is not a direct observable quantity. Most techniques for estimating the stellar mass rely on a determination of a mass-to-light ratio. The  $M/L$  of a galaxy strongly depends on the age, metallicity, and the stellar initial mass function (IMF) of its stellar population. Typically, the observed colors, multi-wavelength broadband photometry, or spectra are compared to stellar population synthesis (SPS) models to estimate the  $M/L$  ratio (for a review see Conroy 2013).

In this chapter, we focus on the relation between the  $M/L$  and color, as was first explored by Bell & de Jong (2001). They used SPS models and derived a tight relation between rest-frame  $B - R$  color and  $M/L_B$ , from which it is possible to estimate the  $M/L$  of a galaxy to an accuracy of  $\sim 0.2$  dex. Because their results were based on SPS models, they suffer from uncertainties due to assumptions regarding the star formation history (SFH), metallicity, IMF, and SPS code. More recent work indeed suggest that the uncertainties are larger (0.2-0.4 dex; Bell et al. 2003; Zibetti et al. 2009; Taylor et al. 2011), in particular when using rest-frame NIR colors.

Direct stellar kinematic mass measurements yield dynamical  $M/L$ , which do not rely on any assumptions regarding the SPS models, metallicity, and IMF. At low-redshift, dynamical mass measurements of galaxies have proven to be extremely useful for studying the  $M/L$  (e.g., Cappellari et al. 2006; de Jong & Bell 2007; Taylor et al. 2010). For example, Cappellari et al. (2006) find that the stellar  $M/L$  is tightly correlated with  $\sigma_e$ , and Taylor et al. (2010) find that the stellar  $M/L$  is a good predictor of the dynamical  $M/L$  if the Sérsic index is taken into account when calculating dynamical masses (i.e.,  $M_{\text{dyn}} \propto K(n)r_c\sigma_e^2$ ). van der Wel et al. (2006) studied the relation between the dynamical  $M/L_K$  and rest-frame  $B - K$  color of early-type galaxies out to  $z \sim 1$ , and find that there are large discrepancies between different SPS models in the NIR. However, one of the major limitations in this measurement was the low number of galaxies, and the small dynamic range in  $M/L_K$  ( $\sim 0.4$  dex).

In order to accurately constrain the relation between the dynamical  $M/L$  and color, we need a sample of early-type galaxies with a large range in age. This study requires kinematic measurements from  $z \sim 0$  to  $z \sim 2$ , such that we measure the  $M/L$  and color in early-type galaxies with both the oldest ( $z \sim 0$ ) and youngest ( $z \sim 2$ ) stellar populations.

However, due to observational challenges very few such measurements exist. At high-redshift, kinematic studies of quiescent galaxies become much more difficult as the bulk of the stellar light, and stellar absorption features used to measure velocity dispersions, shift into the near-infrared (NIR) (e.g., Kriek et al. 2009). With the advent of fully depleted, high-resistivity CCDs (e.g., Keck-LRIS), and new NIR spectrographs, such as VLT-X-SHOOTER (Vernet et al., 2011), and Keck-MOSFIRE (McLean et al., 2012), it is now possible to obtain rest-frame optical spectra of quiescent galaxies out to  $z \sim 2$ .

Table 5.1: Data references sample

Survey & Field	$N_{\text{gal}}$	$z$	Spectroscopy	Telescope & Instrument	Photometric Catalog	Structural Parameters
SDSS DR7	4621	$0.05 < z < 0.07$	Abazajian et al. (2009)	SDSS	Blanton et al. (2005)	Simard et al. (2011)
NMBS-COSMOS	3	$0.7 < z < 0.9$	Bezanson et al. (2013b)	Keck-DEIMOS	Skelton et al. (2014)	Bezanson et al. (2011)
UKIDSS-UWS	10	$0.6 < z < 0.7$	Bezanson et al. (2013b)	Keck-DEIMOS	Whitaker et al. (2011)	van der Wel et al. (2012)
	3	$0.6 < z < 0.7$	Bezanson et al. (2013b)	Keck-DEIMOS	Skelton et al. (2014)	van der Wel et al. (2012)
	1	$0.6 < z < 0.7$	Bezanson et al. (2013b)	Keck-DEIMOS	Williams et al. (2009)	van der Wel et al. (2012)
MS 1054-0321	8	$z = 0.83$	Wuyts et al. (2004)	Keck-LRIS	Förster Schreiber et al. 2006	Blakeslee et al. (2006)
GOODS-S	7	$0.9 < z < 1.2$	van der Wel et al. (2005)	VLT-FORS2	Skelton et al. (2014)	van der Wel et al. (2012)
GOODS-N	1	$z = 1.315$	Newman et al. (2010)	Keck-LRIS	Skelton et al. (2014)	van der Wel et al. (2012)
EGS	8	$1.0 < z < 1.3$	Belli et al. (2014a)	Keck-LRIS	Skelton et al. (2014)	van der Wel et al. (2012)
COSMOS	6	$1.1 < z < 1.3$	Belli et al. (2014a)	Keck-LRIS	Skelton et al. (2014)	van der Wel et al. (2012)
GOODS-S	1	$z = 1.419$	Belli et al. (2014a)	Keck-LRIS	Skelton et al. (2014)	van der Wel et al. (2012)
NMBS-COSMOS	4	$1.2 < z < 1.5$	Bezanson et al. (2013a)	Keck-LRIS	Whitaker et al. (2011)	Bezanson et al. (2013a)
NMBS-AEGIS	2	$1.4 < z < 1.6$	Bezanson et al. (2013a)	Keck-LRIS	Whitaker et al. (2011)	Bezanson et al. (2013a)
NMBS-COSMOS	2	$1.6 < z < 2.1$	van de Sande et al. (2013)	VLT-XShooter	Skelton et al. (2014)	van de Sande et al. (2013)
UKIDSS-UWS	1	$1.4 < z < 2.1$	van de Sande et al. (2013)	VLT-XShooter	Whitaker et al. (2011)	van de Sande et al. (2013)
	1	$1.4 < z < 2.1$	van de Sande et al. (2013)	VLT-XShooter	Skelton et al. (2014)	van de Sande et al. (2013)
	1	$1.4 < z < 2.1$	van de Sande et al. (2013)	VLT-XShooter	Williams et al. (2009)	van de Sande et al. (2013)
COSMOS	1	$z = 1.823$	Onodera et al. (2012)	Subaru-MOIRCS	Muzzin et al. (2013a)	Onodera et al. (2012)
MUSYC 1255	1	$z = 2.286$	van Dokkum et al. (2009)	Gemini-GNIRS	Blanc et al. (2008)	van Dokkum et al. (2009)
COSMOS	2	$2.1 < z < 2.3$	Belli et al. (2014b)	Keck-MOSFIRE	Skelton et al. (2014)	Belli et al. (2014b)

For example, Bezanson et al. (2013a) measured accurate dynamical masses for 8 galaxies at  $1.2 < z < 1.6$ . Furthermore, in van de Sande et al. (2011; 2013) we obtained stellar kinematic measurements for 5 massive quiescent galaxies up to redshift  $z = 2.1$  (see also Toft et al. 2012; Belli et al. 2014b). Combined with high-resolution imaging and multi-wavelength catalogs, these recently acquired kinematic measurements increase the dynamic range of the  $M/L$  and rest-frame color.

In this chapter, we use a sample of massive quiescent galaxies from  $z \sim 2$  to  $z \sim 0$  with kinematic measurements and multi-band photometry with the aim of exploring the relation between the  $M/L$  and rest-frame color, assessing SPS models, and constraining the IMF. The chapter is organized as follows. In Section 5.2 we present our sample of  $0.05 < z < 2.1$  galaxies, discuss the photometric and spectroscopic data, and describe the derived galaxy properties such as effective radii, rest-frame fluxes, and stellar population parameters. In Section 5.3 we explore the relation between the  $M/L$  and the rest-frame color over a large dynamic range for several pass-bands. We compare our  $M/L$  vs. rest-frame color to predictions from stellar population models in Section 5.4. In Section 5.5 we use the  $M/L$  vs. color and stellar population models to constrain the IMF in massive galaxies, as first proposed by Tinsley (1972; 1980; see also van Dokkum 2008a who first applied this technique to measure the IMF out to  $z \sim 1$ ). In Section 5.6 we compare our results with previous measurements and discuss several uncertainties. Finally, in Section 5.7 we summarize our results and conclusions. Throughout the chapter we assume a  $\Lambda$ CDM cosmology with  $\Omega_m=0.3$   $\Omega_\Lambda = 0.7$ , and  $H_0 = 70 \text{ km s}^{-1} \text{ Mpc}^{-1}$ . All broadband data are given in the AB-based photometric system.

## 5.2 Data

### 5.2.1 Low and high-redshift sample

One of the primary goals of this chapter is to explore the relation between the  $M/L$  and rest-frame color over a large dynamic range. Early-type galaxies are ideal candidates for such a measurement, as they have homogeneous stellar populations. At  $z \sim 0$  their spectral energy distributions are dominated by old stellar populations (e.g., Kuntschner et al. 2010), and they have experienced very little to no star formation since  $z \sim 2$  (e.g., Kriek et al. 2008).

Here, we use a variety of datasets, which all contain stellar kinematic measurements of individual galaxies and multi-wavelength medium and broad-band photometric catalogs. We adopt a mass limit of  $M_* > 10^{11} M_\odot$  to homogenize the final sample. Our mass-selected sample contains 73 massive galaxies at  $0.5 < z < 2.2$ . We note, however, that our sample remains relatively heterogeneous relative to mass-complete photometric samples and in particular the higher redshift samples are biased toward the brightest galaxies.

We use the  $U - V$  vs.  $V - J$  rest-frame color selection to distinguish quiescent galaxies from (dusty) star-forming galaxies. (e.g., Wuyts et al. 2007; Williams et al. 2009). Figure 5.1 shows the mass selected sample in the UVJ diagram, in which quiescent galaxies have  $U - V > (V - J) \times 0.88 + 0.59$ . Out of the 73 galaxies in the mass selected sample, 61 are selected as quiescent galaxies and included in our sample. This criterion is slightly different from previous work, as we do not require that  $U - V > 1.3$  or  $V - J < 1.5$ . These criteria would remove, respectively, post-starburst and the oldest galaxies. As we benefit from a large

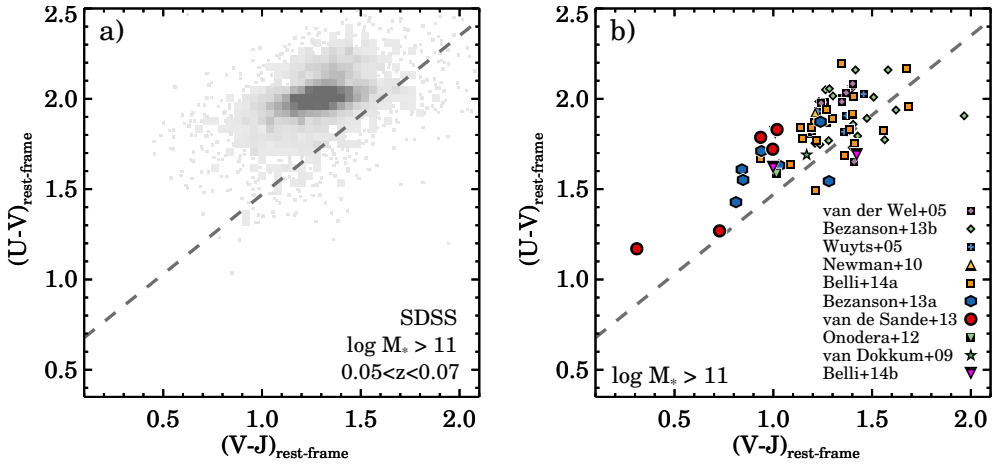


**Figure 5.1:** Rest-frame  $U - V$  color vs.  $V - J$  color. Panel (a) shows massive ( $M_* > 10^{11} M_\odot$ ) galaxies in the SDSS at  $z \sim 0.06$ , and Panel (b) shows massive galaxies at  $z > 0.5$ . Different symbols for the intermediate to high-redshift samples are indicated in the legend and described in Section 5.2. The dashed lines shows our separation of star-forming and quiescent galaxies, where quiescent galaxies are selected to have  $U - V > (V - J) \times 0.88 + 0.59$ . We only use the quiescent galaxies in the remainder of the chapter.

**Table 5.2:** Absolute magnitudes of the Sun in different filters

$M_{\odot,U}$	$M_{\odot,B}$	$M_{\odot,V}$	$M_{\odot,R}$	$M_{\odot,I}$	$M_{\odot,u}$	$M_{\odot,g}$	$M_{\odot,r}$	$M_{\odot,i}$	$M_{\odot,z}$	$M_{\odot,J}$	$M_{\odot,H}$	$M_{\odot,K}$
6.34	5.33	4.81	4.65	4.55	6.45	5.14	4.65	4.54	4.52	4.57	4.71	5.19

range in age in this chapter, we omit the latter criteria and thereby keep the youngest and oldest galaxies in our sample. Photometry for the high-redshift sample is adopted from the 3D-HST catalogs version 4.1 (Brammer et al. 2012; Skelton et al. 2014) where possible, which cover the following CANDELS fields: AEGIS, COSMOS, GOODS-N, GOODS-S and UKIDSS-UDS. We list the references for all kinematic studies, photometric catalogs, and structural parameters for the final sample in Table 5.1.

## 5.2.2 Derived galaxy properties

All velocity dispersions were measured from stellar absorption features in the rest-frame near-UV and/or optical. We apply an aperture correction to the velocity dispersion measurements as if they were observed within a circular aperture radius of one  $r_e$ , following the method as described in van de Sande et al. (2013). This method includes a correction for the radial dependence of the velocity dispersion (e.g., Cappellari et al. 2006), and takes into account the effects of the non-circular aperture, seeing, and optimal extraction of the 1-D spectrum.

For the intermediate to high-redshift sample, effective radii and other structural parameters, such as Sérsic index and axis ratio, are determined using 2D Sérsic fits with GALFIT (Peng et al., 2010). For galaxies in the SDSS, we use the structural parameters from Simard et al. (2011), who determined 2D Sérsic fits with GIMD2D (Simard, 1998) on the SDSS  $g$  band



imaging data. The effective radii are circularized, i.e.,  $r_e = \sqrt{ab}$ . All sizes are measured from rest-frame optical data, i.e., redwards of 4000 Å, with the exception of COSMOS-13412 ( $z = 1.24$ ) from Bezanson et al. (2013a), and COSMOS-254025 ( $z = 1.82$ ) from Onodera et al. (2012) for which the *HST*-F775W band is used. For massive galaxies at  $z > 1$ , the median color gradient is  $r_{e,u}/r_{e,g} = 1.12$  (Szomoru et al., 2013). Thus the  $M/L$  for these two galaxies may be overestimate by  $\sim 0.05$  dex.

All rest-frame fluxes, including those for the SDSS sample, are calculated using the photometric redshift code EAZY (v46; Brammer et al. 2008). We use the same set of templates that were used for the UltraVISTA catalog by Muzzin et al. (2013a). Stellar masses for the high-redshift sample are derived using the stellar population fitting code FAST (Kriek et al., 2009). We use the Bruzual & Charlot (2003) SPS models and assume an exponentially declining star formation history (SFH), solar metallicity ( $Z = 0.02$ ), the Calzetti et al. (2000) dust attenuation law, and the Chabrier (2003) IMF. For galaxies in the SDSS, stellar masses are from the MPA-JHU DR7<sup>1</sup> release which are based on Brinchmann et al. (2004), assuming a Chabrier (2003) IMF. The photometry and thus also the stellar mass are corrected for missing flux using the best-fit Sérsic luminosity (Taylor et al., 2010).

Dynamical masses are estimated from the size and velocity dispersion measurements using the following expression:

$$M_{\text{dyn}} = \frac{\beta(n) \sigma_c^2 r_e}{G}. \quad (5.1)$$

Here  $\beta(n)$  is an analytic expression as a function of the Sérsic index, as described by Cappellari et al. (2006):

$$\beta(n) = 8.87 - 0.831n + 0.0241n^2. \quad (5.2)$$

We note that if we use a fixed virial constant of  $\beta = 5$  for all galaxies our conclusion would not change. We derive mass-to-light ratios ( $M/L_\lambda$ ) using the dynamical mass from Equation 5.1 divided by the total luminosity, in units of  $M_\odot L_{\odot,\lambda}^{-1}$ . The total luminosities for different wave bands ( $\lambda$ ) are calculated from rest-frame fluxes, as derived using EAZY. We normalize the total luminosity using the absolute magnitude of the Sun in that particular filter, which is measured from the solar spectrum taken from the CALSPEC database<sup>2</sup>. The solar absolute magnitudes for all filters are listed in Table 5.2.

## 5.3 Empirical relation between the $M/L$ and color

### 5.3.1 Color and the $M/L$ evolution

In Figure 5.2(a) and (c) we show the rest-frame  $g - z$  color and  $M_{\text{dyn}}/L_g$  as a function of redshift. We find a large range in  $g - z$  color ( $\sim 1$ mag) and  $\log_{10} M_{\text{dyn}}/L_g$  ( $\sim 1.6$  dex). At  $z > 1$ , massive galaxies are bluer and have lower  $M/L$  as compared to low-redshift. In Chapter 4, we showed that this spectroscopic sample is biased toward young quiescent galaxies at high-redshift. While this bias complicated the analysis of the fundamental plane as presented in that work, here we take advantage of that same bias, as it enables us to study massive quiescent galaxies with a large range in stellar population properties.

<sup>1</sup><http://www.mpa-garching.mpg.de/SDSS/DR7/>

<sup>2</sup><http://www.stsci.edu/hst/observatory/cdbs/calspec.html>

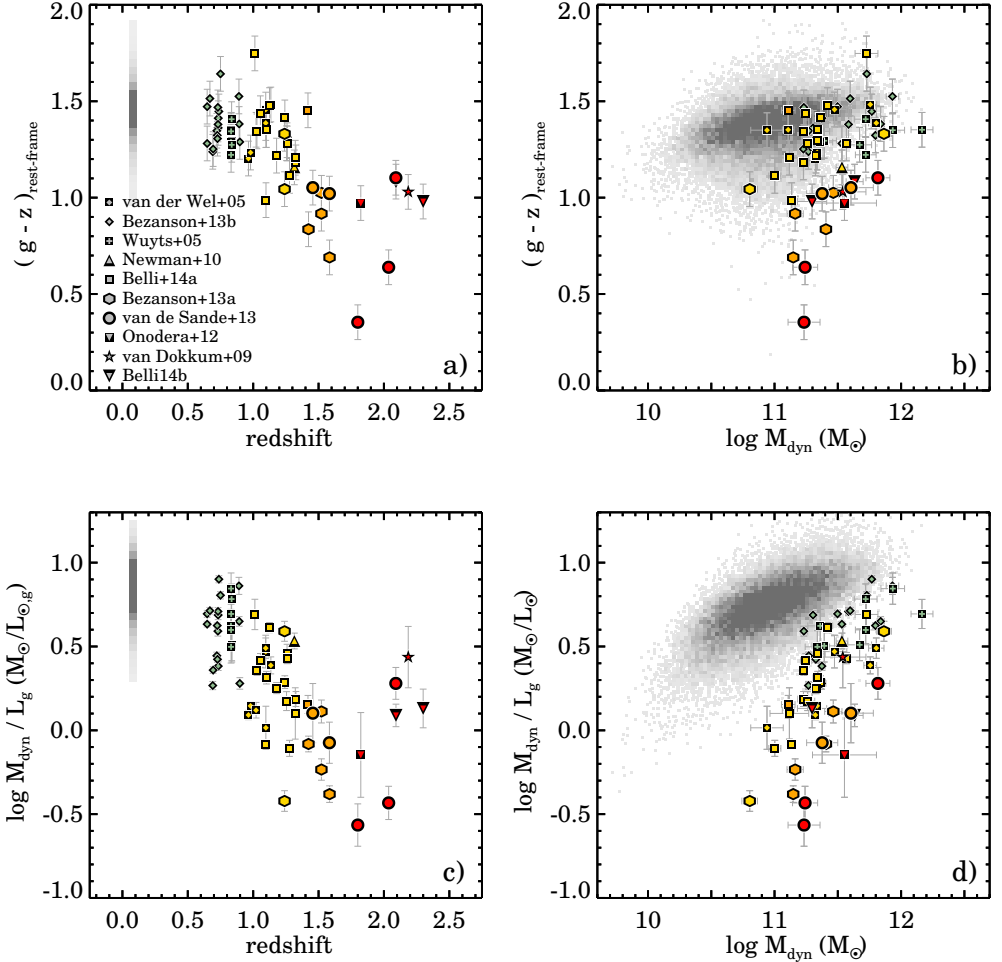


**Figure 5.2:** Panel (a): Rest-frame  $g - z$  color vs. redshift. For massive quiescent galaxies in the SDSS at  $z \sim 0.06$ , we show the median with  $1\sigma$  scatter as the gray squares. Different intermediate to high-redshift samples are indicated in the legend and described in Section 5.2. Galaxies are color coded by redshift, from low (blue) to high redshift (red). We find that the complete sample has a large range in colors. Panel (b): Rest-frame  $g - z$  color vs. dynamical mass. Panel (c):  $M_{\text{dyn}}/L_g$  in the rest-frame  $g$  band vs. redshift. We find that the complete sample has a large dynamic range with a factor of  $\sim 25$  in  $M_{\text{dyn}}/L_g$ . Panel (d):  $M_{\text{dyn}}/L_g$  vs. dynamical mass. Similar to Panel (b), we color code by redshift. From Panel (a) to (d) we conclude that, within the sample at fixed dynamical mass, the highest-redshift galaxies show the bluest colors with the lowest  $M/L$ .

We show  $(g - z)_{\text{rest-frame}}$  vs. the dynamical mass in Figure 5.2(b). We find a weak trend between dynamical mass and color for low-redshift galaxies. At  $z > 1.5$  the lowest mass galaxies have the bluest colors. Figure 5.2(d) shows the  $M_{\text{dyn}}/L_g$  vs. the dynamical mass. For galaxies in the SDSS, there is a positive correlation such that low mass galaxies also have lower  $M/L$  as compared to more massive galaxies. In the mass range of  $10^{11} < M_{\text{dyn}}/M_{\odot} < 10^{12}$ , the  $M_{\text{dyn}}/L_g$  increases by about  $\sim 0.2$  dex.

### 5.3.2 Empirical relation between the $M/L$ and the color

Next, we examine empirical relations between the  $M/L$  and color, as first predicted by Tinsley (1972; 1980). In Figure 5.3(a-d) we show the dynamical  $M/L$  vs. rest-frame  $g - z$  color in the following filters:  $u$ ,  $g$ ,  $z$ , and  $K$ . Figure 5.3(e) and (f) shows the rest-frame  $g - K$  colors vs. the  $M/L_g$  and  $M/L_K$ . Symbols are similar to Figure 5.2. Massive quiescent galaxies ( $> 10^{11} M_{\odot}$ ) from the SDSS are shown by the gray contour, which encloses 68% of all galaxies. We find that the  $\log_{10} M/L_u$  varies most, from  $\sim -0.7$  to  $\sim 1.1$ . The range in  $\log_{10} M/L$  slowly decreases with increasing wavelength from 1.8 dex in the  $u$  band, to 1.6 dex in the  $g$  band, and 1.3 dex in the  $z$  and  $K$  band.

As expected, we find a strong positive correlation between the  $M/L$  in all passbands and rest-frame colors. Following Bell & de Jong (2001), we fit the simple relation:

$$\log_{10} M_{\text{dyn}} / L_{\lambda} = a_{\lambda} * color + b_{\lambda} \quad (5.3)$$

We use the IDL routine *FITEXY* to measure  $a_{\lambda}$  and  $b_{\lambda}$ , which minimizes the  $\chi^2$  in the fit for both  $x$  (rest-frame color) and  $y$  ( $M/L$ ). In the fit we give equal weight to the SDSS galaxy sample and our sample of galaxies at intermediate to high redshift, instead of anchoring the fit to the median of the SDSS galaxies. In practice this means that we add 61 galaxies to the intermediate and high- $z$  sample, which have a  $M/L$  and color equal to the median of all SDSS galaxies. The results are summarized in Table 5.3 using the SDSS filters and in Table 5.4 where we use the Johnson-Cousin Filters.

Besides the coefficients, we also report the root-mean-square ( $\text{rms}_o$ ) scatter, which is a good indicator for the significance of each relation. The scatter around the linear relation increases from 0.12 to 0.16 when going from rest-frame optical  $M/L_u$  to rest-frame near-infrared  $M/L_K$ . Furthermore, we find that for the  $M_{\text{dyn}}/L_g$  the scatter is lower when we use the rest-frame  $g - z$  color as compared to the rest-frame  $g - K$  color.

For the color  $(g - z)_{\text{rest-frame}}$ , we find that the slope of the relation becomes flatter from the UV to the near-infrared. To investigate this trend in more detail, we plot the slope  $a_{\lambda}$  as a function of wavelength from the  $M/L_{\lambda}$  vs.  $(g - z)_{\text{rest-frame}}$  relation in Figure 5.4. We find that the slope becomes flatter when we go from the  $u$  to  $i$  waveband, while the slope is approximately constant ( $\sim 1.35$ ) from  $i$  to  $K$ .

These results indicate that the  $M/L$  of an early-type galaxy can be predicted by a single rest-frame color  $g - z$  to an accuracy of  $\sim 0.26$  dex. In particular the rest-frame  $g - z$  color in combination with the rest-frame  $g$  band luminosity, provides a good constrain for mass measurements of quiescent galaxies.

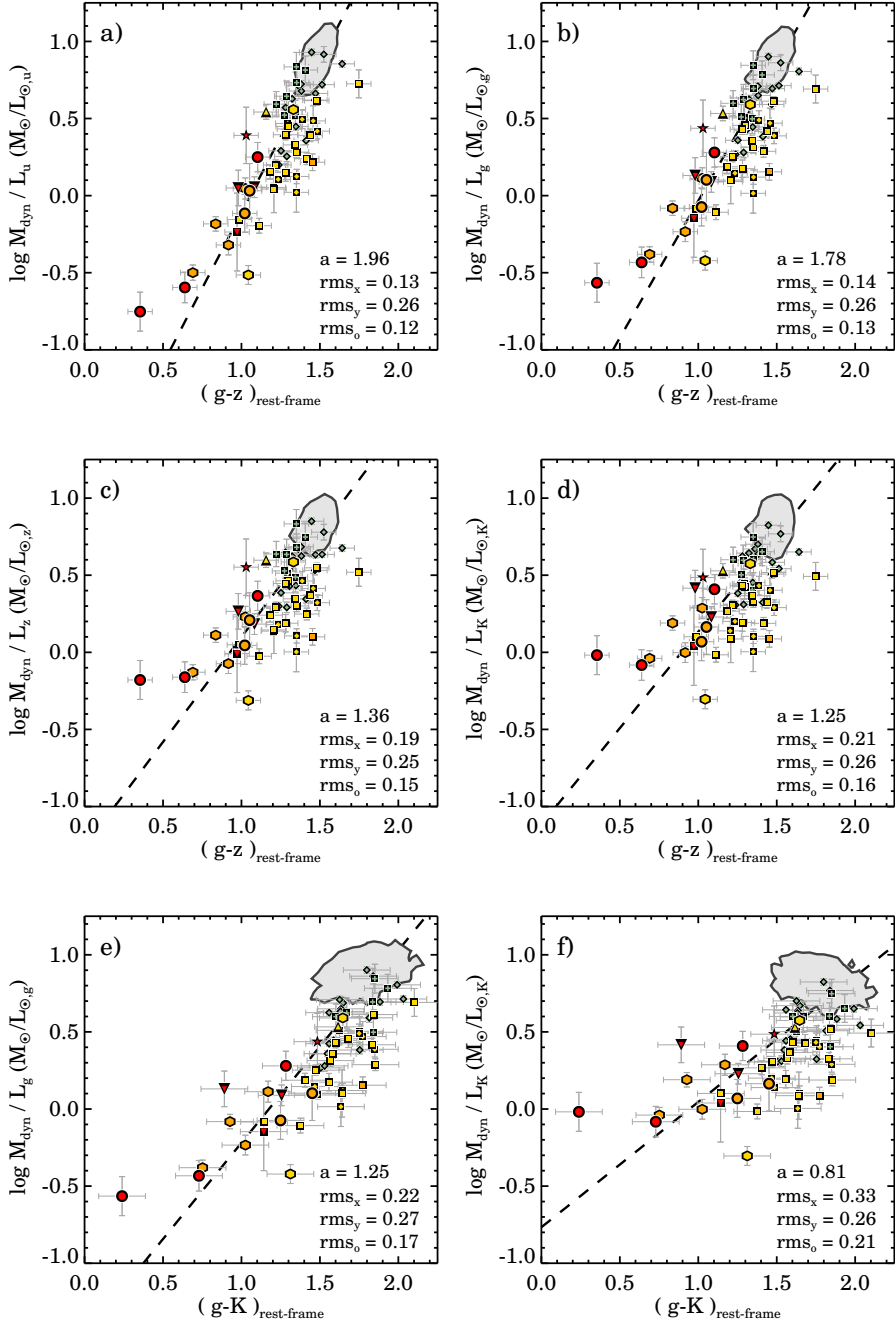


**Figure 5.3:**  $M/L$  vs. rest-frame color for massive galaxies between  $z = 0$  and  $z = 2$  for different luminosity bands and rest-frame colors. Symbols are similar as in Figure 5.1, and color coded by redshift. From the rest-frame  $u$  to the  $K$  band, there is a large range in the  $M/L$ : 1.8 dex in rest-frame  $M/L_u$ , 1.6 dex in  $M/L_g$ , and 1.3 dex in  $M/L_K$ . We find a strong correlation between the  $M/L$  for different luminosity bands and the rest-frame  $g - z$  color. The  $M_{\text{dyn}}/L_u$  vs.  $(g - z)_{\text{rest-frame}}$  show the least amount of scatter. We use a linear fit to the data to describe the relation between the  $M/L$  and rest-frame color, in which galaxies from the SDSS (gray contour) are given equal weight as the high-redshift data. The best-fit values are summarized in Table 5.3 & 5.4. For each fit we furthermore give the rms scatter orthogonal to the best-fitting line. Overall, the  $M_{\text{dyn}}/L_g$  vs.  $g - z$  color gives the least scatter ( $\text{rms}_o \sim 0.12$  dex), whereas the scatter is higher when we use the rest-frame  $g - K$  color ( $\text{rms}_o \sim 0.17$  dex).

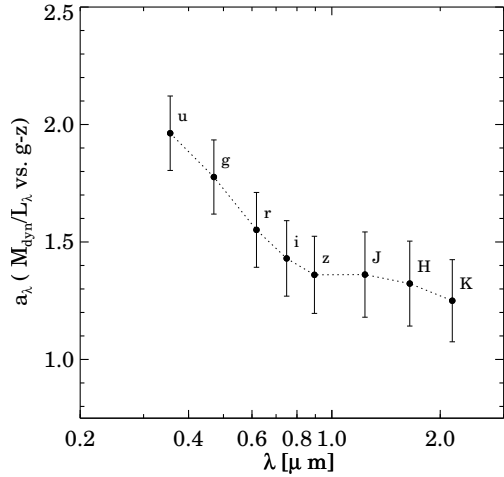


**Figure 5.4:** Slope  $a_\lambda$  from the  $M/L_\lambda$  vs.  $(g-z)_{\text{rest-frame}}$  relation vs. wavelength  $\lambda$ . For each luminosity band, we use the values from Table 5.3, and the errors are derived from bootstrapping the data. In the rest-frame  $u$  band, we find a steep slope of  $\sim 2.0$ . The slope  $a_\lambda$  decreases when we go from the  $u$  to  $i$  band. Redwards of the  $z$  band, we find that the relation between the  $M/L$  vs.  $g-z$  color is approximately  $\sim 1.3$ .

## 5.4 Comparisons with stellar population synthesis models

Here, we compare our dynamical  $M/L$  vs. rest-frame color to the predictions from stellar population synthesis models. Our main aim is to test whether the different SPS models can reproduce the relations in the optical and NIR and to what accuracy. For the comparison we use the SPS models by Bruzual & Charlot (2003; BC03), Maraston & Strömbäck (2011; Ma11), and Conroy & Gunn (2010) (FSPS, v2.4). We use the BC03 simple stellar population (SSP) models with the Padova stellar evolution tracks (Bertelli et al., 1994), and the STELIB stellar library (Le Borgne et al., 2003). For the Ma11 models, which are based on Maraston (2005; Ma05) with the Cassisi et al. (1997a), Cassisi et al. (1997b), and Cassisi et al. (2000) stellar evolution tracks and isochrones, we use SSPs with the red horizontal branch morphology and the MILES (Sánchez-Blázquez et al., 2006) stellar library. For the FSPS models, which use the latest Padova stellar evolution tracks (Marigo & Girardi 2007; Marigo et al. 2008), we use the standard program settings, and the MILES stellar library.

For all models we use a Salpeter (1955) IMF and a truncated SFH with a constant star formation rate for the first 0.5 Gyr. However, different SFHs result in nearly identical tracks. For example a longer star formation timescale will smooth out some of the small time-scale variations, but will not change any of our conclusions. For all models we use the total stellar mass, which is the sum of living stars and remnants. We note that our dynamical mass estimates include both stellar mass and dark matter mass. At this point we ignore the effect of dark matter, but we come back to this issue in section 5.6.5.

In Figure 5.5 we show the  $M_{\text{dyn}}/L_g$  vs.  $(g-z)_{\text{rest-frame}}$  (left column) and  $M_{\text{dyn}}/L_K$  vs.  $(g-K)_{\text{rest-frame}}$  (right column). A different model is shown in each row from top to bottom: FSPS, BC03, and Ma11. For each model, we show three different metallicities: solar (green), sub-solar (blue) and super-solar (red). Metallicity values for the specific models are indicated in each Panel. Furthermore, we indicate various model ages on the tracks with different symbols: 0.1 Gyr (upside down triangle), 1.0 Gyr (circle), 3.0 Gyr (diamond), 10 Gyr (triangle).

Table 5.3: Empirical relations for the  $M/L$  vs. rest-frame color using SDSS filters

color	$a_u$	$b_u$	rms <sub>u</sub>	$a_g$	$b_g$	rms <sub>g</sub>	$a_r$	$b_r$	rms <sub>r</sub>	$a_i$	$b_i$	rms <sub>i</sub>	$a_z$	$b_z$	rms <sub>z</sub>	$a_j$	$b_j$	rms <sub>j</sub>	$a_H$	$b_H$	rms <sub>H</sub>	$a_K$	$b_K$	rms <sub>K</sub>
$u-g$	4.70	-6.85	0.07	4.40	-6.37	0.08	3.96	-5.66	0.08	3.72	-5.28	0.09	3.62	-5.14	0.09	3.75	-5.38	0.09	3.67	-5.26	0.09	3.49	-4.95	0.10
$u-r$	1.98	-4.04	0.12	1.79	-3.59	0.13	1.56	-3.04	0.14	1.43	-2.75	0.15	1.37	-2.62	0.15	1.37	-2.64	0.16	1.33	-2.55	0.16	1.26	-2.36	0.16
$u-i$	1.49	-3.37	0.33	1.34	-2.96	0.31	1.16	-2.47	0.30	1.07	-2.22	0.30	1.01	-2.11	0.29	1.01	-2.11	0.29	0.98	-2.04	0.29	0.93	-1.88	0.28
$u-z$	1.30	-3.23	0.66	1.17	-2.83	0.62	1.01	-2.35	0.58	0.92	-2.10	0.57	0.88	-1.99	0.55	0.86	-1.98	0.54	0.84	-1.90	0.54	0.79	-1.76	0.53
$u-J$	1.17	-3.25	1.12	1.04	-2.82	1.05	0.89	-2.31	0.99	0.81	-2.05	0.96	0.76	-1.91	0.94	0.74	-1.86	0.92	0.71	-1.78	0.92	0.67	-1.63	0.91
$u-H$	1.10	-3.25	1.33	0.98	-2.82	1.26	0.84	-2.32	1.19	0.77	-2.06	1.15	0.72	-1.93	1.13	0.70	-1.87	1.11	0.68	-1.79	1.10	0.64	-1.64	1.09
$u-K$	1.02	-2.71	0.98	0.91	-2.34	0.93	0.78	-1.92	0.89	0.71	-1.70	0.86	0.67	-1.60	0.85	0.65	-1.56	0.84	0.63	-1.49	0.83	0.59	-1.34	0.82
$g-r$	3.85	-2.30	0.07	3.54	-2.08	0.08	3.20	-1.81	0.09	3.00	-1.66	0.09	2.91	-1.61	0.09	2.97	-1.68	0.10	2.90	-1.63	0.10	2.77	-1.51	0.10
$g-i$	2.40	-1.98	0.10	2.18	-1.74	0.11	1.93	-1.45	0.12	1.78	-1.30	0.13	1.71	-1.25	0.13	1.72	-1.28	0.14	1.67	-1.24	0.14	1.58	-1.12	0.14
$g-z$	1.96	-2.07	0.12	1.78	-1.81	0.13	1.55	-1.49	0.14	1.43	-1.33	0.14	1.36	-1.26	0.15	1.36	-1.28	0.16	1.32	-1.24	0.16	1.25	-1.12	0.16
$g-J$	1.73	-2.36	0.15	1.55	-2.04	0.16	1.32	-1.65	0.17	1.20	-1.44	0.18	1.13	-1.35	0.18	1.11	-1.33	0.19	1.07	-1.27	0.19	1.00	-1.13	0.20
$g-H$	1.60	-2.43	0.16	1.43	-2.10	0.16	1.22	-1.70	0.17	1.11	-1.49	0.18	1.05	-1.39	0.18	1.02	-1.37	0.20	0.98	-1.30	0.20	0.93	-1.17	0.17
$g-K$	1.40	-1.72	0.16	1.25	-1.47	0.17	1.07	-1.17	0.18	0.98	-1.01	0.18	0.93	-0.95	0.19	0.91	-0.93	0.20	0.87	-0.89	0.20	0.81	-0.77	0.21
$r-i$	7.37	-1.75	0.04	6.87	-1.58	0.04	6.32	-1.40	0.05	6.06	-1.31	0.05	5.94	-1.30	0.05	6.12	-1.38	0.05	5.98	-1.34	0.05	5.79	-1.26	0.05
$r-z$	4.67	-2.22	0.06	4.32	-2.00	0.07	3.91	-1.74	0.07	3.70	-1.61	0.08	3.62	-1.59	0.08	3.75	-1.69	0.09	3.67	-1.64	0.09	3.51	-1.53	0.09
$r-J$	4.03	-3.24	0.12	3.66	-2.87	0.12	3.20	-2.42	0.13	2.93	-2.17	0.13	2.83	-2.10	0.13	3.01	-2.29	0.14	2.90	-2.19	0.14	2.69	-1.97	0.14
$r-H$	3.25	-3.10	0.12	2.93	-2.72	0.13	2.53	-2.26	0.13	2.31	-2.01	0.14	2.20	-1.91	0.14	2.26	-2.00	0.15	2.18	-1.91	0.15	2.02	-1.71	0.16
$r-K$	2.46	-1.62	0.14	2.20	-1.38	0.14	1.90	-1.09	0.15	1.73	-0.94	0.15	1.64	-0.89	0.16	1.64	-0.91	0.17	1.58	-0.86	0.17	1.46	-0.73	0.17

Table 5.4: Empirical relations for the  $M/L$  vs. rest-frame color using Johnson-Cousin filters

color	$a_U$	$b_U$	rms <sub>U</sub>	$a_B$	$b_B$	rms <sub>B</sub>	$a_V$	$b_V$	rms <sub>V</sub>	$a_R$	$b_R$	rms <sub>R</sub>	$a_I$	$b_I$	rms <sub>I</sub>	$a_J$	$b_J$	rms <sub>J</sub>	$a_H$	$b_H$	rms <sub>H</sub>	$a_K$	$b_K$	rms <sub>K</sub>
$U-B$	4.70	-6.85	0.07	4.40	-6.37	0.08	3.96	-5.66	0.08	3.72	-5.28	0.09	3.62	-5.14	0.09	3.75	-5.38	0.09	3.67	-5.26	0.09	3.49	-4.95	0.10
$U-V$	1.98	-4.04	0.12	1.79	-3.59	0.13	1.56	-3.04	0.14	1.43	-2.75	0.15	1.37	-2.62	0.15	1.37	-2.64	0.16	1.33	-2.55	0.16	1.26	-2.36	0.16
$U-R$	1.49	-3.37	0.33	1.34	-2.96	0.31	1.16	-2.47	0.30	1.07	-2.22	0.30	1.01	-2.11	0.29	1.01	-2.11	0.29	0.98	-2.04	0.29	0.93	-1.88	0.28
$U-I$	1.30	-3.23	0.66	1.17	-2.83	0.62	1.01	-2.35	0.58	0.92	-2.10	0.57	0.88	-1.99	0.55	0.86	-1.98	0.54	0.84	-1.90	0.54	0.79	-1.76	0.53
$U-J$	1.17	-3.25	1.12	1.04	-2.82	1.05	0.89	-2.31	0.99	0.81	-2.05	0.96	0.76	-1.91	0.94	0.74	-1.86	0.92	0.71	-1.78	0.92	0.67	-1.63	0.91
$U-H$	1.10	-3.25	1.33	0.98	-2.82	1.26	0.84	-2.32	1.19	0.77	-2.06	1.15	0.72	-1.93	1.13	0.70	-1.87	1.11	0.68	-1.79	1.10	0.64	-1.64	1.09
$U-K$	1.02	-2.71	0.98	0.91	-2.34	0.93	0.78	-1.92	0.89	0.71	-1.70	0.86	0.67	-1.60	0.85	0.65	-1.56	0.84	0.63	-1.49	0.83	0.59	-1.34	0.82
$B-V$	3.85	-2.32	0.07	3.54	-2.08	0.08	3.20	-1.81	0.09	3.00	-1.66	0.09	2.91	-1.61	0.09	2.97	-1.68	0.10	2.90	-1.63	0.10	2.77	-1.51	0.10
$B-R$	2.40	-1.98	0.10	2.18	-1.74	0.11	1.93	-1.45	0.12	1.78	-1.30	0.13	1.71	-1.25	0.13	1.72	-1.28	0.14	1.67	-1.24	0.14	1.58	-1.12	0.14
$B-I$	1.96	-2.07	0.12	1.78	-1.81	0.13	1.55	-1.49	0.14	1.43	-1.33	0.14	1.36	-1.26	0.15	1.36	-1.28	0.16	1.32	-1.24	0.16	1.25	-1.12	0.16
$B-J$	1.73	-2.36	0.15	1.55	-2.04	0.16	1.32	-1.65	0.17	1.20	-1.44	0.18	1.13	-1.35	0.18	1.11	-1.33	0.19	1.07	-1.27	0.19	1.00	-1.13	0.20
$B-H$	1.60	-2.43	0.16	1.43	-2.10	0.16	1.22	-1.70	0.17	1.11	-1.49	0.18	1.05	-1.39	0.18	1.02	-1.37	0.20	0.98	-1.30	0.20	0.93	-1.17	0.17
$B-K$	1.40	-1.72	0.16	1.25	-1.47	0.17	1.07	-1.17	0.18	0.98	-1.01	0.18	0.93	-0.95	0.19	0.91	-0.93	0.20	0.87	-0.89	0.20	0.81	-0.77	0.21
$V-I$	7.37	-1.75	0.04	6.87	-1.58	0.04	6.32	-1.40	0.05	6.06	-1.31	0.05	5.94	-1.30	0.05	6.12	-1.38	0.05	5.98	-1.34	0.05	5.79	-1.26	0.05
$V-J$	4.67	-2.22	0.06	4.32	-2.00	0.07	3.91	-1.74	0.07	3.70	-1.61	0.08	3.62	-1.59	0.08	3.75	-1.69	0.09	3.67	-1.64	0.09	3.51	-1.53	0.09
$V-H$	4.03	-3.24	0.12	3.66	-2.87	0.12	3.20	-2.42	0.13	2.93	-2.17	0.13	2.83	-2.10	0.13	3.01	-2.29	0.14	2.90	-2.19	0.14	2.69	-1.97	0.14
$V-K$	3.25	-3.10	0.12	2.93	-2.72	0.13	2.53	-2.26	0.13	2.31	-2.01	0.14	2.20	-1.91	0.14	2.26	-2.00	0.15	2.18	-1.91	0.15	2.02	-1.71	0.16
$V-K$	2.46	-1.62	0.14	2.20	-1.38	0.14	1.90	-1.09	0.15	1.73	-0.94	0.15	1.64	-0.89	0.16	1.64	-0.91	0.17	1.58	-0.86	0.17	1.46	-0.73	0.17

We indicate the effect of dust with the black arrow, assuming a Calzetti et al. (2000) dust law and  $A_V = 0.5$ . For the  $M_{\text{dyn}}/L_g$  vs. rest-frame  $g - z$  color, we find that the dust vector runs parallel to the model. Dust has, however, almost no effect on the rest-frame  $K$  band luminosity and therefore runs nearly horizontal.

To quantify how well the models match the data, we calculate the scatter orthogonal to the model tracks ( $\text{rms}_o$ ). For the three models with different metallicities this scatter is given in Table 5.5.

Table 5.5: Scatter around SPS models with different metallicities

SPS Model	$M/L$	color	Sub-Solar	Solar	Super-Solar
FSPS	$M/L_g$	$g - z$	0.32	0.14	0.15
	$M/L_K$	$g - K$	0.78	0.21	0.18
BC03	$M/L_g$	$g - z$	0.24	0.15	0.14
	$M/L_K$	$g - K$	0.73	0.28	0.20
Ma11	$M/L_g$	$g - z$	0.16	0.11	0.17
	$M/L_K$	$g - K$	0.34	0.33	0.19

#### 5.4.1 FSPS models

In Figure 5.5(a) we show the  $M_{\text{dyn}}/L_g$  vs.  $(g - z)_{\text{rest-frame}}$  color in combination with the FSPS models. The difference between the solar ( $Z = 0.02$ ) and super-solar ( $Z = 0.03$ ) tracks is small, whereas the sub-solar model is at all times too blue at fixed  $M/L$ . Both models with solar and super-solar match the  $M_{\text{dyn}}/L_g$  and  $(g - z)_{\text{rest-frame}}$  color for low-redshift galaxies ( $z < 1$ ), but are unable to reproduce the low  $M_{\text{dyn}}/L_g$  for the bluest galaxies with  $(g - z)_{\text{rest-frame}} < 1$ . It is interesting to note that the scatter around the Solar metallicity model (0.14, Table 5.5) is about similar to the scatter when assuming the linear fit (0.12, Figure 5.3(b)).

In Figure 5.5(b) we show the  $M_{\text{dyn}}/L_K$  vs. the  $(g - K)_{\text{rest-frame}}$  color. The FSPS model tracks show a clear transition from a constant  $M_{\text{dyn}}/L_K$  for  $(g - K)_{\text{rest-frame}} < 1.75$ , to a very steep relation at  $(g - K)_{\text{rest-frame}} > 1.75$ . The color difference between the solar ( $Z = 0.02$ ) and sub-solar ( $Z = 0.003$ ) tracks is large ( $\Delta(g - z)_{\text{rest-frame}} \sim 0.8$ ) and more distinct as compared to the rest-frame  $g - z$  color. The difference between solar and super-solar metallicity tracks is small for the FSPS models, especially when compared to other models. The scatter for the Super-Solar metallicity model (0.18) is similar to the scatter for the linear fit (0.20, Figure 5.3(f)), even though the FSPS model track is far from linear.

As in Figure 5.5(a), we find that both solar and super-solar tracks are able to match the low-redshift galaxies ( $z < 1$ ), but cannot simultaneously match the bluest galaxies with  $(g - K)_{\text{rest-frame}} < 1.5$  colors, for which the model  $M/L$  is too high.

#### 5.4.2 BC03 models

For the BC03 models, the solar-metallicity track matches the low-redshift galaxies well for the rest-frame optical colors (Figure 5.5(c)), but the  $M/L$  of the bluest galaxies is still over-estimated by  $\sim 0.2$  dex. The difference between the solar and super-solar metallicity tracks is larger than for the FSPS models, but this is mainly due to the fact that the BC03 super-solar metallicity ( $Z = 0.05$ ) track is significantly higher than the FSPS models ( $Z = 0.03$ ). For low-redshift galaxies in the SDSS, the super-solar ( $Z = 0.05$ ) model predicts a  $M/L$  that is too low by  $\sim 0.3$  dex, while the scatter for the  $z > 0.5$  data with the super-solar model (0.14)

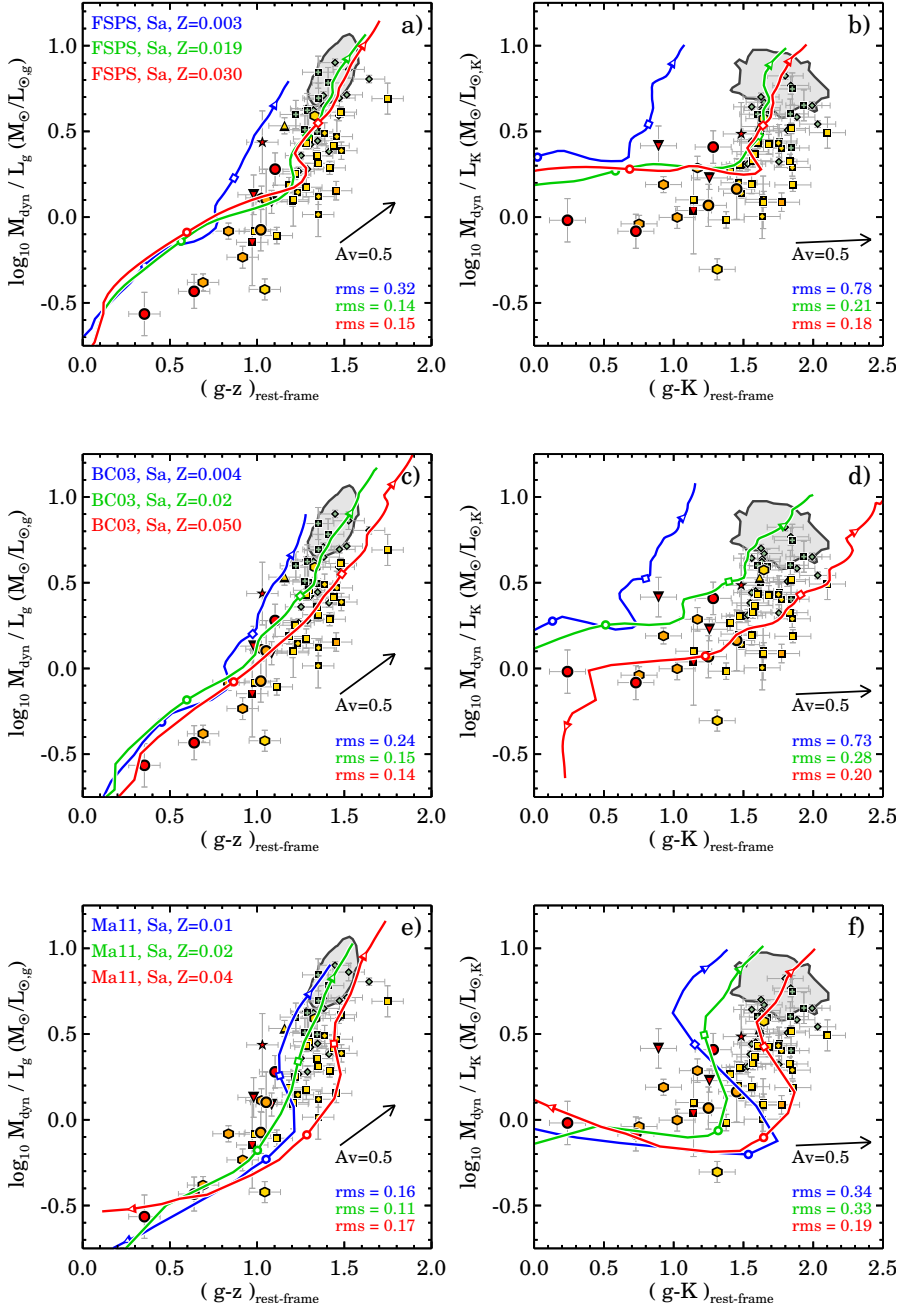


**Figure 5.5:**  $M/L$  vs. rest-frame color for the spectroscopic samples compared to the following SPS models: FSPS (top row), BC03 (middle row), and Ma11 (bottom row). The left column shows the  $M_{\text{dyn}}/L_g$  vs.  $(g-z)_{\text{rest-frame}}$ , while the right column shows the  $M_{\text{dyn}}/L_K$  vs.  $(g-K)_{\text{rest-frame}}$ . For each model we show three different metallicities: solar metallicity ( $Z = 0.02$ , green), sub-solar metallicity (blue) and super-solar (red), and we indicate various model ages on the tracks with different symbols: 0.1 Gyr (upside down triangle), 1.0 Gyr (circle), 3.0 Gyr (diamond), 10 Gyr (triangle). The effect of dust is indicated by the black arrow. We find that none of the models are able to match both the rest-frame optical color and the rest-frame infrared color in combination with the  $M/L$  simultaneously.



is almost the same as the scatter for the solar model (0.15). The sub-solar ( $Z=0.004$ ) model shows colors that are too blue at fixed  $M_{\text{dyn}}/L_g$  at all times.

In Figure 5.5(d), there is a larger color separation between the three metallicity tracks as compared to Figure 5.5(c). At fixed age the color difference in rest-frame  $g - K$  is approximately twice as large as the color difference in the rest-frame  $g - z$  color, indicating that the first color provides a better constraint for metallicity (see also Bell & de Jong 2001). Interestingly, the slope of the BC03 models remain almost linear for the rest-frame  $g - K$  color, in contrast with the other two models. Neither solar nor super-solar tracks provide a good match to all the data, but the super-solar metallicity track has significantly lower scatter than the solar metallicity (super-solar=0.20 vs. solar = 0.28). While the solar metallicity model is unable to reproduce the low  $M/L$  of the bluest galaxies, the super-solar metallicity model is unable to reproduce the color and the  $M/L$  for SDSS galaxies.

### 5.4.3 Ma11 models

The Ma11 models are systematically different than the other models (Figure 5.5(e) and (f)). The Ma11 models exhibit an "S-shaped" relation between the  $M/L$  and rest-frame color, in particular for the  $g - K$  colors. The trend in the Ma11 models is such that for blue colors there is a small increase in the  $M/L$ , whereas there is a steep nearly vertical upturn in the  $M/L$  at late ages. It is interesting to note that the Ma11 solar metallicity track is able to match the  $M/L$  and rest-frame  $g - z$  color of all galaxies. Furthermore, the Ma11 model shows the lowest scatter as compared to the other models: rms = 0.11.

However, for the  $(g - K)_{\text{rest-frame}}$  color the sub-solar and solar metallicity tracks provide a poor match (Figure 5.5(f)). The  $Z = 0.02$  model has a sharp increase in the  $M/L$  around  $(g - K)_{\text{rest-frame}} \sim 1.4$ , after which it is too blue by  $\sim 0.5$  mag compared to the data. The super-solar metallicity model is able to match all galaxies at  $z < 1$ , but around 1 Gyr the  $M/L$  is too low by  $\sim 0.2$  dex.

### 5.4.4 Summary

All the models reproduce the general observed trend in  $M/L$  vs. rest-frame color. Even though certain models with specific metallicity tracks match one  $M/L$  vs. color, none of the models are able to simultaneously match the data in both the rest-frame  $g - z$  vs.  $M_{\text{dyn}}/L_g$  and  $g - K$  vs.  $M_{\text{dyn}}/L_K$ . In particular for FSPS and BC03, the models are unable to match the low  $M/L$  for the bluest galaxies in combination with the rest of the data. For the  $(g - z)_{\text{rest-frame}}$  color, the Ma11 models are able to predict the low  $M/L$  for the bluest galaxies at the same time as the  $M/L$  for galaxies in the SDSS, with lower rms scatter as compared to the other models. We furthermore find that the SPS models exhibit different relations between the  $M/L$  and rest-frame color, most prominently visible in the rest-frame  $g - K$  color. The cause for the discrepancies between the models and the data, but also among the different models, can be due to several factors as there are a number of systematic differences in the SPS models. It is beyond the scope of this Chapter to address these differences, but we refer the reader to Conroy & Gunn (2010) for a recent comparison of several popular models.

## 5.5 Constraints on the IMF

In the previous Section we found that the models reproduce the general observed trend, but cannot match all the data. Adapting a different IMF could provide a solution to this problem. The IMF influences the evolution and scaling of the  $M/L$ , while it has a smaller effect on the color evolution (Tinsley 1972; 1980). Generally speaking, a bottom-heavy IMF ( $\alpha > 2.35$ ) will give a flatter  $M/L$  vs. color relation as compared to a bottom-light IMF ( $\alpha < 2.35$ ). In this Section, we explore the effect of the IMF on the different SPS models in the  $M/L$  vs. color plane.

### 5.5.1 IMF comparison

We show the FSPS (top row) and BC03 (bottom row) models with four different realizations of the IMF in Figure 5.6. We do not further explore the Ma11 models, because these models with different IMFs were not available to us. In this section we use solar metallicity models (FSPS  $Z = 0.0198$ ; BC03  $Z = 0.02$ ), and a truncated SFH with a constant star formation rate for the first 0.5 Gyr. The Salpeter IMF with slope  $\alpha = 2.35$  is shown in blue and was the assumed IMF in Figure 5.5. A bottom-light IMF with slope  $\alpha = 1.35$  is shown in green, the bottom-heavy  $\alpha = 3.35$  IMF in red, and the Chabrier IMF in pink.

In Figure 5.6(a) we find that the FSPS model with the bottom-heavy IMF ( $\alpha = 3.35$ ) has a  $M/L$  that is always too high and does not match any of the data. The steepest  $M/L$  vs. color relation is predicted by the bottom-light IMF ( $\alpha = 1.35$ ). For the Salpeter and the bottom-light IMF we measure a similar rms scatter (0.14-0.15), but both IMFs have a  $M/L$  that is on average too high by  $\sim 0.1 - 0.2$  dex. The Chabrier IMF has a very similar behavior in the  $M/L$  vs. color plane as the Salpeter IMF, but with a lower  $M/L$  by about  $\sim 0.2$  dex. For the bluest galaxies the Chabrier IMF reproduces the low  $M/L$ , but the  $M/L$  is too low by 0.2 dex for galaxies in the SDSS. Out of all four realizations of the IMF that we show in Figure 5.6(a), we measure the least scatter for the Chabrier IMF (0.12 dex).

For the  $M_{\text{dyn}}/L_K$  vs.  $(g - K)_{\text{rest-frame}}$  (Figure 5.6(b)), we find similar differences between the IMFs as for the  $M_{\text{dyn}}/L_K$  vs.  $(g - z)_{\text{rest-frame}}$  (Figure 5.6(a)). The bottom-heavy IMF ( $\alpha = 3.35$ ) overpredicts the  $M/L$  by more than a dex and does not match any of the data. Compared to the Salpeter IMF, we find that the bottom-light IMF has a steeper  $M/L$  vs. color relation, with a steep vertical upturn around 3 Gyr. Interestingly, the Chabrier IMF is able to match all data with very little scatter (0.15 dex).

In Figure 5.6(c), we show the BC03 models with the four different realizations of the IMF. Again, the bottom-heavy IMF does not match any of the data. The bottom-light and Chabrier IMF both provide an excellent match to the intermediate and high-redshift data with the least rms scatter (0.11 dex). However, the Chabrier IMF again predicts a  $M/L$  that is slightly too low for the SDSS sample.

The bottom-light IMF which gave a perfect match for the  $M_{\text{dyn}}/L_g$  vs.  $(g - z)_{\text{rest-frame}}$ , however, does not provide a good match for the intermediate galaxies in the  $M_{\text{dyn}}/L_K$  vs. rest-frame  $g - K$  color plane (Figure 5.6(d)). At  $(g - K)_{\text{rest-frame}} > 1.4$  the  $M/L$  of the bottom-light IMF is on average too high by  $\sim 0.2$  dex. The bottom-light IMF still provides a better prediction than the Salpeter IMF with a respective rms of 0.20 vs. 0.29. Again, we

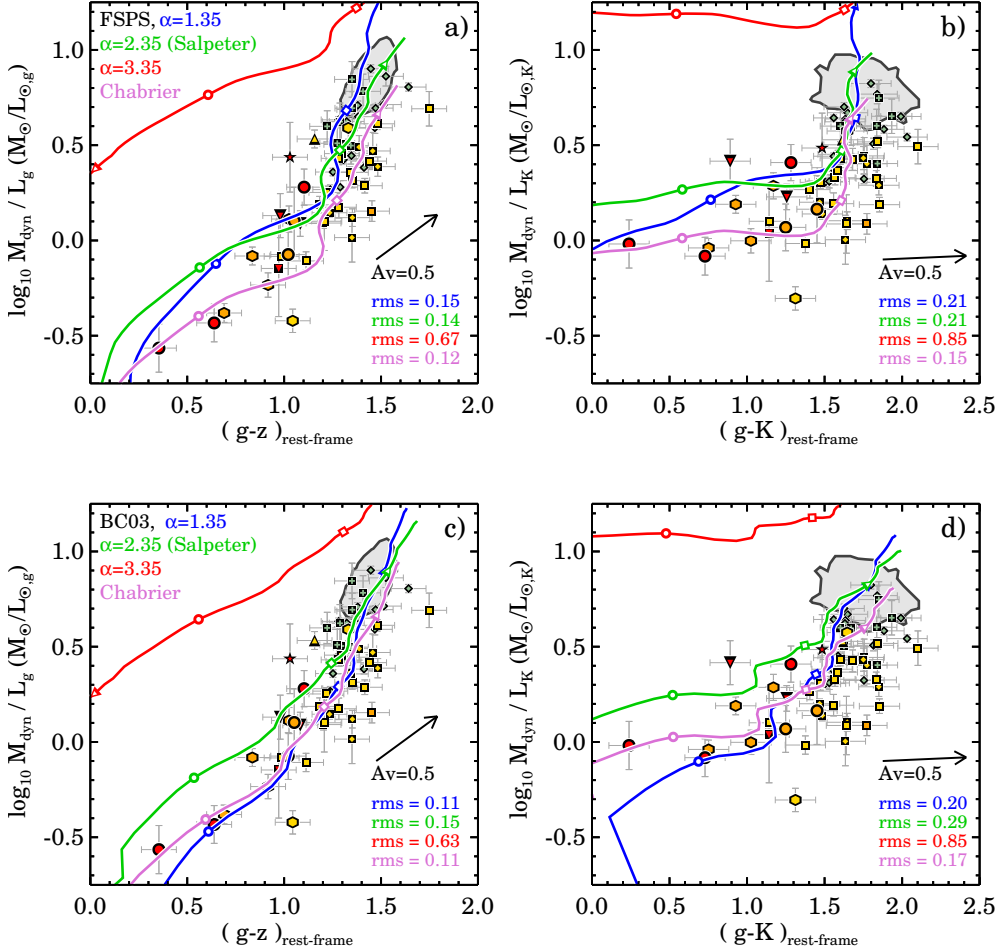


**Figure 5.6:**  $M/L$  vs. rest-frame color: comparing IMFs with different slopes. We use FSPS (top row) and BC03 (bottom row) models with solar metallicity ( $Z = 0.02$ ). The IMF is defined as a single power-law with slope  $\alpha$ . Different curves are IMFs with different realizations of  $\alpha$ . While the FSPS do not favor an IMF with  $\alpha = 1.35$  (green) over  $\alpha = 2.35$ , the BC03 has less scatter for the IMF with  $\alpha = 1.35$  as compared to  $\alpha = 2.35$ . Whereas a Chabrier IMF is able to reproduce the low  $M/L$  for the bluest galaxies, it does not match the  $M/L$  of low redshift SDSS galaxies in Panel (a) and (c). It does show an excellent match to the data in Panel (b) and (d) with very little scatter.

find that the Chabrier IMF best matches all the data based on the rms scatter (0.17), but does not provide a perfect match either.

Overall, we find that the BC03 model favors an IMF with a slope of  $\alpha = 1.35$  over an IMF with  $\alpha = 2.35$ , while for the FSPS models we find no statistical preference for one of the two. We get an excellent match to the data with the FSPS model when using a Chabrier IMF for the rest-frame  $g - K$  color, but for the rest-frame  $g - z$  color this IMF underpredicts the  $M/L$  for galaxies in the SDSS.

As we still have not identified a model that can simultaneously match the  $M/L$  vs.  $(g - z)_{\text{rest-frame}}$  and  $(g - K)_{\text{rest-frame}}$  colors, we explore a more exotic IMF in the next Section.

Table 5.6: Scatter around SPS models with different realizations of the IMF

SPS Model	$M/L$	color	x=1.35	x=2.35	x=3.35	Chabrier
FSPS	$M/L_g$	$g - z$	0.15	0.14	0.67	0.12
	$M/L_K$	$g - K$	0.21	0.21	0.85	0.15
BC03	$M/L_g$	$g - z$	0.11	0.15	0.63	0.11
	$M/L_K$	$g - K$	0.20	0.29	0.85	0.17

## 5.5.2 Broken IMF

As the  $M/L$  vs. color relation is mostly sensitive to the IMF around the main sequence turnoff-point of stars in the HR-diagram, we experiment with a broken IMF, in which we only vary the slope between  $1M_{\odot}$  and  $4M_{\odot}$ :

$$\frac{dN}{dM} \propto M^{-2.35} \quad \text{for, } [0.08 < M_*/M_{\odot} < 1] \quad (5.4)$$

$$\frac{dN}{dM} \propto M^{-\alpha} \quad \text{for, } [1 < M_*/M_{\odot} < 4] \quad (5.5)$$

$$\frac{dN}{dM} \propto M^{-2.35} \quad \text{for, } [4 < M_*/M_{\odot} < 100] \quad (5.6)$$

One advantage of this approach is that different realizations of the IMF will cause the SPS tracks to naturally intersect at late ages when most of the integrated light will come from low-mass stars with  $M_* < 1M_{\odot}$ .

Figure 5.7 shows the three different realizations of the IMF using Equation 5.5:  $\alpha = 1.35$  (green),  $\alpha = 2.35$  (blue, normal Salpeter), and  $\alpha = 3.35$  (red). As before, we use solar metallicity models (FSPS  $Z = 0.0198$ ; BC03  $Z = 0.02$ ), and a truncated SFH with a constant star formation rate for the first 0.5 Gyr.

As expected, in Figure 5.7(a) we find that the different tracks now all match the oldest  $z \sim 0$  SDSS galaxies. This Figure also clearly shows that the  $M/L$  vs. color relation becomes increasingly steep with decreasing slope of the IMF. We find that the FSPS model with  $\alpha = 1.35$  IMF is able to reproduce the low  $M/L$  for the bluest galaxies and matches all the other data as well, with very little scatter (rms=0.11). Furthermore, the broken IMF with  $\alpha = 1.35$  provides a better match to the data than the IMF with slope  $\alpha = 2.35$ . The bottom-heavy IMF matches the highest  $M/L$  galaxies, but for all galaxies bluer than  $(g - z)_{\text{rest-frame}} < 1.2$  the model  $M/L$  is still too high. Most interestingly, in Figure 5.7(b) the FSPS model with  $\alpha = 1.35$  IMF matches all the data for the  $M_{\text{dyn}}/L_K$  vs.  $(g - K)_{\text{rest-frame}}$  with very little scatter (rms=0.15).

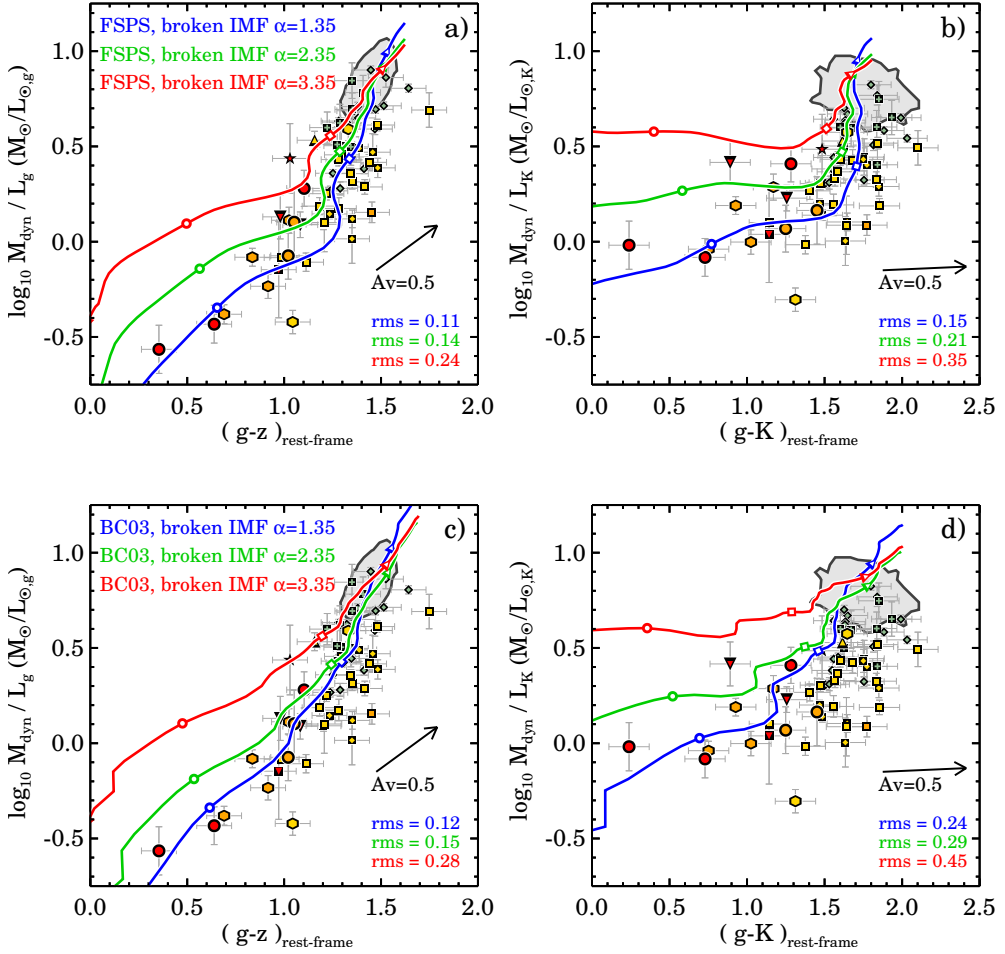
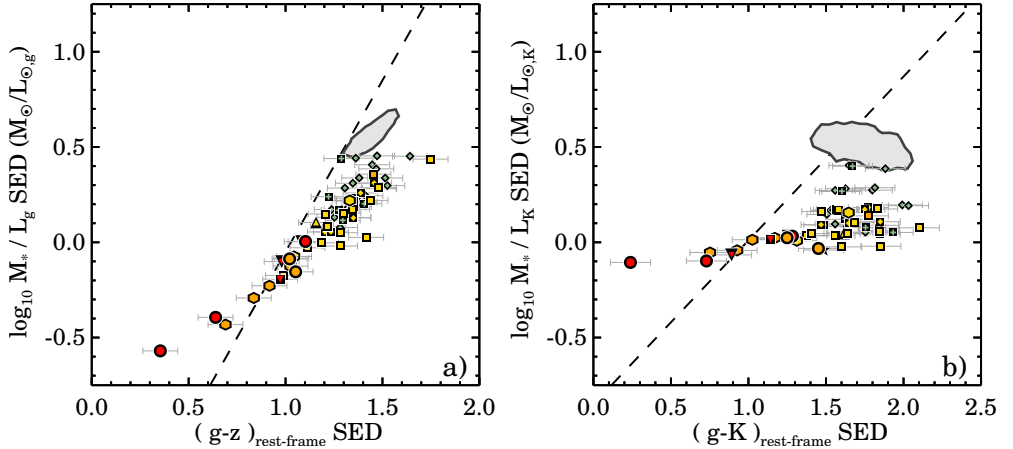


Figure 5.7:  $M/L$  ratio vs. rest-frame color for an IMF with different slopes between  $1$  and  $4 M_{\odot}$ . Below  $1 M_{\odot}$  and above  $4 M_{\odot}$ , this IMF has a Salpeter slope, as defined according to Equation 5.5. We use FSPS (top row) and BC03 (bottom row) models with solar metallicity ( $Z = 0.02$ ). Based on the rms scatter, the models favor an IMF with a slope of  $\alpha = 1.35$  over  $\alpha = 2.35$ . The FSPS model with a broken IMF of  $\alpha = 1.35$  is able to reproduce both the  $M/L$  vs.  $g - z$  and  $g - K$  rest-frame color.



**Figure 5.8:**  $M_*/L_g$  vs. rest-frame  $g - z$ . Here the  $M/L$  ratios have been determined by fitting solar metallicity BC03 models to the full broad-band data. a) The galaxies lie along a tight sequence, but the relation is shallower as compared to the best-fit dynamical relation (dashed-line) from Section 5.3.2. b) the SED derived  $M_*/L_K$  show a rather complex trend with  $(g - K)_{\text{rest-frame}}$  color similar to the trends for the FSPS and Ma11 models.

In Figure 5.7(c) we show the BC03 models with different realizations of the broken IMF. The broken IMF with  $\alpha = 1.35$  matches all the data from  $z \sim 2$  to  $z \sim 0$ . However, for the  $M_{\text{dyn}}/L_K$  vs.  $(g - K)_{\text{rest-frame}}$  color this IMF over-predicts the  $M/L$  by  $\sim 0.2$  dex (Figure 5.7(d)). Therefore, based on the rms scatter, we conclude that both the FSPS and BC03 models

favor a slope of the broken IMF of  $\alpha = 1.35$  over  $\alpha = 2.35$ . We note that the FSPS model with a broken IMF of  $\alpha = 1.35$  is the only model that can reproduce both the  $M/L$  vs.  $g - z$  and  $g - K$  rest-frame color.

**Table 5.7:** Scatter around SPS models with different realizations of the broken IMF

SPS Model	$M/L$	color	$x=1.35$	$x=2.35$	$x=3.35$
FSPS	$M/L_g$	$g - z$	0.11	0.14	0.24
	$M/L_K$	$g - K$	0.15	0.21	0.35
BC03	$M/L_g$	$g - z$	0.12	0.15	0.28
	$M/L_K$	$g - K$	0.24	0.29	0.45

## 5.6 Discussion and comparison to previous studies

### 5.6.1 SED derived $M/L$

To investigate the implication of the results, we first compare our relation of  $M_{\text{dyn}}/L$  vs. rest-frame color to the relation of  $(M_*/L)_{\text{SED}}$  vs. rest-frame color. The  $(M_*/L)_{\text{SED}}$  has been determined by fitting solar metallicity BC03 models to the full photometric broad-band dataset (see Section 5.2.2). We show the results for our sample in Figure 5.8. In Figure 5.8a we compare the  $(M_*/L_g)_{\text{SED}}$  vs. rest-frame  $g - z$  color with our best-fit dynamical relation from

Section 5.3.2 (dashed line). As expected, the galaxies lie along a tight sequence. We note, however, that the best-fit dynamical relation is steeper. This difference in the steepness of the relation is consistent with the fact that the BC03 model tracks do not quite track the trends of Figure 5.5(c). Figure 5.8b shows the  $(M_*/L_K)_{\text{SED}}$  vs.  $(g - K)_{\text{rest-frame}}$ . The derived  $(M_*/L_K)_{\text{SED}}$  show a rather complex trend with  $(g - K)_{\text{rest-frame}}$  color. This complex trend is similar to the trends for the FSPS (Figure 5.5(b)) and Ma11 (Figure 5.5(f)) SPS models.

The mismatch between the  $(M_*/L_g)_{\text{SED}}$  (using the BC03 models) and the  $M_{\text{dyn}}/L_g$  is highlighted in Figure 5.9, where we compare the two estimates directly. In the case that the dynamical  $M/L$  corresponds well to the SED based  $M/L$ , we expect to see a one-to-one linear relation (dashed line) with potentially a constant offset due to dark matter or low-mass stars. However, Figure 5.9 shows a relation that has a shallower slope than the dashed-line, such that galaxies with a lower  $M/L$  are further offset from the one-to-one relation. This non-constant offset is similar to the results by van de Sande et al. (2013), in which we showed that  $M_*/M_{\text{dyn}}$  changes slightly as a function of redshift, where the  $z \sim 2$  galaxies had the highest  $M_*/M_{\text{dyn}}$ . However, as redshift, color, and  $M_{\text{dyn}}/L$  are correlated in our sample (see Figure 5.2(a) and (c)), the  $M_*/M_{\text{dyn}}$  trend with redshift could also be caused by the non-constant offset in  $(M_*/L_g)_{\text{SED}}$  vs.  $M_{\text{dyn}}/L_g$ . Without additional information (e.g., high signal-to-noise spectroscopy) it is hard to establish whether the trend is driven by galaxy structure evolution/dark matter fraction evolution, IMF variations (Section 5.5), or discrepancies in SPS models.

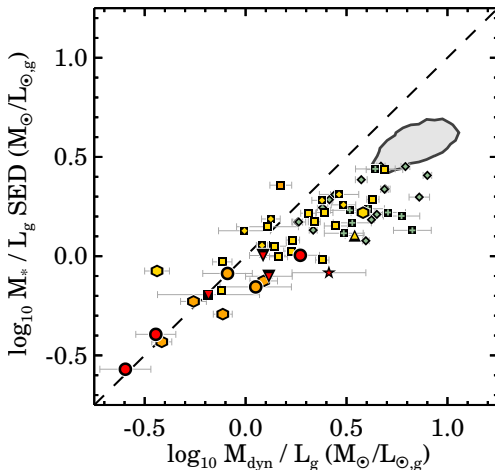


Figure 5.9:  $M_*/L_g$  from SED fits vs. the  $M_{\text{dyn}}/L_g$ . The  $M/L$  ratios have been determined by fitting solar metallicity BC03 models to the full broad-band data. We find a non-linear relation, which could be due to an evolving dark matter fraction or IMF variations.

## 5.6.2 Intrinsic scatter

From the  $M_{\text{dyn}}/L_g$  vs.  $(g - z)_{\text{rest-frame}}$  color relation, we find that we can predict the  $M/L$  of a galaxy with an accuracy of  $\sim 0.26$  dex. However, our dynamical  $M/L$  estimates suffer from large (systematic) uncertainties. To quantify the intrinsic scatter in the relation, we calculate the fraction of the scatter induced by uncertainties in the size, and velocity dispersion measurements. As the formal errors on the rest-frame colors are small ( $< 0.01$  mag), the scatter will be dominated by errors in the dynamical mass. From Monte-Carlo simulations, we find that 0.11 dex of the 0.26 dex scatter can be explained by measurement uncertainties. Thus our intrinsic scatter in the  $M_{\text{dyn}}/L_g$  vs.  $(g - z)_{\text{rest-frame}}$  relation is 0.22 dex. However, if the

(systematic) errors on the rest-frame colors are larger, for example  $\sim 0.1$  mag, the intrinsic scatter would be 0.14 dex.

We furthermore consider the fact that a single color might not provide an accurate constraint and that the full broad-band SED fit yields a tighter relation. We use the SED derived stellar  $M/L$  (see also Section 5.6.1) to estimate the scatter when using the full broad-band dataset. We find a mean ratio of  $M_*/M_{\text{dyn}} = -0.20$  with an rms scatter of 0.20 dex. This scatter of 0.20 dex suggests that a single color (which had a  $M/L$  accuracy of 0.26 dex) only provides a slightly worse  $M/L$  prediction as compared to full broad-band SED fitting.

### 5.6.3 Comparison to literature

#### 5.6.3.1 Single-burst SPS models

The evolution of the rest-frame K-band  $M/L$  out to  $z \sim 1$  was measured for the first time by van der Wel et al. (2006), for a sample with a small dynamic range of approximately  $\sim 0.4$  dex in  $M/L_K$ . They concluded that single-burst BC03 models with a Salpeter IMF were offset with respect to the data and that the Ma05 models with a Salpeter IMF provided the best match. While we come to a similar conclusion for the BC03 models, we still find a large offset between the data and the Maraston models with a Salpeter IMF, as the Maraston solar metallicity tracks are too blue by 0.5 mag in rest-frame  $g - K$ . The different conclusion can be explained by the fact that van der Wel et al. (2006) used relative  $M/L$  and colors, while we only use absolute values. We could not find other direct comparisons between  $M_{\text{dyn}}/L$  vs. color relations and SPS models in the literature.

#### 5.6.3.2 Star-forming galaxies and extended SFH

The relation between  $M/L$  vs. color was first explored by Bell & de Jong (2001) for spiral galaxies. They used an early version of the BC03 models, and found that the  $B - R$  provided a good estimate of the  $M/L$ . Follow up work by Bell et al. (2003) used the Pegase SPS models with more extended SFHs to estimate SED based  $M/L$ , which were then used to derive observationally-constrained  $M/L$  vs. color relations. They found that the optical  $M/L$  vs. color relations were in good agreement with Bell & de Jong (2001), but they found a shallower slope in the NIR  $M/L$  vs. color relation due to unaccounted metallicity effects. Zibetti et al. (2009) used the latest SPS models from Charlot & Bruzual (in Prep.) to directly derive the  $M/L$  vs. color relation from the model. Similar to the results by Gallazzi & Bell (2009) they found a steeper slope of in the  $M/L_i$  vs.  $(g - i)_{\text{rest-frame}}$  relation as compared to Bell et al. (2003). Using BC03 models Taylor et al. (2011) follow a similar method as Bell et al. (2003) and found that slope for the  $M/L_i$  vs.  $(g - i)$  relation is steeper than Bell et al. (2003), but shallower than Zibetti et al. (2009).

In this chapter, we found that the slope for the  $M/L_i$  vs. rest-frame  $(g - i)$  relation is considerably steeper than in previous work (e.g. Bell et al. 2003; Zibetti et al. 2009; Taylor et al. 2011). The difference is easily explained as the  $M/L$  vs. color relations in these studies were derived from samples that include star-forming galaxies, with variable (exponentially declining) star formation histories, and dust. This naturally leads to a shallower slope. In addition, we found in Section 5.4 that most model tracks predict a shallower relation as compared to our dynamical data. If this trend is indeed caused by stellar population effects, it would imply that



the masses of star forming galaxies need recalibration, and may have systematic uncertainties at a level of 0.2 dex.

### 5.6.4 Constraints on the IMF

Several authors have constrained the IMF's using a differential analysis of color evolution against  $M/L$  evolution, inspired by early work by Tinsley (1972; 1980). van Dokkum (2008a) used galaxies in clusters at  $0 < z < 0.8$  and found an IMF slope around  $1M_{\odot}$  of  $\alpha = 0.7^{+0.4}_{-0.7}$ . Holden et al. (2010) used a larger sample, and analyzed the evolution at fixed velocity dispersion, and found an IMF slope of  $\alpha = 1.9 \pm 0.2$ . van Dokkum & Conroy (2012) repeated this analysis with the latest population models (Conroy & van Dokkum, 2012) and found a slope of  $\alpha = 1.81 \pm 0.27$ . Although the techniques used by these authors are quite different, the results are quite similar to those presented here. However, with our larger range in  $M/L$  and rest-frame color, we find that the variations between different models with the same IMF are larger than the variations due to the IMF with the same model. Therefore, with the current models it is still hard to put a robust constraint on the IMF.

### 5.6.5 Dark matter

In this chapter we use dynamical mass estimates for calculating the  $M/L$ . The dynamical mass includes both stellar mass and dark matter mass, but to this point we have ignored the contribution of dark matter to the dynamical mass. At low-redshift the dynamical to stellar mass fraction is approximately a factor of 1.6 within one effective radius, due to the contribution of dark matter to the total mass. If we include dark matter in the  $M/L$  of the models, this fraction would shift all curves in Figure 5.5-5.7 vertically up by  $\sim 0.2$  dex. This shift would not solve the discrepancies between the models and the data, because the discrepancies are in the slope and cannot be solved by a constant offset (see Figure 5.9).

However, whether the dark matter fraction within one  $r_e$  is constant over time is still subject to debate. The size growth of massive quiescent galaxies may result in an increase of the dark matter to stellar mass fraction within one  $r_e$ , because the dark matter profile is less steep than the stellar mass profile (see also Hilz et al. 2013). Thus, the dark matter fraction within one  $r_e$  may increase over time. In van de Sande et al. (2013), we indeed find a hint of an evolving dark matter fraction, i.e., the median  $M_*/M_{dyn}$  is higher by 50% at  $z > 1.5$  compared to massive SDSS galaxies ( $M_*/M_{dyn} \propto (1+z)^{0.17 \pm 0.011}$ ). From hydrodynamical simulations, Hopkins et al. (2009) find that for galaxies with  $M_* \sim 10^{11}$ , the stellar to dynamical mass ( $M_*/M_{dyn}$ ) at  $z \sim 2$  is lower by 0.1 dex. Thus, if we correct for an evolving dark matter fraction the  $M/L$  for high-redshift galaxies would decrease by approximately 0.1 dex and for SDSS galaxies by about 0.2 dex. As this correction decreases the slope of the empirical  $M/L$  vs. color relation, it would make the slope of the data more consistent with a Chabrier ( $\alpha = 2.35$ ) IMF (see Figure 5.6).

### 5.6.6 Metallicity & complex star formation histories

In the comparison of the models with the data, we used model tracks with single metallicities. As galaxies grow in size and mass over time, for example through minor mergers, metallicity

may also evolve as the satellite galaxies have lower metallicities (e.g., Gallazzi et al. 2005; 2014; Choi et al. 2014). The core will likely keep the same metallicity, while the metallicity in the outskirts may decrease (Greene et al. 2013; Montes et al. 2014). Without additional data (e.g., resolved images and spectroscopy) we cannot quantify this effect.

Furthermore, we have assumed a single SFH for all galaxies. While massive galaxies in general are thought to have simple SFHs, for individual galaxies the SFH could be far more complex due to merging events. The fact that we find that none of the SPS models are able to simultaneously match all the data for both the rest-frame optical and NIR data could imply that the effect of a complex SFH is more important than assumed here.

### 5.6.7 Systematic sample variations

While the approach of using a mass selected sample has provided us with many insights it is clear that for comparing the  $M/L$  of galaxies at different redshifts, this static mass selection could introduce a bias. Recent studies find that several properties of massive quiescent galaxies may change over time: they were smaller than their present-day counterparts (e.g., Daddi et al. 2005; Trujillo et al. 2006; van Dokkum et al. 2008b; Franx et al. 2008; van der Wel et al. 2008; and numerous others), their stellar masses increase by a factor of  $\sim 2$  from  $z \sim 2$  to  $z \sim 0$  (e.g., van Dokkum et al. 2010, Patel et al. 2013), and the effective velocity dispersion may also decrease (e.g., Oser et al. 2012; van de Sande et al. 2013). Thus, our samples and measurements at different redshifts may not be directly comparable.

A possible additional complication is progenitor bias (e.g., van Dokkum & Franx 1996; 2001): the number density of massive galaxies changes by a factor of  $\sim 10$  from  $z \sim 2$  to  $z \sim 0$  (Muzzin et al., 2013b). Thus, a substantial fraction of the current day early-type galaxies were star-forming galaxies at  $z \sim 2$  (see also van der Wel et al. 2009). If the properties of the descendants of these  $z \sim 2$  star-forming galaxies are systematically different from the descendants of the quiescent galaxies at  $z \sim 2$ , the simple single burst SPS models which we used here may produce a biased result.

## 5.7 Conclusions

In this chapter, we have used a sample of massive galaxies ( $> 10^{11} M_{\odot}$ ) out to  $z \sim 2$  with stellar kinematic, structural, and photometric measurements. The primary goals of this chapter are to study the empirical relation between the dynamical  $M/L$  and rest-frame color, assess the ability of SPS models to reproduce this relation, and study the effect of the IMF on the  $M/L$  vs. color relation.

We find that our sample spans a large range in  $M/L$ : 1.8 dex in rest-frame  $\log M_{\text{dyn}}/L_u$ , 1.6 dex in  $\log M_{\text{dyn}}/L_g$ , and 1.3 dex in  $\log M_{\text{dyn}}/L_K$ . As expected for a passively evolving stellar population, we find a strong correlation between the  $M/L$  for different bands and rest-frame colors. For rest-frame optical colors, the correlation is well approximated by a linear relation, and we provide coefficients of the linear fits for a large number of  $M/L$  vs. color correlations. The root-mean-square scatter in the  $\log M_{\text{dyn}}/L$  residuals is  $\sim 0.26$  dex. Thus, these relations are ideal for estimating masses for quiescent galaxies with an accuracy of  $\sim 0.26$  dex.

We compare a combination of two  $M/L$  vs. rest-frame color relations with stellar population synthesis (SPS) models by Bruzual & Charlot (2003), Maraston & Strömbäck (2011), and Conroy et al. (2009). Under the assumption of a Salpeter initial mass function (IMF), none of the SPS models are able to simultaneously match the data in  $M_{\text{dyn}}/L_g$  vs.  $(g - z)_{\text{rest-frame}}$  color and  $M_{\text{dyn}}/L_K$  vs.  $(g - K)_{\text{rest-frame}}$  color.

By changing the IMF, we test whether we can obtain a better match. IMFs with different slopes are still unable to simultaneously match the low  $M/L$  of the bluest galaxies in combination with the other data. While a Chabrier IMF underpredicts the  $M/L$  for  $z \sim 0$  SDSS galaxies in the  $M_{\text{dyn}}/L_g$  vs.  $(g - z)_{\text{rest-frame}}$ , it provides an excellent match to all other data.

We also explore a broken IMF with a Salpeter slope at  $< 1M_{\odot}$  and  $> 4M_{\odot}$ , and we find that the models favor a slope of  $\alpha = 1.35$  over  $\alpha = 2.35$  in the intermediate region, based on the rms scatter. This time, the FSPS model with an IMF slope of  $\alpha = 1.35$ , is able to simultaneously match both the  $M/L$  vs.  $(g - z)_{\text{rest-frame}}$  and  $(g - K)_{\text{rest-frame}}$ .

The combination of the  $M/L$  and color is a powerful tool for studying the shape of the IMF near  $1M_{\odot}$ . However, this work shows that the variations between different SPS models are comparable to the variations induced by changing the IMF. There are several caveats which may change our data or models tracks, among which an evolving dark matter fraction, an evolving metallicity, complicated star formation histories, and an evolving mass-selection limit. More complete and higher resolution empirical stellar libraries, improved stellar evolution models, and larger spectroscopic samples at high-redshift, are needed to provide more accurate constraints on the IMF.

## Acknowledgments

It is a pleasure to acknowledge the contribution to this work by the NMBS and 3DHST collaboration. We also thank Rik Williams and Ryan Quadri for their help with the UDS catalogs, and thank Andrew Newman for providing the corrected stellar masses. The authors furthermore wish to thank Daniel Szomoru and Adam Muzzin interesting discussions which contributed to this chapter. This research was supported by grants from the Netherlands Foundation for Research (NWO), the Leids Kerkhoven-Bosscha Fonds. This work is based on observations taken by the 3D-HST Treasury Program (GO 12177 and 12328) with the NASA/ESA *HST*, which is operated by the Association of Universities for Research in Astronomy, Inc., under NASA contract NAS5-26555.

## References

- Abazajian, K. N., Adelman-McCarthy, J. K., Agüeros, M. A., et al. 2009, *ApJS*, 182, 543
- Bell, E. F., McIntosh, D. H., Katz, N., & Weinberg, M. D. 2003, *ApJS*, 149, 289
- Bell, E. F., & de Jong, R. S. 2001, *ApJ*, 550, 212
- Belli, S., Newman, A. B., Ellis, R. S., & Konidaris, N. P. 2014b, *ApJ*, 788, L29
- Belli, S., Newman, A. B., & Ellis, R. S. 2014a, *ApJ*, 783, 117
- Bertelli, G., Bressan, A., Chiosi, C., Fagotto, F., & Nasi, E. 1994, *A&AS*, 106, 275
- Bezanson, R., van Dokkum, P., van de Sande, J., Franx, M., & Kriek, M. 2013a, *ApJ*, 764, L8
- Bezanson, R., van Dokkum, P. G., van de Sande, J., et al. 2013b, arXiv:1309.6638
- Bezanson, R., van Dokkum, P. G., Franx, M., et al. 2011, *ApJ*, 737, L31
- Blakeslee, J. P., Holden, B. P., Franx, M., et al. 2006, *ApJ*, 644, 30
- Blanc, G. A., Lira, P., Barrientos, L. F., et al. 2008, *ApJ*, 681, 1099
- Blanton, M. R., Schlegel, D. J., Strauss, M. A., et al. 2005, *AJ*, 129, 2562
- Brammer, G. B., van Dokkum, P. G., & Coppi, P. 2008, *ApJ*, 686, 1503
- Brammer, G. B., van Dokkum, P. G., Franx, M., et al. 2012, *ApJS*, 200, 13
- Brinchmann, J., Charlot, S., White, S. D. M., et al. 2004, *MNRAS*, 351, 1151
- Bruzual, G., & Charlot, S. 2003, *MNRAS*, 344, 1000
- Bundy, K., Ellis, R. S., Conselice, C. J., et al. 2006, *ApJ*, 651, 120
- Calzetti, D., Armus, L., Bohlin, R. C., et al. 2000, *ApJ*, 533, 682
- Cappellari, M., Bacon, R., Bureau, M., et al. 2006, *MNRAS*, 366, 1126
- Cassisi, S., Castellani, M., & Castellani, V. 1997a, *A&A*, 317, 108
- Cassisi, S., degl'Innocenti, S., & Salaris, M. 1997b, *MNRAS*, 290, 515
- Cassisi, S., Castellani, V., Ciarcelluti, P., Piotto, G., & Zoccali, M. 2000, *MNRAS*, 315, 679
- Chabrier, G. 2003, *PASP*, 115, 763
- Choi, J., Conroy, C., Moustakas, J., et al. 2014, arXiv:1403.4932
- Conroy, C. 2013, *ARA&A*, 51, 393
- Conroy, C., & van Dokkum, P. 2012, *ApJ*, 747, 69
- Conroy, C., & Gunn, J. E. 2010, *ApJ*, 712, 833
- Conroy, C., Gunn, J. E., & White, M. 2009, *ApJ*, 699, 486
- Courteau, S., Cappellari, M., de Jong, R. S., et al. 2013, arXiv:1309.3276
- Daddi, E., et al. 2005, *ApJ*, 626, 680
- de Jong, R. S., & Bell, E. F. 2007, *Island Universes - Structure and Evolution of Disk Galaxies*, 107
- De Lucia, G., & Blaizot, J. 2007, *MNRAS*, 375, 2
- Förster Schreiber, N. M., Franx, M., Labbé, I., et al. 2006, *AJ*, 131, 1891
- Franx, M., van Dokkum, P. G., Schreiber, N. M. F., Wuyts, S., Labbé, I., & Toft, S. 2008, *ApJ*, 688, 770
- Gallazzi, A., Bell, E. F., Zibetti, S., Brinchmann, J., & Kelson, D. D. 2014, *ApJ*, 788, 72
- Gallazzi, A., & Bell, E. F. 2009, *ApJS*, 185, 253
- Gallazzi, A., Charlot, S., Brinchmann, J., White, S. D. M., & Tremonti, C. A. 2005, *MNRAS*, 362, 41
- Greene, J. E., Murphy, J. D., Graves, G. J., et al. 2013, *ApJ*, 776, 64
- Hilz, M., Naab, T., & Ostriker, J. P. 2013, *MNRAS*, 429, 2924
- Holden, B. P., van der Wel, A., Kelson, D. D., Franx, M., & Illingworth, G. D. 2010, *ApJ*, 724, 714
- Hopkins, P. F., Hernquist, L., Cox, T. J., Keres, D., & Wuyts, S. 2009, *ApJ*, 691, 1424
- Ilbert, O., McCracken, H. J., Le Fèvre, O., et al. 2013, *A&A*, 556, A55
- Kauffmann, G., Heckman, T. M., White, S. D. M., et al. 2003, *MNRAS*, 341, 54
- Kriek, M., van Dokkum, P. G., Labbé, I., et al. 2009, *ApJ*, 700, 221
- Kriek, M., van der Wel, A., van Dokkum, P. G., Franx, M., & Illingworth, G. D. 2008, *ApJ*, 682, 896
- Kuntschner, H., Emsellem, E., Bacon, R., et al. 2010, *MNRAS*, 408, 97
- Le Borgne, J.-F., Bruzual, G., Pelló, R., et al. 2003, *A&A*, 402, 433
- Maraston, C. 2005, *MNRAS*, 362, 799
- Maraston, C., & Strömbäck, G. 2011, *MNRAS*, 418, 2785
- Marchesini, D., van Dokkum, P. G., Förster Schreiber, N. M., et al. 2009, *ApJ*, 701, 1765
- Marigo, P., Girardi, L., Bressan, A., et al. 2008, *A&A*, 482, 883
- Marigo, P., & Girardi, L. 2007, *A&A*, 469, 239
- McLean, I. S., Steidel, C. C., Epps, H. W., et al. 2012, *Proc. SPIE*, 8446
- Montes, M., Trujillo, I., Prieto, M. A., & Acosta-Pulido, J. A. 2014, *MNRAS*, 439, 990

- Muzzin, A., Marchesini, D., Stefanon, M., et al. 2013b, *ApJ*, 777, 18  
Muzzin, A., Marchesini, D., Stefanon, M., et al. 2013a, *ApJS*, 206, 8  
Newman, A. B., Ellis, R. S., Treu, T., & Bundy, K. 2010, *ApJ*, 717, L103  
Oser, L., Naab, T., Ostriker, J. P., & Johansson, P. H. 2012, *ApJ*, 744, 63  
Patel, S. G., van Dokkum, P. G., Franx, M., et al. 2013, *ApJ*, 766, 15  
Peng, C. Y., Ho, L. C., Impey, C. D., & Rix, H.-W. 2010, *AJ*, 139, 2097  
Onodera, M., Renzini, A., Carollo, M., et al. 2012, *ApJ*, 755, 26  
Salpeter, E. E. 1955, *ApJ*, 121, 161  
Sánchez-Blázquez, P., Peletier, R. F., Jiménez-Vicente, J., et al. 2006, *MNRAS*, 371, 703  
Simard, L., Mendel, J. T., Patton, D. R., Ellison, S. L., & McConnachie, A. W. 2011, *ApJS*, 196, 11  
Simard, L. 1998, *Astronomical Data Analysis Software and Systems VII*, 145, 108  
Skelton, R. E., Whitaker, K. E., Momcheva, I. G., et al. 2014, arXiv:1403.3689  
Szomoru, D., Franx, M., van Dokkum, P. G., et al. 2013, *ApJ*, 763, 73  
Taylor, E. N., Hopkins, A. M., Baldry, I. K., et al. 2011, *MNRAS*, 418, 1587  
Taylor, E. N., Franx, M., Brinchmann, J., van der Wel, A., & van Dokkum, P. G. 2010, *ApJ*, 722, 1  
Tinsley, B. M. 1980, *Fund. Cosmic Phys.*, 5, 287  
Tinsley, B. M. 1972, *ApJ*, 178, 319  
Toft, S., Gallazzi, A., Zirm, A., et al. 2012, *ApJ*, 754, 3  
Tremonti, C. A., Heckman, T. M., Kauffmann, G., et al. 2004, *ApJ*, 613, 898  
Trujillo, I., et al. 2006, *MNRAS*, 373, L36  
van de Sande, J., Kriek, M., Franx, M., et al. 2013, *ApJ*, 771, 85  
van de Sande, J., Kriek, M., Franx, M., et al. 2011, *ApJ*, 736, L9  
van der Wel, A., Bell, E. F., Häussler, B., et al. 2012, *ApJS*, 203, 24  
van der Wel, A., Bell, E. F., van den Bosch, F. C., Gallazzi, A., & Rix, H.-W. 2009, *ApJ*, 698, 1232  
van der Wel, A., Holden, B. P., Zirm, A. W., et al. 2008, *ApJ*, 688, 48  
van der Wel, A., Franx, M., van Dokkum, P. G., et al. 2006, *ApJ*, 636, L21  
van der Wel, A., Franx, M., van Dokkum, P. G., et al. 2005, *ApJ*, 631, 145  
van Dokkum, P. G., & Conroy, C. 2012, *ApJ*, 760, 70  
van Dokkum, P. G., et al. 2010, *ApJ*, 709, 1018  
van Dokkum, P. G., Kriek, M., & Franx, M. 2009, *Nature*, 460, 717  
van Dokkum, P. G., et al. 2008b, *ApJ*, 677, L5  
van Dokkum, P. G. 2008a, *ApJ*, 674, 29  
van Dokkum, P. G., & Franx, M. 2001, *ApJ*, 553, 90  
van Dokkum, P. G., & Franx, M. 1996, *MNRAS*, 281, 985  
Vernet, J., Dekker, H., D'Odorico, S., et al. 2011, *A&A*, 536, A105  
Whitaker, K. E., Labbé, I., van Dokkum, P. G., et al. 2011, *ApJ*, 735, 86  
Williams, R. J., Quadri, R. F., Franx, M., van Dokkum, P., & Labbé, I. 2009, *ApJ*, 691, 1879  
Wuyts, S., Labbé, I., Franx, M., et al. 2007, *ApJ*, 655, 51  
Wuyts, S., van Dokkum, P. G., Kelson, D. D., Franx, M., & Illingworth, G. D. 2004, *ApJ*, 605, 677  
Zibetti, S., Charlot, S., & Rix, H.-W. 2009, *MNRAS*, 400, 1181

# Nederlandse samenvatting

## Dawn of the Red and Dead

### Stellar Kinematics of Massive Quiescent Galaxies out to $z = 2$

De titel van dit proefschrift refereert naar *de opkomst van rode en dode sterrenstelsels* in het jonge heelal. Het bestuderen van deze *passieve en massieve sterrenstelsels* is van groot belang om het ontstaan en de evolutie van sterrenstelsels beter te begrijpen. Het licht van deze rode en dode sterrenstelsels werd uitgezonden toen het heelal slechts 3 miljard jaar oud was en is ongeveer 11 miljard jaar onderweg geweest. De ontdekking van deze sterrenstelsels verbaasde vele astronomen, vooral omdat ze veel kleiner in afmeting waren dan gedacht.

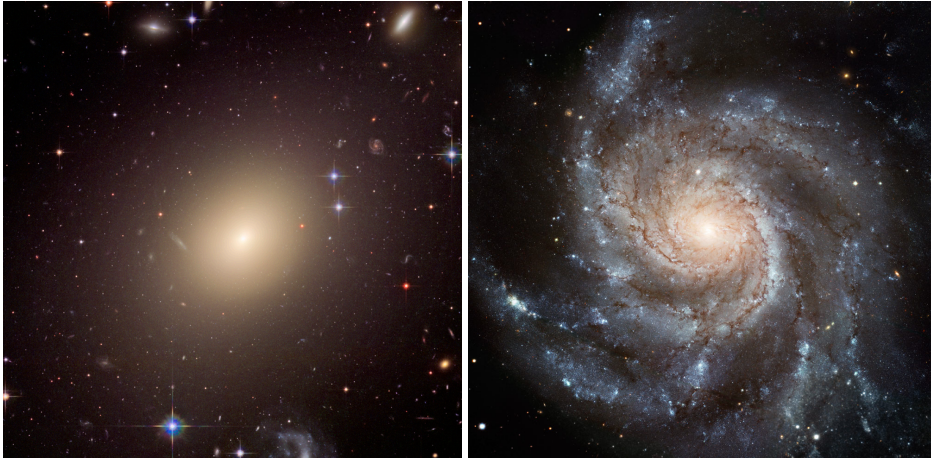
In dit proefschrift worden deze recente bevindingen kritisch bekeken, in het bijzonder de massabepalingen van deze sterrenstelsels. Er wordt gebruik gemaakt van een techniek waarmee de gemiddelde beweging van sterren in een sterrenstelsel getraceerd kan worden, ook wel *stellaire kinematica* genoemd. Uit deze kinematische informatie blijkt dat rode en dode sterrenstelsels in het jonge heelal erg massief zijn, maar dat ze qua afmeting en structuur erg verschillen van sterrenstelsels in het nabije heelal.

## De Melkweg

Op een heldere, donkere nacht kun je aan de hemel een zwakke, witte band zien die zich uitstrekt van horizon tot horizon: de Melkweg. Galileo Galilei ontdekte in de 17 eeuw met één van de eerste telescopen, dat deze witte wolk uit duizenden sterren bestond. Immanuel Kant kwam met het idee dat de Melkweg een sterrenstelsel is. Kant zag de Melkweg als een grote, roterende schijf van duizenden sterren die bijeen wordt gehouden door de zwaartekracht. Hij was geïnspireerd door het werk van Nicolaus Copernicus, de eerste astronoom die postuleerde dat de Aarde om de Zon draait.

Waarnemingen met de eerste telescopen lieten zien dat er behalve sterren ook diffuse nevels aan de hemel staan; dit zijn nevels die onregelmatig van vorm zijn. Kant stelde voor dat deze nevels individuele sterrenstelsels waren, net als de Melkweg. De astronoom Charles Messier stelde de eerste catalogus van deze nevels samen. De Andromeda Nevel, of Messier 31, is één van de bekendste objecten uit zijn catalogus. Deze catalogus werd onder meer uitgebreid door William Herschel en Earl of Rosse. Ondanks deze nieuwe waarnemingen, konden de astronomen niet bewijzen dat deze nevels sterrenstelsels waren.

Pas in 1922 bewees Edwin Hubble dat deze nevels zich buiten de Melkweg bevinden, wat een grote doorbraak was. Hij maakte slim gebruik van sterren die variabel zijn in helderheid. Hij kon daarmee laten zien dat de Andromeda Nevel zich op een afstand van ongeveer één miljoen lichtjaar van de Aarde bevindt, ver verwijderd van de Melkweg. Sinds Hubble's



**Figuur 5.10:** Een voorbeeld van een elliptisch sterrenstelsel (*links*, Abel-S0740) en een spiraalvormig sterrenstelsel (*rechts*, M101). *Bron: NASA, ESA, en The Hubble Heritage Team (STScI/AURA).*

ontdekking zijn miljoenen nieuwe sterrenstelsels waargenomen, waarvan ook de afstand is bepaald. Bijna honderd jaar later is onze kennis over sterrenstelsels enorm toegenomen.

## Elliptische en spiraalvormige sterrenstelsels

Waarnemingen in de nabije omgeving van de Melkweg laten een grote verscheidenheid aan sterrenstelsels zien. De introductie van een classificatiesysteem voor sterrenstelsels is een andere grote bijdrage van Hubble aan de wetenschap. Hij onderscheidde grofweg twee types: elliptische en spiraalvormige sterrenstelsels (zie Figuur 5.10).

Elliptische stelsels zijn ronde of langwerpige objecten met een egale, rode lichtverdeling. Spiraalvormige stelsels zijn platte schijven met daarin een centrale verdikking of *bulge*. De schijf bestaat uit stof en blauwe sterren, terwijl de bulge voornamelijk rode sterren bevat. Een grote centrale balk, die zich soms uitstrekt tot ver in de schijf, komt bij spiraalvormige stelsels vaak voor. Op basis van deze classificatie kwam Hubble tot de conclusie dat sterrenstelsels beginnen als ronde elliptische stelsels die uitgroeien tot spiraalvormige stelsels. Tegenwoordig denken astronomen het tegenovergestelde: elliptische stelsels ontstaan uit botsingen van twee spiraalvormige stelsels. Deze paradigmaverschuiving komt onder andere voort uit onderzoek naar de sterpopulaties in sterrenstelsels en door het meten van de fundamentele eigenschappen van stelsels, zoals grootte en massa.

Een sterrenstelsel, zoals de Melkweg of Andromeda, bestaat uit gemiddeld 500 miljard tot 1000 miljard sterren. Sterren komen voor in allerlei vormen en maten; daarom is het cruciaal voor het bestuderen van sterrenstelsels om gedetailleerde kennis op te doen over de grote verscheidenheid aan sterren. Blauwe sterren zijn vaak massief en hebben een hoge lichtkracht (of helderheid). Daartegenover hebben ze een korte levensduur: een paar miljoen jaar. Rode sterren hebben doorgaans een lagere massa en zijn minder helder, maar leven lang: tientallen

miljarden jaren. Een jonge populatie sterren is daarom voornamelijk blauw, een oude populatie sterren is rood. De massa van sterren wordt uitgedrukt in eenheden relatief tot de Zon. De zwaarste sterren hebben een massa van 100 keer onze Zon ( $100M_{\odot}$ ), terwijl de lichtste sterren tien keer lichter zijn dan de Zon ( $0.1M_{\odot}$ ). Bij metingen aan grote hoeveelheden sterren in de Melkweg, komt naar voren dat lichte sterren duizenden malen vaker voorkomen dan zware sterren.

De kleur van een sterrenstelsel geeft ons inzicht in de populatie van sterren die daar voorkomt. Elliptische stelsels zijn gemiddeld rood, wat er op duidt dat ze opgebouwd zijn uit oude sterren met weinig massa. De rode kernen van spiraalvormige stelsels bestaan dus ook uit oude sterren met weinig massa, maar de spiraalarmen van deze stelsels zijn blauw, wat betekent dat er hoofdzakelijk jonge, massieve sterren voorkomen.

De kleur van een sterrenstelsel vertelt ons ook hoeveel nieuwe sterren er recent zijn "geboren". Op het moment dat er geen nieuwe sterren geboren worden, noemen we een stelsel passief of dood. Hoe blauwer het sterrenstelsel, hoe meer nieuwe sterren bij de bestaande populatie zijn gekomen. De rode kleur van elliptische stelsels laat zien dat de laatste nieuwe sterren lang geleden zijn gevormd. Dit geeft ze de bijnaam: rood en dood.

Naast de kleur van een sterrenstelsel is ook de totale helderheid van groot belang om sterrenstelsels goed te kunnen analyseren. Deze helderheid laat zien hoeveel sterren zich in een sterrenstelsel bevinden. Hieruit kunnen we afleiden hoe zwaar een sterrenstelsel is. Deze manier van massabepaling is gecompliceerd, omdat blauwe sterren vele malen helderder zijn dan rode sterren. Het is echter de combinatie van kleur en totale helderheid die astronomen genoeg informatie geeft om tot een nauwkeurige massabepaling van een stelsel te komen.

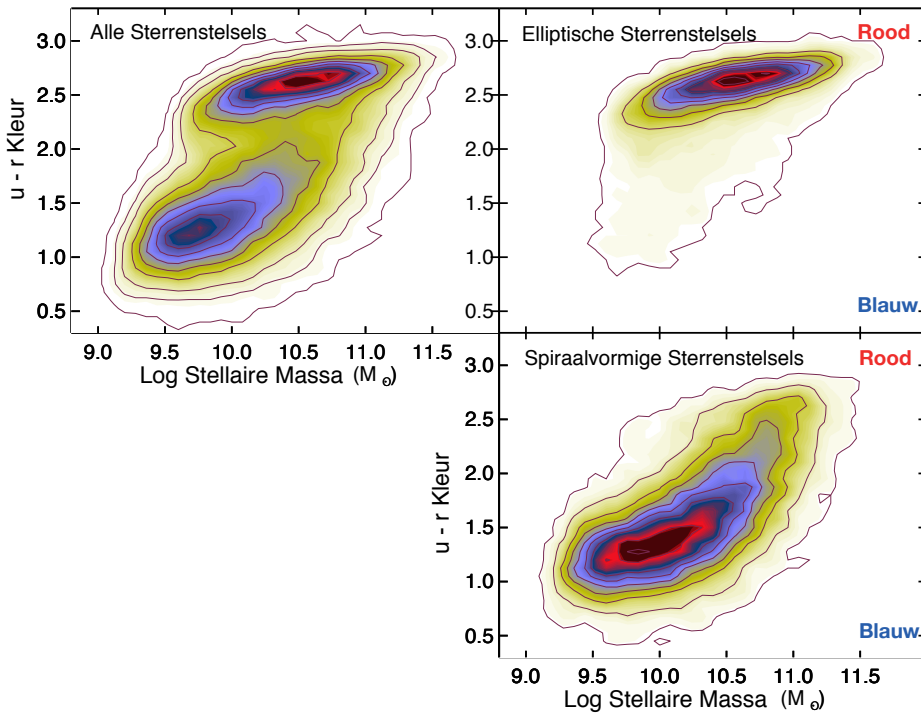
In Figuur 5.11 zijn metingen van de Sloan Digital Sky Survey (SDSS) weergegeven. Door de immense schaal van deze *survey* heeft de sterrenkunde grote stappen kunnen zetten in extragalactisch onderzoek. Deze Figuur laat de kleur tegen de massa van sterrenstelsels zien in het huidige heelal. Naast het feit dat elliptische en spiraalvormige stelsels een andere vorm hebben, namelijk rond en plat, blijkt uit Figuur 5.11 dat deze twee type stelsels ook drastisch verschillen in massa en kleur. Elliptische stelsels zijn gemiddeld bijna tien keer zwaarder dan spiraalvormige stelsels. De duizenden elliptische stelsels uit de SDSS vormen samen de *red sequence*, de spiraalvormige stelsels vormen samen de *blue cloud*. Het feit dat de twee soorten sterrenstelsels een duidelijke tweedeling vertonen, suggereert dat ze ook een uiteenlopende ontstaansgeschiedenis hebben. Deze tweedeling wordt bimodaliteit genoemd.

De ontdekking van de bimodaliteit leidt tot de fundamentele vraag binnen het extragalactisch onderzoek: waardoor wordt deze bimodaliteit veroorzaakt? De botsingen tussen spiraalvormige stelsels zijn volgens de huidige theorie verantwoordelijk voor de overgang naar de elliptische vorm. Elliptische sterrenstelsels zijn dus het eindproduct van deze botsingen. Dit roept twee vragen op. Zorgen deze botsingen ook voor het stopzetten van stervorming in elliptische stelsels? En wanneer hebben deze botsingen plaatsgevonden?

Als de elliptische vorm de laatste fase van de evolutie van sterrenstelsels is, dan zijn dit de stelsels die extra onderzoek verdienen. Maar elliptische stelsels in het huidige heelal zijn net als fossielen: ze geven ons voornamelijk informatie van vlak voor hun dood. Om een goed beeld te krijgen van de ontwikkeling van sterrenstelsels zouden we niet alleen moeten kijken naar het eindproduct. Wat we willen, is sterrenstelsels in elke fase van hun evolutie bekijken.

Sterrenkunde is terugkijken in de tijd. De lichtstralen van een object dat ver weg staat in het heelal, doen er een tijd over om bij ons te arriveren. Het licht van de Zon, bijvoorbeeld,





**Figuur 5.11:** Bimodaliteit in de populatie van sterrenstelsels. Elliptische sterrenstelsels zijn gemiddeld roder en zwaarder dan spiraalvormige sterrenstelsels. Elliptische stelsels vormen de *rode reeks*, terwijl spiraalvormige stelsels zich in de *blauwe wolk* bevinden. Bron: Scharwinski et al. 2014.

doet er zo'n acht minuten over om bij de Aarde te komen. Het licht van het Andromeda stelsel doet er 2,5 miljoen jaar over. Het licht van verstaande sterrenstelsels is dus lang onderweg en bijzonder oud. Verder weg kijken is terug kijken in de tijd. Als we sterrenstelsels observeren op een steeds grotere afstand, dan is het mogelijk om sterrenstelsels te zien in hun jonge jaren. Deze methode wordt gebruikt om de verschillende evolutionaire fases van sterrenstelsels te bestuderen.

## Vorming van sterrenstelsels

De huidige theorie over de vorming van sterrenstelsels begint bij de oerknal, 13,8 miljard jaar geleden. Deze tijdsperiode net na de oerknal wordt door astronomen het jonge heelal genoemd. Uit waarnemingen blijkt dat het jonge heelal homogeen en isotroop was: het bezat op iedere plaats dezelfde eigenschappen (homogeen) en het zag er op grote schaal in alle richtingen hetzelfde uit (isotroop). Dit staat bekend als het *kosmologische principe*. Dit is aangetoond met metingen van de kosmische achtergrondstraling (zie Figuur 1.1). Uit deze metingen blijkt

ook dat er ook kleine fluctuaties bestaan. Juist deze kleine fluctuaties groeien in de loop der tijd uit tot sterrenstelsels.

Sterren, planeten, en ook de mens zijn opgebouwd uit zichtbare materie, maar *donkere materie* zorgt voor de vorming van de eerste sterrenstelsels. Donkere materie is een hypothetische soort materie in het heelal die niet direct waarneembaar is. Toch zijn astronomen overtuigd van haar bestaan. Het voornaamste bewijs komt van indirecte zwaartekrachtmetingen in sterrenstelsels. Donkere materie is overal in het heelal aanwezig en beslaat grofweg vijf keer meer massa dan zichtbare materie. In de huidige theorie ontstaan sterrenstelsels in grote, bolvormige wolken of *halo's* van donkere materie. Binnen een halo kunnen in de loop van de tijd de eerste sterren ontstaan uit grote wolken van gas door middel van zwaartekracht. Daarna groeien deze eerste sterrenstelsels als gevolg van onderlinge botsingen uit tot steeds grotere en zwaardere sterrenstelsels.

## Observaties van sterrenstelsels in het jonge heelal

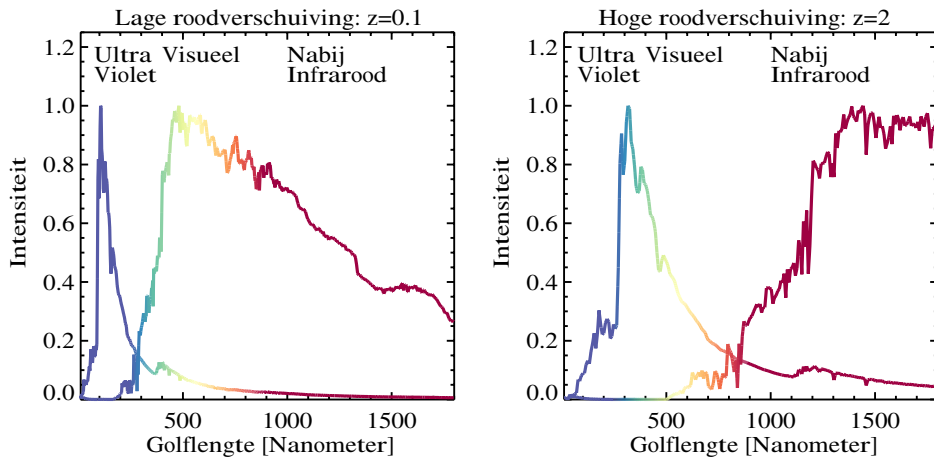
Het ontdekken van sterrenstelsels op steeds grotere afstand is één van de grootste uitdagingen van de sterrenkunde. Een grotere afstand betekent een grotere *terugkijktijd*. Het ontdekken van sterrenstelsels in het jonge heelal wordt gecompliceerd door de volgende drie zaken.

Ten eerste wordt het licht van sterrenstelsels zwakker als ze op grote afstand staan. Om dezelfde kwaliteit waarnemingen te verkrijgen als voor sterrenstelsels in het nabije heelal zijn steeds grotere telescopen nodig en camera's die telkens lichtgevoeliger zijn. De Very Large Telescope (VLT) met een spiegel diameter van 8,2 meter en de Keck telescopen met een spiegel diameter van 10 meter zijn hier voorbeelden van.

Ten tweede worden sterrenstelsels ogenschijnlijk kleiner als ze op grote afstand staan. In theorie zijn huidige telescopen en camera's goed genoeg om sterrenstelsels in het jonge heelal te onderscheiden. Turbulentie in de atmosfeer van de Aarde maakt de waarnemingen echter troebel. Een mooi twinkelende sterrenhemel is voor astronomen een ramp omdat er bij dergelijke condities geen scherpe beelden gemaakt kunnen worden. Eén van de oplossingen is observeren vanuit de ruimte met een satelliet zoals de *Hubble Space Telescope*.

Ten derde hebben we een spectrum nodig om een afstand te kunnen meten tot een sterrenstelsel. Een spectrum geeft aan wat de intensiteit of helderheid van het licht is bij een bepaalde golflengte of kleur. Een klassiek voorbeeld van een spectrum is wit licht dat door een prisma gebroken wordt in de kleuren van de regenboog. In het een spectrum heeft blauw licht een korte golflengte, terwijl rood licht een lange golflengte heeft. Het spectrum van een sterrenstelsel is opgebouwd uit de individuele spectra van vele miljarden sterren. Jonge sterren schijnen vooral in het ultraviolette en blauwe deel van het spectrum, terwijl oude sterren vooral rood licht uitstralen. Figuur 5.12a laat de spectra zien van een jong en oud sterrenstelsel in het nabije heelal. Het spectrum van het jonge sterrenstelsel piekt in het ultraviolet en het spectrum van het oude sterrenstelsel wordt gedomineerd door geel en rood licht. In de Figuur zie je dat de spectra kleine dipjes vertonen, dit noemen we *absorptielijnen*. Op deze golflengtes wordt het licht geabsorbeerd door atomen en moleculen. De absorptielijnen geven astronomen extra informatie over de leeftijd en afstand van een sterrenstelsel.

Het heelal is aan het uitdijen sinds de oerknal. De golflengte van het licht van verstaande



**Figuur 5.12:** Modelspectra van twee sterrenstelsel op lage (*links*) en hoge roodverschuiving (*rechts*). *Links:* Twee verschillende spectra van een jonge sterpopulatie die piekt in het ultraviolet, en een oude sterpopulatie waarvan het spectrum wordt gedomineerd door geel en rood licht. *Rechts:* Dezelfde spectra, maar nu zoals we deze zouden waarnemen als de sterrenstelsels op hoge roodverschuiving zouden staan. De piek van het jonge stelsel is verschoven van 100 nanometer naar 300 nanometer. Het oude stelsel straalt nu vooral in het Nabije-Infrarood.

sterrenstelsels wordt opgerekt door deze expansie van het heelal. Dit effect is vergelijkbaar met het Dopplereffect voor geluidsgolven: denk aan de sirenetoon die verandert bij een ambulance die met hoge snelheid langs ons rijdt. Door de hoge snelheidsverandering worden de geluidsgolven uitgerekt, waardoor de toon van het geluid lager wordt. Op vergelijkbare wijze verandert ook de golflengte van het licht van sterrenstelsels als ze op grote afstand staan. De uitdijning van het heelal zorgt ervoor dat de verste sterrenstelsels zich met grote snelheid van de Aarde af bewegen. Hoe verder weg een sterrenstelsel staat, des te sneller het zich van ons verwijdert. Het licht van zo'n sterrenstelsel wordt hierdoor verschoven naar langere golflengtes en dus naar het rode deel van het spectrum. Dit effect heet roodverschuiving. Een nabij stelsel heeft een lage roodverschuiving, een sterrenstelsel dat zich op een grote afstand bevindt heeft een hoge roodverschuiving.

Figuur 5.12b laat een jong en een oud sterrenstelsel zien op hoge roodverschuiving. Voor het jonge sterrenstelsel is de piek van de intensiteit verschoven van 100 nanometer naar 300 nanometer. Het oude sterrenstelsel straalt op hoge roodverschuiving het grootste deel van zijn licht uit in het *Nabije-Infrarood*, 800 nanometer en hoger. Alle absorptielijnen verschuiven mee naar het rode deel van het spectrum. Omgekeerd vertelt de plek van deze absorptielijnen ons precies in welke mate het stelsel is *roodverschuiven*. Uit deze roodverschuiving kunnen we de afstand tot een sterrenstelsel afleiden. Een spectrum van een sterrenstelsel is als het ware een vingerafdruk: het vertelt ons hoe ver weg een sterrenstelsel staat en hoe oud het stelsel is.

## Rode en dode sterrenstelsels in het jonge heelal

De eerste waarnemingen van sterrenstelsels op hoge roodverschuiving lieten een heelal zien dat gedomineerd werd door blauwe, spiraalvormige sterrenstelsels. Elliptische stelsels leken nog niet te zijn gevormd, maar zouden volgens theoretische modellen wel al moeten bestaan. De elliptische stelsels werden niet waargenomen omdat metingen in het Nabije-Infrarood in technisch opzicht bijzonder uitdagend zijn. Met recente ontwikkelingen in Nabije-Infrarood detectortechnologie hebben astronomen grote vooruitgang geboekt. Rode en dode sterrenstelsels zijn daarmee al ontdekt slechts 3 miljard jaar na de oerknal, in een relatief jonge fase van het heelal. Zowel op lage als hoge roodverschuiving vinden we een *rode reeks* en *blauwe wolk* voor sterrenstelsels. Dit suggereert dat het proces, waarbij de verandering van spiraal-naar elliptische vorm plaatsvindt, al vroeg voorkomt in het heelal.

Deze rode en dode stelsels op hoge roodverschuiving bleken veel kleiner in afmeting te zijn dan verwacht. Dit kwam voor astronomen als een grote verrassing. In vergelijking met even massieve sterrenstelsels in het nabije heelal zijn ze 4 tot 5 keer zo klein. Deze extreem compacte stelsels bestaan niet in het nabije heelal, wat suggereert dat ze in de loop van de tijd zeer snel zijn gegroeid. Deze reeds elliptische sterrenstelsels op hoge roodverschuiving kunnen mogelijk de kernen zijn van de huidige elliptische sterrenstelsels. Voor de snelle groei van een rood en dood stelsel zijn vermoedelijk veel botsingen nodig van het rode en dode stelsel met kleine, lichte sterrenstelsels. Hierdoor wordt materiaal toegevoegd aan de buitenkant van de rode kern. Toch is het onduidelijk of dit type botsing verantwoordelijk is voor de snelle groei, want metingen op hoge roodverschuiving vinden niet genoeg kleine, lichte sterrenstelsels.

Een belangrijke vraag in het onderzoek naar de groei van rode en dode stelsels is: hoe betrouwbaar zijn metingen op hoge roodverschuiving? Aanvankelijk dachten astronomen dat de afmetingen van deze sterrenstelsels werden onderschat, want het is heel lastig om het zwakke licht aan de randen van sterrenstelsels te meten. Dit probleem lijkt te zijn opgelost met de komst van een nieuwe camera op de *Hubble Space Telescope*, de Wide Field Camera 3. Extreem nauwkeurige metingen laten zien dat de fouten op de afmetingen van sterrenstelsels beperkt zijn.

Een andere grote onzekerheid komt voort uit de massabepaling van sterrenstelsels op hoge roodverschuiving. De gangbare methode om de massa van een sterrenstelsel te bepalen, is door te kijken naar de kleur en de totale helderheid van het stelsel. Deze methode is niet volledig betrouwbaar door het grote aantal aannames dat gedaan moet worden. Onderzoek heeft uitgewezen dat de fouten in de massabepaling van sterrenstelsels kunnen oplopen tot bijna een factor 6. Als rode en dode sterrenstelsels op hoge roodverschuiving veel minder massief zijn dan gedacht, dan is hun kleine afmeting eigenlijk geen grote verrassing. De veronderstelling van een snelle groei in afmeting is niet langer nodig. In dat geval heeft er in 11 miljard jaar nauwelijks evolutie van sterrenstelsels plaatsgevonden. Rode en dode stelsels op hoge roodverschuiving zien er nagenoeg hetzelfde uit als rode en dode stelsels op lage roodverschuiving.

## Dit proefschrift

Mijn coauteurs en ik presenteren in dit proefschrift nieuwe waarnemingen waarmee we de nauwkeurigheid van bestaande massametingen op hoge roodverschuiving kunnen bepalen. In

plaats van alleen te kijken naar de totale hoeveelheid licht en kleur van een stelsel, maken we gebruik van een massabepalingsmethode die gebaseerd is op de beweging van sterren binnen een sterrenstelsel. Het resultaat van deze bepaling heet een *dynamische massa*. In een elliptisch stelsels bewegen individuele sterren in een baan rond het centrum, maar de richting en snelheid is voor iedere ster anders. Uit de spreiding van de snelheid kunnen we afleiden hoe zwaar een sterrenstelsel is. Deze spreiding van snelheid, of *snelheidsdispersie*, is te meten uit het spectrum van een sterrenstelsel. In grote, massieve, elliptische stelsels meten we gemiddeld een hoge snelheidsdispersie, terwijl we in kleine, lichte stelsels een lage snelheidsdispersie meten. Met nauwkeurig waargenomen spectra van stelsels op hoge roodverschuiving is het dus mogelijk om de eerdere massabepalingen te verifiëren.

Het meten van spectra, *spectroscopie*, is vele malen lastiger voor verre objecten. Het licht in een spectrograaf, een instrument te vergelijken met de werking van een prisma, wordt uitgesmeerd over een groot golflengtegebied en is daardoor ook zwakker. Alleen met de grootste telescopen en meest gevoelige instrumenten is het mogelijk om een spectrum waar te nemen van een sterrenstelsel op hoge roodverschuiving. Vanwege de hoge moeilijkheidsgraad is deze methode slechts één keer toegepast. Deze meting was echter onnauwkeurig. De doorbraak kwam in 2009, toen er op de Very Large Telescope een nieuw geavanceerd instrument werd geplaatst: X-Shooter. Dit instrument maakte het voor ons mogelijk om nauwkeurige spectra te verkrijgen van sterrenstelsels op hoge roodverschuiving. In dit proefschrift beschrijven we X-Shooter metingen aan vijf massieve, rode en dode sterrenstelsels op hoge roodverschuiving. Deze spectra hebben we gecombineerd met waarnemingen van andere telescopen waaronder de *Hubble Space Telescope*. Naast onze eigen metingen met X-Shooter gebruiken we ook snelheidsdispersiemetingen van sterrenstelsels op lagere roodverschuiving van andere teams.

In **Hoofdstuk 2** wordt een pilotstudie gepresenteerd van een compact rood en dood sterrenstelsel op hoge roodverschuiving. We laten zien dat met de nieuwe generatie spectrografen het mogelijk is om een nauwkeurige snelheidsdispersie te meten. Gecombineerd met de afmeting verkregen van *Hubble Space Telescope* observaties bepalen we een dynamische massa. Deze dynamische massa is in goede overeenkomst met de massa die is afgeleid uit de totale helderheid en de kleur. De resultaten suggereren dat de massabepalingen op hoge roodverschuiving wel degelijk betrouwbaar zijn.

In **Hoofdstuk 3** maken we gebruik van onze complete set spectra om uit te zoeken of massieve, rode en dode sterrenstelsels in het jonge heelal echt zo compact zijn als wordt beweerd. Uit de spectra van deze vijf stelsels meten we hoge snelheidsdispersies en uit de *Hubble Space Telescope* observaties vinden we kleine afmetingen. Gecombineerd laten deze metingen zien dat rode en dode sterrenstelsels erg massief zijn. Opnieuw vinden we dat de dynamische massa goed overeenkomt met de voorheen gemeten massa. Verder vinden we dat deze stelsels gemiddeld erg compact zijn, in andere woorden een erg hoge dichtheid hebben, terwijl de dichtheid in de kern van deze stelsels grofweg hetzelfde is als stelsels in het nabije heelal. Deze bevindingen suggereren dat rode en dode stelsels voornamelijk aan de buitenkant groeien in de loop van de tijd. Deze groei aan de buitenkant lijkt ondanks eerdere twijfels toch te worden veroorzaakt door botsingen met kleine stelsels.

Nabije elliptische stelsels vertonen een sterke correlatie tussen de afmeting, snelheidsdispersie en helderheid. Deze correlatie wordt de *fundamental plane* genoemd. In **Hoofdstuk 4** onderzoeken we of de *fundamental plane* ook bestaat voor rode en dode sterrenstelsels op hoge roodverschuiving. We vinden sterke aanwijzingen dat dit inderdaad het geval is. Maar de se-

lectie op basis van helderheid van deze sterrenstelsels, om nauwkeurige spectra te verkrijgen, blijkt de analyse te bemoeilijken. De sterpopulaties in de vijf stelsels in ons X-Shooter sample blijken veel jonger dan de sterpopulaties in een gemiddeld elliptische sterrenstelsel op hoge roodverschuiving. We lossen dit op door een correctie toe te passen op ons sample en daarna berekenen we wanneer deze sterrenstelsels waarschijnlijk zijn gevormd.

In **Hoofdstuk 5** verkennen we de relatie tussen de kleur en de dynamische massa-lichtkracht-verhouding (*mass-to-light ratio*) van een sterrenstelsel. Onze verzameling sterrenstelsels is hiervoor bij uitstek geschikt, omdat we sterrenstelsels hebben met een groot bereik aan leeftijden. Jonge, elliptische sterrenstelsels blijken relatief blauw te zijn en hebben een extreem lage massa-lichtkracht-verhouding ( $M/L$ ), terwijl oude, elliptische sterrenstelsels erg rood zijn en een hoge  $M/L$  hebben. Er is een sterke correlatie tussen  $M/L$  en kleur. Hiermee laten we zien dat de  $M/L$  van een sterrenstelsel nauwkeurig te voorspellen valt aan de hand zijn kleur. We testen verschillende sterpopulatiemodellen, maar we vinden dat geen enkel model de gemeten trends in  $M/L$  tegen kleur goed kan voorspellen. De overeenkomst tussen de data en de modellen verbetert enigszins met andere aannames. Een voorbeeld van zo'n aanname is een andere verhouding tussen lichte en zware sterren. De verschillende modellen vertonen variaties die dusdanig groot zijn, dat het niet mogelijk is om nauwkeurige voorspellingen te doen over de aannames die worden gebruikt in elk van de modellen.



# Curriculum Vitae



I was born on March 18, 1986 in Meppel and spent my childhood in the small village of Oldemarkt in Overijssel. I went to high-school at "Het Linde College" in Wolvega, Friesland. Besides high-school, I worked as a construction worker and welder at All Metal Technics where I learned to build anything from stainless steel. After graduating from high-school (*VWO*) I moved to the "big city" to study astronomy at Leiden University. During my second year I went observing at La Palma with the Isaac Newton Telescope, and discovered my passion for doing research. For my bachelor's thesis I studied the evolution of the axis-ratio distribution of galaxies under supervision of Prof. dr. Marijn Franx. I obtained my Bachelor's degree in August 2007.

During my Master's degree I worked on ionospheric turbulence and predictions for LOFAR supervised by Prof. dr. Huub Röttgering & dr. Shridaran Rengaswamy, and I spent time at Bonn University and the Effelsberg LOFAR Station of the MPIfR. I also assisted Raymond Oonk with observations of Cluster Halos at the Giant Meterwave Radio Telescope in India. At Yale University, where I worked with Prof. dr. Pieter van Dokkum, I worked on my main research project. I spent 3 months measuring color gradients of galaxies from Hubble Space Telescope data. I finished the analysis at Leiden University with Prof. dr. Marijn Franx, after which I received my Master's degree in October 2009 with honors (*Cum Laude*). During my time as a student I was the chair of the student astronomy association 'L.A.D. F. Kaiser', a public lecturer and tour guide at the Leiden Old Observatory, and the chair of the Student Climbing and Alpine association Leiden (LSAC).

In November 2009, I began my doctoral research at Leiden Observatory, working with Prof. dr. Marijn Franx and Prof. dr. Mariska Kriek on the evolution of massive galaxies using Near-Infrared Spectroscopy. My project started with five observing nights at the Very Large Telescope in Chili, using the brand-new spectrograph X-Shooter. I spent a total of seven months working in the USA with Prof. dr. Mariska Kriek at Princeton University, the Harvard-Smithsonian Center for Astrophysics, the University of California at Berkeley, and with Prof. dr. Pieter van Dokkum at Yale University. I have traveled the world to present my work at conferences in Turku (Finland), Beijing (China), Texel (NL), Leiden (NL), given presentation in Cambridge (CfA), Berkeley (UCB), Santa Cruz (UCSC), Pasadena (Caltech and Carnegie), attended the ELIXER school in Astrum, Germany, and the IAC's 2011 Winter School on "Secular Evolution of Galaxies" on Tenerife, Spain.

Besides my doctoral work, I was a teaching assistant to the Bachelor's course on stellar evolution, and the course on galaxies and cosmology. I co-supervised two Bachelor research projects. Furthermore, I was a member of an educational committee and also active in the public outreach committee, where we answered the questions of curious and enthusiastic youth, stubborn old men, and numerous crackpots.





# Nawoord

Het schrijven van dit proefschrift was voor mij onmogelijk geweest zonder alle hulp en steun die ik heb gekregen van collega's, vrienden en familie. Als ik iedereen zo uitgebreid kon bedanken als dat ik zou willen, dan was dit boek twee keer zo dik geweest.

Om te beginnen met de Sterrewacht, waar ik tien jaar geleden voor het eerst een voet over de drempel zette en wat nu een vertrouwde werkplek is geworden met ontzettend veel goede herinneringen. Allereerst wil ik de computer groep bedanken: Erik, David, Niels, Aart, Tycho. Het fantastische werk dat jullie doen wordt veel te weinig gewaardeerd. De dames van het secretariaat: Anita, Alexandra, Kirsten, Liesbeth en in het bijzonder Jeanne. Zonder jullie zou de Sterrewacht een complete chaos worden. Evelijn, dankjewel voor de support bij al mijn verre reizen, en alle overige financiële en Sterrewacht-gerelateerde zaken. Jan, zonder jouw integriteitscontrole was de Sterrewacht een ongeordende boel geweest. Het was een eer om in jouw kantoor mijn proefschrift af te mogen maken. Huub en Xander wil ik bijzonder bedanken voor hun luisterend oor en geweldige ondersteuning met de laatste loodjes.

Many thanks go out to my office mates Gilles and Marissa, who had to listen to all my ranting and swearing at my computer, whilst working on this Thesis. Marissa, you always keep amazing me. Your high-productivity, ideal work-life balance, and the many (well deserved) holidays you found time for: I don't know how you do it. Gilles, er bestaat geen beter officemaatje dan jij. Altijd bereid om te helpen, altijd en overal een goed antwoord op, en niet te vergeten prop-tennis om vijf uur. Ik ben supertrots op het feit dat een toekomstige Nobelprijswinnaar mijn Paranimf wil zijn.

To my galaxy group-members: Daniel, bedankt voor je luisterend oor tijdens de verboden Lavazza koffie, alle ondersteuning en antwoorden op mijn vele domme vragen. Mattia: from Leiden, to Beijing, to Turku, you were a fantastic friend and colleague to be traveling with. Adam, I'm always glad to see you made it another day, and tell us kids how science is really done. Shannon, my favorite American-bro, Wu-Tang out. Moein, you possess a calm that always helped me to relax. Caroline, bedankt voor de gezellige tijd in Finland. Joanna, my gratitude for always listening and for sharing all your wisdom and enthusiasm. Thanks also to Allison's shoes, who soon will be the lonely "soles" of the group. To all the older members of the Leiden mafia: Arjen, Maaike, Ivo, Ryan, Rik, Simone, and Stijn. You have always inspired and impressed me with your high-quality research.

To my dearest friends at the Sterrewacht: Remco, zonder ons thee klaagurtje was ik allang ontploft en gestopt. Voor jou is geen avontuur gek genoeg en ik zal onze gestoorde strandmars nooit vergeten. Renske, ik kan altijd op je rekenen als ik Nederlandse gebruiken of tradities probeer te verdedigen, zonder jou was het een saaie boel geweest. Saskia, zonder jou was ik de opleiding sterrenkunde nooit doorgekomen. Sascha, jouw doorzettingsvermogen is ongelooflijk. Jayne, my most heartfelt thanks for being the person that understood my crazy love for Doctor Who and *HIMYM*. Berenice, you never let me get away with unfounded arguments

and your critical view on the Dutch and the world is always refreshing. Rob, your dark sense of humor always brightened my day. Jeanette, if it wasn't for you I wouldn't have started with salsa, and my life would be complete different. To all my other friends and colleagues at the Sterrewacht: Ali, Alex, Edith, Ernst, Gerard, Henriette, Irene, Koen, Monica, Marcel vD, Marcel H, Marco & Silvia, Maria, Marijke, Maryam, Matteo, Rychard, Thanja, Tiffany, Tim vW., Tim S., and Willem. Coffee, lunch, and borrel would not have been the same without you.

To my close collaborator Rachel, I owe you so much. This thesis wouldn't be half as good if it wasn't for you. To all the people that I met at Yale: Danilo, Gabe, Erica, Joel, Tomer, and Ros. Thank you so much for the great times I spent there. To the wonderful ladies at Berkeley: Ann-Marie, Freeke, Therese, and Sedona. I'm immensely grateful for the way you made me feel at home in California.

Lieve klimvrienden: Sid, Marie-José, Pjotr, Menno, Tiemen, Stefan, Dick, en mijn alpine maatje Wouter. Dankzij jullie voelden zelfs tweedaagse klimtripjes als twee weken vakantie. Pepijn, ik vind het fantastisch hoe jij mijn grootse ideeën tot een voorkant hebt weten te smeden. Patric, jouw koppigheid en ons gekibbel als een getrouwd stel haalt uiteindelijk altijd het beste in mij naar boven, laten we daar vooral mee doorgaan. Lieve Daniëlle, ondanks dat onze wegen gescheiden zijn, wil ik je ontzettend bedanken voor de geweldige tijd die we samen hebben gehad, voor het aanleren van de Canadese *eb*, en mijn verslaving aan Doctor Who.

Aan de nieuwste leden van de familie: David, Jos, Tinus en Piet. Wat ben ik blij dat jullie erbij zijn gekomen. Lieve neefjes en nichtjes, jullie zijn nog veel te klein om dit te lezen, maar jullie malle fratsen en streken helpen mij altijd om het leven en werk niet zo serieus te nemen. Lieve papa, dankjewel voor alles wat je me geleerd hebt: dat ik alles met mijn eigen handen kan maken en uitvinden, en dat je alles kan bereiken door zelfstudie en met een goede dosis doorzettingsvermogen. Lieve mama, was iedereen maar zo lief en vergevingsgezind als jij, de wereld zou er een stuk mooier uitzien. Ontzettend veel dank gaat uit naar mijn broer en zussen, die mij net zo hard hebben proberen op te voeden. Eljakim, je dapperheid en doorzettingsvermogen zijn altijd een inspiratie voor me geweest. Mirjam, ik ben stiekem een beetje jaloers op je kalmte, bergen energie en creativiteit. Alles lijkt je makkelijk af te gaan. Sara, wat ben ik trots op wat je allemaal hebt bereikt, ik vertel je dat veel te weinig. Lea, wie had gedacht dat na onze kinderlijke slaapkamerruzies we opnieuw een kleine studentenkamer zouden delen (al was het maar voor een maandje): wat is er veel veranderd. Naast surf-, klim- en bouldermaatje, ben je een fantastische vriendin. *Onwijs* bedankt voor je steun, advies en kritische blik op het leven. Ik vind het een grote eer dat je mijn Paranimf wilt zijn.

Allerliefste Marlies. Ondanks het feit dat je mij leerde kennen in de meest hectische, chaotische, en onzekere tijd van mijn leven, koos je toch voor mij. Daarvoor ben ik je eeuwig dankbaar. Zonder jouw geduld, onbevooroordeelde mening, liefde, en oneindige gezelligheid, was dit boek niet hetzelfde geweest. Ons avontuur is pas net begonnen.





*"Times change and so must I.  
We all change when you think about it.  
We're all different people all through our lives.*

*And that's ok, that's good, as long as you  
keep moving, as long as you remember  
all the people that you used to be.*

*I will not forget one line of this,  
not one day, I swear."*

-- The Doctor

